5-2011

CELLULOSE NANOCRYSTALS PROPERTIES AND APPLICATIONS IN RENEWABLE NANOCOMPOSITES

Esteban Urena benavides
Clemson University, eurenab@clemson.edu

Recommended Citation

Urena benavides, Esteban, "CELLULOSE NANOCRYSTALS PROPERTIES AND APPLICATIONS IN RENEWABLE NANOCOMPOSITES" (2011). *All Dissertations*. 704.
https://tigerprints.clemson.edu/all_dissertations/704

CELLULOSE NANOCRYSTALS PROPERTIES AND APPLICATIONS IN RENEWABLE NANOCOMPOSITES

A Dissertation
Presented to
the Graduate School of
Clemson University

In Partial Fulfillment
of the Requirements for the Degree
Doctor of Philosophy
Chemical Engineering

---

by
Esteban Eduardo Ureña Benavides
May 2011

Accepted by:
Dr. Christopher L. Kitchens, Committee Chair
Dr. Amod A. Ogale
Dr. Douglas E. Hirt
Dr. Philip J. Brown

ABSTRACT

Development of novel bio-based nanocomposites is fundamental to reduce the dependence on fossil resources and provide a sustainable future. In light of this global problem, cellulose nanocrystals (CNCs) have raised interest due to their remarkable mechanical properties. Adequate design of nanocomposites requires a fundamental understanding of how the structure affects the mechanical properties of the material. However, contradictory results in the literature have revealed a lack of comprehension of this relationship for CNC based composites. Consequently, this work provides an explanation to unusual results for CNC nanocomposites presented in the literature and demonstrates the ability to achieve property enhancements in biopolymer nanocomposites that are attributed to the nanoscale structure and self-assembly of CNCs.

The phase behavior and rheology of CNC aqueous suspension is first studied. The twisted shape of the cellulose crystals induces the transition of aqueous CNC suspensions from an isotropic fluid to a chiral nematic liquid crystal; at even higher concentrations a birefringent gel is obtained. The structural transformations can be identified from rheological measurements given that they affect the viscoelastic properties of the suspensions.

When the CNC aqueous suspensions are blended with sodium alginate solutions, the nanocrystals induce ordering of the alginate chains. These solutions were wet spun to form CNC – calcium alginate nanocomposite fibers. The twisted shape of the cellulose crystals induce the formation of a helical structure where the CNCs spiral around the fiber axis; this structural orientation is coincident with a reduced elastic modulus and an increased elongation at break. Until now this orientation had been observed only in native cellulose fibers and is deterministic of their unique mechanical properties. The presence of CNCs in the dope solution enables an increase in the stretching capacity during fiber spinning and an increase in the apparent jet stretch (J_{A}). Wet spinning at the maximum possible J_{A} retards the appearance of a spiral assembly of the CNC and consequently improves the mechanical properties of the fibers, which is expected with the addition of a rigid nanoparticle. Tensile testing at maximum J_{A} showed a 38% increase in tenacity and a 123% increase in tensile modulus at 10 wt % CNC loading.

Given the importance of realistic measurements of CNC dimensions in suspension, a simple method to analyze static light scattering (SLS) data was developed. The applicability of Debye's expansion of the form factor was extended beyond the second order of the scattering vector. Simple analytical expressions were derived for the fourth and sixth moments of the distances within a nanoparticle that are valid for all shapes and can be used to solve for the average dimensions of monodispersed and polydisperse tri-axial nanorod populations. Without needing to solve for the dimensions, the moments provide information about aspect ratio regardless of the particle's geometry. This methodology can be easily applied to nanoparticles or macromolecules of complex shapes.

DEDICATION

Dedico este trabajo a mis padres, mi esposa y mi hermano. No lo hubiera logrado sin ellos.

I dedicate this work to my parents, my wife and my brother. I could not have done it without them.

ACKNOWLEDGMENTS

I thank my advisor Dr. Christopher L. Kitchens for all the trust that he has invested in me. His guidance has made me grow as a person and a researcher. I deeply thank his kindness, support, patience, perseverance and wisdom throughout the most difficult moments of my adventure in Clemson.

I also thank Dr. Philip J. Brown who gave me a jump start when I had no idea what to do with my project. I am grateful to Dr. Virginia A. Davis for teaching me what I know about liquid crystals and making possible the rheological studies on the cellulose nanocrystal suspensions. I express my gratitude to Dr. Amod A. Ogale for his thoughtful recommendations and instruction throughout my project and Dr. Douglas E. Hirt for reviewing this manuscript and his advice.

I am grateful to Cody Reynolds for teaching me the technique of wet spinning, Marlon Morales for his invaluable help with the wide angle X-ray diffraction experiments and Ao Geyou for the hard work with the rheology experiments. I thank my labmates Dr. Gregory Von White II, Jose Luis Orellana and Fiaz Mohammed for their help, support and invaluable friendship. I also thank all the people who at some point collaborated with this project: Dr. Yong-Jin Chun, Jennifer Moffitt, Chris Powell and Ashley Hart.

Last but not least, I thank all my family for their support and especially my wonderful wife Dr. Linda C. Mota for the endless encouragement, recommendations, guidance and enormous amount of patience required to stand the writing of this dissertation. I thank God for giving me the best wife of the world and a very happy life.

TABLE OF CONTENTS

Page

TITLE PAGE i

ABSTRACT ii

DEDICATION iv

ACKNOWLEDGMENTS v

LIST OF TABLES viii

LIST OF FIGURES ix

CHAPTER

I. INTRODUCTION AND BACKGROUND 1

- Cellulose Nanocrystal Suspension Properties 8
- Nanocomposites from Cellulose Nanocrystals 11
- Dissertation Outline 14
- References 16

II. RHEOLOGY AND PHASE BEHAVIOR OF CONCENTRATED CELLULOSE NANOCRYSTAL AQUEOUS SUSPENSIONS 22

- Introduction 22
- Experimental Section 24
- Results and Discussion 27
- Conclusions 45
- References 46

III. EFFECT OF JET STRETCH AND PARTICLE LOAD ON CELLULOSE NANOCRYSTAL – ALGINATE NANOCOMPOSITE FIBERS 48

- Introduction 48
- Experimental Section 50
- Results and Discussion 56
- Conclusions 72

Table of Contents (Continued)

Page

References ... 73

IV. WIDE ANGLE X-RAY DIFFRACTION OF CELLULOSE NANOCRYSTAL – ALGINATE NANOCOMPOSITE FIBERS ... 78

Introduction ... 78
Experimental Section ... 80
Results and Discussion ... 84
Conclusions ... 100
References ... 101

V. STATIC LIGHT SCATTERING OF DILUTE NANOPARTICLE SUSPENSIONS IN THE RAYLEIGH-GANS-DEBYE REGIME: APPLICATION TO CELLULOSE NANOCRYSTALS ... 104

Introduction ... 104
Theory of Light Scattering ... 106
Moments of r_{ij} ... 108
Results and Discussion ... 119
Conclusions ... 127
Experimental Section ... 127
References ... 129

VI. CONCLUSIONS AND RECOMMENDATIONS ... 132

Conclusions ... 132
Recommendations ... 134
References ... 139

APPENDICES ... 140

A: Details Regarding Rheology Experiments ... 141
B: Supporting Information for Chapter III ... 147
C: Representative Force vs. Deformation Curves ... 156
D: Wide Angle X-Ray Diffraction Patterns ... 158
E: Derivation of Equations for Chapter IV ... 163
F: Correction of AFM Images for Tip Broadening ... 170
G: Permissions ... 177

LIST OF TABLES

Table Page

1.1 Size of CNC Isolated from Various Cellulose Sources 6

3.1 Chemical Composition of Alginates Isolated from *Macrocystis pyrifera* 51

3.2 Fiber Yarn Denier and Calcium Content Expressed in Percentage of Negatively Charged Sites Occupied by a Calcium Ion 67

4.1 Comparison of Tensile Properties with Spiral Angles and Peak Widths of the Cellulose (2,0,0) Intensity Distribution in CNC – Calcium Alginate Fibers 95

5.1 Moments of the Difference of Distances within Nanoparticles of Different Shapes 110

5.2 Moments, and Molecular Weight Measured with Light Scattering and Calculated from AFM Dimensions 121

5.3 Comparison of number average dimensions of CNC measured from AFM and light scattering 124

B.1 Yarn denier of CNC-Alginate fibers at Different Apparent Jet Stretches and CNC Loads 152

B.2 Elongation at break of CNC-Alginate fibers at Different Apparent Jet Stretches and CNC Loads 152

B.3 Tenacity of CNC-Alginate fibers at Different Apparent Jet Stretches and CNC Loads 153

B.4 Modulus of CNC-Alginate fibers at Different Apparent Jet Stretches and CNC Loads 153

B.5 Tensile Energy at Break of CNC-Alginate Fibers at Different Apparent Jet Stretches and CNC Loads 154

LIST OF FIGURES

Figure Page

1.1 Cellulose chemical structure showing a cellobiose repeat unit composed of two anhydroglucose subunits 2

1.2 Schematic representation of the cellulose Iβ unit cell 2

1.3 Schematic representation of the isolation of CNC... 4

1.4 AFM image of CNC isolated from wood pulp 7

1.5 Size distribution histogram of CNC isolated from wood pulp 8

1.6 Polarized light imaging 9

1.7 Phase behavior of CNC suspensions isolated from cotton 11

2.1 Size distribution of CNC used in Chapter 2... 28

2.2 Cross polarized images showing the phase separation of CNC suspensions.. 29

2.3 Amount of liquid crystalline phase as a function of CNC concentration and temperature 30

2.4 Polarized light microscopy of CNC suspensions at variable concentration and temperature 31

2.5 Steady shear and complex viscosities of several CNC suspensions.. 33

2.6 Time-concentration superposition of the viscosities of CNC suspensions.. 35

2.7 Rheological properties versus concentration of CNC suspensions.. 37

2.8 Linear viscoelstic properties of CNC suspensions with various concentrations 40

List of Figures (Continued)

Figure Page

2.9 Time – concentration superposition of the viscoelstic properties of CNC suspensions 41

2.10 Flow curves of CNC suspensions at various temperatures 44

3.1 Atomic force microscopy (AFM) image of CNC isolated from cotton powder 57

3.2 Size distribution histograms of CNC used in Chapter 3 59

3.3 Viscosity vs shear rate of CNCs suspended in sodium alginate solutions 61

3.4 Image of CNCs suspensions between crossed polarized sheets 62

3.5 FESEM images of alginate fibers 64

3.6 Tensile properties of alginate fibers 65

3.7 Effect of CNCs load on the maximum apparent jet stretch 68

3.8 Effect of jet stretch on the mechanical properties of alginate fibers 69

4.1 WAXD of a calcium alginate fiber spun at a J_A of 2.4 85

4.2 Schematic structure of MG and GG dimers 86

4.3 WAXD of a 10 wt % CNC – calcium alginate fiber spun at a J_A of 2.4 88

4.4 “Powder” diffraction pattern of the calcium alginate component 89

4.5 “Powder” diffraction pattern of the CNC component 90

4.6 Effect of CNC load on the degree of orientation of the crystallites 92

4.7 Azimuthal intensity scan of the (2,0,0) cellulose reflection 94

List of Figures (Continued)

Figure Page

4.8 Schematic representation of the assembly of CNC in a calcium alginate fiber 97

4.9 CNC load calibration curve 100

5.1 Form factors calculated for a cuboid and an ellipsoid 111

5.2 Normalized moments versus aspect ratio 114

5.3 Normalized moments of triaxial nanoparticles versus ratio of axes C/A 117

5.4 Effect of volume polydispersity on the behavior of the normalized moments 118

5.5 Scattering intensity construction for several CNC samples 120

5.6 Atomic force microscopy image of CNC isolated from cotton 122

6.1 Titration of CNC with sodium hydroxide 135

6.2 Proposed wet spinning setup 137

A.1 Transient response of a 12.0 wt % CNC suspensions 141

A.2 Amplitude sweep of a 21.8 wt % CNC suspensions 143

B.1 Diagram of Teflon tube used to wind up fibers 148

B.2 Apparatus for wet spinning 148

B.3 The wet spun fiber is directed using glass rods 149

B.4 Spinneret, O-ring, filter and housing 149

B.5 Spinneret used for wet spinning 150

B.6 Fiber on Teflon tube inside a water bath 150

List of Figures (Continued)

Figure Page

B.7 Picture of CNC-Alginate fibers filled with 25%CNC spun at an apparent jet stretch of 4.6 151

B.8 Polarized light microscopy pictures of a 50%wt CNC/sodium alginate film 151

B.9 WAXD pattern and azymuthal peak of the fiber containing 5%wt CNC 154

B.10 WAXD pattern and azymuthal peak of the fiber containing 10%wt CNC 155

B.11 DTG traces of CNC and CNC-alginate fibers 155

C.1 Force vs. deformation curves for a pure Calcium alginate fiber spun at $J_A = 2.4$ 156

C.2 Force vs. deformation curves for a Calcium alginate fiber with 10 wt % CNC spun at $J_A = 4.2$ 156

C.3 Force vs. deformation curves for a Calcium alginate fiber with 50 wt % CNC spun at $J_A = 2.4$ 157

D.1 WAXD, 0 wt % CNC fiber, $J_A = 2.4$ 158

D.2 WAXD, 2 wt % CNC fiber, $J_A = 2.4$ 158

D.3 WAXD, 2 wt % CNC fiber, $J_A = 3.4$ 159

D.4 WAXD, 5 wt % CNC fiber, $J_A = 2.4$ 159

D.5 WAXD, 5 wt % CNC fiber, $J_A = 3.8$ 160

D.6 WAXD, 10 wt % CNC fiber, $J_A = 2.4$ 160

D.7 WAXD, 10 wt % CNC fiber, $J_A = 4.2$ 161

D.8 WAXD, 25 wt % CNC fiber, $J_A = 4.6$ 161

D.9 WAXD, 50 wt % CNC fiber, $J_A = 2.4$ 162

List of Figures (Continued)

Figure Page

D.10 WAXD, 50 wt % CNC fiber, J_A = 2.8 162

F.1 Snapshot of a Gwyddion 2.22 session showing an AFM raw data image 170

F.2 Nanoparticles masked during a Gwyddion 2.22 session 171

F.3 Removal of background from an AFM image 172

F.4 Image corrected for background and scan lines 173

F.5 AFM image of a porous aluminum surface during a Gwyddion 2.22 session 174

F.6 Blind tip estimation window 175

F.7 Tip model estimated with Gwyddion 2.22 175

F.8 Surface reconstruction and tip image windows 176

F.9 Image after tip deconvolution with Gwyddion 2.22 176

CHAPTER ONE

INTRODUCTION AND BACKGROUND

Cellulose nanocrystals (CNCs) are crystalline nanoparticles made from cellulose, which are highly relevant for the development of new bio-based materials with enhanced properties. They are a potential nanocomposite reinforcement agent given their relatively low density (1.6 g/ml), high strength (10 GPa)[1] and high modulus (143 GPa)[2]. CNCs can also be processed into materials with unique optical properties that reflect a specific wavelength of light or are transparent.[3-5] They are relevant for the preparation of biomedical devices, implants, and textiles given that they are biocompatible and non-toxic.[1, 6] Moreover, CNCs are extensively available all around the world and a potential byproduct of the future cellulosic biofuels industry.[1, 6]

Cellulose is the most abundant polymer of earth;[4, 7] it is the main component of most plant biomass, it is found in tunicates (sea animals), in green algae, fungi and can be synthesized by cellulose producing bacteria.[6, 8] It is a polycarbohydrate composed of a series of cellobiose units, each of which is formed by two anhydroglucose subunits rotated by 180° from each other (Figure 1.1). Cellulose chains can assemble in different crystalline structures that vary depending on source and following processing. Cellulose II is the most common allomorph, found in regenerated cellulose, and the most thermodynamically stable structure. Cellulose Iα and Iβ are the most abundant in nature.[8, 9] Algal and bacterial cellulose are rich in the Iα structure, while cellulose Iβ is the major component in tunicate and higher plants like cotton, wood pulp, ramie, etc.[8, 10]

There have been reports that the metastable Iα allomorph can be transformed into the Iβ structure by annealing.[10, 11] Focus is given here to the cellulose Iβ structure since cellulose nanocrystal (CNC) suspensions are most commonly isolated from specimens that are rich in this allomorph.

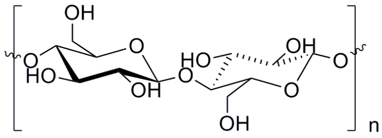

Figure 1.1. Cellulose chemical structure showing a cellobiose repeat unit composed of two anhydroglucose subunits.

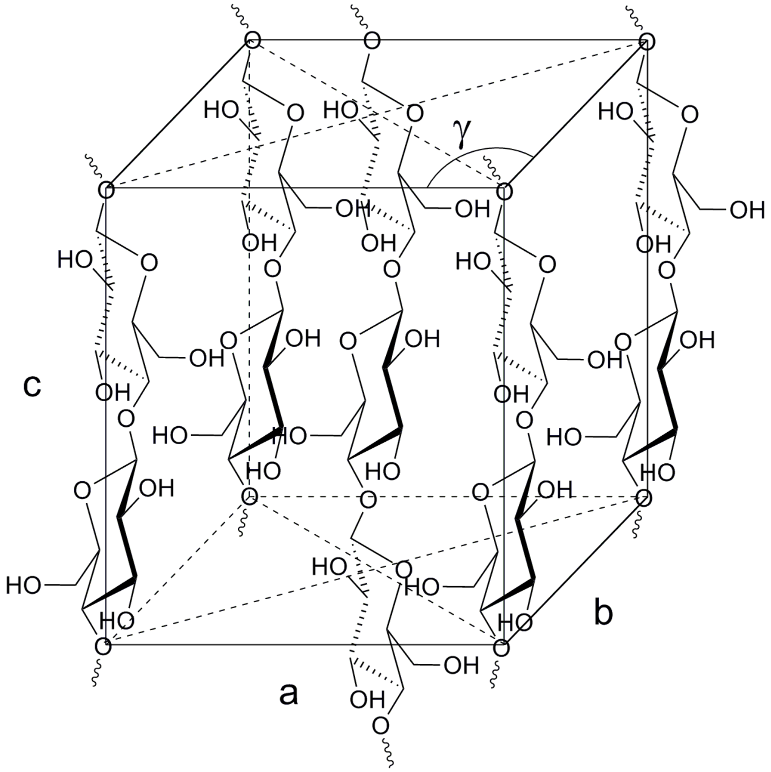

Figure 1.2. Schematic representation of the cellulose Iβ unit cell.

The crystalline structure of cellulose Iβ has been described as monoclinic with two parallel cellulose chains crossing each unit cell, one at the center, and the other at the corner. A very thorough analysis of this structure by Nishiyama et al. has given a complete description of the structure, that has lattice parameters $a = 0.7785$ nm, $b = 0.8202$ nm, $c = 1.038$ nm (chain axis) and $\gamma = 96.5°$. The study also gives specific coordinates for all the atoms, including hydrogen.[12] A single cellulose Iβ crystallite is an elongated domain formed by a tridimensional repetition of the unit cell represented in Figure 1.2; where the largest axis of the crystallite is parallel to the c lattice parameter. Natural cellulose fibrils are formed by several crystallites that are interconnected by disordered cellulose chains; very often hemicellulose is also present. In the lateral directions the fibril is held together by hydrogen bond interactions; however in the axial direction covalent glycosidic bonds are dominant. It must be noted that a single cellulose chain can grow through multiple crystallites.

Isolation of CNC is achieved by controlled preferential acid hydrolysis of the disordered regions which forms low molecular weight carbohydrates (mostly glucose) and releases the crystalline domains. This was first reported by Rånby in 1951, who was able to obtain electron microscopy images of single crystals isolated from wood through sulfuric acid hydrolysis.[13] Since then, methods have been developed for the isolation of CNC using mineral acids, mostly hydrochloric and sulfuric acids. When HCl is employed, the suspended CNCs easily agglomerate due to hydrogen bonding between crystallites forming micron size agglomerates. When the hydrolysis is performed with H_2SO_4, the negatively charged sulfate groups are introduced on the surface of the crystallites, which prevents agglomeration, yielding a stable suspension of nanosized crystalline particles (Figure 1.3).

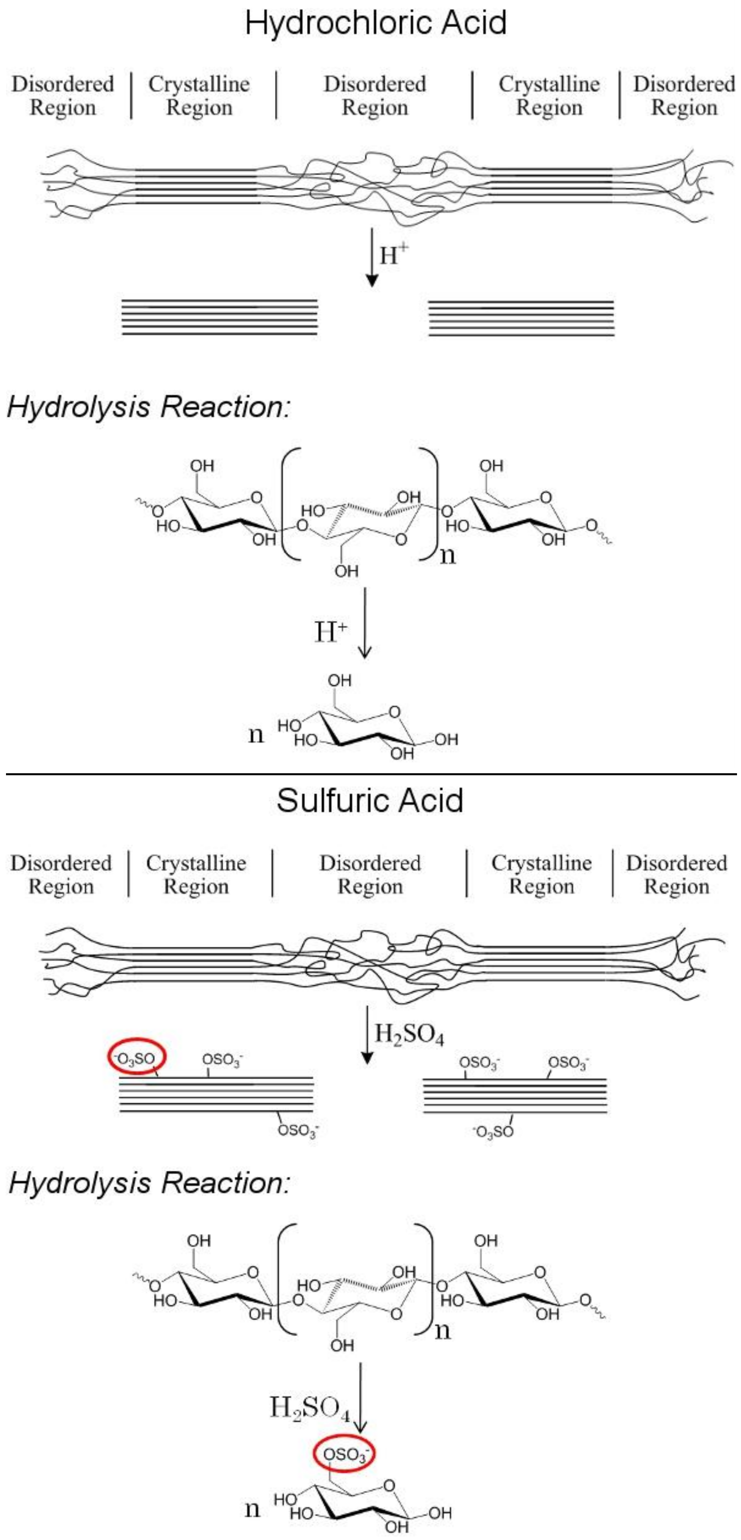

Figure 1.3. Schematic representation of the isolation of CNC.

The reaction conditions depend on the acid used. For HCl, typical reaction conditions are 105 °C (reflux temperature), for a variable time depending on source (20 min for cotton) and an acid concentration of 2.5 to 4 M.[7, 14] In the case of H_2SO_4, 45 °C to 50 °C, for 45 to 60 min, with an acid concentration of 64 to 65 % are common.[7, 15, 16] Purification of the suspensions is achieved by successive centrifugation and decantation of the supernatant liquid until the particles no longer precipitate, followed by extensive dialysis against deionized water or a buffer solution. In some cases the suspension is further purified using ion exchange resin.[15, 17] The final step is generally ultrasonication for 7 min, 5 times with an approximate power of 120 W to disperse the nanoparticles. The purification also varies depending on the type of acid used.[18]

The isolated crystallites have traditionally been referred to as microcrystalline cellulose (MCC). The terms nanocrystals, nanocellulose and nanowhiskers have been adopted for the suspensions composed of crystallites with nanoscale dimensions due to a growing interest in the area of bio-nanocomposites. These terms also refer to agglomerated samples of individual crystallites; as long as all the disordered cellulose has been removed. Commercial grade MCC is mostly formed by partially hydrolyzed cellulose fibrils which still contain disordered cellulose.[19, 20] It has found applications in the food industry as a fat substitute in emulsions, such as salad dressings, dairy products, bakery, etc.[21] The pharmaceutical industry has extensively employed MCC as a tablet excipient.[19, 22, 23]

Table 1.1. Size of CNC Isolated from Various Cellulose Sources.[7]

Cellulose Source	Length (nm)	Width (nm)	Technique
Bacterial	100 – 1000	10 – 50	TEM
Cotton	100 – 150	5 – 10	TEM
Cotton	150 – 210	5 – 11	AFM
MCC	35 – 265	3 – 48	TEM
Ramie	150 – 250	6 – 8	TEM
Sisal	100 – 500	3 – 5	TEM
Soft Wood	100 – 150	4 – 5	AFM
Hard Wood	140 – 150	4 – 5	AFM
Tunicate	1000 – 3000	15 – 30	TEM
Tunicate	---	8.8 x 18.2	SANS
Valonia[24]	>100	14 – 18	TEM

The individual cellulose crystallites have sizes that vary depending on the source of cellulose. Habibi et al. have provided sizes of CNC depending on the source;[7] some of these values are reproduced in Table 1.1. The hydrolysis conditions also affect the dimensions and size distribution of the isolated particles; longer hydrolysis times and higher temperatures typically yield shorter rods.[16, 25, 26] However, a level-off degree of polymerization is typically obtained which corresponds to the length of the actual crystalline domain in the cellulose source.[16] If the hydrolysis conditions are too harsh the crystalline domains can be completely hydrolyzed. The dimensions of CNC are readily determined by atomic force microscopy (AFM),[27] transmission electron microscopy

(TEM),[27] or by scattering techniques such as small angle neutron scattering (SANS),[28] small angle X-ray scattering (SAXS)[28] and static light scattering (SLS)[14]. A representative AFM image of CNC isolated from wood pulp is observed in Figure 1.4 and a size distribution is shown in Figure 1.5. Some differences may arise from one technique to another; thus the method used to measure the dimensions is also provided in Table 1.1.

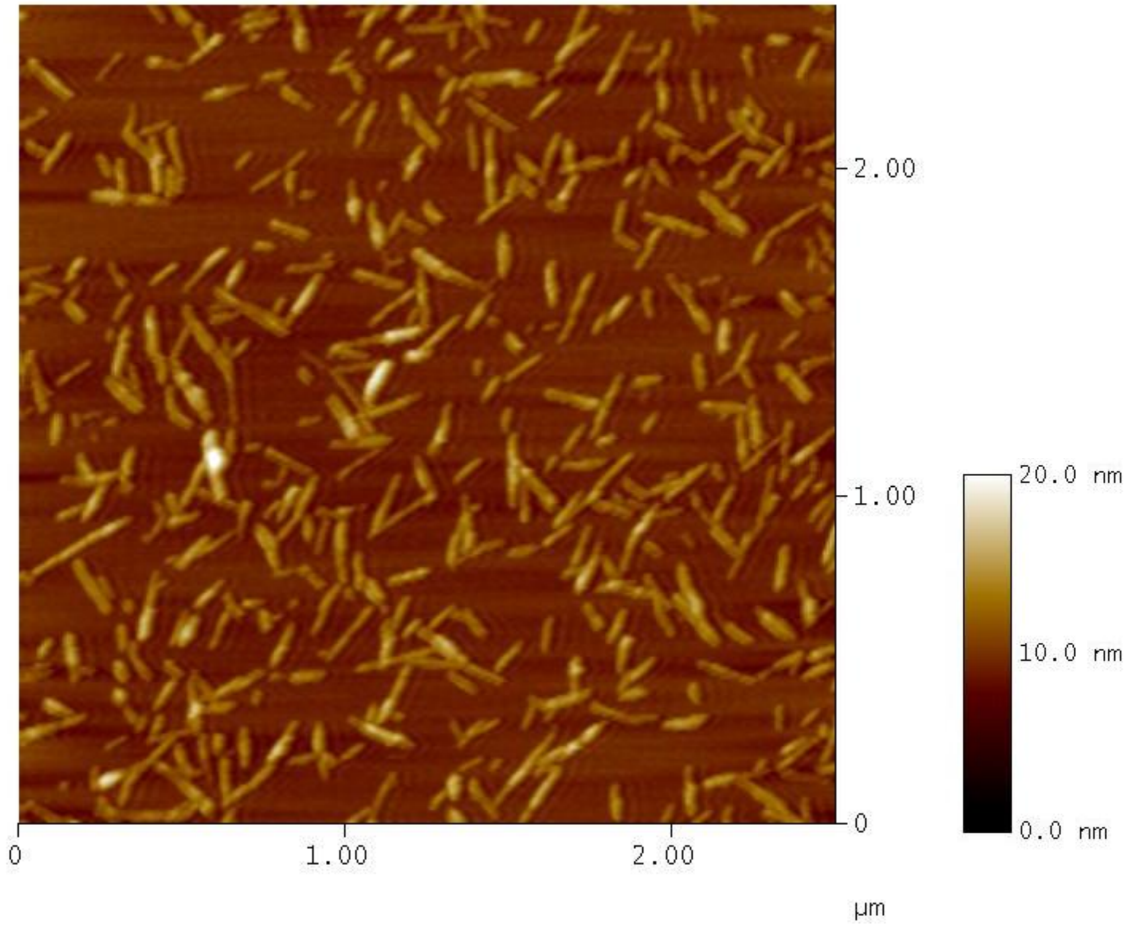

Figure 1.4. AFM image of CNC isolated from wood pulp.

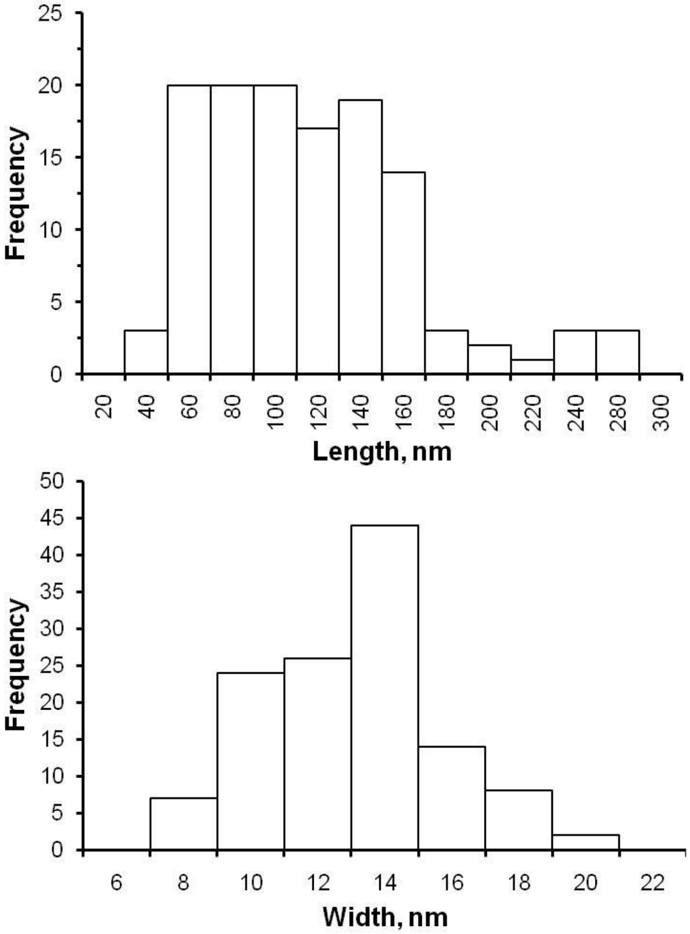

Figure 1.5. Size distribution histogram of CNC isolated from wood pulp.

Cellulose Nanocrystals Suspension Properties

CNC isolated via sulfuric acid hydrolysis form very stable dispersions that possess extremely rich phase behavior that is of significant interest from a fundamental standpoint, as well as for practical applications of rod-shaped nanoparticles and liquid crystalline materials. The CNC stability arises from the electrostatic interactions between the negatively charged surface sulfate groups. At dilute concentrations, the CNCs are dispersed in an aqueous solution and possess random orientation, forming an isotropic phase. As the concentration of CNCs increases, a phase boundary is reached where a dense liquid crystalline, anisotropic phase appears and remains in equilibrium with the isotropic suspension.[17, 29] Revol et al. first identified the liquid crystalline phase as chiral nematic (also known as cholesteric).[29] This type of structure is composed of layers of suspension in which the nanoparticles orient in a preferential direction (director); however the director of each layer is rotated with respect to the previous one;[30] a schematic representation is provided in Figure 1.6a. The vertical distance required to complete a 360° rotation of the director is known as the helical pitch (P).

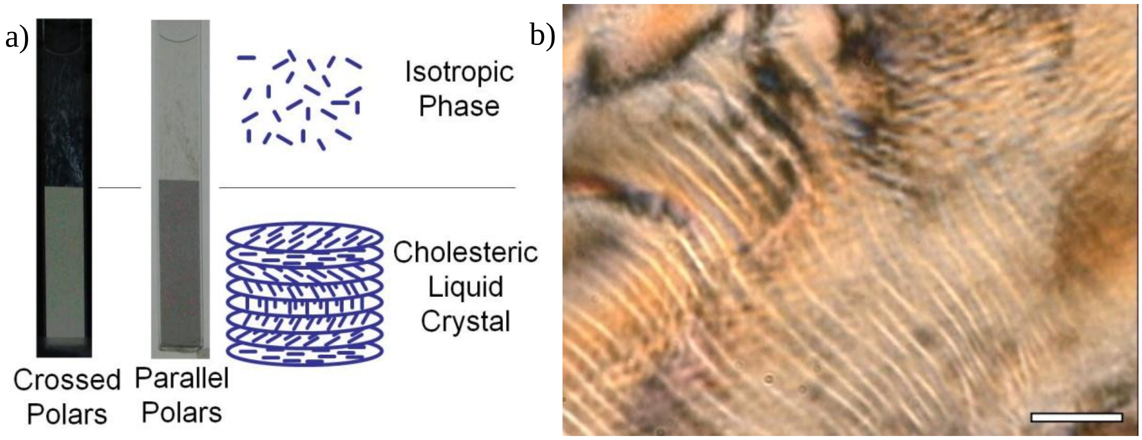

Figure 1.6. Polarized light imaging. a) Macroscopic phase separation in a suspension containing 0.095 g/ml of CNC. b) Fingerprint texture from a cholesteric CNC film, the scale bar corresponds to 50 µm.

An optically anisotropic material (like a liquid crystal) can be identified by observation with polarized light. The refractive index of these materials varies with direction; as a consequence the polarized light is rotated as it travels through the sample. In Figure 1.6a the isotropic phase looks dark when viewed between cross polarized films, but it appears clear if the polarization is parallel; the opposite occurs with the liquid crystalline phase which rotates the light polarization. Macroscopic birefringence is an indication of optical anisotropy but does not allow distinguishing the type of order; polarized light microscopy is employed for this purpose.[17, 29] Figure 1.6b shows a polarized light microscopy picture of a film prepared by drying a CNC suspension on a microscope slide; a fingerprint texture can be observed which is characteristic of the cholesteric type of ordering. The same texture is observed if the anisotropic liquid sample is imaged before drying. [17, 29]

The relative volume of liquid crystalline (anisotropic) and disordered (isotropic) phases can be easily quantified on the macroscale by measuring the height from CNC dispersions that have been allowed to settle. Also if a sample is drawn from each phase, the concentration can be measured by gravimetric methods. The volume of liquid crystalline phase in any suspension of rods should increase linearly with total particle composition if the concentration in the isotropic (c_i) and anisotropic (c_a) phases remain constant throughout the biphasic region.[17] According to the Stroobants-Lekkerkerker-Odijk (SLO) theory this is not expected to occur for charged and polydispersed rods like CNCs. Indeed, Figure 1.7 shows a monotonic increase of c_i and c_a and a non-linear relation of the anisotropic volume with concentration. However if the ionic strength is maintained constant for all samples then an almost linear relation can be obtained.[17] According to Flory theory, the critical concentrations that identify the phase transitions are a function of length and polydispersity. Longer rods orient at a lower concentration; consequently, a larger polydispersity broadens the biphasic region.[15-17] In Figure 1.7, a step increase is observed for the volume of liquid crystal at 14.4 wt %; however it is not a real indication of a phase transition, instead it may be a consequence of an increased viscosity which prevents separation of the anisotropic (liquid crystalline) phase.

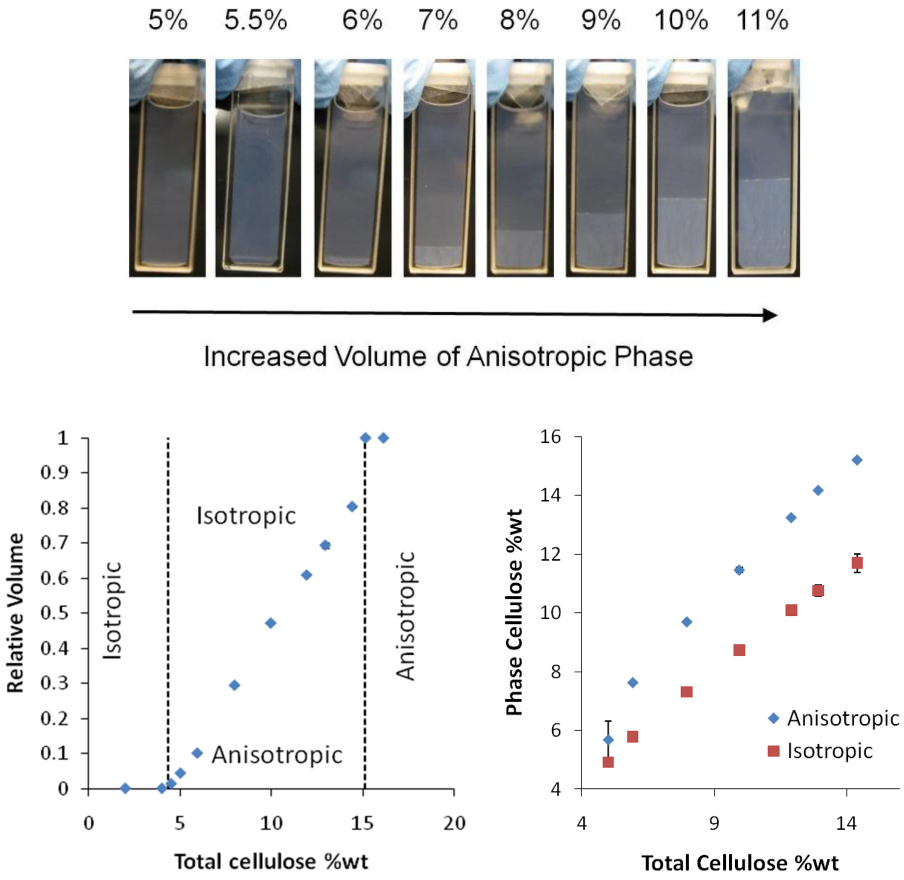

Figure 1.7. Pictures showing phase separation CNC suspensions from cotton (top), phase behavior measurements (bottom). CNC length = 102 nm, standard deviation = 56nm

Nanocomposites from Cellulose Nanocrystals

The first report of a nanocomposite material was done in 1989; researchers from Toyota prepared a polyamide 6 reinforced with montmorillonite clay obtaining significant improvements in tensile strength, modulus and heat resistance.[1, 31] The reinforcement effect of nanosize fillers is strongly related to their large surface area, which facilitates the stress transfer from the matrix to the filler. Moreover, data has shown that nanoparticles can induce crystallization[32] of the matrix material improving its thermomechanical properties.[1, 33] Favier et al. published the first CNC reinforced nanocomposite, they used tunicate nanocrystals to increase the shear modulus of a styrene-co-butyl acrylate latex material.[34] Since then, there has been an increased interest in the preparation of nanocomposites from cellulose nanoparticles.[1]

Some examples of biobased polymers studied are poly(hydroxyoctanoate) (PHO),[35] cellulose acetate butyrate (CAB),[36] polylactic acid (PLA),[37, 38] and plasticized starch.[39, 40] CNCs have also been utilized to reinforce synthetic polymers like polypropylene,[41] poly(oxyethylene) (POE),[42] poly(styrene-*co*-butyl acrylate),[34] poly(vinyl chloride) (PVC),[43] polyaniline,[44] and poly(*p*-phenylene ethynylene).[44] Significant reinforcement is generally achieved above the glass transition temperature (T_g), e.g. bacterial cellulose dispersed in a CAB nanocomposite increased the storage modulus 25 times at 10 wt. % CNCs and at temperatures above the CAB T_g.[36] Below the T_g little reinforcement is generally obtained; for the CAB example only a two-fold increase was observed.[36] The reinforcing nature of CNC nanocomposites has been attributed to a percolation effect, where the nanocrystals form a “skeleton” inside the matrix presumably caused by hydrogen bonding between the particles themselves.[1] The percolation model is consistent with the reinforcement above the T_g. As the polymer chains gain mobility causing the matrix to soften, the CNC network remains strong leading to the significant improvement of mechanical performance at high temperatures.

Given the hydrophilic nature of the CNCs, Grunert et al. modified their surface to improve the compatibility with the hydrophobic CAB. Although, the chemical treatment did not change the morphology or the crystallinity of the CNCs, it reduced their reinforcing capacity.[36] Similar trends have been observed in other systems like natural rubber reinforced with chitin whiskers.[1] This highly unusual finding has been attributed to the percolation effect since strong particle – matrix interactions screen the hydrogen bonds that build up the cellulose network.

Another consequence of percolation is the necessity to use high CNC loads to allow interaction of the nanoparticles. An example is the addition of CNCs into a plasticized starch matrix reported by Anglès and Dufresne where a negligible reinforcement was obtained at cellulose loads below 25 wt %; moreover, in a humid environment, the rubbery modulus decreased upon addition of the nanocrystals.[39, 40] The use of large aspect ratio crystals reduces the required cellulose concentration; consequently the crystallites isolated from tunicate have become very popular.[1] Nevertheless, improvement of the mechanical properties can also be achieved with lower aspect ratio particles; since cotton and wood pulp are relatively low cost cellulose sources the shorter CNC isolated from them have also gained interest. The percolation model explains the behaviors observed at high CNCs loads; however there is a lack of understanding of the low reinforcement obtained at concentrations below the formation of the network.

Important optical properties can be obtained from nanocomposites based on CNC. This is achieved by thin film interference principles[5] or from the chiral nematic order,[3] which can be induced into an organic or inorganic matrix. According to the former principle, the films provide different colors depending on the thickness of the films. This is caused by destructive interference of the light reflected from the film/air interface and the film/substrate interface.[5] The latter principle relies on the fact that films with a chiral structure reflect light with a wavelength equal to nP, where n is the refractive index and P is the helical pitch.[3] The size of the pitch depends on parameters like temperature, concentration, ionic strength and presence of a magnetic field.[45] The pitch can also vary with length and consequently with CNC source. Beck-Candanedo et al. showed that samples isolated from black spruce (softwood) and eucalyptus (hardwood) have pitches that increase from 7 to 21 μm when the average length varied from 105 to 147 nm;[15] moreover pitches of 140 to 250 μm have been reported for suspensions isolated from tunicate.[46] All the previous factors should be considered for tuning the optical properties of CNC based composites.

Dissertation Outline

The liquid crystal (LC) ordering present in solutions of stiff polymer chains and in suspensions of anisotropic nanoparticles have an important effect on the viscoelastic properties of the material.[47, 48] As previously discussed, the transition from isotropic to LC is dependent on concentration; consequently, for nematic and chiral nematic liquid crystals, a maximum viscosity is often detected in the biphasic region, followed by a minimum located near the beginning of the completely liquid crystalline section of the phase diagram.[47, 49] In CNC suspensions, this behavior has not been observed; moreover no studies have been published regarding their linear viscoelastic properties. To appropriately understand the structure of CNC suspensions, their viscoelastic properties are studied in Chapter 2 at variable concentration and temperature. The rheological measurements are complemented with polarized light microscopy to better understand the evolution of the ordering. Until now, the effect of temperature on the viscosity and phase behavior had never been considered. Moreover, previous studies have been limited to concentrations below the gel formation;[50-53] here the gel region is considered.

The properties of any material are strongly influenced by its structure, which in turn can be affected by the addition of small amounts of nanofillers. Nanoparticles often behave as templates that induce crystallization of the matrix in which they are introduced, CNCs are not an exception.[32, 54] Understanding the structure of viscoelastic CNC suspensions, as is studied in Chapter 2, facilitates the interpretation of their effect on the ordering of a nanocomposite material. The structure-property relations in CNC nanocomposites have not been clearly understood and are thus an important component of this dissertation.

In Chapter 3, CNC – calcium alginate nanocomposite fibers are formed by wet-spinning a sodium alginate – CNC dope solution into a calcium chloride bath. The properties of the dope solution are studied first to detect if the CNCs induce ordering of the alginate chains prior to wet spinning. The nanocomposite fibers are produced in a batch mode as described in the chapter and in Appendix B. The morphology of the resulting material is analyzed using scanning electron microscopy, and their mechanical properties are measured by tensile testing. Surprisingly the tenacity and tensile modulus both decrease upon addition of the CNCs; however the elongation at break increases, as well as the capacity to stretch the fibers during spinning. Ultimately, reinforcement is possible by increasing the drawing speed (apparent jet stretch) to the maximum allowable value at each CNC concentration; however, several questions remain open regarding the structure of the fibers which are addressed in the following chapter.

A detailed wide angle X-ray diffraction (WAXD) analysis of the CNC – alginate fibers is provided in Chapter 4. WAXD is used to determine the structure of the fibers and the orientation of the CNC, and draw relationships between the mechanical properties, fiber drawing parameters, and the orientation / assembly of the crystallites within the alginate matrix. It is observed here that the helical structures observed in native cellulose fibers are detected in the CNC – alginate nanocomposite fibers, caused by a twist analogous to the formation of chiral nematic suspensions in aqueous CNC systems. The discussion presented in this chapter contributes significantly to understanding the unusual behavior of CNC nanocomposites presented in the literature.

Given the importance of accurate measurement of nanoparticle dimensions for all types of applications, Chapter 5 provides an improved method to analyze static light scattering data from dilute nanoparticle suspensions. It is demonstrated that Debye's expansion of the form factor[55, 56] can be used to obtain information about elongation of the nanoparticles without any previous knowledge about the shape. Moreover, equations are derived that can be used to calculate the exact dimensions of triaxial particles with or without polydispersity. The methods derived in this section can be applied to other scattering techniques such as SANS or SAXS.

References

1. Azizi Samir, M. A. S.; Alloin, F.; Dufresne, A. Review of Recent Research into Cellulosic Whiskers, their Properties and their Application in Nanocomposite Field. *Biomacromolecules* **2005**, *6*, 612-626.

2. Šturcova, A.; Davies, G. R.; Eichhorn, S. J. Elastic Modulus and Stress-Transfer Properties of Tunicate Cellulose Whiskers. *Biomacromolecules* **2005**, *6*, 1055-1061.

3. Shopsowitz, K. E.; Qi, H.; Hamad, W. Y.; MacLachlan, M. J. Free-Standing Mesoporous Silica Films with Tunable Chiral Nematic Structures. *Nature* **2010**, *468*, 422-425.

4. Eichhorn, S. J. et al Review: Current International Research into Cellulose Nanofibres and Nanocomposites. *J. Mater. Sci.* **2010**, *45*, 1-33.

5. Cranston, E. D.; Gray, D. G. Morphological and Optical Characterization of Polyelectrolyte Multilayers Incorporating Nanocrystalline Cellulose. *Biomacromolecules* **2006**, *7*, 2522-2530.

6. De Souza Lima, M. M.; Borsali, R. Rodlike Cellulose Microcrystals: Structure, Properties, and Applications. *Macromolecular Rapid Communications* **2004**, *25*, 771-787.

7. Habibi, Y.; Lucia, L. A.; Rojas, O. J. Cellulose Nanocrystals: Chemistry, Self-Assembly, and Applications. *Chem. Rev.* **2010**, *110*, 3479-3500.

8. O'Sullivan, A. C. Cellulose: The Structure Slowly Unravels. *Cellulose* **1997**, *4*, 173-207.

9. Klemm, D.; Heublein, B.; Fink, H. -.; Bohn, A. Cellulose: Fascinating Biopolymer and Sustainable Raw Material. *Angew. Chem. ,Int. Ed.* **2005**, *44*, 3358-3393.

10. Nishiyama, Y.; Sugiyama, J.; Chanzy, H.; Langan, P. Crystal Structure and Hydrogen Bonding System in Cellulose I[Alpha] from Synchrotron X-Ray and Neutron Fiber Diffraction. *J. Am. Chem. Soc.* **2003**, *125*, 14300-14306.

11. Horii, F.; Yamamoto, H.; Kitamaru, R.; Tanahashi, M.; Higuchi, T. Transformation of Native Cellulose Crystals Induced by Saturated Steam at High Temperatures. *Macromolecules* **1987**, *20*, 2946-2949.

12. Nishiyama, Y.; Langan, P.; Chanzy, H. Crystal Structure and Hydrogen-Bonding System in Cellulose I[Beta] from Synchrotron X-Ray and Neutron Fiber Diffraction. *J. Am. Chem. Soc.* **2002**, *124*, 9074-9082.

13. Rånby, B. G. Fibrous Macromolecular Systems. Cellulose and Muscle. the Colloidal Properties of Cellulose Micelles. *Discuss. Faraday Soc.* **1951**, *11*, 158-164.

14. Braun, B.; Dorgan, J. R.; Chandler, J. P. Cellulosic Nanowhiskers. Theory and Application of Light Scattering from Polydisperse Spheroids in the Rayleigh-Gans-Debye Regime. *Biomacromolecules* **2008**, *9*, 1255-1263.

15. Beck-Candanedo, S.; Roman, M.; Gray, D. G. Effect of Reaction Conditions on the Properties and Behavior of Wood Cellulose Nanocrystal Suspensions. *Biomacromolecules* **2005**, *6*, 1048-1054.

16. Dong, X. M.; Revol, J.; Gray, D. G. Effect of Microcrystallite Preparation Conditions on the Formation of Colloid Crystals of Cellulose. *Cellulose* **1998**, *5*, 19-32.

17. Dong, X. M.; Kimura, T.; Revol, J.; Gray, D. G. Effects of Ionic Strength on the Isotropic-Chiral Nematic Phase Transition of Suspensions of Cellulose Crystallites. *Langmuir* **1996**, *12*, 2076-2082.

18. Braun, B.; Dorgan, J. R. Single-Step Method for the Isolation and Surface Functionalization of Cellulosic Nanowhiskers. *Biomacromolecules* **2009**, *10*, 334-341.

19. Farag Badawy, S. I.; Gray, D. B.; Hussain, M. A. A Study on the Effect of Wet Granulation on Microcrystalline Cellulose Particle Structure and Performance. *Pharm. Res.* **2006**, *23*, 634-640.

20. Evans, R.; Luner, P. Coagulation of Microcrystalline Cellulose Dispersions. *J. Colloid Interface Sci.* **1989**, *128*, 464-476.

21. McClements, D. J.; Demetriades, K. An Integrated Approach to the Development of Reduced-Fat Food Emulsions. *Crit. Rev. Food Sci. Nutr.* **1998**, *38*, 511-536.

22. Ek, R.; Wormald, P.; Östelius, J.; Iversen, T.; Nyström, C. Crystallinity Index of Microcrystalline Cellulose Particles Compressed into Tablets. *Int. J. Pharm.* **1995**, *125*, 257-264.

23. Ishikawa, T.; Mukai, B.; Shiraishi, S.; Utoguchi, N.; Fuji, M.; Matsumoto, M.; Watanabe, Y. Preparation of Rapidly Disintegrating Tablet using New Types of Microcrystalline Cellulose (PH-M Series) and Low Substituted-Hydroxypropylcellulose Or Spherical Sugar Granules by Direct Compression Method. *Chem. Pharm. Bull.* **2001**, *49*, 134-139.

24. Bourret, A.; Chanzy, H.; Lazaro, R. Crystallite Features of Valonia Cellulose by Electron Diffraction and Dark-Field Electron Microscopy. *Biopolymers* **1972**, *11*, 893-898.

25. Elazzouzi-Hafraoui, S.; Nishiyama, Y.; Putaux, J.; Heux, L.; Dubreuil, F.; Rochas, C. The Shape and Size Distribution of Crystalline Nanoparticles Prepared by Acid Hydrolysis of Native Cellulose. *Biomacromolecules* **2008**, *9*, 57-65.

26. Bondeson, D.; Mathew, A.; Oksman, K. Optimization of the Isolation of Nanocrystals from Microcrystalline Cellulose by Acid Hydrolysis. *Cellulose* **2006**, *13*, 171-180.

27. Kvien, I.; Tanem, B. S.; Oksman, K. Characterization of Cellulose Whiskers and their Nanocomposites by Atomic Force and Electron Microscopy. *Biomacromolecules* **2005**, *6*, 3160-3165.

28. Terech, P.; Chazeau, L.; Cavaillé, J. Y. Small-Angle Scattering Study of Cellulose Whiskers in Aqueous Suspensions. *Macromolecules* **1999**, *32*, 1872-1875.

29. Revol, J. -.; Godbout, L.; Dong, X. -.; Gray, D. G.; Chanzy, H.; Maret, G. Chiral Nematic Suspensions of Cellulose Crystallites; Phase Separation and Magnetic Field Orientation. *Liq. Cryst.* **1994**, *16*, 127-134.

30. Fleming, K.; Gray, D. G.; Matthews, S. Cellulose Crystallites. *Chemistry - A European Journal* **2001**, *7*, 1831-1835.

31. Okada, A.; Kawasumi, M.; Usuki, A.; Kojima, Y.; Kurauchi, T.; Kamigaito, O. Nylon 6–Clay Hybrid. *Mater. Res. Soc. Symp. Proc.* **1989**, *171*, 45-50.

32. Dufresne, A.; Kellerhals, M. B.; Witholt, B. Transcrystallization in Mcl-PHAs/cellulose Whiskers Composites. *Macromolecules* **1999**, *32*, 7396-7401.

33. Capadona, J. R.; Van, D. B.; Capadona, L. A.; Schroeter, M.; Rowan, S. J.; Tyler, D. J.; Weder, C. A Versatile Approach for the Processing of Polymer Nanocomposites with Self-Assembled Nanofibre Templates. *Nat Nano* **2007**, *2*, 765-769.

34. Favier, V.; Canova, G. R.; Cavaillé, J. Y.; Chanzy, H.; Dufresne, A.; Gauthier, C. Nanocomposite Materials from Latex and Cellulose Whiskers. *Polym. Adv. Technol.* **1995**, *6*, 351-355.

35. Dubief, D.; Samain, E.; Dufresne, A. Polysaccharide Microcrystals Reinforced Amorphous Poly(-Hydroxyoctanoate) Nanocomposite Materials. *Macromolecules* **1999**, *32*, 5765-5771.

36. Grunert, M.; Winter, W. T. Nanocomposites of Cellulose Acetate Butyrate Reinforced with Cellulose Nanocrystals. *J. Polym. Environ.* **2002**, *10*, 27-30.

37. Lin, N.; Chen, G.; Huang, J.; Dufresne, A.; Chang, P. R. Effects of Polymer-Grafted Natural Nanocrystals on the Structure and Mechanical Properties of Poly(Lactic Acid): A Case of Cellulose Whisker-Graft-Polycaprolactone. *J. Appl. Polym. Sci.* **2009**, *113*, 3417-3425.

38. Bondeson, D.; Oksman, K. Polylactic acid/cellulose Whisker Nanocomposites Modified by Polyvinyl Alcohol. *Composites Part A: Applied Science and Manufacturing* **2007**, *38*, 2486-2492.

39. Anglès, M. N.; Dufresne, A. Plasticized starch/tunicin Whiskers Nanocomposites. 1. Structural Analysis. *Macromolecules* **2000**, *33*, 8344-8353.

40. Anglès, M. N.; Dufresne, A. Plasticized starch/tunicin Whiskers Nanocomposite Materials. 2: Mechanical Behavior. *Macromolecules* **2001**, *34*, 2921-2931.

41. Ljungberg, N.; Cavaillé, J. -.Y; Heux, L. Nanocomposites of Isotactic Polypropylene Reinforced with Rod-Like Cellulose Whiskers. *Polymer* **2006**, *47*, 6285-6292.

42. Samir, M. A. S. A.; Allein, F.; Gorecki, W.; Sanchez, J.; Dufresne, A. Nanocomposite Polymer Electrolytes Based on Poly(Oxyethylene) and Cellulose Nanocrystals. *J. Phys. Chem. B* **2004**, *108*, 10845-10852.

43. Chazeau, L.; Cavaillé, J. Y.; Perez, J. Plasticized PVC Reinforced with Cellulose Whiskers. II. Plastic Behavior. *Journal of Polymer Science Part B: Polymer Physics* **2000**, *38*, 383-392.

44. van den Berg, O.; Schroeter, M.; Capadona, J. R.; Weder, C. Nanocomposites Based on Cellulose Whiskers and (Semi)Conducting Conjugated Polymers. *J. Mater. Chem.* **2007**, *17*, 2746-2753.

45. Pan, J.; Hamad, W.; Straus, S. K. Parameters Affecting the Chiral Nematic Phase of Nanocrystalline Cellulose Films. *Macromolecules* **2010**, *43*, 3851-3858.

46. Kimura, F.; Kimura, T.; Tamura, M.; Hirai, A.; Ikuno, M.; Horii, F. Magnetic Alignment of the Chiral Nematic Phase of a Cellulose Microfibril Suspension. *Langmuir* **2005**, *21*, 2034-2037.

47. Noël, C.; Navard, P. Liquid Crystal Polymers. *Progress in Polymer Science* **1991**, *16*, 55-110.

48. Schadt, M. Liquid Crystal Materials and Liquid Crystal Displays. *Annu. Rev. Mater. Sci.* **1997**, *27*, 305-379.

49. Lee, H.; Brant, D. A. Rheology of Concentrated Isotropic and Anisotropic Xanthan Solutions. 1. A Rodlike Low Molecular Weight Sample. *Macromolecules* **2002**, *35*, 2212-2222.

50. Bercea, M.; Navard, P. Shear Dynamics of Aqueous Suspensions of Cellulose Whiskers. *Macromolecules* **2000**, *33*, 6011-6016.

51. Araki, J.; Wada, M.; Kuga, S.; Okano, T. Flow Properties of Microcrystalline Cellulose Suspension Prepared by Acid Treatment of Native Cellulose. *Colloids Surf. Physicochem. Eng. Aspects* **1998**, *142*, 75-82.

52. Ebeling, T.; Paillet, M.; Borsali, R.; Diat, O.; Dufresne, A.; Cavaillé, J. Y.; Chanzy, H. Shear-Induced Orientation Phenomena in Suspensions of Cellulose Microcrystals, Revealed by Small Angle X-Ray Scattering. *Langmuir* **1999**, *15*, 6123-6126.

53. Orts, W. J.; Godbout, L.; Marchessault, R. H.; Revol, J. -. Enhanced Ordering of Liquid Crystalline Suspensions of Cellulose Microfibrils: A Small Angle Neutron Scattering Study. *Macromolecules* **1998**, *31*, 5717-5725.

54. Gray, D. G. Transcrystallization of Polypropylene at Cellulose Nanocrystal Surfaces. *Cellulose* **2008**, *15*, 297-301.

55. Debye, P. Molecular-Weight Determination by Light Scattering. *J. Phys. Chem.* **1947**, *51*, 18-32.

56. Goldstein, M. Scattering Factors for Certain Polydisperse Systems. *J. Chem. Phys.* **1953**, *21*, 1255-1258.

CHAPTER TWO

RHEOLOGY AND PHASE BEHAVIOR OF CONCENTRATED CELLULOSE NANOCRYSTAL AQUEOUS SUSPENSIONS

Reproduced with permission from Ureña-Benavides, E. E.; Ao, G.; Davis, V.A.; Kitchens, C. L. *Macromolecules*, to be submitted for publication. Unpublished work

Introduction

Cellulose nanocrystals (CNC) are renewable and low cost nanomaterials with important optical and mechanical properties. They have been incorporated into renewable polymer matrices to create environmentally friendly nanocomposites with improved mechanical properties.[1, 2] They can be processed into optically active films or materials that selectively reflect a specific wavelength of light.[3, 4] The properties of CNC based materials are greatly dependent on the assembly of the nanoparticles, which is itself affected by processing techniques and external flow fields.[5, 6]

It has been observed that aqueous suspensions of CNC transition from an isotropic material to a biphasic suspension where a liquid crystal coexists with an isotropic phase; at higher concentrations the suspensions turn into entirely liquid crystalline fluids.[7] The suspensions transition into a gel like material at larger concentrations.[8] The type of liquid crystalline (LC) order was identified as chiral nematic (cholesteric) by Revol et al.;[9] this structure is what gives rise to many of the optical and mechanical properties. Moreover, it has been demonstrated that blending CNC with macromolecules such as alginate,[10] or inorganic materials like silica[3] can induce similar types of ordering in the resultant mixtures. The effect of electrolytes and macromolecules such as dextrans on the phase behavior has been extensively studied,[11, 12] yet no studies exist about the effect of temperature. Nevertheless it has been reported that increasing the temperature of a CNC suspension during drying yield a film with a larger pitch.[13]

Liquid crystals possess rheological characteristics that vary significantly with common polymer solutions and polymer melts. For lyotropic systems (solutions or suspensions), the structural changes that accompany the concentration dependent phase transitions significantly affect the rheological behavior of the material.[14] Suspensions of single wall carbon nanotubes in superacids transition from isotropic to nematic liquid crystal ordering with increasing concentration, which causes the viscosity to go through a local maximum, and then a minimum; similar to polymeric liquid crystalline suspensions.[15, 16] Aqueous solutions of xanthan[17] and schizophyllan[18] show analogous behavior, but a cholesteric ordering is obtained at high concentrations instead of nematic. In the case of xanthan, the complex viscosities and loss modulus were superimposed into a master curve, but the same was not possible for the storage modulus and steady shear viscosities. The authors suggested that the relaxation mechanism varied with concentration under steady shear conditions, but under oscillatory shear the relaxation processes were the same regardless of the structure; however an explanation was not provided as for why the storage modulus did not conform to a master curve.

Some rheological studies have been performed for suspensions of CNC isolated from different sources. A small angle scattering study confirmed that CNC isolated from black spruce bleached Kraft pulp formed chiral nematic suspensions at rest, yet the particles tend to orient with the larger axis parallel to the direction of the flow as the shear rate is increased.[19] Suspensions of micron length CNC derived from tunicate showed a very small decrease in viscosity upon appearance of a liquid crystalline phase followed by a monotonic increase in viscosity with concentration.[20] A three region behavior has been observed for the liquid crystalline samples of tunicate CNC analogous to LC polymers; the isotropic suspensions instead behave as a common polymer solution.[20].The previous works on CNC suspensions has been limited to the steady shear flow properties of the suspensions, and has not taken into account the effect of temperature. Furthermore, no studies exist on structural characteristics of the viscoelastic suspensions.

In this work we study the effect of temperature and concentration on CNC ordering via polarized microscopy and imaging. The amount of liquid crystalline phase was determined as a function of concentration at three different temperatures. We also relate the observed structures with the linear viscoelastic properties of the suspensions and the steady shear viscosities. Understanding the assembly of CNC in aqueous suspensions and how it is affected by an external flow field, concentration, and temperature is vital for proper processing of this material into advanced nanomaterials with enhanced optical and mechanical properties.

Experimental Section

Isolation of Cellulose Nanocrystals.

Whatman cellulose filter aid (cotton powder) was used as the raw material for CNC isolation. The CNC were isolated via acid hydrolysis of cotton cellulose with 64 wt %

sulfuric acid at 45°C for 50 min. Upon completion, the reaction was quenched with cold deionized water. The resulting slurry was allowed to precipitate, and the supernatant liquid was decanted. The solids were dialyzed against deionized water for several days until the pH remained constant. Ultrasonication was used to redisperse the CNC. The batch was divided into several samples and the concentration of each was adjusted by slowly evaporating the water under a nitrogen stream. Further details of CNC isolation can be found in the following chapter and elsewhere.[10, 21]

Nanocrystals Size Characterization

Atomic force microscopy (AFM) was used to measure the dimensions of the CNC. A droplet of a CNC suspension with an approximate concentration of 0.01 wt % was allowed to dry on a freshly cleaved mica surface (~ 1.5 cm^2).[22] A Digital Instruments/Veeco Bioscope was employed to image the nanoparticles on the surface using tapping mode. In order to avoid artifacts due to particles lying on top of another, only the isolated CNC were included in the count. The tip employed had a nominal radius of less than 10 nm. An image of the tip was obtained using a porous aluminum standard surface; this image was used to deconvolute the shape of the particles from the geometry of the tip.[23] Both the standard surface and the tip were purchased from MikroMasch.

Phase Behavior

The CNC isolated from cotton using sulfuric acid form a bi-phasic dispersion at concentrations ranging from 0.045 to 0.170 g/ml. Samples of 0.049, 0.063, 0.079 and

0.102 g/ml were introduced into 2 mm path length sealed UV-Vis cuvettes, and allowed to rest for at least 12 days at the desired temperature. The cuvettes were placed between crossed polarized films and pictures were taken using a digital camera. The percent liquid crystalline phase was measured from the images.[12, 24] The experiments were performed at 4°C, 20°C, and 45°C; the same cuvettes were used at all temperatures. Before each stabilization step the samples were homogenized using a vortex stirrer. Suspensions with concentrations larger than 0.102 g/ml did not form a visible interface, and could not be quantified by this method.

Polarized Light Microscopy

A droplet of each suspension was placed on a temperature controlled stage. Pictures were taken at a 200x magnification between polarized films at room temperature (23 °C), 50°C and 60°C. All samples were allowed to stabilize at the desired temperature for one hour before taking the image.

Rheological Measurements

Aqueous suspensions with CNC concentrations ranging from 0.050 to 0.283 g/ml were analyzed using an MCR301 Anton Parr rheometer. Flow curves were generated for each sample from a shear rate of 0.1 to 100 s^{-1}. The time required to reach steady state for each sample was determined by a preliminary step rate test at 0.1 s^{-1}; the sampling time was decreased linearly with increasing shear rate. Frequency sweeps were also performed on each sample from 0.1 to 100 rad/s; the percent strain was chosen inside the linear viscoelastic region according to amplitude sweep experiments performed at a frequency of 10 rad/s. All the suspensions were tested at 10°C; however the effect of temperature on the steady shear viscosities was also studied for samples of 0.050, 0.114, and 0.198 g/ml. In order to get an appropriate torque, the low viscosity samples were analyzed using Mooney-Ewart or double gap geometries; the high viscosity samples were measured using parallel plates and cone and plate geometries. Two different geometries were used to provide consistency to the measurements.

Results and Discussion

Phase Behavior

The size distributions of the CNC measured with AFM are shown in Figure 2.1. They are elongated particles with rectangular cross section.[10, 25, 26] The average length is 107 nm with a standard deviation (s) of 55 nm, the average width is 20.5 nm (s = 6.1 nm), and the average height is 8.9 nm (s = 2.8 nm). The CNC suspensions are acidic due to the presence of –SO_3H groups introduced on the surface of the nanocrystals during the hydrolysis step. A suspension of 0.026 g/ml has a pH of 2.9; a conductometric titration with sodium hydroxide (4.2×10^{-3} M) was performed to determine the number of sulfate groups on the surface; it was found that there are 1.71×10^{-4} moles of -OSO_3H per gram of cellulose. It is important to keep in mind the acidic nature of the CNC since the pH can impact the phase behavior.

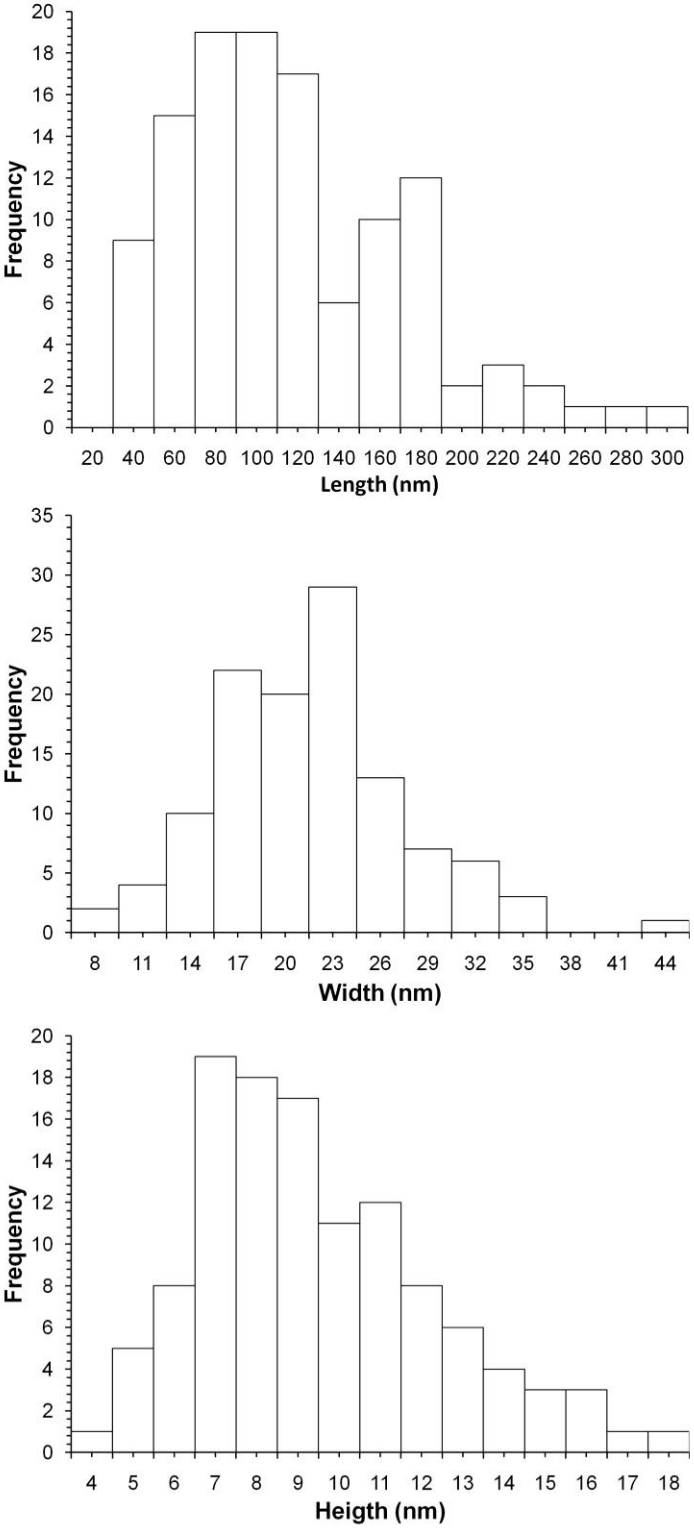

Figure 2.1. Size distribution of CNC used in Chapter 2.

Revol et al. first observed that the suspensions of CNC phase separate at high concentrations; they determined that the liquid crystal has chiral nematic (cholesteric) order.[9] Figure 2.2 shows four suspensions imaged between crossed polarizers, where the bottom liquid crystalline phase shows birefringence of light indicating anisotropy of the suspension. The pictures were used to measure the amount of liquid crystalline phase as a function of CNC concentration at three different temperatures (Figure 2.3).

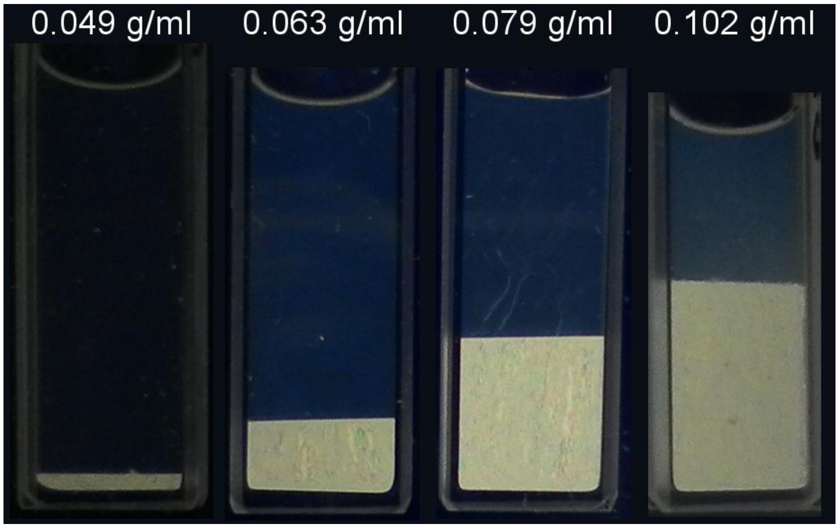

Figure 2.2. Cross polarized images showing the phase separation of CNC suspensions of variable concentration; the lower liquid crystalline phase is birefringent while the upper isotropic phase appears dark.

No significant difference was observed between 4°C and 20°C, although at 45°C the volume of liquid crystalline phase is reduced; at this temperature the particles have more energy to rotate and translate, thus the smaller ones will stay in the isotropic phase rather than assembling in an ordered liquid crystal. Moreover the slope of the trendline decreases at higher temperatures evidencing an enlargement of the two phase region. It must be noted that at CNC concentrations larger than 0.102 g/ml, the interface was not distinguishable and it was not possible to quantify the amount of liquid crystalline phase;

very likely the larger viscosity of the suspensions did not allow the coalescence and separation of the dispersed phase. Nonetheless polarized light microscopy showed the presence of isotropic sections at concentrations as large as 0.170 g/ml at room temperature.

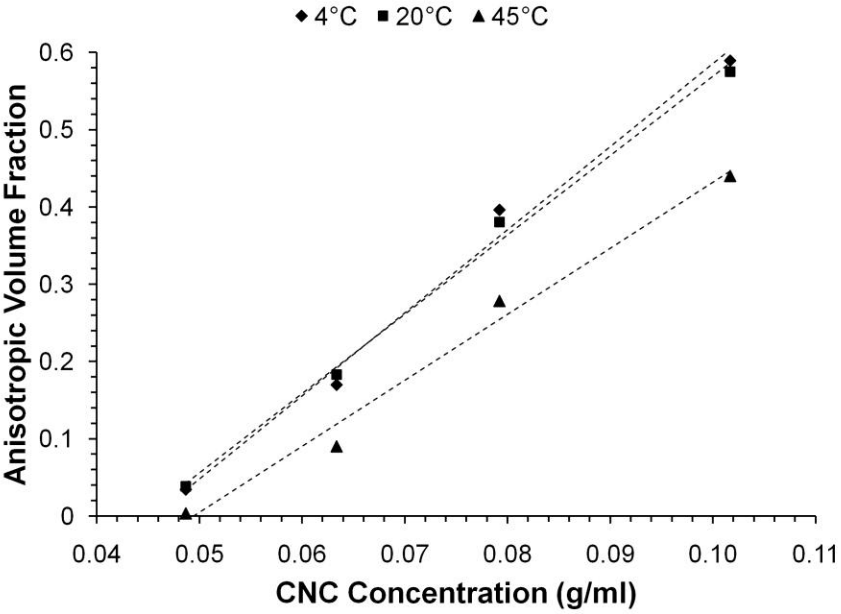

Figure 2.3. Amount of liquid crystalline (anisotropic) phase as a function of CNC concentration at 4°C, 20°C, and 45°C.

The effect of temperature and concentration was also analyzed using polarized light microscopy (Figure 2.4). The 0.238 g/ml suspension showed a colorful precholesteric type of order at room temperature, which can be regarded as a distorted cholesteric. Based on the rheological analyses that will be discussed later in this chapter, the sample behaves as a gel like material. It is believed that the strong network hinders the assembly of the CNC into a well ordered cholesteric. However, after heating to 60 °C and holding for 1 hour a fingerprint appeared which indicates the formation of a cholesteric liquid crystal.

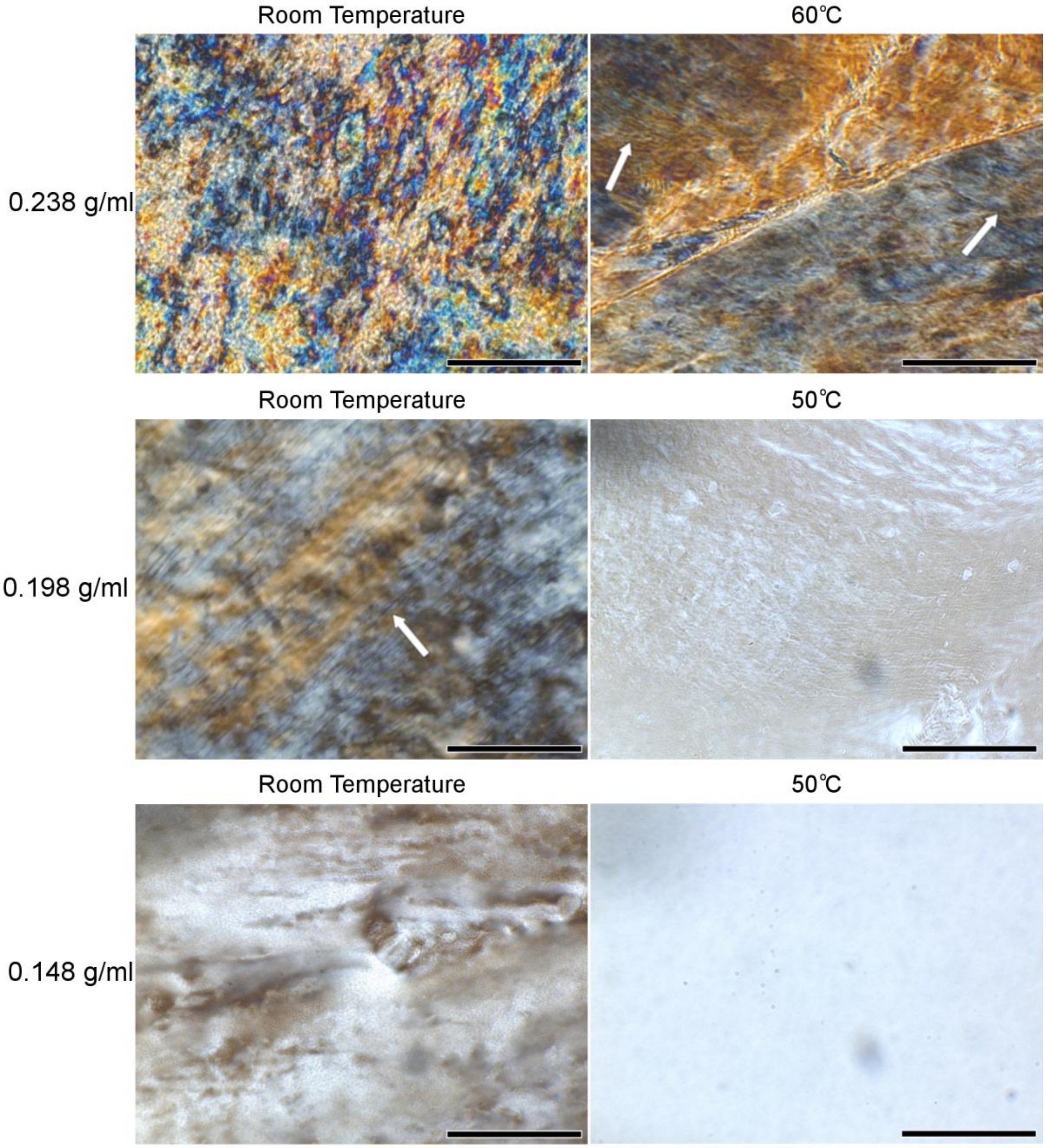

Figure 2.4. Polarized light microscopy of CNC suspensions at variable concentration and temperature. The arrows indicate the direction of the chiral axis. Scale bars: 200 μm.

At 0.198 g/ml the suspension is fully liquid crystalline at room temperature, moreover it possesses the fingerprint texture characteristic of a cholesteric material. After heating the suspension to 50 °C the colors disappeared yet retained some birefringence, which evidences a transition into the biphasic region. At a CNC concentration of 0.148 g/ml the sample showed obvious isotropic and liquid crystalline sections at room temperature. Increasing the temperature to 50 °C reduced the birefringence, but the sample still behaved as biphasic. The polarized light microscopy is consistent with the plot shown in Figure 2.3. The data suggest that increasing the temperature, within the experimental conditions studied here, shifts the transitions to higher concentrations.

Viscosity Dependence on CNC Concentration

The phase behavior and the rheological properties are closely interrelated. In order to understand the behavior of the suspensions it is useful to study them simultaneously. The flow curves for each suspension are shown in Figure 2.5 together with the complex viscosities. When the CNC concentration is 0.198 g/ml and above, the curves show a strictly shear thinning behavior during the entire shear rate and frequency ranges. The samples between 0.170 and 0.126 g/ml show a low shear/frequency plateau followed by a shear thinning region. Although not totally evident, the suspensions containing 0.103 and 0.082 g/ml of CNC show an initial shear thinning segment (Region I), which is more easily observed for the steady shear viscosity, followed by a Newtonian plateau (Region II) and a second shear thinning section (Region III) which is the typical behavior of liquid crystalline polymers.[14] The lowest concentration sample (0.050 g/ml) was mostly

Newtonian for the shear rate range studied; a frequency sweep could not be performed with this sample because the torque was too low to measure. It is worth noting that the flow curves of the two most concentrated suspensions start to level off at high shear rates evidencing the presence of a high shear plateau.

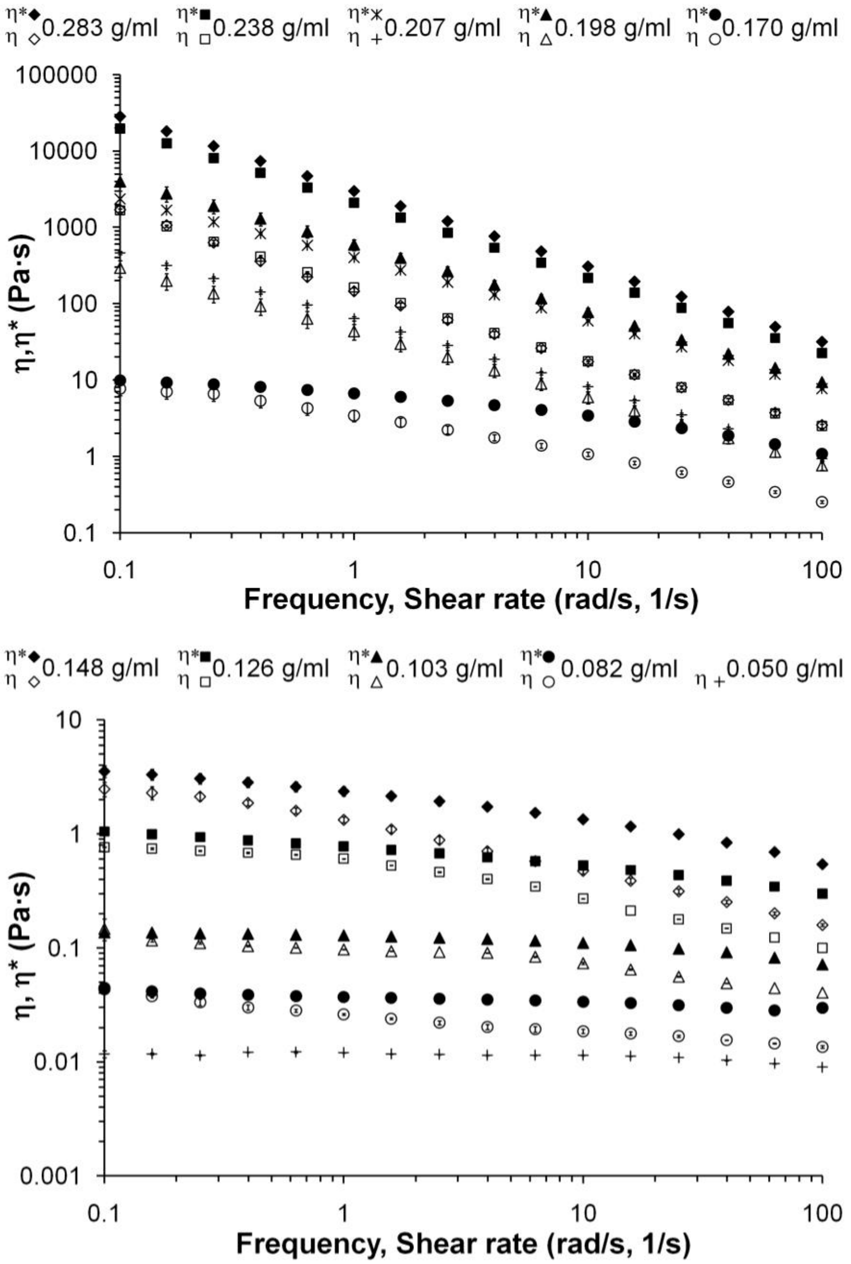

Figure 2.5. Steady shear and complex viscosities of several CNC suspensions.

It is also observed that the Cox-Merz rule is not obeyed for most of the samples and frequencies studied. This means that the oscillatory shear curves are not equal to the steady shear flow curves. Only at low concentrations and shear rates/frequencies, when the suspensions behave mostly Newtonian, the complex viscosity approximates the steady shear viscosity. Similar behavior has been observed for suspensions of multiwall carbon nanotubes, where the Cox-Merz rule was met when a Newtonian plateau was present either at low or high shear rates/frequencies.[27]

The curves for the complex and steady viscosities were superposed by plotting a reduced viscosity versus a reduced shear rate and reduced frequency; the superposition is shown in Figure 2.6. The reduced variables are defined as follows:

$$\eta_r = \eta \frac{\eta_{0\ \mathrm{ref}}}{\eta_0}, \qquad \eta_r^* = \eta^* \frac{\eta_{0\ \mathrm{ref}}^*}{\eta_0}, \qquad \dot{\gamma}_r = \dot{\gamma} \frac{\eta_0 \cdot c_{\mathrm{ref}}}{c \cdot \eta_{0\ \mathrm{ref}}}, \qquad \omega_r = \omega \frac{\eta_0^* \cdot c_{\mathrm{ref}}}{c \cdot \eta_{0\ \mathrm{ref}}^*}$$

where η is the steady shear viscosity, η^* is the complex viscosity, $\dot{\gamma}$ is the shear rate, ω is the frequency and c is the concentration; the subindex 0 refers to the Newtonian plateau, r indicates a reduced variable and ref corresponds to the reference sample, which has a concentration of 0.103 g/ml.

Inspection of Figure 2.6 reveals that η_r for all the suspensions up to a concentration of 0.207 g/ml superpose onto a master curve when plotted against $\dot{\gamma}_r$. The master curve has the characteristic shape of a liquid crystalline suspension with a Newtonian plateau enclosed by two shear thinning regions. The suspension with a concentration of 0.05 g/ml is an exception since it does not have a Region I; instead it has a large Newtonian plateau with a small shear thinning segment at high shear rates. Region I has been related to a refinement of a defect texture product of the polydomain nature of liquid crystalline polymers.[28, 29] In the case of cholesterics, it has also been suggested that the persistence of the cholesteric order may also cause region I behavior.[30]

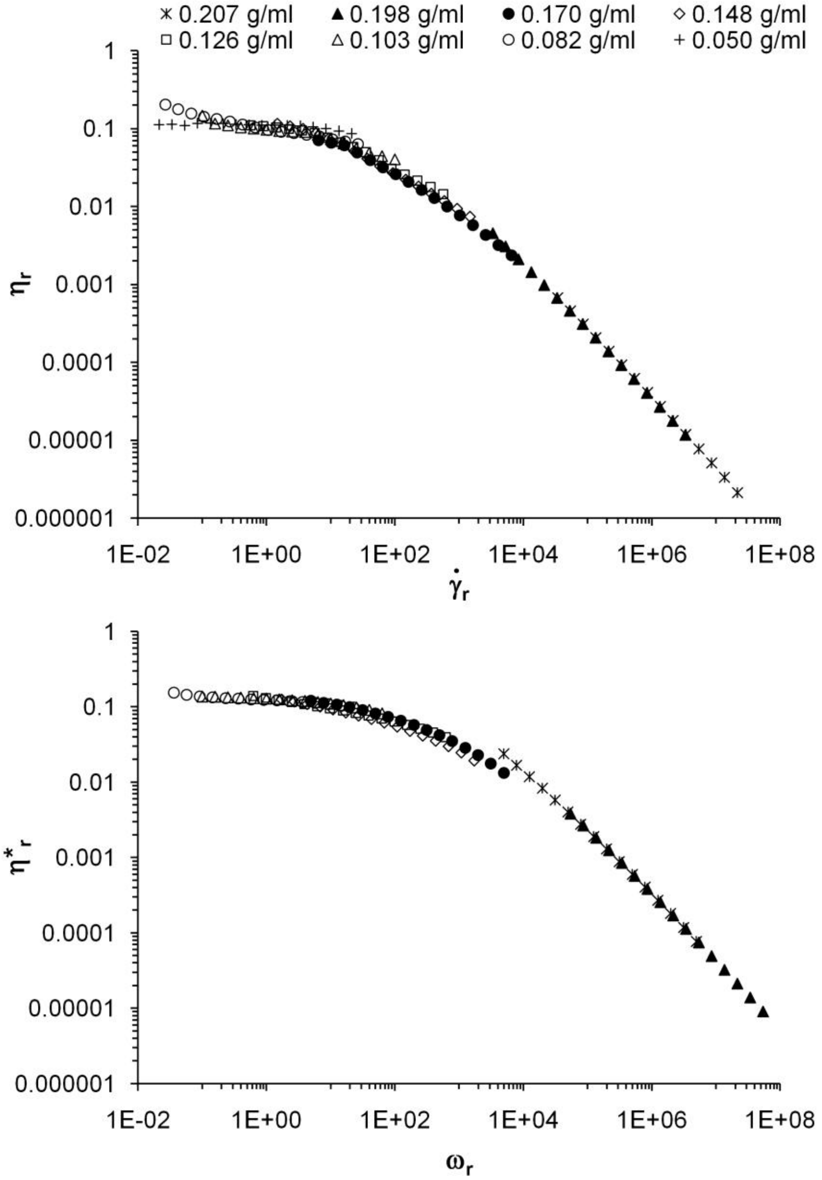

Figure 2.6. Time-concentration superposition of the viscosities of CNC suspensions.

Since the 0.050 g/ml sample has a negligible amount of liquid crystalline phase we expect it to behave like an isotropic at rest suspension. Moreover, the isotropic/anisotropic interface, which is nearly indistinguishable at 0.050 g/ml CNC, also contributes to the viscosity and can induce shear thinning. Bercea and Navard reported that isotropic at rest CNC suspensions from tunicin (high aspect ratio) behave like polymer melts or solutions; they have two plateaus, at low shear and at high shear, enclosing an intermediate shear thinning region.[20] Our nanocrystals isolated from cotton are very short compared to tunicin whiskers, therefore the rotational diffusion time (τ_{rot}) is much smaller. This parameter equals the inverse of the critical shear rate ($\dot{\gamma}_c$) that marks the transition between the Newtonian plateau and the shear thinning region; which thus has a relatively large value.[20, 31] Consequently, we observed only the low shear plateau and the beginning of the shear thinning region.

The superposition of the complex viscosity curves collapse on a master curve up to a concentration of 0.170 g/ml, but a discontinuity occurs afterwards. The highest concentration at which an isotropic section was detected using cross polarized microscopy is also 0.170 g/ml, evidencing a possible variation in the relaxation mechanism. Interestingly, the sample with the next largest concentration (0.198 g/ml) shows a maximum in the complex viscosity (Figure 2.7) which is absent in the case of the steady shear viscosity. Given the broad size distribution, the CNC may find difficulties assembling, thus forming a relatively high energy network. When the concentration is further increased, the smallest CNC may assemble more easily causing a reduction of the complex viscosity. Under steady shear conditions the network can be disrupted, and consequently the maximum is not observed.

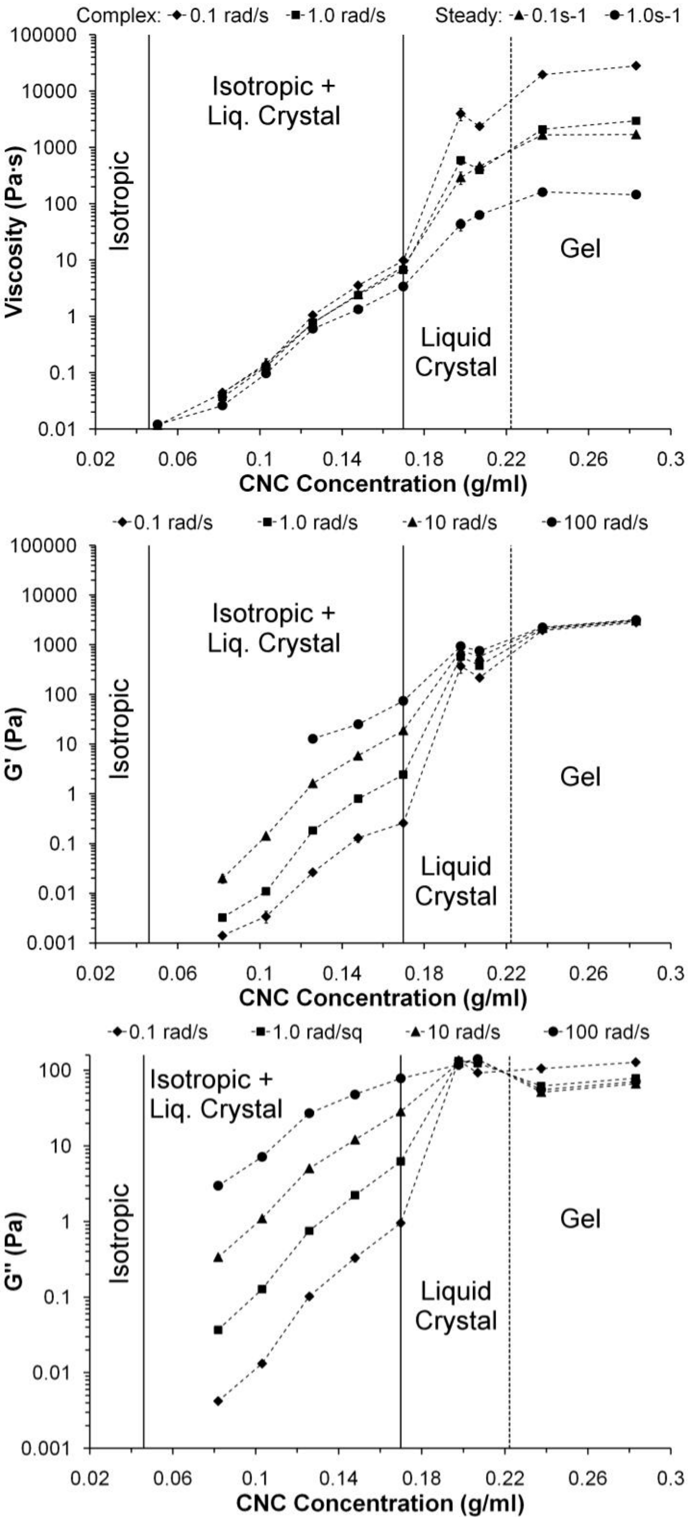

Figure 2.7. Rheological properties versus concentration of CNC suspensions. The solid vertical lines indicate a phase transition; the discontinuous vertical line indicates that the liquid crystal to gel transition is approximate.

At 0.126 g/ml reduction in the slopes of the viscosity versus concentration curves are observed (Figure 2.7). All biphasic samples at this concentration and below show coalescence of the liquid crystalline droplets that are dispersed in a continuous isotropic phase. Consequently a clear macro-scale phase boundary is observed which could be imaged between cross polarized films (Figure 2.2). Higher concentration biphasic samples, at 0.148 and 0.170 g/ml, did not coalesce in the quiescent state, nevertheless polarized light microscopy revealed the presence of isotropic sections. The noticeable variation in slope evidences an evolution from an isotropic rich material to a liquid crystalline rich suspension.

Moduli Dependence on CNC Concentration

A summary of the viscoelastic properties of the suspensions is shown in Figure 2.8. The storage moduli (G') of the samples with 0.283, and 0.238 g/ml CNC are frequency independent indicating that they behave as stiff gels; these two samples are depicted in Figure 2.7 as part of the gel phase. In Figure 2.4, a precholesteric structure was observed at room temperature at 0.238 g/ml. It is assumed that the high elasticity in that sample hinders the movement of the CNC; thus prohibiting the assembly of the nanoparticles in a purely cholesteric order. Nevertheless, after increasing the temperature to 60°C a clear fingerprint appeared, presumably caused by a higher mobility of the CNC, and an enhancement of the viscous component of the suspension.

The transition from liquid crystal to gel is unclear; however at the temperature used for the rheological measurements (10 °C), it must be somewhere between 0.207 and 0.238

g/ml. The suspensions with 0.198 and 0.207 g/ml did not show frequency independence for which they are not considered gels; still in both cases the tangent of the phase angle, tan(δ), is less than 1 indicative of a dominant elastic behavior. A maximum in G' is also observed at 0.198 g/ml, just like the complex viscosity; this supports the hypothesis of a brittle network at this concentration. Moreover, tan(δ) indicates that at 0.198 g/ml the CNC suspension is more elastic than at 0.207 g/ml for the entire frequency range (Figure 2.8).

The loss modulus (G") increases with concentration monotonically until it reaches a maximum in the liquid crystalline region. The position of the maximum moves from 0.198 g/ml ,at low frequencies, to 0.207 g/ml, at high frequencies. A minimum in G" seems to determine the transition from liquid crystal to gel. This behavior occurs throughout the entire frequency range, except at 0.1 rad/s, and is interpreted as a reduction of the viscous energy dissipated by the material as it evolves into a more elastic structure.

A time – concentration superposition of G' and G" was also attempted by plotting the reduced storage and loss moduli against the reduced frequency. The reduced moduli are defined as follows:

$$G'_{\mathrm{r}} = G' \frac{c_{\mathrm{ref}}}{c},$$

$$G''_{\mathrm{r}} = G'' \frac{c_{\mathrm{ref}}}{c}$$

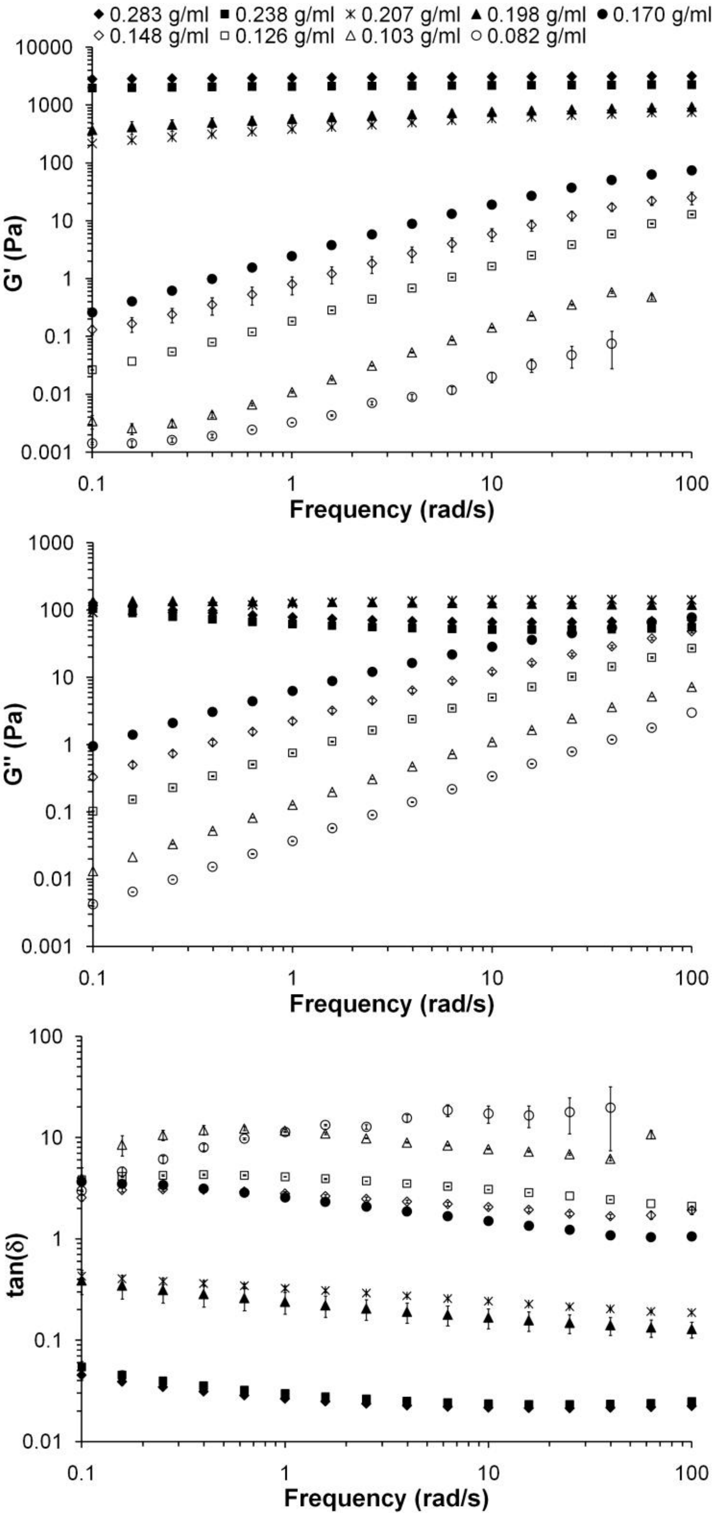

Figure 2.8. Linear viscoelstic properties of CNC suspensions with various concentrations.

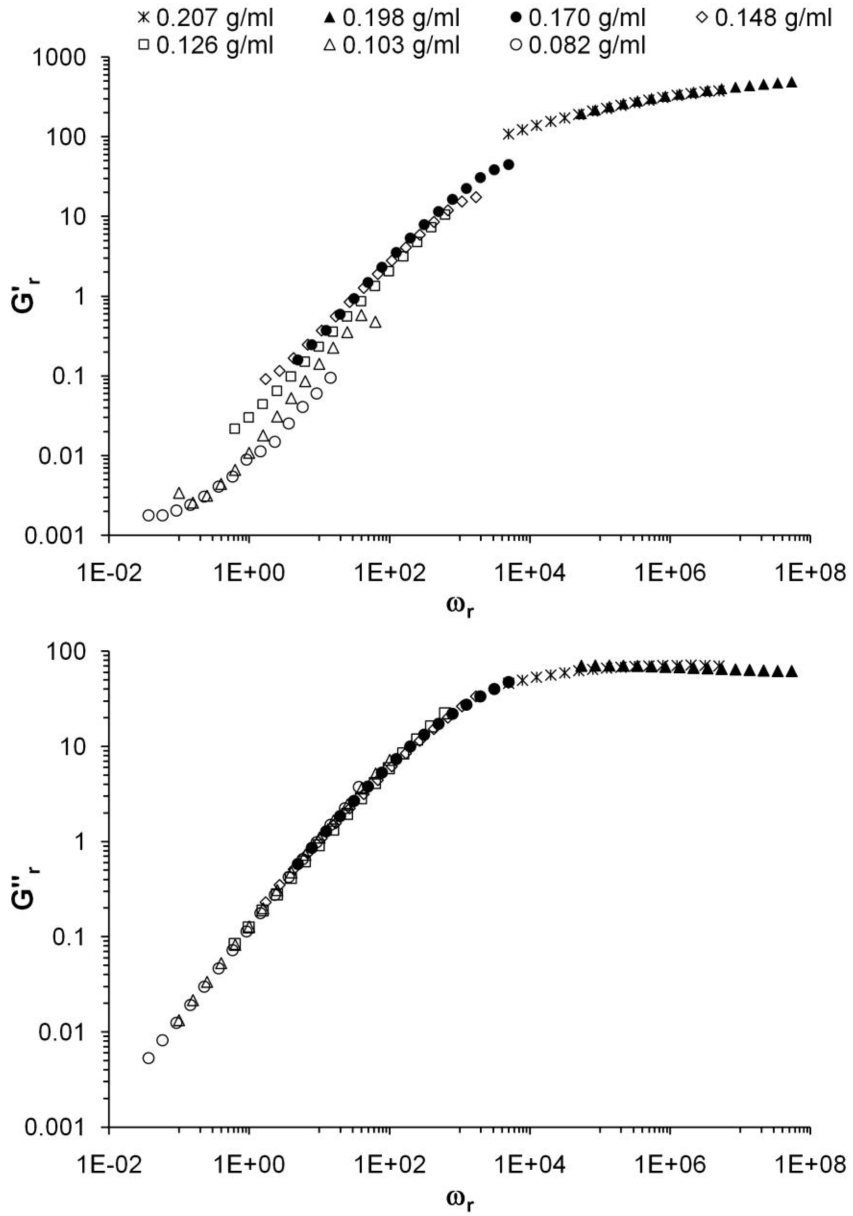

Figure 2.9. Time – concentration superposition of the viscoelstic properties of CNC suspensions.

The superposition results are shown in Figure 2.9. The storage modulus do not collapse onto a master curve for the most part of the frequency range, however the G" does collapse satisfactorily. An analogous behavior has been observed in biphasic Xanthan solutions; however the authors did not provide a satisfactory explanation. [17] In mixtures of immiscible phases, the interfacial tension contributes significantly to the viscoelastic properties.[32] The relaxation of a droplet after it is deformed affects mostly the elastic component, while the viscous contribution is very small.[33] The effect is larger as the interfacial tension and area increase; the latter clearly varies depending on the volume of the anistropic phase.[34] Moreover, the morphology of the mixture may change from dispersed droplets (or fibrils) of liquid crystal in a continuous isotropic matrix, to a co-continuous blend, and then to dispersed droplets (or fibrils) of isotropic suspension in a continuous liquid crystalline phase. As a result, the relaxation times and mechanisms change significantly with increased CNC concentration, but this has a small effect on G" which can be collapsed onto a master curve. It is not surprising that in Figure 2.6 the complex viscosity superposed nicely up to a concentration of 0.170 g/ml. That is because the low concentration suspensions are more viscous than elastic, which is evidenced by the large value of tan(δ) (Figure 2.8).

Predictions of the linear viscoelastic properties are relatively easy for the case of dispersed droplets in a continuous phase. Olroyd obtained a model for a blend of two immiscible Newtonian fluids;[35] Parliene derived a generalized model for polydispersed droplets of a viscoelastic fluid dispersed in a viscoelastic matrix.[36] Graebling et al. observed that the effect of polydispersity can be neglected as long as R_v/R_n is less than 2 (R_v refers to volume average drop radius and R_n is the number average drop radius).[34] For two Maxwell fluids, at low frequencies G" is directly proportional to the frequency, consequently a log-log plot of G" versus frequency should yield a straight line with a slope of 1. The slope of G"/c in Figure 2.9 is 0.966 at low frequencies which is in good agreement with the theory. At low frequencies a log-log plot of G' versus frequency is expected to have a plateau surrounded by two straight lines with a slope of 2. In some cases the plateau looks more like a shoulder on the G' curve.[34] Even though the frequency range of our measurements is too small to clearly observe this behavior, the tails observed at low frequency for the lowest concentrations suspensions suggest evidence of the plateau.

Dependence of Steady Shear Viscosity with Temperature

For all samples the viscosity generally decreases with increasing temperature as expected. Surprisingly the sample at 0.198 g/ml showed viscosity independence with temperature from 10 °C to 35 °C, followed by an increase at 40 °C. It is probable that the suspension suffered from water evaporation thus increasing the concentration and the viscosity; in which case Figure 2.10a would not represent the viscosity at 0.198 g/ml. The shape of the curves did not change significantly for the temperature range studied, except at 0.050 g/ml. The Newtonian plateau was enlarged as the temperature increased. When the sample was tested at 10 °C there was evidence of a shear thinning region at high shear rates, however at larger temperatures the plateau clearly extended to the entire shear rate range. This observation is consistent with the phase behavior results described in Figure 2.3 where at a similar CNC concentration the isotropic – anisotropic phase boundary was indistinguishable at 45 °C.

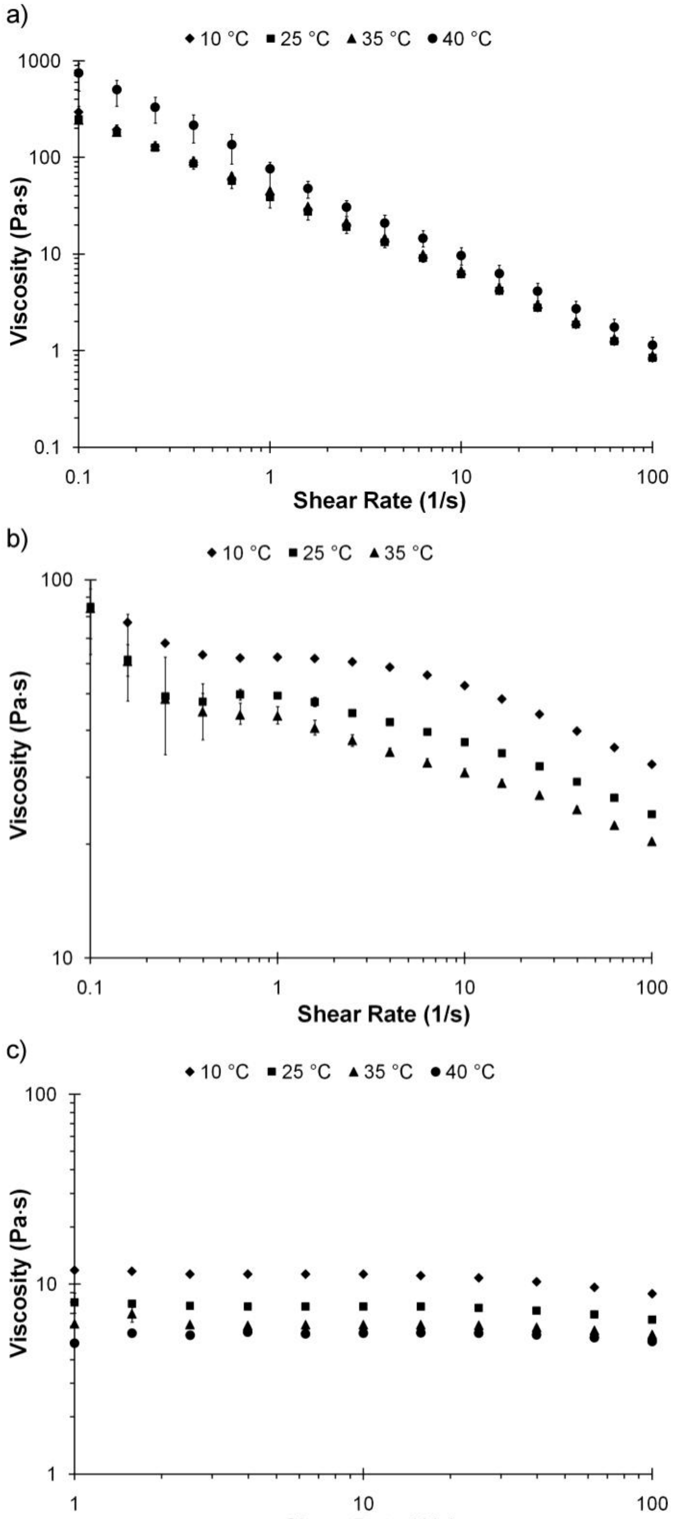

Figure 2.10. Flow curves at various temperatures of CNC suspensions with concentrations of a) 0.198 g/ml, b) 0.114 g/ml, and c) 0.050 g/ml.

Conclusions

We have studied the effect of CNC concentration and temperature on the phase behavior and rheological properties of concentrated CNC suspensions. The suspensions go through a biphasic region where an isotropic phase coexists with a liquid crystal phase. Heating the samples above 20°C induces a reduction in the volume of anisotropic phase, while broadening the biphasic region. The suspensions initially are coalescent in the quiescent state; however as the liquid crystalline phase increases, the coalescence ceases. This transition coincides with a variation in the slope of the viscosity versus concentration curve. Beyond the biphasic region the suspensions are entirely liquid crystal; a fingerprint texture is observed which evidences a cholesteric order. Within this region, a maximum and a minimum are observed in G' and η^* indicating the formation of semistable network which is easily broken under steady shear conditions. The suspensions then transition into a gel region which can be identified by a minimum in G". The gels were birefringent and showed a pre-cholesteric morphology at room temperature; however heating to 60°C induced the formation of a cholesteric liquid crystal at 0.238 g/ml. The relaxation mechanism changed within the biphasic region as the morphology and interfacial area varied. Since the interface has a small viscous effect G" and η^* can be superpositioned on a mastercurve but not G'. Increasing the temperature reduces the suspension viscosity as expected; however at 0.198 g/ml the viscosity did not change with temperature.

References

1. Eichhorn, S. J.; et al. *J. Mater. Sci.* **2010**, 45, 1-33.

2. Azizi Samir, M. A. S.; Alloin, F.; Dufresne, A. *Biomacromolecules* **2005**, 6, 612-626.

3. Shopsowitz, K. E.; Qi, H.; Hamad, W. Y.; MacLachlan, M. J. *Nature* **2010**, 468, 422-425.

4. Cranston, E. D.; Gray, D. G. *Biomacromolecules* **2006**, 7, 2522-2530.

5. Habibi, Y.; Lucia, L. A.; Rojas, O. J. *Chem. Rev.* **2010**, 110, 3479-3500.

6. De Souza Lima, M. M.; Borsali, R. *Macromolecular Rapid Communications* **2004**, 25, 771-787.

7. Beck-Candanedo, S.; Roman, M.; Gray, D. G. *Biomacromolecules* **2005**, 6, 1048-1054.

8. Liu, D.; Chen, X.; Yue, Y.; Chen, M.; Wu, Q. *Carbohydr. Polym.* **2011**, 84, 316-322.

9. Revol, J. -F.; Godbout, L.; Dong, X. -M.; Gray, D. G.; Chanzy, H.; Maret, G. *Liq. Cryst.* **1994**, 16, 127-134.

10. Ureña-Benavides, E. E.; Brown, P. J.; Kitchens, C. L. *Langmuir* **2010**, 26, 14263-14270.

11. Beck-Candanedo, S.; Viet, D.; Gray, D. G. *Macromolecules* **2007**, 40, 3429-3436.

12. Hirai, A.; Inui, O.; Horii, F.; Tsuji, M. *Langmuir* **2009**, 25, 497-502.

13. Pan, J.; Hamad, W.; Straus, S. K. *Macromolecules* **2010**, 43, 3851-3858.

14. Noël, C.; Navard, P. *Progress in Polymer Science* **1991**, 16, 55-110.

15. Davis, V. A.; Ericson, L. M.; Parra-Vasquez, A.; Fan, H.; Wang, Y.; Prieto, V.; Longoria, J. A.; Ramesh, S.; Saini, R. K.; Kittrell, C.; Billups, W. E.; Adams, W. W.; Hauge, R. H.; Smalley, R. E.; Pasquali, M. *Macromolecules* **2004**, 37, 154-160.

16. Davis, V. A.; Parra-VasquezA, N. G.; Green, M. J.; Rai, P. K.; Behabtu, N.; Prieto, V.; Booker, R. D.; Schmidt, J.; Kesselman, E.; Zhou, W.; Fan, H.; Adams, W. W.; Hauge, R. H.; Fischer, J. E.; Cohen, Y.; Talmon, Y.; Smalley, R. E.; Pasquali, M. *Nat Nano* **2009**, 4, 830-834.

17. Lee, H.; Brant, D. A. *Macromolecules* **2002**, 35, 2212-2222.

18. Fang, Y.; Takemasa, M.; Katsuta, K.; Nishinari, K. *J. Rheol.* **200**4, 48, 1147-1166.

19. Orts, W. J.; Godbout, L.; Marchessault, R. H.; Revol, J. -F. *Macromolecules* **1998**, 31, 5717-5725.

20. Bercea, M.; Navard, P. *Macromolecules* **2000**, 33, 6011-6016.

21. Dong, X. M.; Revol, J.-F.; Gray, D. G. *Cellulose* **1998**, 5, 19-32.

22. Kvien, I.; Tanem, B. S.; Oksman, K. *Biomacromolecules* **2005**, 6, 3160-3165.

23. Villarrubia, J. S. *J. Res. Natl. Inst. Stand. Technol.* **1997**, 102, 425-454.

24. Dong, X. M.; Kimura, T.; Revol, J.-F.; Gray, D. G. *Langmuir* **1996**, 12, 2076-2082.

25. Terech, P.; Chazeau, L.; Cavaillé, J. Y. *Macromolecules* **1999**, 32, 1872-1875.

26. Elazzouzi-Hafraoui, S.; Nishiyama, Y.; Putaux, J.; Heux, L.; Dubreuil, F.; Rochas, C. *Biomacromolecules* **2008**, 9, 57-65.

27. Fan, Z.; Advani, S. G. *J. Rheol.* **2007**, 51, 585-604.

28. Walker, L. *J. Rheol.* **1994**, 38, 1525-1547.

29. Pochan, J.; Erhardt, P. *Phys. Rev. Lett.* **1971**, 27, 790-791.

30. Hongladarom, K.; Burghardt, W. R. *Rheologica Acta* **1998**, 37, 46-53.

31. Doi, M.; Edwards, S. F. In Oxford University Press: New York, **1986**; pp 289-380.

32. Vinckier, I.; Laun, H. M. *J. Rheol.* **2001**, 45, 1373-1385.

33. Tucker III, C. L.; Moldenaers, P. *Annu. Rev. Fluid Mech.* **2002**, 34, 177-210.

34. Graebling, D.; Muller, R.; Palierne, J. F. *Macromolecules* **1993**, 26, 320-329.

35. Olroyd, J. G. *Proc. R. Soc. London, Ser. A* **1953**, 218, 122-132.

36. Palierne, J. F. *Rheologica Acta* **1990,** 29, 204-214.

CHAPTER THREE

EFFECT OF JET STRETCH AND PARTICLE LOAD ON CELLULOSE NANOCRYSTAL – ALGINATE NANOCOMPOSITE FIBERS

Reproduced with permission from Ureña-Benavides, E. E.; Brown, P. J.; Kitchens, C. L. *Langmuir* **2010**, 26 (17), pp 14263-14270. Copyright 2010 American Chemical Society

Introduction

Alginate is a biopolymer isolated from brown seaweeds, which is composed of two monomers: (1→4) β-D-mannuronate and (1→4) α-L-guluronate. This polycarbohydrate has properties such as biocompatibility, water absorption capacity, ability to form gels, and acceptable strength, which have given it several important medical applications.[1-4] Some of its uses are drug delivery,[5-7] biosensing devices,[8] and the confection of dressings to treat exuding wounds.[3, 4] It has also been utilized for separation of water/alcohol mixtures[9] and as a thickener for food products. Nevertheless, its applications are still limited by a relatively low strength, especially when the material is wet. A one order of magnitude decrease in strength has been reported for wet fibers.[10]

Several attempts to improve the mechanical properties of alginate have been performed with different outcomes; most of these involve blending the alginate with a water-soluble polymer or some type of particle filler.[10] Some improvements have been possible, but a higher degree of reinforcement is still desirable. It is expected that cellulose nanofillers can positively impact the mechanical properties of alginate fibers. CNCs are biocompatible, nontoxic, environmentally friendly, cost-effective (compared to other nanoparticles), and very strong; their tensile strength has been estimated to be in the order of 10 GPa,[11] and their modulus is near 143 GPa.[12] The chemical structure of cellulose is very similar to alginate, both being polycarbohydrates, which suggests very good particle-matrix interactions. In addition, CNCs prepared from sulfuric acid hydrolysis contain negatively charged sulfate groups on the surface,[13, 14] which may allow electrostatic cross-linking between of the CNCs and the alginate via the Ca^{2+} ions in the coagulating bath.[15-17]

CNCs have been introduced into a wide variety of materials with the objective of improving their strength and modulus such as poly(β-hydroxyoctanoate) (PHO),[11, 18] starch,[19] silk fibroin,[20] cellulose acetate butyrate (CAB),[21] polycaprolactone (PCL),[22] and others. Different results have been observed depending on processing technique, particle-particle interactions, and particles-matrix interactions.[11] Very often, little or no reinforcement has been observed for small loads of CNCs, but considerable improvements in mechanical properties have been observed at high CNCs concentrations. Explanations of the lack of reinforcement at low concentrations are limited.

In general, the strength of a polymer fiber can be improved by increasing the degree of alignment inside the fiber; this is achieved by stretching the material during processing. However, there are practical limitations because the fiber can be broken if it is stretched too much. The addition of fillers into a polymer matrix is known to modify its properties; consequently, it can also change the ideal processing conditions of the composite. Thus, it is desirable to study the effect of CNCs on the stretching capacity of alginate fibers during processing and its subsequent impact on mechanical properties.

In this chapter I measured the dimensions of the CNCs using atomic force microscopy and examined the stability of CNCs dispersions in sodium alginate aqueous solutions as a preliminary step for fiber spinning. The dispersions were used to wet spin calcium alginate fibers while studying the effect of CNCs concentration on the maximum possible apparent jet stretch. The apparent jet stretch (J_A) is defined as the ratio of the first roller tangential velocity (V_2) over the extrusion linear velocity of the spinning dope (V_1). The velocities are calculated using the equations $V_2 = R \cdot \Omega$, and $V_1 = Q/A$; where R is the radius of the first roller (m), Ω is the angular velocity of the same roller (rad/s), Q is the volumetric flow rate of the dope solution (m^3/s), and A is the cross-sectional area of all the holes in the spinneret (m^2). The tensile properties of the fibers were measured as a function of cellulose load and J_A at ASTM standard conditions for testing textiles.

Experimental Section

Materials

High-viscosity sodium alginate (98.4% purity) from the seaweed *Macrocystis pyrifera* (kelp) was purchased from MP Biomedicals, LLC (catalog number 154723) and used as received. The chemical composition of the guluronic (G) and mannuronic (M) acids as well as the proportion of blocks in the polymer is dependent on the source of alginate; Table 3.1 shows these values for alginates isolated from *Macrocystis pyrifera*. It is thus assumed that the chemical composition of the alginate used for this study is within the ranges described in Table 3.1; those values correspond to a relatively low concentration of G blocks if compared to alginates from other sources (e.g., *Laminaria hyperborea*).[17, [23, 24] The CNCs were isolated from Whatman cellulose filter aid (cotton powder) using sulfuric acid; the acid was purchased at a concentration of 98% and then diluted to 64% with deionized water. ACS grade acetone and technical grade anhydrous calcium chloride were used for fiber processing.

Table 3.1. Chemical Composition of Alginates Isolated from *Macrocystis pyrifera*[17, 23, 24]

Repeat Unit / Block	Composition (%)
Mannuronic Acid	61.0
Guluronic Acid	39.0
MM Blocks	38.0 – 43.0
GG Blocks	16.0 – 21.0
MG+GM Blocks	36.0 – 46.0

Isolation of Cellulose Nanocrystals

CNCs where isolated from cellulose filter aid via acid hydrolysis with 64 wt % sulfuric acid at 45 °C for 50 min. This method has been widely used by several researchers.[14, 25, 26] The reaction mixture was quenched by a 10-fold dilution with cold deionized water; the particles were allowed to precipitate overnight and were separated from the supernatant liquid by decantation. The resultant slurry was dialyzed against deionized water for several days to remove excess acid, low molecular weight carbohydrates formed during hydrolysis, and other water-soluble impurities; fresh water was provided daily until a constant pH of 5.5. The CNCs dispersion was then ultrasonicated in an ice bath to disperse the CNCs and then filtered to remove any metal particles released from the sonicating horn.

Cellulose Nanocrystals Characterization

The dimensions of the cellulose nanocrystals were determined by atomic force microscopy (AFM) using a Digital Instruments/Veeco Bioscope. A representative sample of the suspension of CNCs was diluted to approximately 0.01 wt %; one drop was then taken from the dilute suspension and let dry on a freshly cleaved mica surface.[27] The specimen was kept in a vacuum oven overnight before analysis. Imaging was performed with a MikroMasch brand tip (NSC15) with a maximum nominal radius of 10 nm. The size of the tip is comparable with the dimensions of the CNCs which causes the nanoparticles to look broader than they are; hence, a blind tip estimation was done by analyzing an image (taken with the same tip) of a standard porous aluminum surface, which was purchased from MikroMasch.[28] The modeled tip was then used to deconvolute the geometries of the nanocrystals and the tip.[28] Free license software (Gwyddion 2.17) was utilized for this purpose. The dimensions of 122 particles were measured; only the particles that seemed isolated (nonaggregated) in the pictures were chosen for the analysis. Tapping mode was used to prevent movement or damage of the crystals.

Characterization of CNCs – Alginate Aqueous Suspensions.

Shear rheology experiments were performed in order to determine the appropriate concentration of the dope solution before wet spinning. For these purpose, solutions of 1%, and 2% sodium alginate were prepared with variable amounts of suspended CNCs. Steady state flow experiments were performed on all suspensions using a TA Instruments AR2000 rheometer. The steady state viscosity of the suspensions at 25 °C was determined using a cone and plate geometry at shear rates ranging from 0.1 to 100 s^{-1}. A cone with a 2° angle and a 20 mm diameter was used for all samples except for the lowest viscosity, which required a cone with a 0.5° angle and 60 mm diameter to obtain a measurable torque.

The stability and phase behavior of the CNCs suspensions in a sodium alginate solution was investigated using crossed polarized imaging.[29, 30] Dispersions with variable concentrations of CNCs in water, and in 1 wt % sodium alginate solution, were poured into 1 mm path length cuvettes and allowed to relax for a period of time of 1 h up to a maximum of 3 days depending on the CNCs concentration; suspensions with a larger amount of CNCs have higher viscosity and may take longer time to relax. The samples were placed in a dark box between crossed polarizers; light was allowed to enter the box on one end, while a camera was placed inside the box on the other end. A picture of each sample was taken and then analyzed.

Preparation of CNCs – Alginate Fiber Nanocomposites

Sodium alginate was dissolved in deionized water and mixed with a CNCs aqueous suspension to obtain a total alginate concentration of 1.0 wt %; the amount of nanocrystals suspension and deionized water was varied to yield CNCs concentrations of 0.020, 0.053, 0.11, 0.33, and 1.00 wt %, which correspond to CNCs loads in the final fiber of 2.0, 5.0, 10, 25, and 50 wt % respectively. Fresh suspensions were prepared and stored in a refrigerator for a maximum of 3 days before spinning. A metering pump was used to pump the suspension at 4.5 cm^3/min through a 10-hole spinneret (400 μm diameter each hole) into a 5% w/v $CaCl_2$ coagulating bath. Only one roller and one bath were available to prepare the fiber which did not allow for a continuous process; for this reason it was necessary to develop a simple method to transfer the fibers from one bath to another while preserving the desired tension. The fiber was wound up on a Teflon tube with threads on the outer surface, which maintains the yarn tense and at the same time keeps it separate from itself to prevent self-adhesion. The Teflon tube with the fiber mounted on it was then transferred to another 5% w/v $CaCl_2$ bath and kept there for 2 h to saturate the fiber with Ca^{2+} ions. The fiber was then washed with deionized water for nearly 1 min to remove excessive salt, dehydrated in an acetone bath overnight, and let dry; all these steps were carried out at room temperature. The yarns were then removed from the Teflon tube for analysis. The jet stretch was varied from 2.0 to 4.6 depending on the stretching capacity of the fiber; its value was controlled by tuning the rpm of the wind up unit to an appropriate value. It must be noted that to calculate the apparent jet stretch, defined in the Introduction section, the outer radius of the Teflon tube was used in the equation instead of the radius of the roller itself. The maximum apparent jet stretch that can be obtained at a specific CNCs load was considered to be 0.2 units below the value at which one or more filaments broke during fiber spinning. *Additional details on the fiber spinning are available in appendix B.*

Fiber Characterization

The tensile modulus, tenacity, and tensile energy to break of the fibers were measured based on the ASTM D2256-02 (2008) standard test method; an INSTRON 5582 was used for this purpose. [31] A total of 21 segments randomly selected from one yarn were broken for the analysis of each fiber; every test specimen contained 10 filaments. The gauge length was equal to 30 mm, and the crosshead speed was 18 mm/min. All tensile tests were performed at the standard atmosphere for testing textiles which is a relative humidity of 65 ± 2% and a temperature of 21 ± 1 °C; the fibers were conditioned for at least 24 h at this conditions before testing.

The fibers morphologies were investigated using a Hitachi S4800 field emission scanning electron microscope (FESEM). The samples were not coated to improve electric conductivity; instead, a low accelerating voltage (0.7-1.0 kV) was employed to reduce charging effects, and beam damage. To determine the calcium content in the fiber, the fibers were sent to the Agricultural Services Laboratory at Clemson University to be analyzed via inductively coupled plasma emission spectrometry (ICP). The results were expressed as the amount of negatively charged sites bound to a Ca^{2+} ion calculated by

$$Ca = \frac{2W_{\mathrm{Ca}}}{2W_{\mathrm{Ca}}/M_{\mathrm{Ca}} + W_{\mathrm{Na}}/M_{\mathrm{Na}}} \cdot 100 \tag{3.1}$$

where W_{Ca} is the percent weight of calcium in the fiber, M_{Ca} is the molar mass of calcium, W_{Na} is the percent weight of sodium in the fiber, and M_{Na} is the molar mass of sodium. It was assumed that only calcium and sodium ions are present and that the purity of the alginate is high enough (98.4%) to consider that most negative sites are in the alginate and the CNCs. [32, 33]

To study the degree of alignment of the CNCs inside the fibers, wide angle X-ray diffraction (WAXD) measurements were performed on the fibers containing 5 wt %

CNCs, and 10%wt CNCs, spun at an apparent jet stretch of 2.4. The azimuthal peaks of the 200 reflections from the monoclinic cellulose Iβ crystals[34] were fitted to a Lorentzian curve, and from the results the full widths at half-maxima were calculated. The source used provided a Cu $K\alpha_1$ X-ray beam with a wavelength of 0.154 nm and a 0.5 mm diameter at the sample position. The WAXD profiles were collected on a Fujifilm BAS-IP MS2325 image plate (IP), and then converted to an image file using an IP scanner (Fujifilm BAS-1800 II).

Results and Discussion

Cellulose Nanocrystals Shape and Dimensions

It is a common practice to approximate the shape of a CNC to a rod with a circular cross section; however, previous reports show that this approximation is not accurate. A TEM analysis of tunicate microcrystals showed that their cross section resembled an elongated hexagon,[35] and a SANS study demonstrated that a model based on a rectangular cross section with dimensions of 8.8 nm by 18.2 nm resulted in a much better fit than a rod-shape model.[36] Also, a MALS analysis of nanocrystals isolated from cotton showed that the value of their fractal dimension is 1.5; this value should be 1.0 for rods and 2.0 for discs.[37] Atomic force microscopy (AFM) was used to determine the length, width, and height of the crystals isolated from cotton powder. Figure 3.1 shows two AFM images of the cellulose nanocrystals; the only correction performed to image on the left was leveling to remove scan lines, and the picture on the right was obtained from the one on the left after applying a surface reconstruction algorithm to correct the tip broadening effects. In order to perform this correction, it was necessary to first model the tip, which is shown in the inset in Figure 3.1. A picture of a porous aluminum surface with sharp edges was taken, and from it the tip was modeled using a blind tip estimation algorithm. A detailed description of the blind tip estimation and the surface reconstruction algorithms was published by Villarubia, J. S.[28]

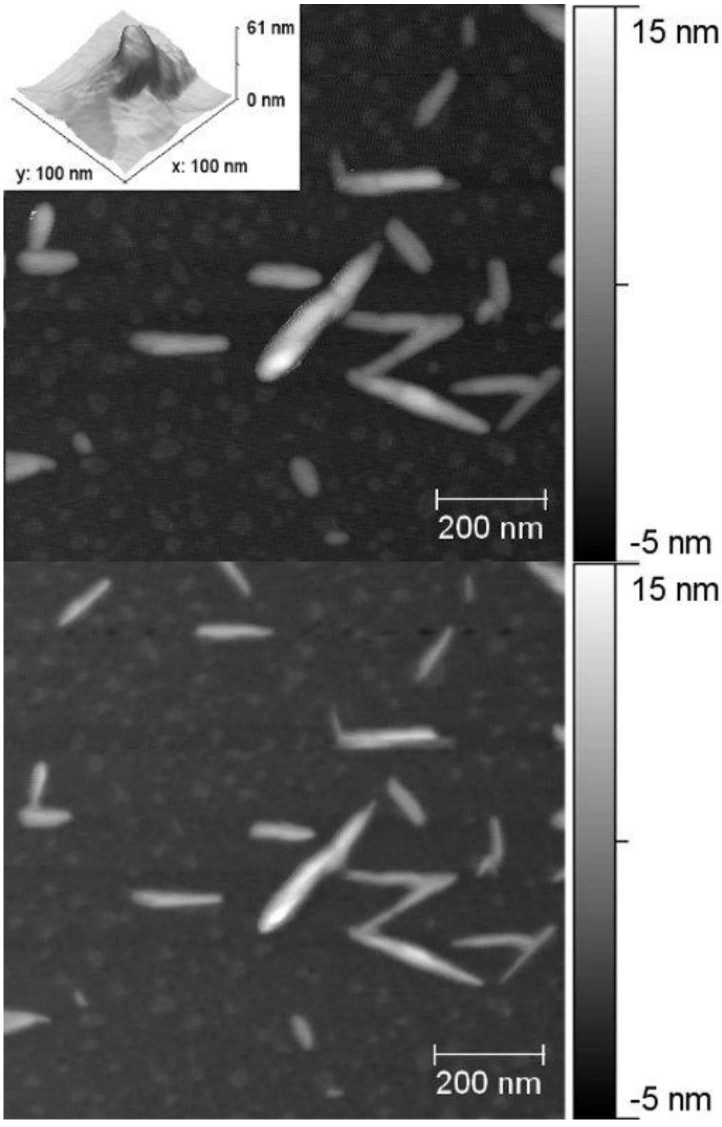

Figure 3.1. Atomic force microscopy (AFM) image of cellulose nanocrystals isolated from cotton powder. The image on the left was leveled; the image on the right was leveled and then deconvoluted to eliminate tip broadening effects. The inset shows the shape of the tip model used to deconvolute the images.

The size distribution histograms of the CNCs are shown in Figure 3.2; the number-average mean and standard deviation of each dimension is also shown. The average length was measured to be 130 nm (s = 63 nm), the average width 20.4 nm (s = 7.8 nm), and the average height 6.8nm (s = 3.3 nm). The average dimensions of the nanocrystals measured in this study are in close agreement with the length and width reported by Elazzouzi-Hafraoui et al, and their height estimate obtained by WAXD.[38] A distinctive feature is the broad distributions which can also be described by the large standard deviations. This is a common characteristic of cellulose nanocrystals populations, regardless of origin.[39, 40] A monodisperse population would be desirable; however, reinforcement of materials can still be obtained from polydispersed nanoparticles.

The length to width, and the width to height aspect ratios were measured for each particle; the average values obtained were 6.6 (s = 2.5), and 3.4 (s = 1.3), respectively. It follows that the width is on average 3.4 times larger than the height; evidently, it would be inaccurate to assume that both dimensions are equal, as would be the case of a circular or squared cross section; thus, the shape of the nanoparticles may be better described by a triaxial geometry, e.g., a scalene ellipsoid. Even when cellulose crystallites are close to have a squared cross section, one particle may be composed by two or more parallel crystallites as was reported by Elazzouzi-Hafraoui et al.[38] For all the particles measured, the width was always larger than the height, which indicates that the particle’s face with the largest area was always oriented parallel to the mica surface.

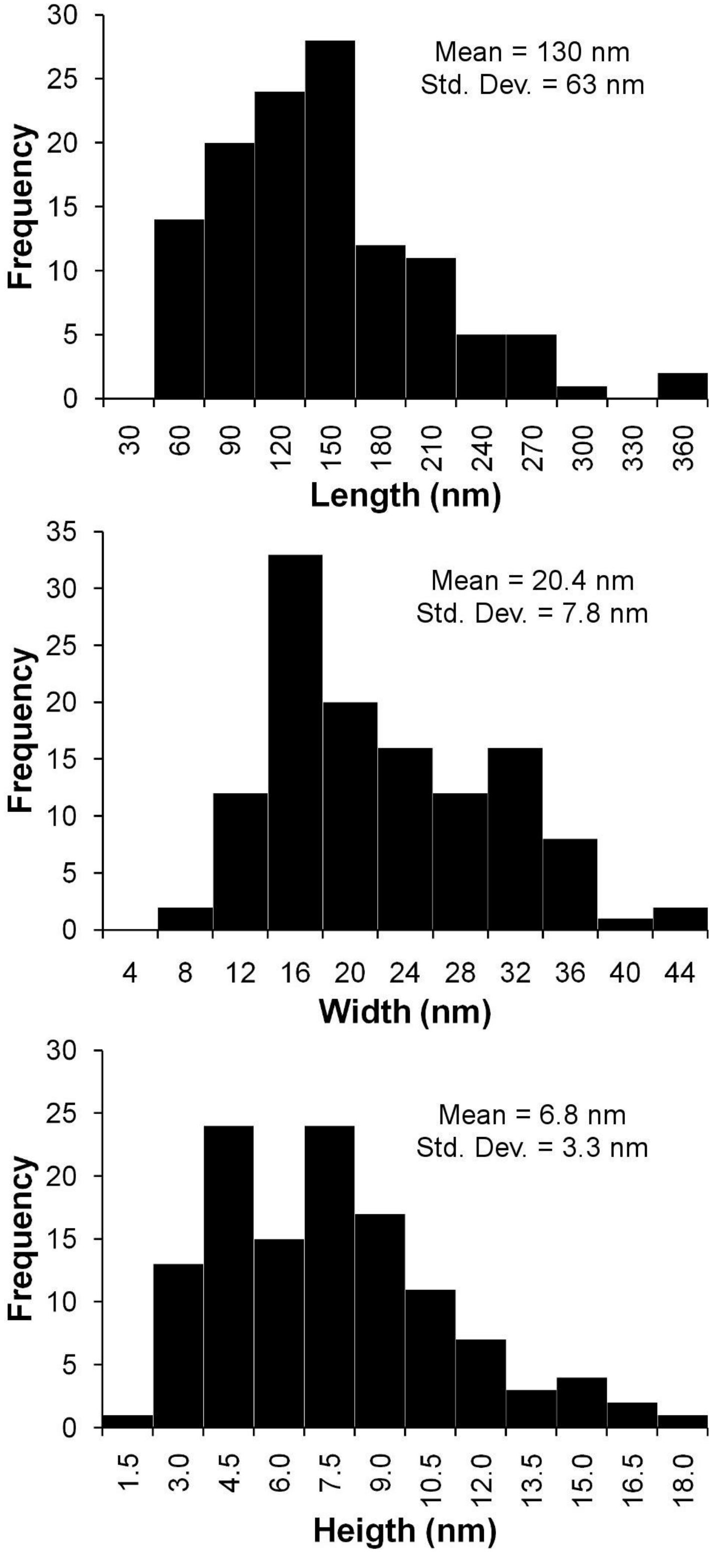

Figure 3.2. Size distribution histograms, mean values, and standard deviation (Std. Dev.) of the cellulose nanocrystals dimensions.

Suspensions Properties

The viscosity of an alginate solution depends on the concentration and the molecular weight of the polymer. To properly wet spin a calcium alginate fiber, the concentration of alginate in the dope solution typically yields a viscosity between 10 and 20 Pa·s. This range can be obtained from a low concentration of high molecular weight polymer or a large concentration of low molecular weight sodium alginate.[17] Solutions with low viscosities will not form filaments when extruded into a coagulating bath, while high viscosities make it difficult to remove air bubbles from the dope solution.

Figure 3.3 shows the viscosity vs shear rate behavior of alginate solutions with different amounts of suspended CNCs. When the alginate concentration was 2 wt %, the viscosity ranged from 50 to 200 Pa·s, which is too large; at a concentration of 1 wt %, the low shear rate viscosities where just slightly below 10 Pa·s for all CNCs loads, which is close to the desired range. All the dope solutions were then prepared with a 1%wt sodium alginate concentration. It can be observed that the presence of cellulose particles has an effect on the steady state viscosity of the suspensions at low shear rates, but at high shear rates all the curves seem to collapse into a single one, as long as the alginate concentration is constant. Low shear conditions are typically found during degassing, but during spinning the shear rates encountered are generally on the order of 10^2 s^{-1} or higher. Thus the addition of a large amount of CNCs may cause difficulties to remove bubbles, but it should have little impact in the ability to pump the solution through the spinneret to form filaments.

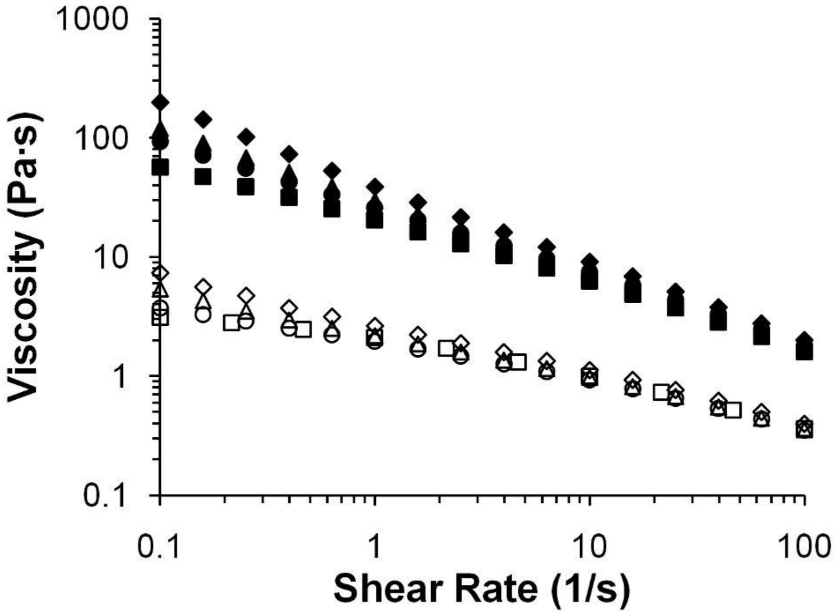

Figure 3.3. Viscosity vs shear rate of CNCs suspended in sodium alginate solutions. Data shown at two different alginate concentrations, 1 wt % (open symbols) and 2 wt % (solid symbols), and four different CNCs concentrations, 0 wt % (squares), 0.26 wt % (circles), 0.51wt % (triangles), and 1.0 wt % (diamonds).

The stability of the dispersion of nanocrystals in a particular media can be qualitatively assessed by monitoring the behavior of the suspensions between polarized films.[30, 41] Stable suspensions of CNCs form chiral nematic liquid crystalline phases above a critical concentration which depends on solvent properties, particle aspect ratio, and surface chemistry.[14, 42] Liquid crystalline ordering causes birefringence of light that can be observed using crossed polarized films, as is shown by the 14.5 wt % suspension in Figure 3.4a, which is completely anisotropic and above the upper critical concentration for liquid crystal formation by CNCs prepared via sulfuric acid hydrolysis. Suspensions below the lower critical concentration for liquid crystal formation, such as the 3.9 wt % sample in Figure 3.4a, are isotropic at rest and thus appear dark between crossed polarizers. When the CNCs are suspended in a 1%wt aqueous solution of sodium alginate, a similar behavior is observed, but the critical concentration is noticeably reduced (Figure 3.4b).

The suspensions with concentrations ranging from 0 to 0.11 wt % CNCs are isotropic, at 0.33 wt % some birefringence can be observed, and at 1.0 wt % birefringence is very evident, indicating the presence of a liquid crystalline ordering. A film prepared by casting the latter suspension on a microscope slide showed that the preferred type of ordering is chiral nematic, but isotropic sections are still present (*pictures provided in appendix B*). As the concentration of CNCs is increased, the particles do not flocculate into agglomerates or precipitate; instead, they orient into a thermodynamically stable ordered structure. This indicates a good dispersion of the CNCs in the sodium alginate solutions and is evidence of good chemical compatibility between the alginate and the cellulose, which is expected given that they are both polycarbohydrates.

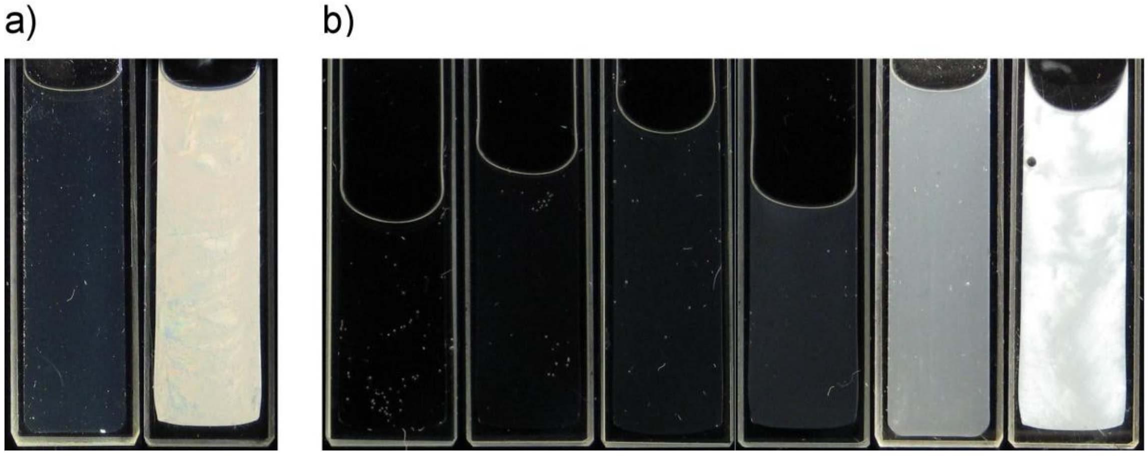

Figure 3.4. Image of CNCs suspensions between crossed polarized sheets. From left to right a) 3.9 and 14.5 wt % (suspended in deionized water); b) 0, 0.020, 0.053, 0.11, 0.33, and 1.0 wt % (suspended in a 1 wt % alginate solution).

The critical concentration at which the liquid crystalline phase appears is clearly lower in the sodium alginate solution than in pure water. A possible explanation is that the presence of 1 wt % alginate in solution reduces the space available to accommodate the CNCs in a disordered phase, thus reducing the critical concentration. Moreover, because a good chemical compatibility is expected between the alginate and the nanocrystals, the latter may behave as templates for the alginate chains to orient along the cellulose axis inducing the formation of a liquid crystalline phase in which alignment of both alginate and CNCs takes place. Orientation of the alginate chains within a fiber happens during wet spinning; however, addition of CNCs may cause an increased alignment and consequently improve the mechanical properties of calcium alginate fibers.

Fibers Morphology

Figure 3.5 shows the cross section and the outer surface of three alginate fibers. The sample in Figure 3.5a does not contain nanocrystals, while Figures 3.5b and 3.5c contain 10 wt % CNCs; Figures 3.5a and 3.5b were spun using an apparent jet stretch of 2.4, while Figure 3.5c was at 4.0. There are no appreciable differences between them, and no agglomerates or defects are visible, which is an indication of good miscibility of the nanocrystals with the alginate matrix. It is also an indication that the apparent jet stretch does not have a noticeable effect on fibers morphology. The surfaces of all the fibers contain striations that are attributed to roughness of the spinneret holes and shrinking during drying.[43] All the other fibers showed the same type of morphology.

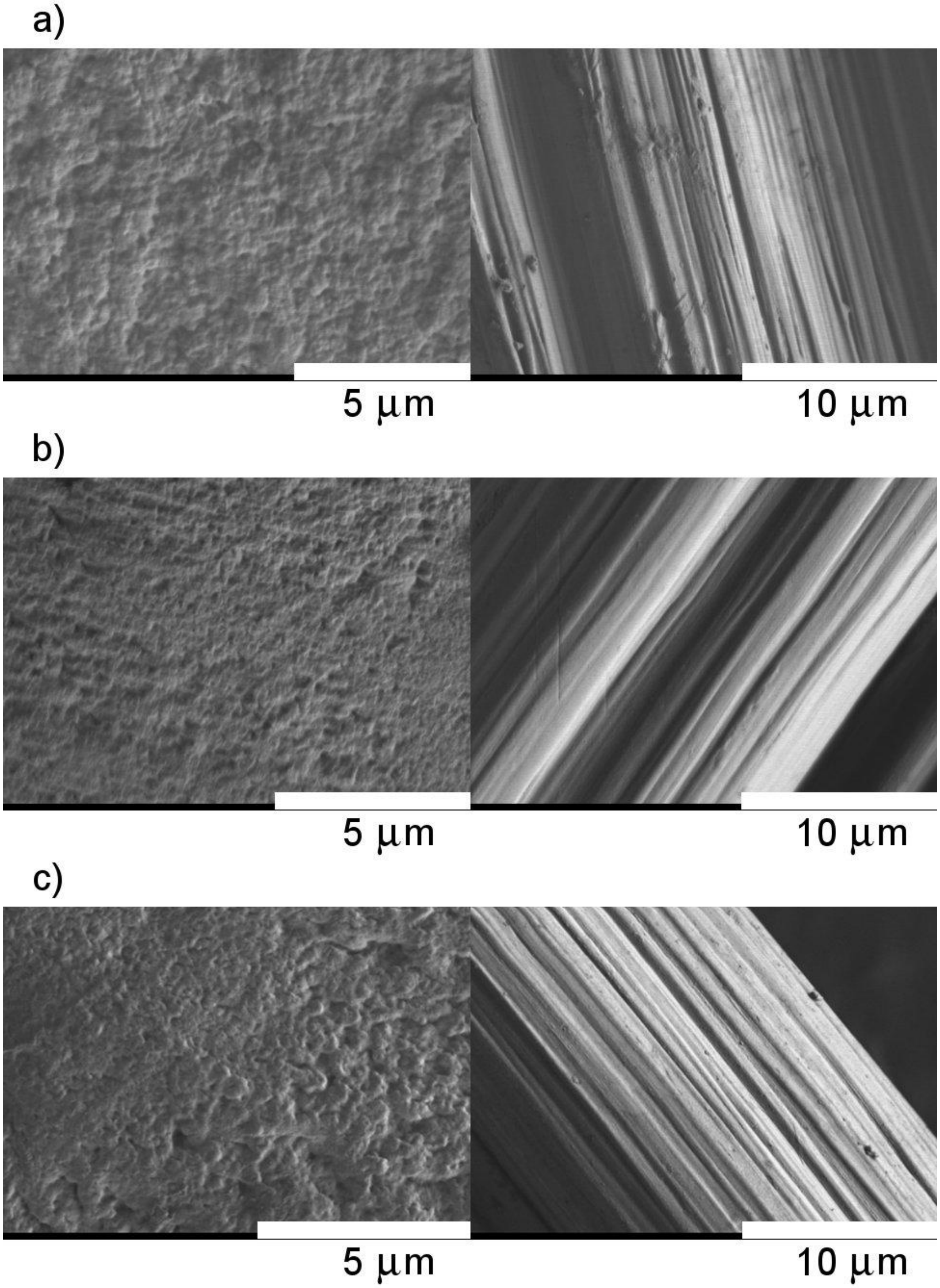

Figure 3.5. FESEM images of alginate fibers: a) 0 wt % CNCs, $J_A = 2.4$, b) 10 wt % CNCs, $J_A = 2.4$, and c) 10 wt % CNCs, $J_A = 4.0$. The cross sections are shown on the left, and the outer surface of the fibers can be observed on the right.

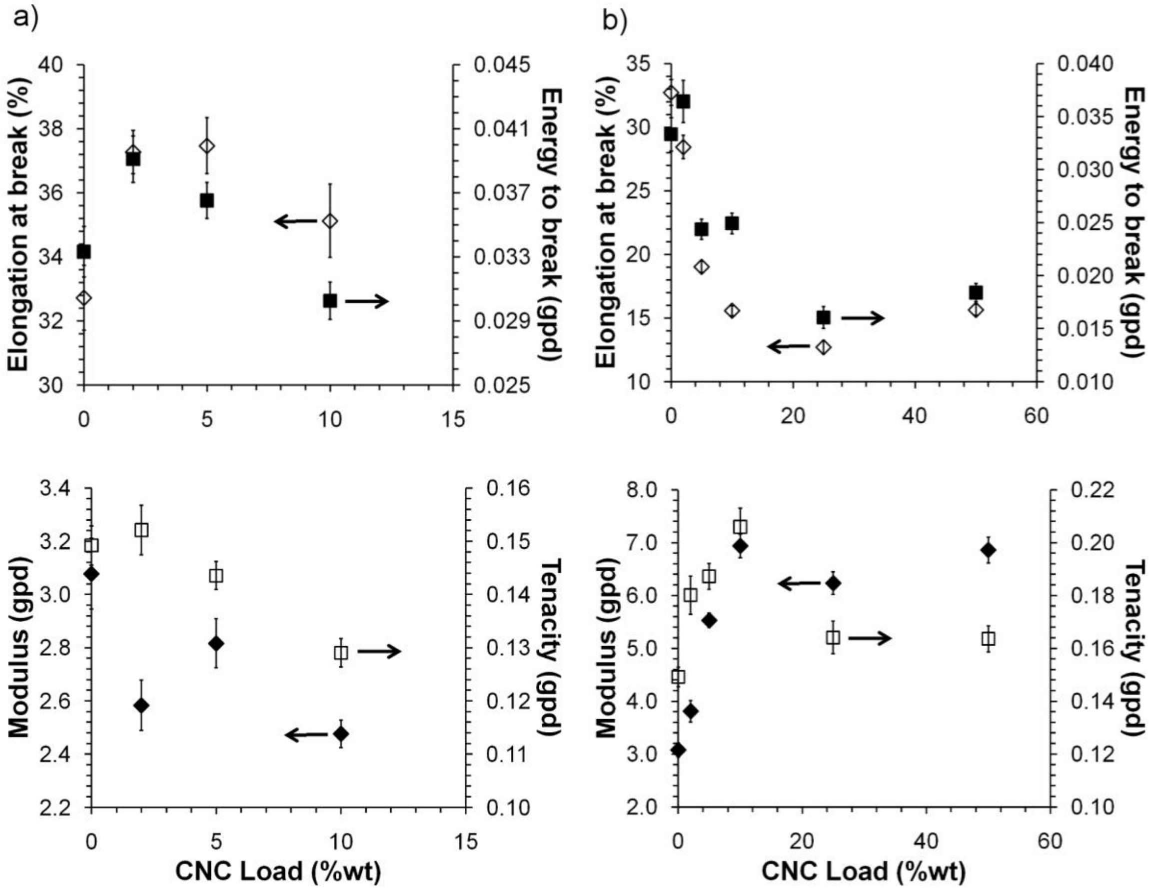

Figure 3.6. Tensile properties of alginate fibers at a) J_A = 2.4, and b) maximum J_A. Symbols key: elongation at break (open diamonds), tensile energy to break (solid squares), modulus (solid diamonds), and tenacity (open squares).

Fibers Mechanical Properties

As a first attempt to reinforce alginate fibers, the cellulose content was varied while all processing conditions were kept constant. The apparent jet stretch used for these experiments was 2.4, which was the maximum value attainable to spin unmodified calcium alginate fibers with the given apparatus. The tensile properties of these fibers are shown in Figure 3.6a. The tenacity and the modulus both decreased with addition of CNCs, while the elongation at break and the tensile energy to break increased until a maximum value at a nanofiller load of 5 wt %, and 2 wt % respectively. These results suggest a detriment of the fiber strength with the presence of the CNCs. *Tabulated data of all fibers tested is presented in appendix B.*

During coagulation, the calcium ions replace the sodium ions and cross-link the alginate chains to form a strong gel, thus the amount of calcium is an important parameter which influences the strength of alginate fibers.[1, 32] The fiber calcium content was measured using ICP analysis to determine if the CNCs limit Ca^{2+} ion diffusion into the fiber, causing a reduction in the electrostatic cross-linking. These measurements are shown in Table 3.2 expressed as the percentage of negatively charged sites bound to a calcium ion.[32, 33]

The calcium content is above 99% in all cases, indicating saturation of the fibers. Also, very little variations were observed as the CNCs load was increased; thus the amount of calcium does not seem to have a significant effect on the properties of the fibers used in this study. Introduction of voids may also cause a detriment of mechanical properties; however, the presence of voids is unexpected due to the good chemical compatibility between the alginate and the cellulose. A more plausible explanation may be a disruption of the egg box structure by the CNCs. The alginate in the GG blocks assemble in a zigzag manner which resembles an egg box; inside, one Ca^{2+} ion ("the egg") is coordinated by four guluronate units from two parallel alginate chains (two consecutive units from each chain). This structure is believed to provide the strength to the alginate fibers.[17] The CNCs may introduce themselves between the GG blocks, disrupting the egg box assembly and weakening the fibers. Another possibility may be a reduction of the degree of orientation within the fibers upon addition of CNCs; further discussion of this topic will be addressed later on this chapter.

Table 3.2. Fiber Yarn Denier and Calcium Content Expressed in Percentage of Negatively Charged Sites Occupied by a Calcium Ion.

CNCs Load (%wt)	At $J_A = 2.4$		At Max. J_A	
	Denier	Ca (%)	Denier	Ca (%)
0	126±2	99.41	126±2	99.41
2	133±4	99.39	92±3	99.58
5	134±2	99.39	78±1	99.50
10	141±1	99.62	74±1	99.63
25	---	---	75±2	99.61
50	169±2	99.57	152±3	99.13

Even though the fibers seem to be weaker with the addition of the CNCs, a maximum in the tensile energy to break and elongation at break was observed with addition of CNCs at constant J_A; suggesting the ability to increase the jet stretch during fiber processing and form a stronger structure to achieve better results. For each CNCs load several fibers were wet spun at increasing values of the apparent jet stretch until it was no longer possible to spin a fiber. Therefore, the maximum apparent jet stretch was 0.2 units below the value at which one or more filaments broke. Figure 3.7 shows the improvement in stretching capacity as the cellulose load is increased up to a maximum of 4.6 at a CNCs concentration of 25 wt %. The effect of jet stretch on the mechanical properties of the material is described in Figure 3.8, where the fibers with 5 wt % CNCs were used as an example. It is clear that both the elongation at break and the tensile energy to break decreased with larger values of J_A indicating an increase in brittleness. However, the most important aspect to highlight is the enhancement of fiber modulus and tenacity, which indicates that they are becoming stiffer and stronger. Moreover, a higher apparent jet stretch increases spinning rate considerably, making a large-scale process more efficient.

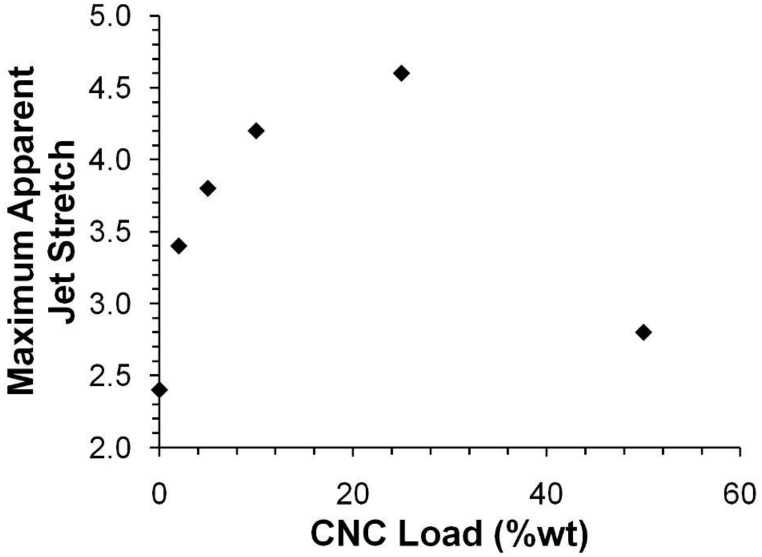

Figure 3.7. Effect of CNCs load on the maximum apparent jet stretch during wet spinning.

The tensile properties of the fibers spun at maximum jet stretch are shown in Figure 3.6b. A large increase in strength was observed up to a maximum value at 10 wt % CNCs, where the tenacity was 38% larger than the strongest calcium alginate fiber. It is possible that beyond this point there is some agglomeration of the nanocrystals in the alginate matrix, even when it was not detected by FESEM. The chemical composition of alginate and the CNCs is so similar that it is very difficult to obtain contrast between them. A similar behavior was observed regarding modulus; at 10 wt % it was possible to obtain an increase of 123% with respect to plain alginate, indicating higher resistance to tensile deformation. The shape of the curves in Figure 3.6b suggest the existence of a local minimum somewhere between 25 and 50 wt %, this could be a percolation limit above which the nanocrystals form a strong interconnected network. [44,45] The elongation at break and the tensile energy to break of the fibers decreased until they reached a minimum value at 25 wt % CNCs thus increasing their brittleness.

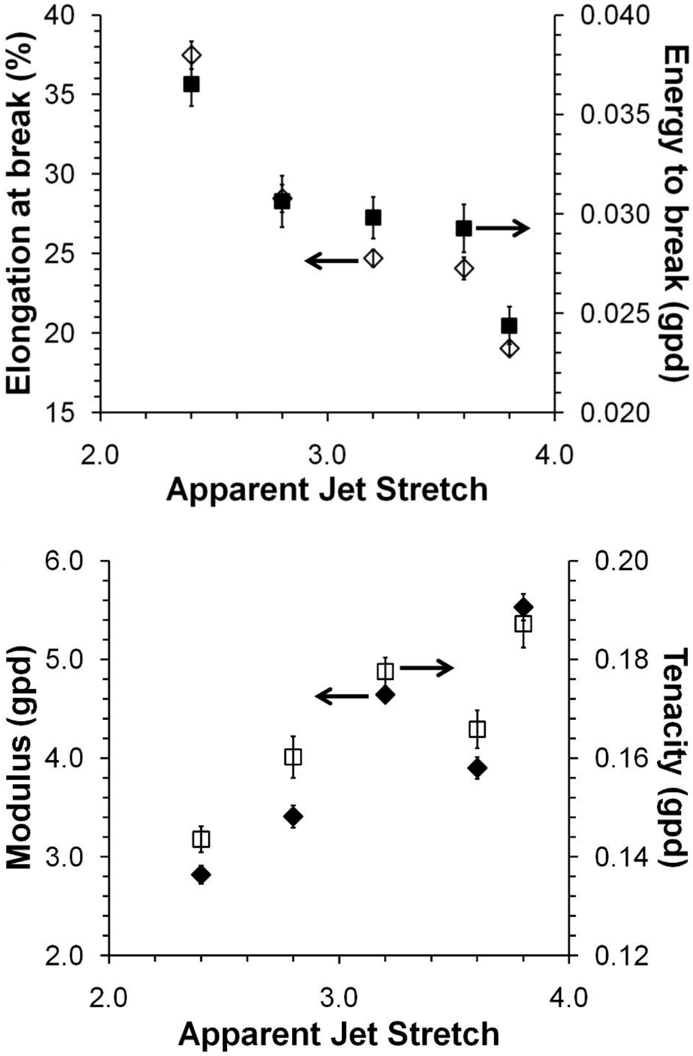

Figure 3.8. Effect of jet stretch on the mechanical properties of alginate fibers with a 5 wt % CNCs load. Symbols key: elongation at break (open diamonds), tensile energy to break (solid squares), modulus (solid diamonds), and tenacity (open squares).

It was previously discussed that the CNCs may induce alignment of the alginate chains, as evidenced by the crossed polarized images of the suspensions at rest, where a liquid crystalline phase was formed at low CNCs concentrations in 1 wt % sodium alginate solutions. Alignment of the CNCs and the alginate would be further accentuated under the shear and elongation conditions present during fiber spinning. Thus, the CNCs induced alignment enables fiber spinning at higher jet stretches. However, it is uncertain why at a constant jet stretch this alignment is not translated to an improvement in mechanical properties; instead, the data suggest a detriment in the structure of the fibers.

There have been reports that the introduction of CNCs in polymers with good particle-matrix interactions may cause a loss of mechanical properties. This was observed for the case of plasticized starch, where a decrease in the rubbery modulus, measured by dynamic mechanical analysis, was observed upon addition of cellulose nanocrystals in moist conditions; the same study showed that during a tensile test experiment no reinforcement was observed for CNCs concentrations below 25%.[19] Another study demonstrated that the tensile storage modulus of CAB, which is hydrophobic, reinforced with silylated CNCs (hydrophobic) was lower than that obtained with unmodified ones (hydrophilic).[21] Also, a natural rubber filled with hydrophobic chitin nanocrystals had a lower modulus and tensile strength when compared with the same material filled with hydrophilic nanocrystals.[46] The explanation given in those studies is that the particle-particle interactions above the percolation limit are thought to be the biggest contributors to the reinforcing effect of cellulose and chitin nanocomposites; a good chemical compatibility may reduce this interaction at the same time that improves the particle-matrix interaction.[11, 44] However, there are no previous studies, to our knowledge, that have taken into account the effect of CNCs on the stretching capacity during processing and its consequent impact on particles alignment and mechanical properties.

Aqueous suspensions of CNCs form chiral nematic, instead of nematic, liquid crystals, which means that they tend to align in layers where the director of each layer is rotated with respect to the previous one.[14, 47] This ordering can be broken by an external force field, as has been proven by shearing a nanocrystals suspension; at high shear rates they orient as a nematic liquid crystal rather than a chiral nematic.[42, 48] The steady shear rheology shown in Figure 3.3 shows a very quick shear thinning of the suspensions that contain CNCs, and all the curves at a constant sodium alginate concentration seem to collapse onto a single one at high shear rates regardless of the CNCs concentration. This behavior suggests alignment of the CNCs and alginate chains at high deformation rates. During extensional flow, as is the case encountered in fiber spinning, the crystals and polymer chains are forced to align parallel to the fiber axis while they try to relax to a "twisted" state along with the chiral alginate molecules. Evidence to support this hypothesis is provided by the fact that the apparent jet stretch could be increased to counterbalance the structural deterioration caused by the addition of CNCs. However, to provide further evidence, the degree of orientation of the CNCs in the fibers with 5 wt % and 10 wt % load, spun at J_A=2.4, was studied.

WAXD measurements were performed to study changes in orientation with addition of CNCs. The azimuthal peak width of the 200 reflection from the cellulose Iβ crystal[34] was used as an indication of the degree of orientation of the CNCs. A sharp peak indicates a narrow distribution of the angles formed by the 200 planes and the fiber axis and consequently a high degree of orientation of the nanocrystals. On the other hand, a broad distribution indicates low degree of orientation. In the case of the fiber with 5 wt % CNCs, the full width at half-maximum of the azimuthal peak was 18 ± 2°, while for the fiber with 10 wt % CNCs the result obtained was 22 ± 1°. The former sample has a higher degree of orientation than the latter; consequently, there was a reduction in the degree of alignment upon addition of CNCs. This supports our hypothesis that CNCs try to twist during fiber spinning, a phenomenon which is accentuated as CNCs loading is increased. Future studies will further investigate the degree of CNCs orientation within the nanocomposite fibers and the influence on the resulting fiber properties. *The WAXD patterns of the two fibers are provided in appendix B.*

Conclusions

Atomic force microscopy (AFM) showed that approximating the cellulose nanoparticles to a biaxial geometry (e.g., rod shape with circular or squared cross section) is inaccurate; instead, the particles may be better represented by a triaxial geometry. The dispersions of these particles are very stable in water and in 1 wt % solutions of sodium alginate, which, to some extent, is evidence of the expected good chemical compatibility between the CNCs and the polymer matrix. Steady shear measurements showed that the nanocrystals considerably increase the viscosity of sodium alginate solutions at low shear rates. However, at high shear rates the CNCs do not affect the viscosity significantly.

Very likely the CNCs and the alginate chains tend to align as the deformation rate is increased.

Calcium alginate fibers filled with CNCs can be obtained by wet spinning through a $CaCl_2$ coagulating bath. Field emission scanning electron microscopy showed that the morphology of the fibers does not change with the addition of CNCs. The presence of CNCs, at loads of 10 wt % and below, decreases the tenacity and tensile modulus of the fibers if the processing conditions are kept constant, presumably due to a reduction in the degree of alignment. However, CNCs inclusion increases the tensile energy to break of the fibers and enables a significant increase in the apparent jet stretch during wet spinning to values that nearly double the native alginate. By tuning the degree of stretch simultaneously with the CNCs load, it is possible to spin stronger and stiffer alginate fibers while reducing the processing time. A reinforcement of 38% in tenacity and 123% in modulus can be obtained in fibers wet spun at an apparent jet stretch of 4.2 and a CNCs load of 10 wt %.

References

(1) Becker, T. A.; Kipke, D. R.; Brandon, T. Calcium Alginate Gel: A Biocompatible and Mechanically Stable Polymer for Endovascular Embolization. *J. Biomed. Mater. Res.* **2001**, *54*, 76-86.

(2) Majima, T.; Funakosi, T.; Iwasaki, N.; Yamane, S. T.; Harada, K.; Nonaka, S.; Minami, A.; Nishimura, S. Alginate and Chitosan Polyion Complex Hybrid Fibers for Scaffolds in Ligament and Tendon Tissue Engineering. *J. Orthop. Sci.* **2005**, *10*, 302-307.

(3) Petrulyte, S. Advanced Textile Materials and Biopolymers in Wound Management. *Dan. Med. Bull.* **2008**, *55*, 72-77.

(4) Qin, Y. The Gel Swelling Properties of Alginate Fibers and their Applications in Wound Management. *Polym. Adv. Technol.* **2008**, *19*, 6-14.

(5) Hermes, R. S.; Narayani, R. Polymeric Alginate Films and Alginate Beads for the Controlled Delivery of Macromolecules. *Trends Biomater. Artif. Organs* **2002**, *15*, 54-56.

(6) Gazori, T.; Khoshayand, M. R.; Azizi, E.; Yazdizade, P.; Nomani, A.; Haririan, I. Evaluation of Alginate/Chitosan Nanoparticles as Antisense Delivery Vector: Formulation, Optimization and in Vitro Characterization. *Carbohydr. Polym.* **2009**, *77*, 599-606.

(7) Wang, Q.; Zhang, N.; Hu, X.; Yang, J.; Du, Y. Alginate/polyethylene Glycol Blend Fibers and their Properties for Drug Controlled Release. *J. Biomed. Mater. Res. A* **2007**, *82*, 122-128.

(8) Kauffman, J. S.; Ellerbrock, B. M.; Stevens, K. A.; Brown, P. J.; Pennington, W. T.; Hanks, T. W. Preparation, Characterization, and Sensing Behavior of Polydiacetylene Liposomes Embedded in Alginate Fibers. *ACS Appl. Mater. Interfaces* **2009**, *1*, 1287-1291.

(9) Huang, R. Y. M.; Pal, R.; Moon, G. Y. Characteristics of Sodium Alginate Membranes for the Pervaporation Dehydration of Ethanol-Water and Isopropanol-Water Mixtures. *J. Membr. Sci.* **1999**, *160*, 101-113.

(10) Wang, Q.; Du, Y.; Hu, X.; Yang, J.; Fan, L.; Feng, T. Preparation of alginate/soy Protein Isolate Blend Fibers through a Novel Coagulating Bath. *J. Appl. Polym. Sci.* **2006**, *101*, 425-431.

(11) Azizi Samir, M. A. S.; Alloin, F.; Dufresne, A. Review of Recent Research into Cellulosic Whiskers, their Properties and their Application in Nanocomposite Field. *Biomacromolecules* **2005**, *6*, 612-626.

(12) Šturcova, A.; Davies, G. R.; Eichhorn, S. J. Elastic Modulus and Stress-Transfer Properties of Tunicate Cellulose Whiskers. *Biomacromolecules* **2005**, *6*, 1055-1061.

(13) Dong, X. M.; Kimura, T.; Revol, J. -F; Gray, D. G. Effects of Ionic Strength on the Isotropic-Chiral Nematic Phase Transition of Suspensions of Cellulose Crystallites. *Langmuir* **1996**, *12*, 2076-2082.

(14) Revol, J. -F.; Godbout, L.; Dong, X. -M.; Gray, D. G.; Chanzy, H.; Maret, G. Chiral Nematic Suspensions of Cellulose Crystallites; Phase Separation and Magnetic Field Orientation. *Liq. Cryst.* **1994**, *16*, 127-34.

(15) Speakman, J. B.; Chamberlain, N. H. The Production of Rayon from Alginic Acid*. *Journal of the Society of Dyers and Colourists* **1944**, *60*, 264-272.

(16) Yang, G.; Zhang, L.; Peng, T.; Zhong, W. Effects of Ca2+ Bridge Cross-Linking on Structure and Pervaporation of cellulose/alginate Blend Membranes. *J. Membr. Sci.* **2000**, *175*, 53-60.

(17) Qin, Y. Alginate Fibres: An Overview of the Production Processes and Applications in Wound Management. *Polym. Int.* **2008**, *57*, 171-180.

(18) Dubief, D.; Samain, E.; Dufresne, A. Polysaccharide Microcrystals Reinforced Amorphous Poly(-Hydroxyoctanoate) Nanocomposite Materials. *Macromolecules* **1999**, *32*, 5765-5771.

(19) Angles, M. N.; Dufresne, A. Plasticized starch/tunicin Whiskers Nanocomposite Materials. 2: Mechanical Behavior. *Macromolecules* **2001**, *34*, 2921-2931.

(20) Noishiki, Y.; Nishiyama, Y.; Wada, M.; Kuga, S.; Magoshi, J. Mechanical Properties of Silk Fibroin-Microcrystalline Cellulose Composite Films. *J. Appl. Polym. Sci.* **2002**, *86*, 3425-3429.

(21) Grunert, M.; Winter, W. T. Nanocomposites of Cellulose Acetate Butyrate Reinforced with Cellulose Nanocrystals. *J. Polym. Environ.* **2002**, *10*, 27-30.

(22) Habibi, Y.; Goffin, A.; Schiltz, N.; Duquesne, E.; Dubois, P.; Dufresne, A. Bionanocomposites Based on Poly(-Caprolactone)-Grafted Cellulose Nanocrystals by Ring-Opening Polymerization. *J. Mater. Chem.* **2008**, *18*, 5002-5010.

(23) Ertesvag, H.; Valla, S. Biosynthesis and Applications of Alginates. *Polym. Degrad. Stab.* **1998**, *59*, 85-91.

(24) Gacesa, P. Alginates. *Carbohydr. Polym.* **1988**, *8*, 161-182.

(25) Rånby, B. G. Fibrous Macromolecular Systems. Cellulose and Muscle. the Colloidal Properties of Cellulose Micelles. *Discuss. Faraday Soc.* **1951**, *11*, 158-164.

(26) Gray, D. G. Transcrystallization of Polypropylene at Cellulose Nanocrystal Surfaces. *Cellulose* **2008**, *15*, 297-301.

(27) Kvien, I.; Tanem, B. S.; Oksman, K. Characterization of Cellulose Whiskers and their Nanocomposites by Atomic Force and Electron Microscopy. *Biomacromolecules* **2005**, *6*, 3160-3165.

(28) Villarrubia, J. S. Algorithms for Scanned Probe Microscope Image Simulation, Surface Reconstruction, and Tip Estimation. *J. Res. Natl. Inst. Stand. Technol.* **1997***, 102*, 425-454.

(29) Habibi, Y.; Chanzy, H.; Vignon, M. R. TEMPO-Mediated Surface Oxidation of Cellulose Whiskers. *Cellulose* **2006***, 13*, 679-687.

(30) De Souza Lima, M. M.; Borsali, R. Static and Dynamic Light Scattering from Polyelectrolyte Microcrystal Cellulose. *Langmuir* **2002***, 18*, 992-996.

(31) ASTM Standard D2256, 2002 (2008), *Standard Test Method for Tensile Properties of Yarns by the Single-Strand Method,*ASTM International, West Conshohocken, PA, 2008; DOI:10.1520/D2256-02, www.astm.org.

(32) Qin, Y. Gel Swelling Properties of Alginate Fibers. *J. Appl. Polym. Sci.* **2004***, 91*, 1641-1645.

(33) Qin, Y. Ion-Exchange Properties of Alginate Fibers. *Text. Res. J.* **2005***, 75*, 165-8.

(34) Nishiyama, Y.; Langan, P.; Chanzy, H. Crystal Structure and Hydrogen-Bonding System in Cellulose I[Beta] from Synchrotron X-Ray and Neutron Fiber Diffraction. *J. Am. Chem. Soc.* **2002***, 124*, 9074-9082.

(35) Helbert, W.; Nishiyama, Y.; Okano, T.; Sugiyama, J. Molecular Imaging of Halocynthia Papillosa Cellulose. *J. Struct. Biol.* **1998***, 124*, 42-50.

(36) Terech, P.; Chazeau, L.; Cavaillé, J. -Y. Small-Angle Scattering Study of Cellulose Whiskers in Aqueous Suspensions. *Macromolecules* **1999***, 32*, 1872-1875.

(37) Braun, B.; Dorgan, J. R.; Chandler, J. P. Cellulosic Nanowhiskers. Theory and Application of Light Scattering from Polydisperse Spheroids in the Rayleigh-Gans-Debye Regime. *Biomacromolecules* **2008***, 9*, 1255-1263.

(38) Elazzouzi-Hafraoui, S.; Nishiyama, Y.; Putaux, J.; Heux, L.; Dubreuil, F.; Rochas, C. The Shape and Size Distribution of Crystalline Nanoparticles Prepared by Acid Hydrolysis of Native Cellulose. *Biomacromolecules* **2008***, 9*, 57-65.

(39) Dong, X. M.; Revol, J. -F; Gray, D. G. Effect of Microcrystallite Preparation Conditions on the Formation of Colloid Crystals of Cellulose. *Cellulose* **1998***, 5*, 19-32.

(40) Beck-Candanedo, S.; Roman, M.; Gray, D. G. Effect of Reaction Conditions on the Properties and Behavior of Wood Cellulose Nanocrystal Suspensions. *Biomacromolecules* **2005***, 6*, 1048-1054.

(41) Azizi Samir, M.A.S.; Alloin, F.; Sanchez, J.-Y.; El Kissi, N.; Dufresne, A. Preparation of Cellulose Whiskers Reinforced Nanocomposites from an Organic Medium Suspension. *Macromolecules* **2004**, *37*, 1386-1393.

(42) Orts, W. J.; Godbout, L.; Marchessault, R. H.; Revol, J. -F. Enhanced Ordering of Liquid Crystalline Suspensions of Cellulose Microfibrils: A Small Angle Neutron Scattering Study. *Macromolecules* **1998**, *31*, 5717-5725.

(43) Watthanaphanit, A.; Supaphol, P.; Tamura, H.; Tokura, S.; Rujiravanit, R. Fabrication, Structure, and Properties of Chitin Whisker-Reinforced Alginate Nanocomposite Fibers. *J. Appl. Polym. Sci.* **2008**, *110*, 890-899.

(44) Favier, V.; Canova, G. R.; Shrivastava, S. C.; Cavaillé, J. -Y. Mechanical Percolation in Cellulose Whisker Nanocomposites. *Polym. Eng. Sci.* **1997**, *37*, 1732-9.

(45) Balberg, I.; Binenbaum, N. Computer Study of the Percolation Threshold in a Two-Dimensional Anisotropic System of Conducting Sticks. *Physical Review B (Condensed Matter)* **1983**, *28*, 3799-812.

(46) Gopalan Nair, K.; Dufresne, A.; Gandini, A.; Belgacem, M. N. Crab Shell Chitin Whiskers Reinforced Natural Rubber Nanocomposites. 3. Effect of Chemical Modification of Chitin Whiskers. *Biomacromolecules* **2003**, *4*, 1835-1842.

(47) Roman, M.; Gray, D. G. Parabolic Focal Conics in Self-Assembled Solid Films of Cellulose Nanocrystals. *Langmuir* **2005**, *21*, 5555-5561.

(48) Ebeling, T.; Paillet, M.; Borsali, R.; Diat, O.; Dufresne, A.; Cavaillé, J. -Y.; Chanzy, H. Shear-Induced Orientation Phenomena in Suspensions of Cellulose Microcrystals, Revealed by Small Angle X-Ray Scattering. *Langmuir* **1999**, *15*, 6123-6126.

CHAPTER FOUR

WIDE ANGLE X-RAY DIFFRACTION OF CELLULOSE NANOCRYSTAL – ALGINATE NANOCOMPOSITE FIBERS

Reproduced with permission from Ureña-Benavides, E. E.; Kitchens, C. L.
Macromolecules **2011**, Available online, doi: 10.1021/ma102731m. Copyright 2011
American Chemical Society

Introduction

Wide angle X-ray diffraction (WAXD) is a powerful technique commonly used to describe the crystalline structure of materials. Its applications to polymer composites include the determination of degree of crystallinity, orientation of crystalline regions, concentration of a solid phase, etc.; which govern the mechanical properties of the material.[2, 3] Increasing the concentration of a stiff material would typically improve the modulus of a composite; and an increase in crystallinity is commonly accompanied by higher alignment and better mechanical performance. However, these trends are not always true, as exemplified in native cellulose fibers. Cotton typically possesses higher degree of crystallinity than ramie, hemp, and flax, but has lower tensile strength, and modulus. In these cases, the mechanical properties are more strongly impacted by the assembly of the crystallites, which spiral around the fiber axis. Cotton fibers have larger spiral angles than bast fibers like ramie, hemp, and flax; In essence, crystallite orientation defines the mechanical performance of native cellulose fibers.[4, 5]

Cellulose nanocrystals (CNC) have recently gained interest as a renewable, environmentally friendly, and cost effective reinforcing agent for composite materials;

however results vary considerably from one study to another.[6-8] In some instances, the hydrophilic CNC have been found to possess little or no reinforcing effect when introduced into hydrophilic polymer matrices; however CNC have improved the mechanical performance of hydrophobic materials. Interestingly, the reinforcing capacity for hydrophobic polymers is reduced if the CNC are surface modified to make them hydrophobic.[9, 10] The processing techniques, particle-matrix interactions, and particle-particle interactions significantly impact the reinforcing capabilities of CNC and are important factors to take into account.[8]

In a recent paper, we reported a reduction of tenacity and tensile modulus of calcium alginate fibers with the addition of CNC. However, small concentrations of the nanoparticles increased the elongation at break and enabled a nearly twofold increase in apparent jet stretch (J_A); ultimately forming stronger fibers (J_A is defined as the tangential velocity of the first roller divided by the linear extrusion velocity).[1] The addition of CNC had a significant impact on the structure of the nanocomposite fiber and thus is the focus of this study.

Calcium alginate fibers are formed by electrostatic crosslinking of polymer chains via. divalent Ca ions; their mechanical performance is primarily dependent on the type and strength of the junction zones.[11] We had hypothesized that the CNC interfered with the formation of junction zones thus disrupting the “egg box” structure and causing a detriment of mechanical properties. However, since increased fiber stretching ultimately led to stronger fibers, it was also believed that the orientation within the fibers played a fundamental role.

In this study, we obtained WAXD profiles of CNC – calcium alginate fibers spun at different J_A and variable cellulose loads. The diffraction patterns were used to study the effects of CNC and processing conditions on the alginate structure and CNC orientation. For this purposes a deconvolution of the profiles was achieved and individual patterns were obtained for alginate and cellulose as separate phases. The degree of orientation and assembly of the cellulose crystallites were quantified by analyzing the intensity distribution of the (2,0,0) reflection. The same signal was used to obtain a calibration curve for the nanocrystals concentration.

Experimental Section

Materials

Alginate fibers were formed using high viscosity sodium alginate with a purity of 98.4%, as purchased from MP Biomedicals, LLC (catalog number 154723). The alginate was isolated by the manufacturer from the seaweed *Macrocystis pyrifera* (kelp). Alginates isolated from the same seaweed have similar chemical compositions; 61.0 % mannuronate (M), and 39.0 % guluronate (G), with fractions of MM, GG, and MG blocks ranging from 0.38 to 0.43, 0.16 to 0.21, and 0.36 to 0.46 respectively. [11-13] It must be noted that a relatively low concentration of G blocks is present for this source of alginate. CNC were isolated from Whatman cellulose filter aid. Sulfuric acid (98%) was purchased and diluted to 64%. Technical grade anhydrous calcium chloride was used for fiber coagulation, and ACS grade acetone was employed for fiber dehydration.

Isolation of Cellulose Nanocrystals

The isolation of the CNC was achieved by acid hydrolysis of cotton cellulose (Whatman filter aid) with 64 wt % sulfuric acid at 45°C for 50 min. The reaction was quenched with cold deionized water, and then the CNC were purified through precipitation, decantation and dialysis. More details regarding this procedure can be found elsewhere. [1, 14-16]

Preparation of CNC – Alginate Fiber Nanocomposites

The calcium alginate fibers filled with CNC were prepared by wet spinning an aqueous suspension of the CNC and sodium alginate into a 5 wt % $CaCl_2$ coagulating bath. Fibers with CNC loads of 2.0, 5.0, 10, 25, and 50 wt % were prepared. The spinning dopes had different stretching capacities depending on cellulose concentration, thus the apparent jet stretch was varied from 2.0 to 4.6 depending on the CNC content. The maximum J_A that can be obtained at a specific CNC load was considered to be 0.2 units below the value at which one or more filaments broke during fiber spinning. More details regarding fiber spinning can be found elsewhere.[1]

Collection of WAXD Data

The fibers were glued to a small tab (5 x 1 cm) made of cardboard file folder with a hole in the center (1 x 0.5 cm) which was aligned with the specimen. Caution was taken to ensure that the yarns were all straight and parallel to each other. The glue was only applied to the ends of the samples to avoid interaction with the beam. The specimen was then fixed to a goniometer head and aligned with the beam to allow the X-rays to pass through the fibers. The Cu Kα_1 X-ray beam had a wavelength (λ) of 0.154 nm and a 0.5 mm diameter at the sample position. The WAXD patterns were recorded on a Fujifilm BAS-IP MS2325 image plate (IP), which was located 112 mm from the sample. The IP was then scanned with a Fujifilm BAS-1800 II scanner to transform the data into an electronic format.

The patterns were corrected for air scattering and cosmic background. This correction was achieved by collecting a diffraction pattern without any sample and subtracting it from the raw data. A Fraser correction was performed to convert the blackening densities and pixel positions to intensities and reciprocal space coordinates.[17]

Extraction of One Dimensional Diffraction Patterns

The intensity at each 2θ, which is twice the Bragg angle, was averaged with respect to the azimuthal angle (ϕ) to obtain a one dimensional, powder like, diffraction pattern for each sample. To account for variations in the intensity of the diffracted beam and exposure time, all data was normalized to the intensity at $2\theta = 54°$, averaged from an equatorial slice ($67° < \phi < 113°$) of the same pattern. This position was chosen because no reflections from cellulose or alginate were observed at that Bragg angle and because the experimental setup did not allow for measuring the intensity at $2\theta = 0°$. The diffraction patterns were divided into two sections ($9.0° < 2\theta < 19.6°$, and $18.0° < 2\theta < 26.6°$), and the cellulose and alginate peaks were deconvoluted in each section by fitting the profile to multiple Lorentzian peaks. During fitting, the center position of each peak was constrained to ±1° of a visual estimate, while for the amorphous halo this range was ±4°; the width and area in all cases were forced to positive values. The signals corresponding to cellulose and alginate were then joined to obtain a complete diffraction pattern for each component of the fiber.

CNC Orientation

From the 2D pattern, a distribution of the intensity (I) with respect to ϕ was obtained by scanning along the arc defined by $2\theta = 22.9°$; which corresponds to the (2,0,0) reflections of the cellulose Iβ crystals.[18] The measured $I(\phi)$ is a convolution of the orientation distribution and instrumental broadening; however the width of the instrumental profile was considered negligible for which $I(\phi)$ was attributed entirely to the orientation of the CNC. $I(\phi)$ for the (2,0,0) reflection was used to quantify the degree of orientation of the nanocrystals within the fiber. For this purpose $I(\phi)$ was fit to a Lorentzian distribution and the full width at half maximum (*FWHM*), which has an inverse relation with alignment, was measured for each of the samples.

Alternatively, an order parameter (S) was calculated from $I(\phi)$ using the procedure described by Alexander.[19] This method calculates the second moment of the orientation distribution function (P_2),

$$S = P_2\left(\cos\phi_{c,z}\right) = \frac{1}{2}\left(3\left\langle\cos^2\phi_{c,z}\right\rangle - 1\right) \tag{4.1}$$

where $\phi_{c,z}$ is the angle formed between the c axis of the cellulose unit cell, and the fiber axis. It was necessary to first calculate $\langle\cos^2\phi_{200,z}\rangle$ from $I(\phi)$ by eq. 4.2:

$$\left\langle \cos^2 \phi_{200,z} \right\rangle = \frac{\int_0^{\pi} I(\phi) \sin\phi \cos^2\phi \, d\phi}{\int_0^{\pi} I(\phi) \sin\phi \, d\phi} \tag{4.2}$$

where $\phi_{200,z}$ is the angle between the (2,0,0) planes and the fiber axis. The integrals were solved numerically for each sample and $\langle \cos^2 \phi_{c,z} \rangle$ was determined using eq. 4.3 which is true for a set of

$$\left\langle \cos^2 \phi_{c.z} \right\rangle = 1 - 2\left\langle \cos^2 \phi_{200,z} \right\rangle \tag{4.3}$$

monoclinic crystals with fiber symmetry. This quantity can be introduced into eq. 4.1 to obtain the order parameter.

Results and Discussion

Calcium Alginate Structure

WAXD measurements were first performed on calcium alginate fibers without CNC; the respective diffraction pattern is shown in Figure 4.1 with the fiber axis in the vertical direction. The broad haloes indicate that the sample has low crystallinity, but there are a few sharp reflections at meridional and near meridional positions. The most distinctive of these is observed at $2\theta = 9.7°$, which corresponds to a d-spacing, $d = \lambda/(2\sin\theta)$, of 0.91 nm. Other weaker and broader reflections are found at 2θ values of 12.2°, 19.1°, and 21.3°, which are attributed to d-spacings of 0.73, 0.46, and 0.42 nm.

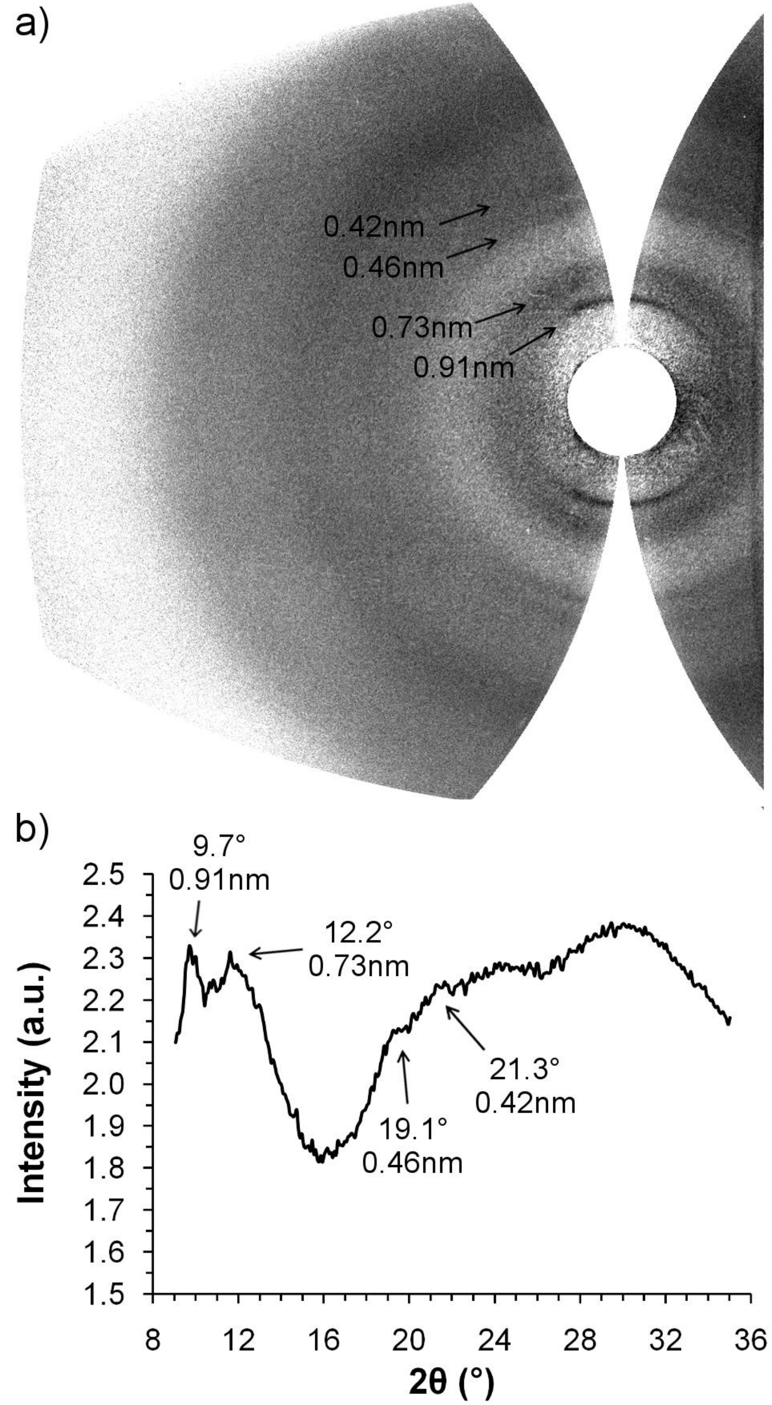

Figure 4.1. WAXD of a calcium alginate fiber spun at a J_A of 2.4. a) Two dimensional fiber diffraction pattern with the fiber axis in the vertical direction; the image contrast was enhanced for clarity. b) One dimensional "powder" diffraction pattern obtained from integrating the unenhanced two dimensional scattering.

The structure of the junction zones in alginate gels are commonly described by the well known “egg-box” model. According to this model the GG blocks in the alginate chains assemble in a zig-zag manner and enclose the divalent calcium cations in a structure that resembles an egg-box. It has been suggested that the MG blocks also take part of the junction zones in calcium alginate gels forming a similar structure.[20] Our measurements support this hypothesis by the presence of a strong and sharp meridional reflection at a d-spacing of 0.91 nm. This signal is attributed to (0,0,1) planes of MG dimers, representing the c lattice parameter (fiber direction) of an MG unit cell (Figure4.2). In the case of a GG dimer this distance would be 0.87 nm, as predicted by the egg-box model (Figure 4.2).

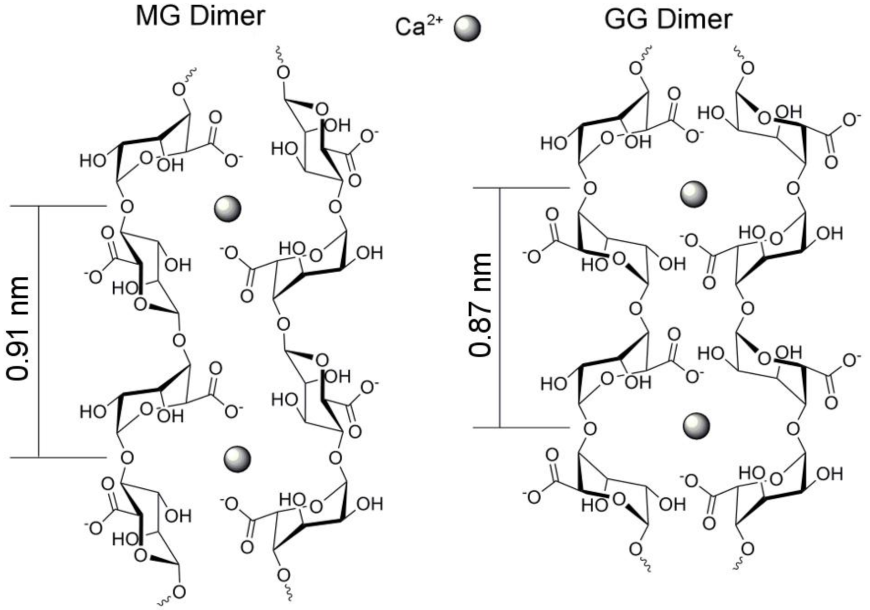

Figure 4.2. Schematic structure of MG and GG dimers in the junction zones of calcium alginate fibers.

Most of the sharp signals come from meridional positions, and virtually no equatorial reflections other than broad halos were observed; indicating that long range order is present along the fiber axis, but not in the radial direction. Thus an ordered array of several dimers is unlikely. It is possible that the poor lateral order enables the presence of the (0,0,1) signal. Lateral chain packing may require the presence of an additional diffracting layer at exactly one half the c axis, which would cause destructive interference of X-rays diffracted at the respective Bragg angle.[21]

The WAXD data did not show the presence of GG blocks in the junction zones. The G content of the alginate used in this study is low; it is possible that the few reflections from GG blocks in the junction zones are buried inside the broad amorphous halos. It is thus assumed that most of the strength of the fibers is product of the interaction between MG blocks.

Effect of CNC on Calcium Alginate Structure

The CNC – alginate fiber diffraction patterns may be regarded as a convolution of a calcium alginate component and a CNC component. Reflections from both, calcium alginate and CNC, can be observed in the 2D profile in Figure 4.3a. The 1D “powder” diffraction pattern in Figure 4.3b was deconvoluted by fitting all the peaks and assigning each of them to alginate and cellulose; thus obtaining individual traces for each component. The fitted profile, which represents the addition of the alginate and CNC components, describe very accurately the shape of the experimentally measured trace. This separation was performed for all fibers, and the results are shown in Figures 4.4 and 4.5.

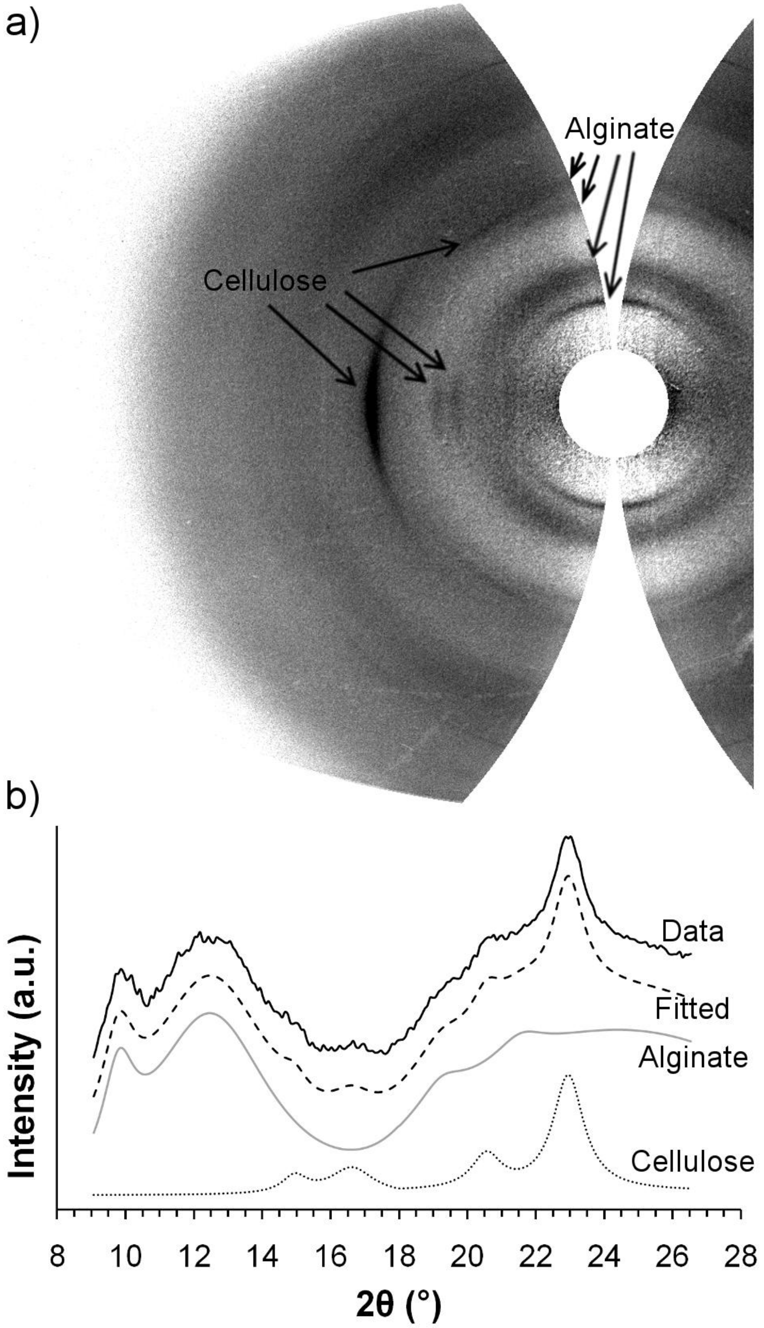

Figure 4.3. WAXD of a 10 wt % CNC – calcium alginate fiber spun at a J_{A} of 2.4. a) Contrast enhanced 2D diffraction pattern with the fiber axis in the vertical direction. b) Deconvolution of the alginate and CNC components of the powder diffraction pattern; curves are offset for clarity.

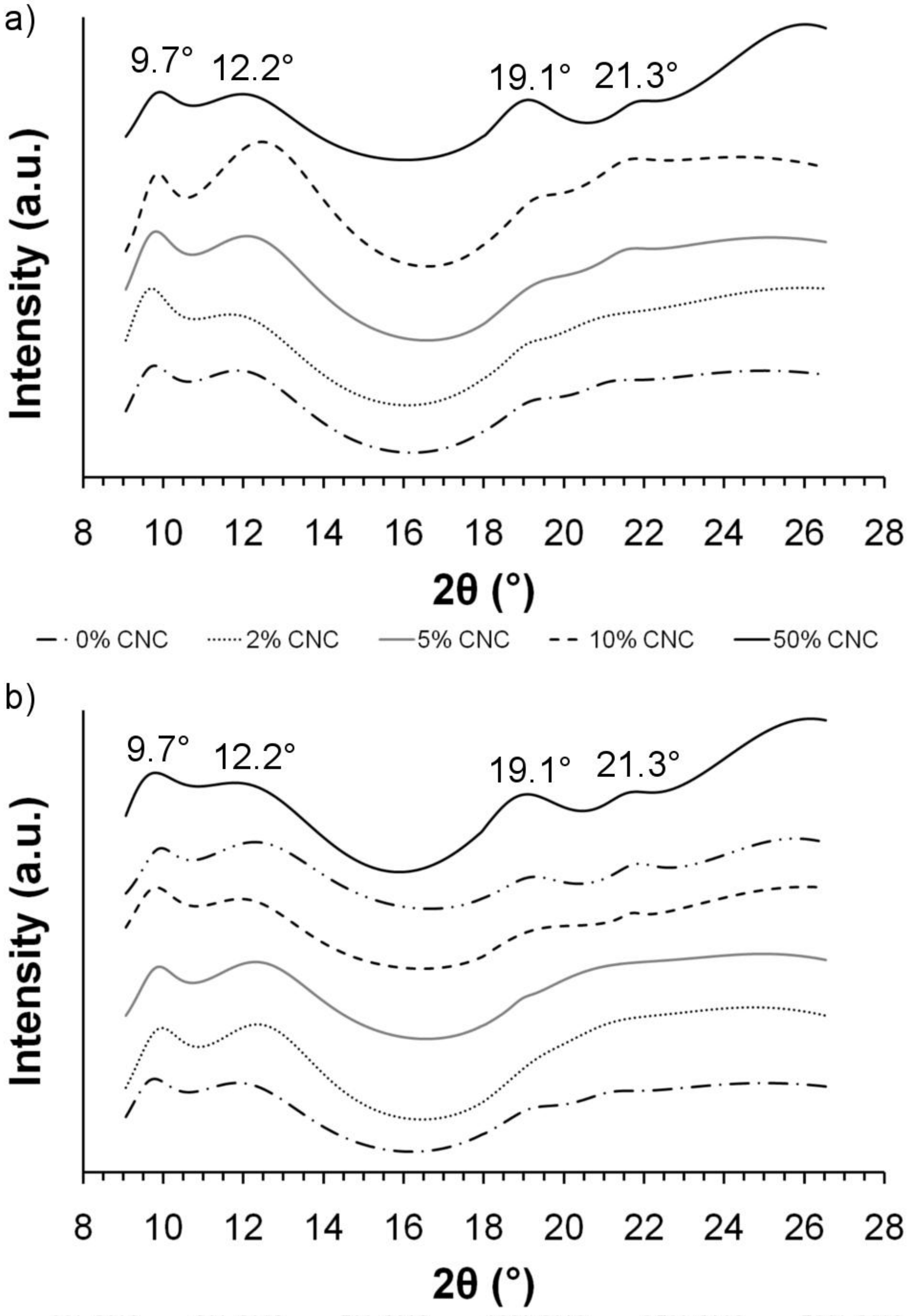

Figure 4.4. "Powder" diffraction pattern of the calcium alginate component; a) shows the traces for fibers spun at a constant J_A of 2.4, and b) shows the traces for the fibers spun at the maximum J_A for the specific CNC load. The peak positions represent the average of all the traces.

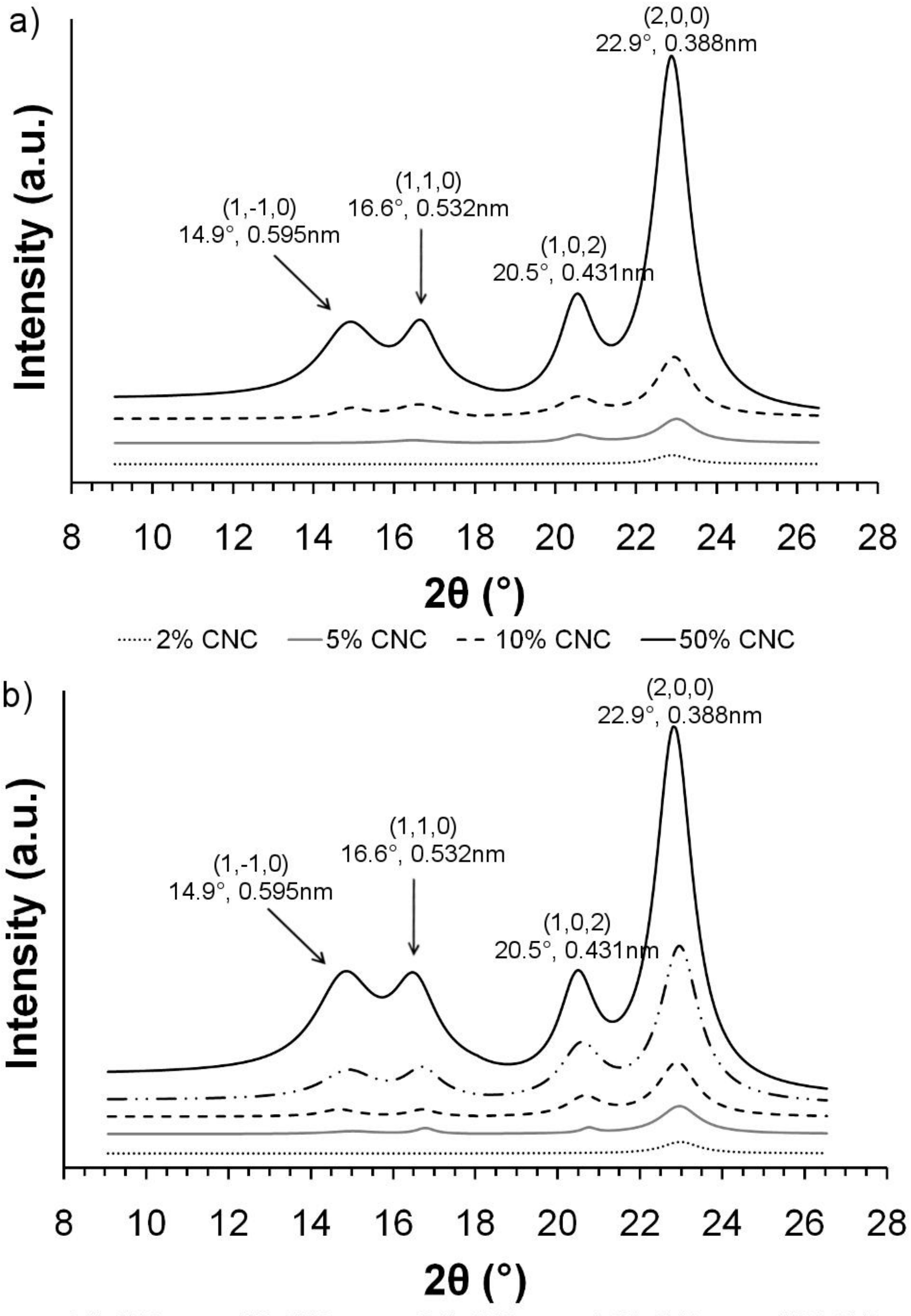

Figure 4.5. "Powder" diffraction pattern of the CNC component; a) shows the traces for fibers spun at a constant J_A of 2.4, and b) shows the traces for the fibers spun at the maximum possible J_A for the specific CNC load. The peak positions represent the average of all the traces.

In the previous chapter, we determined that addition of CNC caused a decrease in the tenacity and modulus of the fibers when the processing conditions were kept constant.[1] Two possible explanations were suggested: the cellulose crystals disrupted the order in the alginate junction zones; or they reduced the degree of alignment within the fibers. Disorder of the junction zones would cause broadening and a reduced intensity of the alginate signals, especially at 9.7°, which is not the case presented in Figure 4.4. Instead, the peak at 19.1° become sharper and more intense; thus the CNC appear to induce ordering of the calcium alginate chains. Previously, we reported that the presence of CNC in a sodium alginate aqueous solution induced the formation of a liquid crystalline phase; this is also an indication that the nanoparticles are templates for alginate orientation.[1] Thus, the detriment of the fibers mechanical properties cannot be attributed to a breakdown of the alginate structure.

The alginate traces may be regarded as a “background” for the CNC diffraction patterns, especially at large cellulose concentrations. The CNC traces extracted from the different fibers are shown in Figure 4.5; they describe the intensity that stands above the alginate profiles. A simulated powder diffraction pattern was obtained based on the cellulose Iβ structure determined by Nishiyama et al.;[18] the results showed four main peaks at 14.9°, 16.7°, 20.6° and 23.0° which corresponds to d-spacings of 0.596, 0.531, 0.431 and 0.387 nm. This supports the method used for separating the component profiles, as well as confirms the structure and crystalline nature of the nanoparticles.

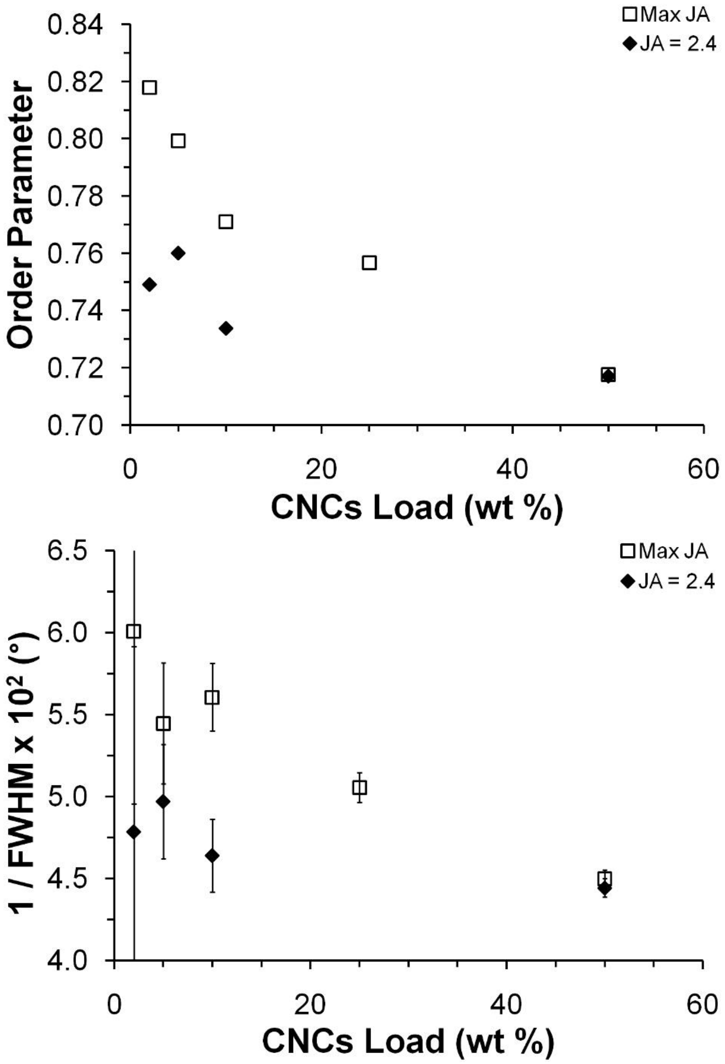

Figure 4.6. Effect of CNC load on the degree of orientation of the crystallites, expressed as order parameter (left), and the inverse of the full width at half maximum of $I(\phi)$ (rigt). Maximum J_A's are 2.4, 3.4, 3.8, 4.2, 4.6 and 2.8 for 0, 2, 5, 10, 25 and 50 wt % loads respectively.

Nanoparticles Orientation

The strongest cellulose peak is located at 22.9° and corresponds to reflections from the (2,0,0) planes. Its intensity is measurable even at 2 wt %; while the other peaks are hardly distinguishable at 5 wt %. The intensity distribution $I(\phi)$ along the (2,0,0) arc in the 2D pattern was used to quantify the alignment of the nanocrystals. A sharp distribution indicates high degree of alignment, while a broad peak represents the opposite. The *FWHM* of $I(\phi)$ was measured by fitting the data to Lorentzian curves; and the order parameter was calculated directly from the experimental data using eqs. 4.1 through 4.3. The results are shown in Figure 4.6 (1/FWHM is plotted for comparison with the order parameter). Both methods show the same trend, a higher degree of CNC alignment for small CNC loads and high jet stretches. These results confirm our hypothesis that the degree of orientation of the nanocrystals is the main cause of the weakening of the alginate fibers upon addition of CNC at constant J_A, and the subsequent reinforcement at maximum J_A.[1] It could be expected that the tenacity and modulus of the nanocomposites would continue to decrease, accompanied by an increment in toughness, as the CNC load is increased to 50 wt % or more, given that the degree of orientation also continues to diminish. However when the cellulose concentration reaches a percolation threshold, the particles form an interconnected network that reinforces the composite.[8, 22]

In native cellulose fibers (e.g. cotton, compression wood, etc.), the crystallites assemble in a spiral around the longitudinal axis of the fiber.[5, 23] It is conceivable that the CNC in the composite fibers may also tend to order in a similar fashion as the load is increased. To analyze this, the azimuthal intensity profile can be resolved into two equal peaks that are separated by twice the spiral angle (ψ).[23, 24] The profiles of all the fibers were fit to two Lorentzian peaks of equal widths (w_i) and areas, with center positions separated by 2ψ. As an example, Figure 4.7 shows the resolved $I(\phi)$ of the (2,0,0) cellulose reflection of a fiber containing 50 wt % CNC; the component peaks are located at 86.4°, and 93.6° each, while the convoluted peak is centered at 90°.

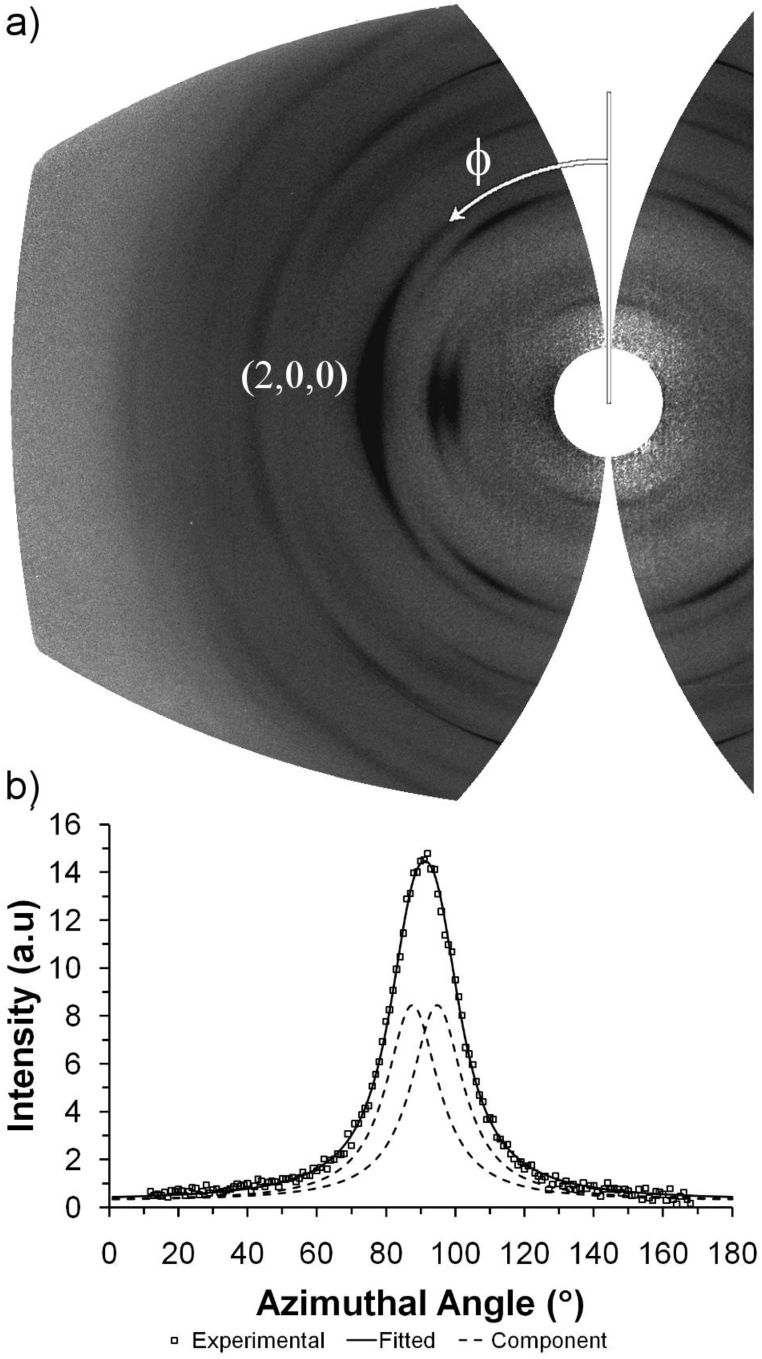

Figure 4.7. Azimuthal intensity scan of the (2,0,0) cellulose reflection. a) 2D diffraction pattern of a 50 wt % CNC – calcium alginate fiber spun at a J_A of 2.4. b) Intensity profile resolved into two equal Lorentzian distributions.

Table 4.1. Comparison of Tensile Properties with the Spiral Angles and Component Peak Widths of the Cellulose (2,0,0) Intensity Distribution in CNC – Calcium Alginate Fibers.

CNC Load (wt%)	At $J_A = 2.4$					At Max J_A				
	Spiral Angle ψ (°)	**Width w_i (°)**	**Tenacity x 10^2 (gpd)**	**Modulus (gpd)**	**Toughness x10^2 (gpd)**	**Spiral Angle ψ (°)**	**Width w_i (°)**	**Tenacity x 10^2 (gpd)**	**Modulus (gpd)**	**Toughness x10^2 (gpd)**
0	---	---	14.9 ± 0.4	3.1 ± 0.1	3.3 ± 0.2	---	---	14.9 ± 0.4	3.1 ± 0.1	3.3 ± 0.2
2	0	21 ± 5	15.2 ± 0.5	2.6 ± 0.1	3.9 ± 0.1	0	17 ± 3	18.0 ± 0.7	3.8 ± 0.2	3.6 ± 0.2
5	3.6 ± 0.8	15 ± 2	14.4 ± 0.3	2.8 ± 0.1	3.7 ± 0.1	0	18 ± 1	18.7 ± 0.5	5.5 ± 0.1	2.4 ± 0.1
10	3.8 ± 0.5	16 ± 2	12.9 ± 0.3	2.5 ± 0.1	3.0 ± 0.1	0	17.8 ± 0.6	20.6 ± 0.7	6.9 ± 0.2	2.5 ± 0.1
25	---	---	---	---	---	3.0 ± 0.2	16.6 ± 0.5	16.4 ± 0.6	6.2 ± 0.2	1.6 ± 0.1
50	3.6 ± 0.2	18.4 ± 0.3	17.8 ± 0.4	6.8 ± 0.2	2.4 ± 0.1	3.2 ± 0.2	19.1 ± 0.4	16.4 ± 0.5	6.9 ± 0.2	1.8 ± 0.1

Maximum J_A's are 2.4, 3.4, 3.8, 4.2, 4.6 and 2.8 for 0, 2, 5, 10, 25 and 50 wt % loads respectively.

Table 4.1 presents the measured spiral angles and peak widths for the fibers, as well as, the tensile properties;[1] interestingly the appearance of a spiral angle coincides with a decrease in the tenacity and modulus of the fibers. At a constant J_A of 2.4, the reduction in modulus happens just before the appearance of the spiral at 2 wt % CNC; which is consistent with the large w_i measured by WAXD. At larger concentrations (e.g 50 wt %), the percolation effect causes an increase in tenacity and modulus. It must also be noted that the toughness was generally large for fibers with low degree of alignment, at small J_A, but also low CNC concentration. Thus at 2 wt % CNC and a J_A of 2.4, there was an 18% increase in toughness without any loss of tenacity.

The Lorentzian peak width, $w_{i,}$ is proportional to the spread of crystallite orientations around a preferred direction, which is the fiber axis when the spiral is absent. However, this direction is tilted by the angle ψ if a spiral is formed. A trend is observed where w_i increases with increasing CNC content, however a step decrease is observed upon appearance of the spiral. The data suggests that increasing the CNC load causes the crystallites to twist away from the longitudinal axis of the fiber, until a more stable, spiral like, assembly is formed. When the cellulose concentration continues to increase, the spread around the preferred (tilted) orientation also increases. It is hypothesized that at even higher CNC concentrations, the spiral angle and w_i, will get larger up to some unknown maximum value for a pure cellulose fiber. A schematic representation of this assembly can be observed in Figure 4.8.

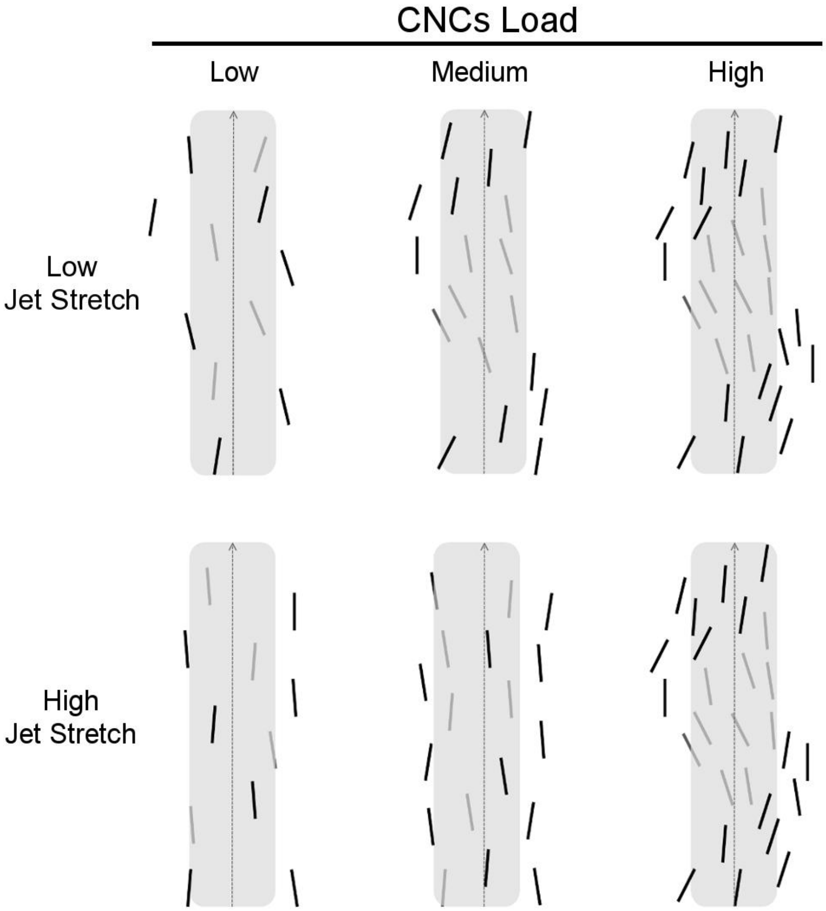

Figure 4.8. Schematic representation of the assembly of CNC in a calcium alginate fiber. The nanocrystals are incorporated within the alginate matrix and spiral around the fiber axis as the load is increased. The angle of the spiral was exaggerated for illustrative purposes.

The nature of the cellulose crystallites is to twist with respect to each other. This is evidenced by the formation of chiral nematic aqueous suspensions of CNC[15] and the spiral assembly of the crystallites in native cellulose fibers.[23] This assembly may be caused by the structure of the individual crystallites; recently Elazzouzi-Hafraoui et al. observed that micron long CNC isolated from tunicate twist themselves forming a ribbon-like geometry. They suggest that nanosized CNC, like those isolated from cotton, possess the same twist but it is not easily detected because the half helical pitch is larger than the crystallites themselves (1.2 – 1.6 μm).[25] During spinning of CNC – calcium alginate fibers, the extensional flow field forces the nanoparticles to align parallel to the fiber axis; but as the crystallites concentration increases, the particle – particle interactions strengthen and compete with the external forces leading to the structures described in Figure 4.8. It must be noted that at maximum J_A the spiral appears at higher concentrations; this is because the larger elongation rate amplifies the external force field, thus requiring a larger CNC load to exceed the extensional forces. Given the good chemical compatibility between the CNC and the alginate matrix, this assembly may be transferred to the alginate chains with CNC acting as a structure directing agent.

It is worth noting that the same relationship observed here between CNC assembly and mechanical performance is observed in natural cellulose fibers. Highly aligned bast fibers, where the crystallites show small spiral angles (e.g. hemp, flax, ramie, etc.) possess higher tensile strength and elastic modulus, and smaller elongation at break than cotton fibers which have large spiral angles and low alignment.[4, 5] This opens a variety of opportunities for the industrial production of cellulose based fibers with a wide range of mechanical properties that can be tuned by modifying simple processing conditions such as jet stretch or draw ratio.

Nanoparticles Content

In Figure 4.5 it was possible to observe that the strongest cellulose peak has a measurable intensity even at 2 wt % CNC. This strong signal may be used to obtain a calibration curve for the nanoparticles load. The expression[26]

$$I_{200} = I_{200}^{0} \frac{w_{\mathrm{CNC}} \left(\mu/\rho\right)_{\mathrm{CNC}}}{w_{\mathrm{CNC}} \left[\left(\mu/\rho\right)_{\mathrm{CNC}} - \left(\mu/\rho\right)_{\mathrm{ALG}}\right] + 100\left(\mu/\rho\right)_{\mathrm{ALG}}} \tag{4.4}$$

was used to described the dependence of the intensity against cellulose load. Here I_{200} refers to the intensity of the (2,0,0) reflection, I_{200}^{0} refers to the intensity of the (2,0,0) reflection of a pure cellulose fiber, w represents CNC load in wt %, μ is the linear absorption coefficient, ρ is the density, the ratio μ/ρ is the mass absorption coefficient, and the sub indexes CNC and ALG refer to cellulose nanocrystals and calcium alginate respectively. Equation 4.4 was originally derived for a symmetrical reflection geometry;[26] however it remains valid for the normal-beam transmission system employed in this study as long as μt remains approximately constant for every sample; where t is the thickness of the specimen. The value of μ can be experimentally determined by measuring the intensity of the direct beam after traveling through a specimen of known thickness.

The intensity versus concentration calibration curve in Figure 4.9 showed an exceptionally good correlation between experimental data and the fitted curve, as evidenced by the R^2. However, caution should be employed when using this curve. The Ca^{2+} ions present in the alginate matrix and on the surface of the nanoparticles as well as the sulfur atoms accompanying the CNC are very strong X-ray absorbents compared to carbon and oxygen. A small variation in the concentration of those elements can affect the mass absorption coefficient of the individual phases and thus change the values of the regression parameters. A curve like the one depicted in Figure 4.9 should not be employed if the elemental composition of each phase is not constant for all samples.

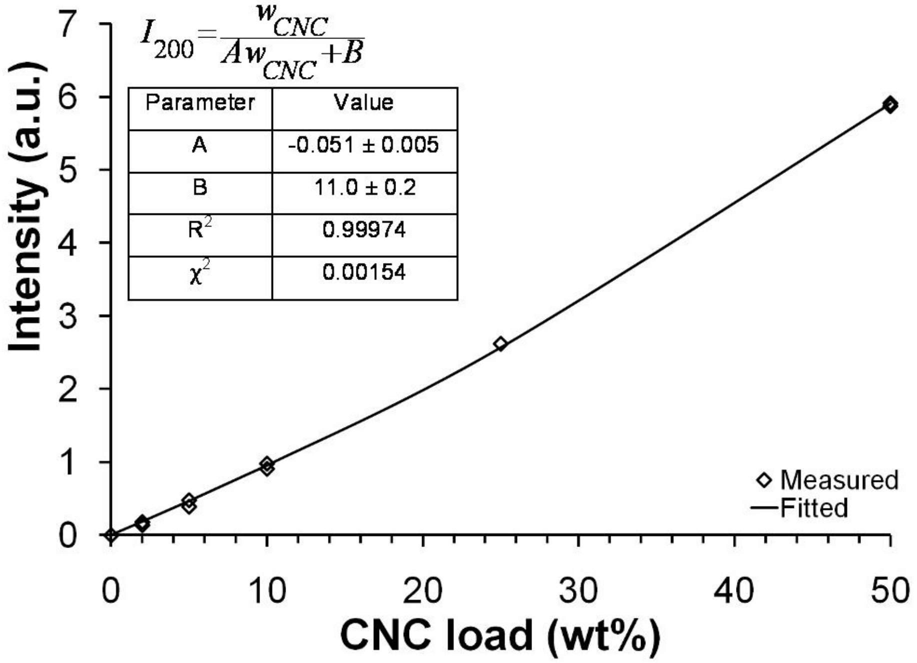

$$I_{200}=\frac{w_{CNC}}{Aw_{CNC}+B}$$

Parameter	Value
A	-0.051 ± 0.005
B	11.0 ± 0.2
R^2	0.99974
χ^2	0.00154

Figure 4.9. CNC load calibration curve showing experimental values as well as the fitted curve.

Another precaution must be taken when dealing with oriented samples. Since the intensity is dependent on azimuthal angle, it is then necessary to “randomize” it by calculating an integrated intensity over the entire angular range; this was done in Figure 4.5. Regardless, WAXD provides a reliable nondestructive method to measure the concentration of a crystalline phase in a solid matrix, which would be very difficult to achieve with other techniques.

Conclusions

WAXD was used to study the effect of CNC on the structure of calcium alginate fibers and to correlate those effects to the mechanical properties measured in our recent paper.[1] The junction zones of the calcium alginate mainly consisted on MG dimers with a repeat distance of 0.91 nm; this structure was present regardless of nanofiller load and processing conditions. A slight increase in alginate crystallinity was observed upon addition of the CNC; however it did not explain the reduction of tenacity and modulus at constant J_A. On the other hand the degree of orientation of the cellulose crystallites was found to decrease as the load increased; since the CNC interparticle interactions induced twisting away from the drawing direction. At high enough concentrations and sufficiently low jet stretches, the crystallites within the alginate matrix assembled in a spiral orientation around the fiber longitudinal axis, similarly to native cellulose fibers. The appearance of the spiral coincided with a reduction in the nanocomposite tenacity and modulus. WAXD was also used as a nondestructive technique to measure the concentration of the crystalline filler inside the fibers. It was demonstrated that a simple variation in processing conditions can be used to tune the mechanical properties of cellulose based nanocomposites, which directly correlate with CNC orientation. Moreover, we demonstrated the ability to produce CNC polymer nanocomposites with improved toughness (18% increase at 2 wt % CNC and a J_A of 2.4) without compromising the tenacity.

References

1. Ureña-Benavides, E. E.; Brown, P. J.; Kitchens, C. L. *Langmuir* **2010,** 26, 14263-14270.

2. Hassan, M.; Abou-Hussein, R.; Zhang, X.; Mark, J.; Noda, I. *Mol. Cryst. Liq. Cryst.* **2006,** 447, 23-44.

3. Takahashi, T.; Yonetake, K.; Koyama, K.; Kikuchi, T. *Macromol. Rapid Commun.* **2003,** 24, 763-767.

4. Eichhorn, S. J.; Baillie, C. A.; Zafeiropoulos, N.; Mwaikambo, L. Y.; Ansell, M. P.; Dufresne, A.; Entwistle, K. M.; Herrera-Franco, P. J.; Escamilla, G. C.; Groom, L.; Hughes, M.; Hill, C.; Rials, T. G.; Wild, P. M. *J. Mater. Sci.* **2001,** 36, 2107-2131.

5. Klemm, D.; Heublein, B.; Fink, H. -P.; Bohn, A. *Angew. Chem. ,Int. Ed.* **2005,** 44, 3358-3393.

6. Habibi, Y.; Lucia, L. A.; Rojas, O. J. *Chem. Rev.* **2010,** 110, 3479-3500.

7. Dufresne, A. *Can. J. Chem* **2008,** 86, 484-494.

8. Azizi Samir, M. A. S.; Alloin, F.; Dufresne, A. *Biomacromolecules* **2005,** 6, 612-626.

9. Anglès, M. N.; Dufresne, A. *Macromolecules* **2001,** 34, 2921-2931.

10. Grunert, M.; Winter, W. T. *J. Polym. Environ.* **2002,** 10, 27-30.

11. Qin, Y. *Polym. Int.* **2008,** 57, 171-180.

12. Ertesvåg, H.; Valla, S. *Polym. Degrad. Stab.* **1998,** 59, 85-91.

13. Gacesa, P. *Carbohydr. Polym.* **1988,** 8, 161-182.

14. Rånby, B. G. *Discuss. Faraday Soc.* **1951,** 11, 158-164.

15. Revol, J. -F.; Godbout, L.; Dong, X. -M.; Gray, D. G.; Chanzy, H.; Maret, G. *Liq. Cryst.* **1994,** 16, 127-134.

16. Gray, D. G. *Cellulose* **2008,** 15, 297-301.

17. Fraser, R. D. B.; Macrae, T. P.; Miller, A.; Rowlands, R. J. *J. Appl. Crystallogr.* **1976,** 9, 81-94.

18. Nishiyama, Y.; Langan, P.; Chanzy, H. *J. Am. Chem. Soc.* **2002,** 124, 9074-9082.

19. Alexander, L. E. In *X-Ray Diffraction Methods in Polymer Science,* Robert E. Krieger Publishing Company: Huntington, New York, 1979; pp 198-277.

20. Donati, I.; Holtan, S.; Mørch, Y. A.; Borgogna, M.; Dentini, M.; Skjåk-Bræk, G. *Biomacromolecules* **2005,** 6, 1031-1040.

21. Sikorski, P.; Mo, F.; Skjåk-Bræk, G.; Stokke, B. T. *Biomacromolecules* **2007,** 8, 2098-2103.

22. Favier, V.; Canova, G. R.; Shrivastava, S. C.; Cavaillé, J. Y. *Polym. Eng. Sci.* **1997,** 37, 1732-9.

23. Sisson, W. A. *Ind. Eng. Chem* **1935,** 27, 51-56.

24. DeLuca, L. B.; Orr, R. S. *J. Polym. Sci.* **1961,** 54, 457-470.

25. Elazzouzi-Hafraoui, S.; Nishiyama, Y.; Putaux, J.; Heux, L.; Dubreuil, F.; Rochas, C. *Biomacromolecules* **2008,** 9, 57-65.

26. Klug, H. P.; Alexander, L. E. In *X-Ray Diffraction Procedures: For Polycrystalline and Amorphous Materials,* 2nd ed.; John Wiley & Sons: New York, 1974; pp 505-565.

CHAPTER FIVE

STATIC LIGHT SCATTERING OF TRIAXIAL NANOPARTICLE SUSPENSIONS IN THE RAYLEIGH-GANS-DEBYE REGIME: APPLICATION TO CELLULOSE NANOCRYSTALS

Reproduced with permission from Ureña-Benavides, E. E.; Kitchens, C. L. *ACS Nano*, submitted for publication. Unpublished work copyright 2011 American Chemical Society.

Introduction

Nanoparticles use has spread to virtually all areas of current techonolgy. They have been used for reinforcement and property enhancement of different materials,[1, 2] catalysis,[3] targeted drug delivery,[4, 5] sensing devices,[6] etc. The types of applications are highly dependent on the size, shape, polydispersity, particle interactions and material that the particles are made from. Thus appropriate characterization of these properties is fundamental for the design of nanomaterials and their application.

The size and morphology of nanoparticles are commonly determined by transmission electron microscopy (TEM), scanning electron microscopy (SEM) or atomic force microscopy (AFM); however several difficulties exist. Obtaining good contrast with TEM can be difficult for bio-based, and polymer based particles; requiring the use of high atomic number staining agents that vary from one nanoparticle to another.[7] SEM presents problems imaging nonconductive materials which require conductive coatings to avoid charging and frequently mask nanosized details; moreover SEM in general has lower resolution than TEM and AFM.[7] None of the electron microscopy techniques provides information about interparticle interactions, they are destructive techniques, require high vacuum and cannot be done in-situ. On the other hand, AFM images are a convolution of the tip shape and the sample being analyzed which can overestimate the lateral dimensions of the particles.[7] Even though AFM measures forces between the tip and a surface, determination of nanoscale interparticle interactions is still not possible with AFM. All the previous techniques require drying a nanoparticle suspension on a surface which can induce agglomeration; cryo-TEM is an alternative, but tradeoffs include reduced contrast, solvent sublimation under high vacuum, and morphology distortion of bio-based samples.[8]

Small Angle Neutron Scattering (SANS), Small Angle X-ray Scattering (SAXS) and static light scattering (SLS) overcome most of the difficulties typically found with microscopy techniques.[8] Neutrons and X-rays can be used to measure from angstrom to a few microns length scales. Scattering methods can be performed in-situ and are non-destructive, which enables time-resolved measurements of a single system. While light scattering has a more restricted size range, it is a lower cost and more accessible technique.[9-11] One of the biggest difficulties of scattering techniques is that the intensity of the scattered light or neutrons must be fit to form factor models. These models are unique for each nanoparticle shape, and the computation becomes difficult for complex geometries.[9, 12] The data can also be fit to a polynomial model (regardless of the shape) which represents a series expansion of the real form factor.[11, 13] Typically, only the first coefficient of the expansion is studied and it is used to determine the radius of gyration, providing information about size.

In this study, we have determined expressions for the second and third coefficients of the expansion which are valid for every nanoparticle shape, and can be applied to any macromolecule conformation. We have analyzed the effect of aspect ratio, shape and polydispersity on these terms to obtain information other than just size of the nanoparticle. Moreover, if a specific shape is assumed or known, the expressions can be solved to calculate up to three different dimensions.

The methods described here have been applied to a suspension of cellulose nanocrystals (CNC) isolated from cotton, and the results compared to measurements obtained from AFM for the same population of particles. Terech et al. used SANS and SAXS to study the size and shape of CNC isolated from tunicate and found that a cuboid (rectangular parallelepiped) model fit their data much better than a rod model.[14] Braun et al. used SLS to determine the dimensions of CNC suspensions isolated from cotton for which they assumed a spheroidal (biaxial) shape for the nanoparticles; however they calculated a larger length than expected, even when the polydispersity was considered.[15] Here we approximate the CNC to triaxial cuboidal and ellipsoidal particles.

Theory of Light Scattering

The relation between scattered intensity, angle (θ), and concentration (c) was described by Zimm who derived the following expression, valid for very dilute samples in the Rayleigh-Gans-Debye regime,[16]

$$\frac{R(\theta,c)}{Kc} = MP(\theta) - 2A_2cM^2P^2(\theta) \tag{5.1}$$

where R(θ,c) is the excess Rayleigh ratio, which describes the intensity scattered by the sample less the solvent (analyte) normalized by the volume observed by the detector. P(θ) is the form factor, M is the molecular weight, A_2 is the second virial coefficient and K is an optical constant defined by

$$K = \frac{4\pi^2 n_S^2}{N_A \lambda_0^4}\left(\frac{\partial n}{\partial c}\right)^2 \tag{5.2}$$

where N_A is the Avogadro's constant, n is the refractive index and λ is the wavelength of light; the subscripts S and 0 refer to the solvent and the incident beam respectively.

Several models exist for P(θ) that are unique for each particle shape or macromolecule conformation, however the exact expression for the form factor of any particle or macromolecule which is independent of shape is given by[13]

$$P(\theta) = \frac{1}{N_\nu^2}\sum_i^{N_\nu}\sum_j^{N_\nu}\frac{\sin(qr_{\mathrm{ij}})}{qr_{\mathrm{ij}}} \tag{5.3}$$

where q is the magnitude of the scattering vector defined as $(4\pi n_S/\lambda_0)\sin(\theta/2)$, r_{ij} is the magnitude of the vector $\mathbf{r_{ij}} = \mathbf{r_i} - \mathbf{r_j}$, which represents the distance between scatterers i and j within a particle, and N_ν is the total number of scatterers in a nanoparticle.

When a polydisperse sample is considered, it is useful to visualize it as a mixture of N_C components; each component, ν, includes several nanoparticles all having the same dimensions and molecular weight (M_ν). In this case M in eq. 5.1 must be replaced by the weight average molecular weight (M_W) and the form factor has to be replaced by the z-average value which becomes[17, 18]

$$\left\langle P(\theta)\right\rangle_z = \frac{1}{M_W}\sum_{\nu}^{N_C} w_\nu M_\nu P(\theta) = \frac{1}{M_W}\int_0^\infty w(M)MP(\theta)dM \tag{5.4}$$

where w_ν represents the weight fraction of component ν, $w(M)$ is any adequate weight distribution function, and $w(M)\mathrm{d}M$ is the weight fraction of all particles with molecular weight between M and $M + \mathrm{d}M$.

A polynomial expansion of eq. 5.3 can be performed to obtain an approximate form factor valid for small values of q[13, 19]

$$\begin{aligned} P(\theta) = 1 - \frac{1}{3}\left[\frac{1}{2N_\nu^2}\sum_i^{N_\nu}\sum_j^{N_\nu} r_{ij}^2\right]q^2 \\ + \frac{1}{60}\left[\frac{1}{2N_\nu^2}\sum_i^{N_\nu}\sum_j^{N_\nu} r_{ij}^4\right]q^4 - \frac{1}{2520}\left[\frac{1}{2N_\nu^2}\sum_i^{N_\nu}\sum_j^{N_\nu} r_{ij}^6\right]q^6 + (Oq^8) \end{aligned} \tag{5.5}$$

the terms in brackets are moments of the difference of the distances, r_{ij}, within a nanoparticle; the following notation will be used from now on to refer to them

$$\frac{1}{2N_\nu^2}\sum_i^{N_\nu}\sum_j^{N_\nu} r_{ij}^n = \Delta r_n \tag{5.6}$$

where the subscript n refers to the order of the moment. If a polydisperse population is considered, the moments have to be replaced by their respective z-average values[18]

$$\left\langle \Delta r_n\right\rangle_z = \frac{1}{M_W}\sum_{\nu}^{N_C} w_\nu M_\nu \Delta r_n = \frac{1}{M_W}\int_0^\infty w(M)M\Delta r_n dM \tag{5.7}$$

Moments of r_{ij}

The second moment is commonly referred to as the square radius of gyration and is an indication of the nanoparticle size; however two nanoparticles with the same volume can have a different Δr_2 if their shapes or aspect ratios are not the same. The higher order terms have not been extensively studied and typically no information is obtained from them. In this section we present general expressions to calculate their values and discuss their significance.

Using Riemann's definition of integral and assuming that the number of scatterers in each nanoparticle is large enough, it is possible to show that

$$\Delta r_n = \frac{1}{2N_v^2}\sum_{i}^{N_v}\sum_{j}^{N_v} r_{ij}^n = \frac{\int\limits_{V_i}\int\limits_{V_j} g(\mathbf{r_i})g(\mathbf{r_j})r_{ij}^n dV_j dV_i}{2\int\limits_{V_i}\int\limits_{V_j} g(\mathbf{r_i})g(\mathbf{r_j})dV_j dV_i} \tag{5.8}$$

where $g(\mathbf{r})$ and V are the radial distribution function and volume of the particle. From the above equation and assuming that the particle is large enough to have a homogeneous mass distribution, such that $g(\mathbf{r}) = 1$, a general expression valid for every nanoparticle shape can be obtained for the moments

$$\Delta r_2 = \frac{1}{V}\int\limits_V r^2 dV \tag{5.9a}$$

$$\Delta r_4 = \frac{1}{V^2}\left[V\int\limits_V r^4 dV + \left(\int\limits_V r^2 dV\right)^2 + 2\int\limits_{V_i}\int\limits_{V_j}(\mathbf{r_i}\cdot\mathbf{r_j})^2 dV_j dV_i\right] \tag{5.9b}$$

$$\Delta r_6 = \frac{1}{V^2}\left[V\int\limits_V r^6 dV + 3\left(\int\limits_V r^4 dV\right)\cdot\left(\int\limits_V r^2 dV\right) + 12\int\limits_{V_i}\int\limits_{V_j} r_i^2(\mathbf{r_i}\cdot\mathbf{r_j})^2 dV_j dV_i\right] \tag{5.9c}$$

Equations 5.9a, 5.9b and 5.9c were solved for a few general shapes and the results are shown in Table 5.1. A light scattering experiment was simulated using an exact expression for the form factors of cuboidal[20] and ellipsoidal[21] particles (*equations* *provided in Appendix E*). The results, presented in Figure 5.1, were compared with the form factors calculated from the expressions in Table 5.1. As expected the agreement improves when the higher order moments are included in the calculation; actually when the (Oq^6) moments are employed an almost perfect coincidence is found for the *q* range analyzed.

Table 5.1. Moments of the Difference of Distances within Nanoparticles of Different Shapes.

Shape	Moments
Rod^A	$\Delta r_2 = \frac{1}{2}\left(R^2 + \frac{L^2}{6}\right)$ $\Delta r_4 = \frac{1}{6}\left(5R^4 + \frac{L^4}{5} + R^2L^2\right)$
Ellipsoid^B	$\Delta r_2 = \frac{1}{5}\left(a^2 + b^2 + c^2\right)$ $\Delta r_4 = \frac{12}{175}\left[3\left(a^4 + b^4 + c^4\right) + 2\left(a^2b^2 + a^2c^2 + b^2c^2\right)\right]$ $\Delta r_6 = \frac{32}{525}\left[5\left(a^6 + b^6 + c^6\right) + 3\left(a^4b^2 + a^4c^2 + b^4a^2 + b^4c^2 + c^4a^2 + c^4b^2\right) + 2a^2b^2c^2\right]$
Cuboid^C	$\Delta r_2 = \frac{1}{12}\left(A^2 + B^2 + C^2\right)$ $\Delta r_4 = \frac{1}{6}\left[\frac{1}{5}\left(A^4 + B^4 + C^4\right) + \frac{1}{6}\left(A^2B^2 + A^2C^2 + B^2C^2\right)\right]$ $\Delta r_6 = \frac{1}{8}\left[\frac{1}{7}\left(A^6 + B^6 + C^6\right) + \frac{2}{15}\left(A^4B^2 + A^4C^2 + B^4A^2 + B^4C^2 + C^4A^2 + C^4B^2\right) + \frac{1}{9}A^2B^2C^2\right]$

A: *R* = Rod diameter, *L* = Length; B: *a*, *b* and *c* are the semi-axes of the nanoparticle; C: *A*, *B*, *C* are the axes. Note that *A* = 2*a*, *B* = 2*b* and *C* = 2*c*.

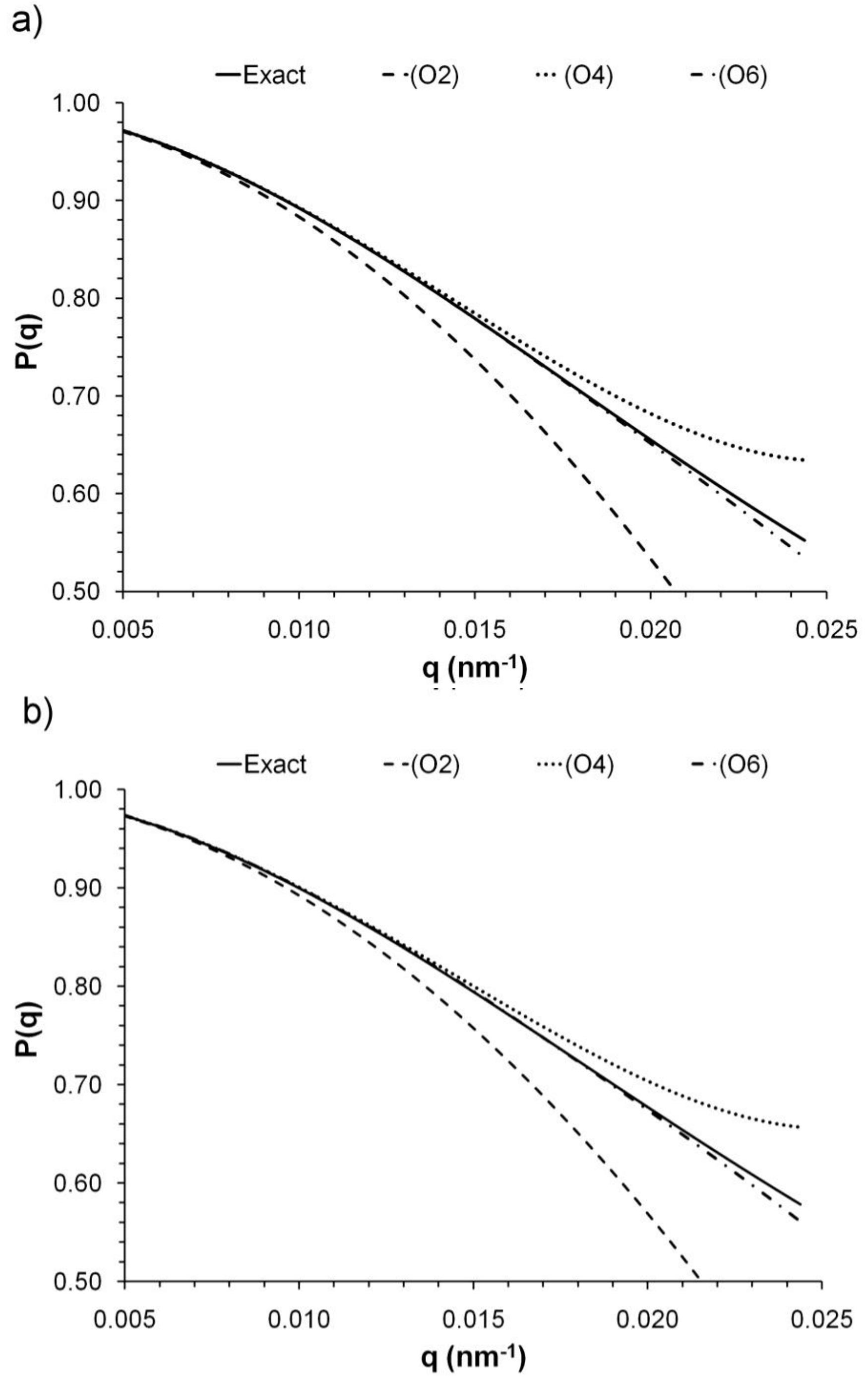

Figure 5.1. Form factors calculated for a) a cuboid with axes A = 20 nm, B = 40 nm, C = 200 nm, and b) an ellipsoid with semi-axes $A/2 = a$ = 12.4 nm, $B/2 = b$ = 24.8 nm and $C/2 = c$ = 124 nm. The volume and the A/B ratio of both particles are the same.

Measurement of the dimensions of triaxial nanoparticles from light scattering is very difficult with current data analysis techniques; which require fitting the experimental results to highly complex models that are unique for different nanoparticle shapes.[9, 12] Braun et al. used the molecular weight (M=ρη$N_A V$) in conjunction with the mean square radius of gyration to solve for the dimensions of spheroidal particles; the symbol ρ refers to crystalline density of the nanoparticle, η is a factor for packing density and crystal imperfections, and ρη is the overall particle density.[15] However, their methodology can only be used to solve for two parameters; thus is not suitable for triaxial particles. Using the first three moments of the form factor and the molecular weight provides four simple equations that can be used to solve for up to four different variables to characterize size and shape.

Some important limitations must be considered before employing this method. Obtaining a reliable value with light scattering for the high order moments is only possible if the particle is large enough. This is because the wavelength of light is too large to access to the high q range. However, since X-rays and neutrons can access high q values,[9, 10] they can be used to measure the higher order moments of small particles. It is also important to consider the magnitude of the characteristic dimensions being analyzed.

The best results can be obtained when $1/q$ is of similar magnitude to the dimensions of interest. However, if one dimension falls outside the q range studied, then it is expected that the molecular weight will provide the extra equation required to solve for it. Another significant consideration is that high order polynomials have more roots; yet after eliminating the complex and negative solutions the number of possible answers will be readily reduced. Finding an exact answer to the system of equations would require a completely error free experiment which is virtually impossible to achieve. Thus, the best option is to find the set of parameters that minimize the differences between the equations and the measured moments. If a polydisperse sample is considered, an assumption must be done with regards to the type of weight distribution function; plus, the number of unknowns is increased given that the polydispersity has to be solved for each dimension.

Interpretation of the Moments

Even if the shape is unknown, important information can still be obtained from the different Δr_n's. The second moment of any distribution indicates how broad it is; thus for the population of r_{ij} within a nanoparticle, it is a measurement of the size.[11] The fourth moment provides information about the "peakedness" of the distribution, and thus for the population of r_{ij}'s, it will provide a measurement of the elongation, or aspect ratio. The sixth moment will give similar information than the fourth moment.

All Δr_n increase with size, yet is possible to obtain normalized moments by dividing $\Delta r_n/(\Delta r_2)^{n/2}$; these values are independent of nanoparticle size and can be used to evaluate the aspect ratio, as evidenced in Figure 5.2a for spheroidal particles of different cross sectional diameter. When the aspect ratio is one (a sphere), the normalized moments go through a minimum which for $\Delta r_4/(\Delta r_2)^2$ is always 20/7 (~2.857), and for $\Delta r_6/(\Delta r_2)^3$ is always 800/81 (~9.876) regardless of the diameter of the sphere. At the left of the minima the nanoparticles are disk like (oblate spheroids); at the right they are rod like (prolate spheroids).

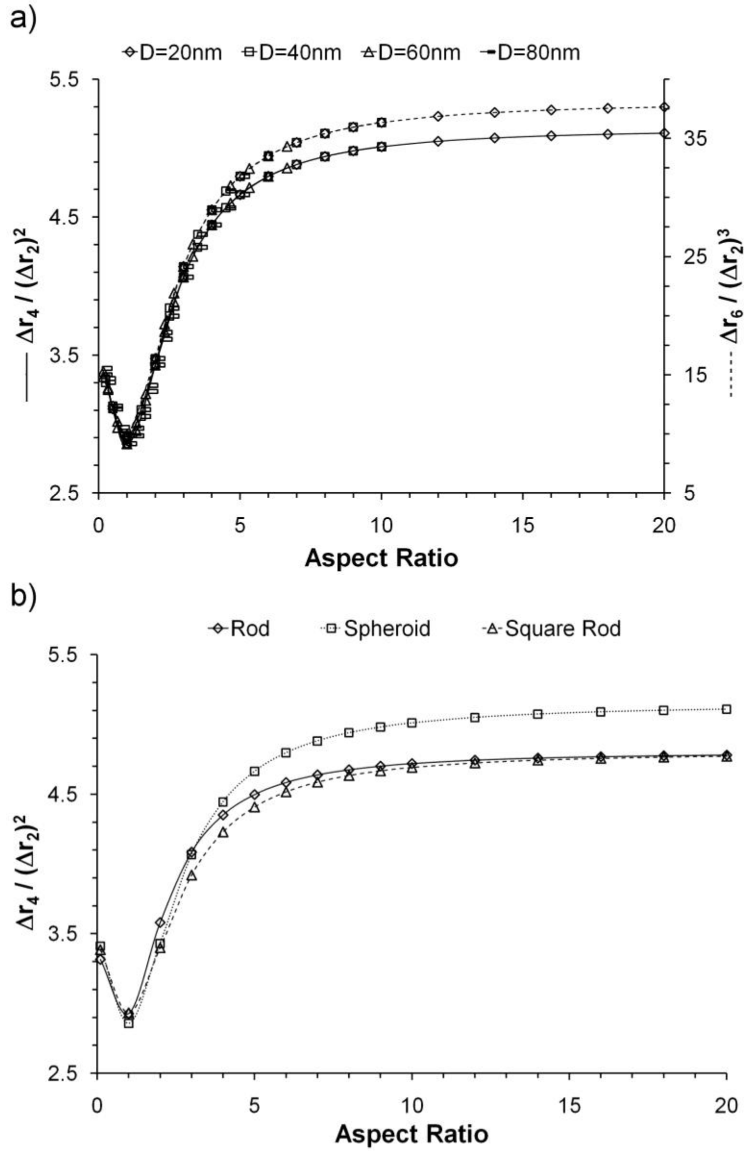

Figure 5.2. Normalized moments versus aspect ratio. a) $\Delta r_4/(\Delta r_2)^2$ and $\Delta r_6/(\Delta r_2)^3$ for spheroids with different diameters and b) $\Delta r_4/(\Delta r_2)^2$ for biaxial nanoparticles of different shapes.

An important observation that can be drawn from Figure 5.2a is that at large aspect ratios the normalized Δr_n reach a plateau and they can no longer be used as an indicator of elongation; however $\Delta r_6/(\Delta r_2)^3$ reaches the plateau at a slightly higher value than $\Delta r_4/(\Delta r_2)^2$. It must be noted that a broad q range is required to accurately measure the dimensions of particles with very large aspect ratios. Since the higher order moments can only be measured at large q values, the order of $\Delta r_n/(\Delta r_2)^{n/2}$ will have to increase to shift the plateau to higher aspect ratios and appropriately represent the elongation of very long particles.

The shape also has an effect on the normalized moments (Figure 5.2b). Again, the minimum occurs when the aspect ratio is one; at the left the particles are disk like, and at the right they are rod like. However it must be noted that at large aspect ratios the nanoparticles with sharp edges, such as the rods, have a smaller moment than the rounded spheroidal particles. Particles with rounded edges have a smaller volume than those with sharp edges for equal characteristic dimensions. Since the moments are normalized by the size (second moment), the particles with smaller volume will have a larger normalized moment at high aspect ratio. Nevertheless, when the aspect ratio is close to one, the opposite occurs; particles with sharp edges, like a cube, have large diagonals and may be considered to be more elongated than a sphere. Consequently, the value of $\Delta r_4/(\Delta r_2)^2$ for a cube is 44/15 (~2.933) which is slightly larger than for a cylinder with aspect ratio of one (366/125 ~ 2.928), which is larger than for a sphere (20/7 ~ 2.857). However, the differences are only significant near the plateau region; thus the normalized moments can still be used as an indication of aspect ratio regardless of shape as long as the measurements correspond to the high slope section of the curve (i.e. if the appropriate order moment is being used for the desired aspect ratio).

The case of triaxial particles is considered in Figure 5.3. The normalized moments depend on the shape and on the ratio of the three dimensions, but not on size. Figure 5.3a shows that as long as the ratio B/A and the shape remain constant, the curves of the normalized moments versus C/A are always equal regardless of the volume. Again the rounded shapes yield higher normalized moments at large aspect ratios, but slightly lower values when the aspect ratio is small. A significant difference is observed with regards to the minima of all the curves. Figures 5.3b and 5.3c show $\Delta r_4/(\Delta r_2)^2$ and $\Delta r_6/(\Delta r_2)^3$ for cuboidal particles; in all cases the minima occurs when the two largest dimensions are equal and the particle resembles a disk more than a rod. The magnitude of the minimum in each curve decreases as the ratio B/A gets smaller until it reaches the lowest value for the case when all dimensions are equal. In general, the normalized moments increase as the degree of symmetry decreases; being a sphere the most symmetric shape with the lowest possible $\Delta r_n/(\Delta r_2)^{n/2}$.

Polydisperse Samples

Polydispersity also has an effect on the normalized moments; Figure 5.4 shows a series of curves generated for populations of nanoparticles with a number average volume (V_n) of 24000 nm^3, and a constant B/A ratio of 2. The integral version of eq. 5.7 was used to generate the curves, where the Schulz-Zimm weight distribution was used (*the distribution function is provided in Appendix E*). If the density is constant for all particles, then M can be replaced by the volume V. The polydispersity is defined as $P = M_w/M_n = V_v/V_n$, where V_v is the volume-average volume and M_n is number average molecular weight.

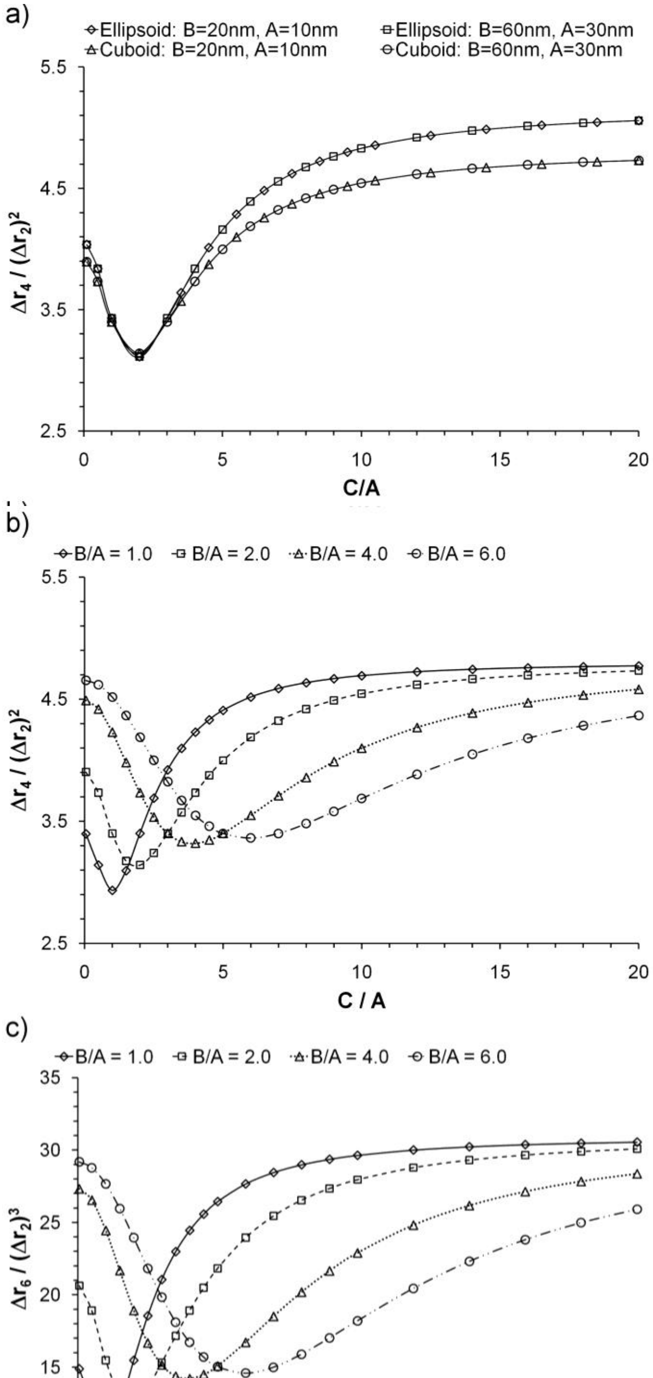

Figure 5.3. Normalized moments of triaxial nanoparticles versus ratio of axes *C*/*A*. a) $\Delta r_4/(\Delta r_2)^2$ for particles of variable shape and size; b) $\Delta r_4/(\Delta r_2)^2$ for cuboidal particles of variable *B*/*A* ratio; and c) $\Delta r_6/(\Delta r_2)^3$ for cuboidal particles of variable *B*/*A* ratio.

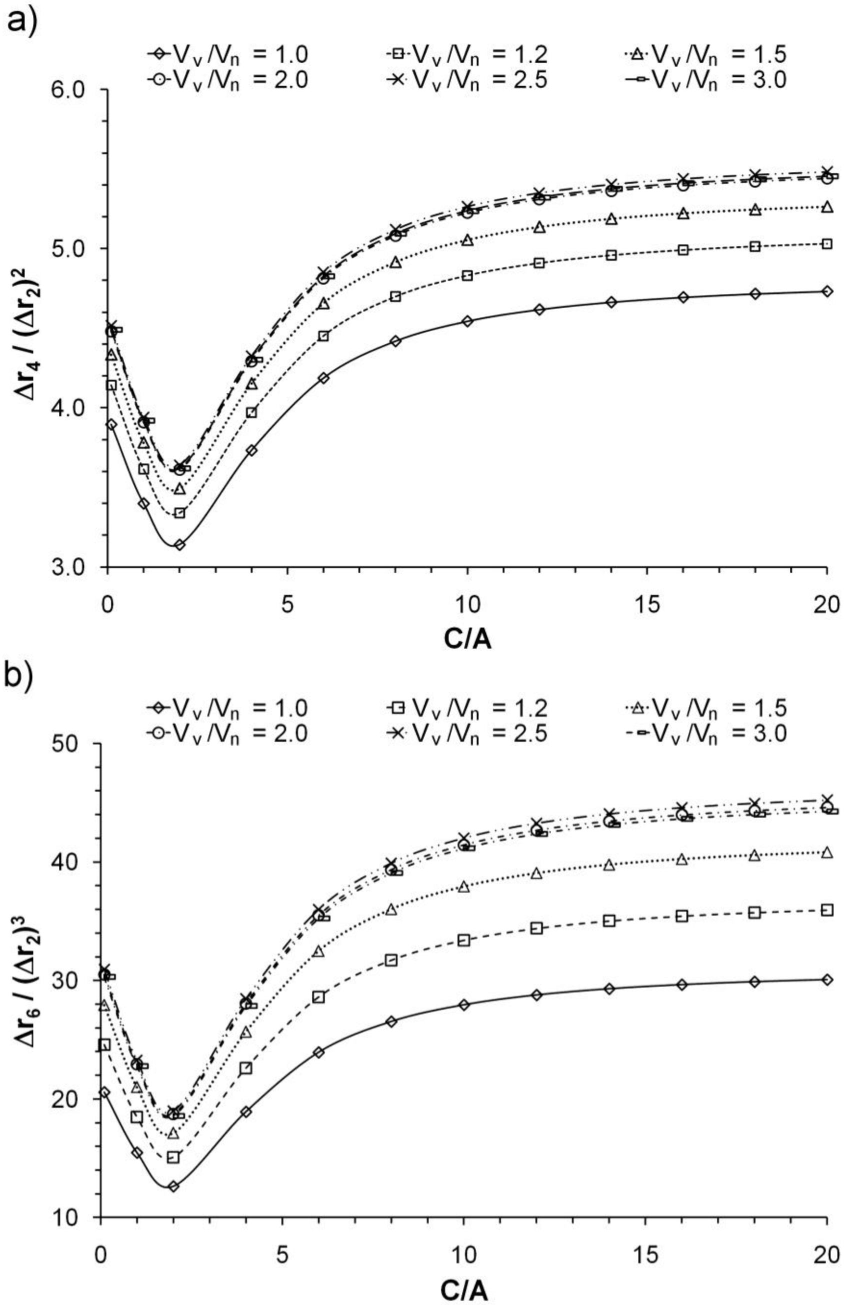

Figure 5.4. Effect of volume polydispersity on the behavior of a) $\Delta r_4/(\Delta r_2)^2$ and b) $\Delta r_6/(\Delta \mathrm{r}_2)^3$ versus C/A for cuboidal particles. Each curve corresponds to particles with a number average volume of 24000 nm^3, and constant B/A of 2.

The normalized moments increase quickly from $P = 1$ to 2, after which the effect diminishes significantly. If a sample is measured and the normalized moments have a value larger than would be expected for an infinite aspect ratio; it is likely that the sample is composed of elongated and polydisperse nanoparticles. However if no information about polydispersity is available, it would generally be difficult to distinguish between monodisperse elongated particles and a polydisperse population with low aspect ratio. Nevertheless, if a light scattering instrument is used in series with a gel permeation chromatorgraph (GPC), which is a common practice, the effect of polydispersity will be considerably minimized.[11] Moreover the normalized moments can be used to assign an aspect ratio to each slice analyzed from the chromatograph. Alternatively, Flow Field Fractionation can also be employed to obtain monodispersed populations of the nanoparticles.

Results and Discussion

Moments of Distances in CNC

According to the method described by Zimm, $Kc/R(\theta,c)$ must be plotted against $\sin^2(\theta)$ because the resulting curve has a longer range of linearity than a plot of $R(\theta,c)/Kc$ vs. $\sin^2(\theta)$.[17] In this study a larger degree of curvature is desired to fit Δr_4 and Δr_6; thus the latter curve is plotted. Figure 5.5 shows the construction of a plot of $R(\theta,c)/Kc$ vs. $\sin^2(\theta) + 5\text{x}10^4 c$ for several CNC concentrations and the extrapolations to zero concentration and zero angle. Analogous to Zimm's method the molecular weight of the nanoparticle is obtained from eq. 5.1 for the case when c = 0 and $\theta = 0$. The moments Δr_2, Δr_4 and Δr_6 are found by fitting the zero concentration curve to an order three polynomial; an order 2 fit does not describe the shape well at the larger angles.

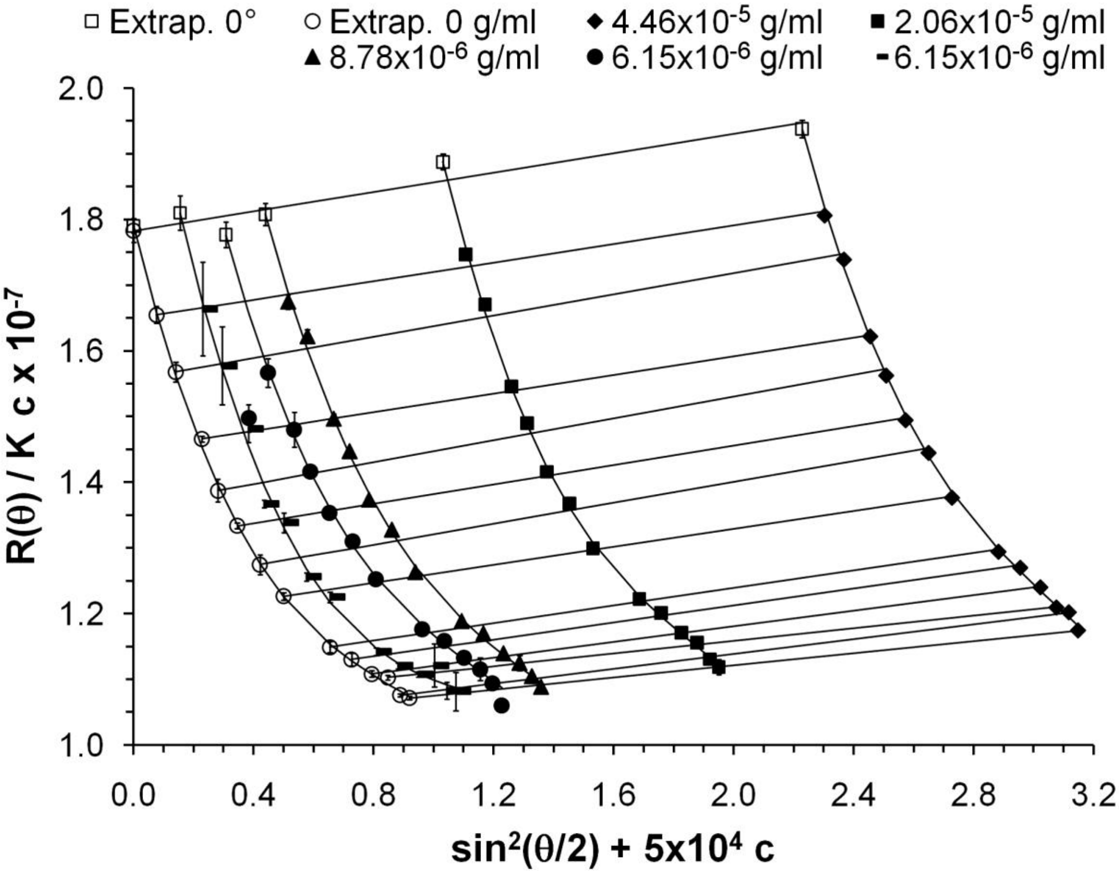

Figure 5.5. Scattering intensity construction for several CNC samples showing the extrapolation to zero angle and zero concentration. The constant $5\text{x}10^4$ is an arbitrary shift factor to differentiate each sample.

A summary of the light scattering measurements is provided in Table 5.2. The magnitude of the fourth normalized moment is large, indicative of elongated particles. Moreover since the value is greater than expected for monodisperse particles of infinite aspect ratio, it is evident that the population is polydisperse, as expected for populations of CNC.[22] Similar information can be obtained from the sixth normalized moment, but caution must be employed. For the higher angles studied the eight order moment becomes important, thus affecting the measurement of the sixth moment and yielding a smaller value. Since the q range studied is limited, fitting the data to an order four polynomial does not yield a good measurement of the sixth order moment either.

Table 5.2. Comparison of the Moments, and Molecular Weight Measured from Light Scattering with those Calculated from the AFM Dimensions.

Moment / M_W	AFM		LS
	Ellipsoid	Cuboid	
M_w (g/mol)	$3.3 \pm 0.3 \times 10^7$	$6.3 \pm 0.6 \times 10^7$	$4.62 \pm 0.03 \times 10^7$
Δr_2 (nm^2)	$3.2 \pm 0.4 \times 10^3$	$5.3 \pm 0.7 \times 10^3$	$4.8 \pm 0.2 \times 10^3$
Δr_4 (nm^4)	$6.7 \pm 1.7 \times 10^7$	$1.8 \pm 0.4 \times 10^8$	$1.4 \pm 0.2 \times 10^8$
Δr_6 (nm^6)	$2.5 \pm 0.8 \times 10^{12}$	$9.4 \pm 3.0 \times 10^{12}$	$3.4 \pm 0.7 \times 10^{12}$
$\Delta r_4/(\Delta r_2)^2$	6.6 ± 2.4	6.2 ± 2.3	6.2 ± 1.0
$\Delta r_6/(\Delta r_2)^3$	76 ± 40	62 ± 32	31 ± 8

The dimensions of the particles were measured from AFM; a representative picture of the cellulose nanoparticles is shown in Figure 5.6. The moments were calculated from the AFM measurements according to eq. 5.7 and assuming cuboidal and ellipsoidal shapes; the values are reported in Table 5.2. There is a closer agreement between AFM and the experimental light scattering moments when the particles are modeled as cuboids. Native cellulosic materials are known to have crystalline regions with rectangular or squared cross sections whose size varies depending of the source.[23, 24] It has been reported that the acid hydrolysis that is employed to isolated the CNC from native cellulose preferentially consume the (2,0,0) crystalline planes that are perpendicular to the diagonals of the cross section, partially rounding the edges.[25] In the case of cotton cellulose, an approximately squared cross section of 6 x 6.1 nm has been suggested for the individual crystallites after acid hydrolysis; the authors indicate that the CNC in suspension might be formed by agglomerations of three or more single crystals.[26] It is consequently expected that the shape of the CNC must be better described by a cuboid with rounded edges rather than an ellipsoid. Our measurements are consistent with this observation.

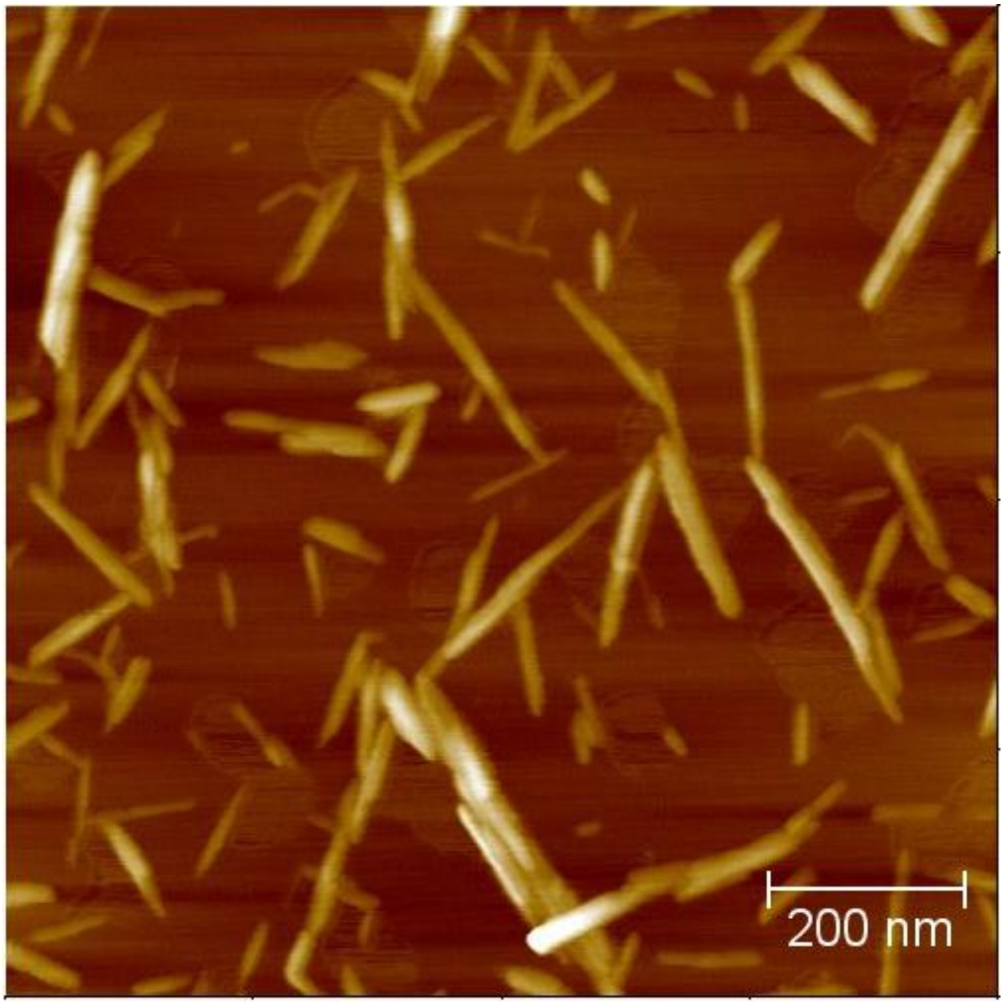

Figure 5.6. Atomic force microscopy image of CNC isolated from cotton.

Interparticle Interactions.

The second virial coefficient has been measured from the slope of the zero angle line according to eq. 5.1; yielding a result of $-8.6 \pm 0.1 \times 10^{-6}$ mol·ml /g^2. A negative value for this parameter indicates a predominantly attractive interaction between the particles. This result seems surprising given that the CNC were isolated through sulfuric acid hydrolysis which introduces negatively charge sulfate groups on the surface, and gives stability to the dispersion. It must be noted however that the surface of the particles is mostly covered by hydroxyl groups which can hydrogen bond between each other. Most likely, the second virial coefficient is a result of opposite competing contributions from the repulsive sulfate groups and the attractive hydroxyl groups; and thus the net result depends on the sulfate surface coverage. Even though A_2 is negative the suspensions are highly stable in water. Similar behaviors have been observed in other systems like small gold nanoparticles for which negative values of A_2 have been measured using SAXS even when the nanoparticle dispersions are stable in the solvent.[27] The second virial coefficient measured by light scattering is measured at constant pressure, as oppose to sedimentation equilibrium measurements where a constant chemical potential exist. Consequently some systems show negative A_2 when measured with light scattering, but positive values when measured by sedimentation equilibrium.[28]

CNC Dimensions

The moments Δr_2, Δr_4 and the molecular weight are employed to calculate the CNC dimensions from light scattering; as previously discussed, the sixth order moment is not used because the accessible q range is not large enough to get a reliable measurement. A shape must be assumed in order to use the expressions from Table 5.1; the cases of an ellipsoid and a cuboid are considered here. The sample is first assumed to be monodisperesed, and thus the systems of equations are solved directly to give the values shown in Table 5.3. There is an overestimation of the dimensions, especially when an ellipsoidal shape is assumed.

Table 5.3. Comparison of number average dimensions of CNC measured from AFM and light scattering.

Particle Axis	AFM		LS Monodisperse		LS Polydisperse	
	$X_n{}^A$	P^B	Ellipsoid	Cuboid	Ellipsoid	Cuboid
A	6.8	1.24	22.3	4.7	6.9	6.4
B	20.4	1.15	52.6	39.8	38.4	28.1
C	130	1.23	319	250	193	152

A: X_n = number average dimension; B: P = polydispersity.

The moments of a polydisperse sample measured from light scattering are z-average values of all particles; thus if the polydispersity is not taken into account, the calculated dimensions will necessarily be larger than real. Since the sample studied here is polydisperse a more realistic measurement of the dimensions can be obtained if the size distribution is taken into account. To determine the average dimensions including the polydispersity over each dimension, the z-average moments are expressed by

$$\left\langle \Delta r_n \right\rangle_z = \frac{\int_0^\infty \int_0^\infty \int_0^\infty w(A)w(B)w(C)ABC\Delta r_n dAdBdC}{\int_0^\infty \int_0^\infty \int_0^\infty w(A)w(B)w(C)ABCdAdBdC} \tag{5.10}$$

The multiplication *w*(*A*)*w*(*B*)*w*(*C*)d*A*d*B*d*C* indicates that the probability of a nanoparticle having dimensions *A*, *B* and *C* between *A* + d*A*, *B* + d*B* and *C* + *dC* simultaneously is being considered. It can be shown that when all the dimensions have a Schulz-Zimm distribution, the following relation applies

$$\int_0^\infty\int_0^\infty\int_0^\infty w(A)w(B)w(C)A^nB^mC^p\,dAdBdC = \left[\frac{A_A^n(k_A+n)!}{(k_A+1)^n\,k_A!}\right]\left[\frac{B_B^m(k_B+n)!}{(k_B+1)^m\,k_B!}\right]\left[\frac{C_C^p(k_C+n)!}{(k_C+1)^m\,k_C!}\right] \quad (5.11)$$

where $k_x = 1/(P_x - 1)$ describes the polydispersity ($P_x = X_x/X_n$) of variable *x*; n, m and p represent any exponent and A_A, B_B and C_C indicate that the dimensions are weighted by themselves (e.g. if *C* is length, C_C would indicate a length-averaged length). Equation 5.11 is then used to solve for the z-average moments of polydispersed nanoparticles; for an ellipsoid the second and fourth moments are

$$\langle \Delta r_2 \rangle_z = \frac{1}{5}\left[a_a^2\frac{(k_a+3)(k_a+2)}{(k_a+1)^2} + b_b^2\frac{(k_b+3)(k_b+2)}{(k_b+1)^2} + c_c^2\frac{(k_c+3)(k_c+2)}{(k_c+1)^2}\right] \quad (5.12a)$$

$$\begin{aligned}\langle \Delta r_4 \rangle_z =& \\ \frac{12}{175}\Bigg\{3\Bigg[& a_a^4\frac{(k_a+5)(k_a+4)(k_a+3)(k_a+2)}{(k_a+1)^4} + b_b^4\frac{(k_b+5)(k_b+4)(k_b+3)(k_b+2)}{(k_b+1)^4} \\ &+ c_c^4\frac{(k_c+5)(k_c+4)(k_c+3)(k_c+2)}{(k_c+1)^4}\Bigg] + 2\Bigg[a_a^2b_b^2\frac{(k_a+3)(k_a+2)}{(k_a+1)^2}\frac{(k_b+3)(k_b+2)}{(k_b+1)^2} \\ &+ a_a^2c_c^2\frac{(k_a+3)(k_a+2)}{(k_a+1)^2}\frac{(k_c+3)(k_c+2)}{(k_c+1)^2} + b_b^2c_c^2\frac{(k_b+3)(k_b+2)}{(k_b+1)^2}\frac{(k_c+3)(k_c+2)}{(k_c+1)^2}\Bigg]\Bigg\}\end{aligned} \quad (5.12b)$$

and for cuboids are

$$\langle \Delta r_2 \rangle_z = \frac{1}{12}\left[A_A^2\frac{(k_A+3)(k_A+2)}{(k_A+1)^2} + B_B^2\frac{(k_B+3)(k_B+2)}{(k_B+1)^2} + C_C^2\frac{(k_C+3)(k_C+2)}{(k_C+1)^2}\right] \quad (5.13a)$$

$$\begin{aligned}
&\left\langle \Delta r_4 \right\rangle_z = \\
&\frac{1}{6}\left\{\frac{1}{5}\left[A_A^4\frac{(k_A+5)(k_A+4)(k_A+3)(k_A+2)}{(k_A+1)^4}+B_B^4\frac{(k_B+5)(k_B+4)(k_B+3)(k_B+2)}{(k_B+1)^4}+\right.\right. \\
&\left.C_C^4\frac{(k_C+5)(k_C+4)(k_C+3)(k_C+2)}{(k_C+1)^4}\right]+2\left[A_A^2B_B^2\frac{(k_A+3)(k_A+2)}{(k_A+1)^2}\frac{(k_B+3)(k_B+2)}{(k_B+1)^2}+\right. \\
&\left.\left.A_A^2C_C^2\frac{(k_A+3)(k_A+2)}{(k_A+1)^2}\frac{(k_C+3)(k_C+2)}{(k_C+1)^2}+B_B^2C_C^2\frac{(k_B+3)(k_B+2)}{(k_B+1)^2}\frac{(k_C+3)(k_C+2)}{(k_C+1)^2}\right]\right\}
\end{aligned} \tag{5.13b}$$

M_w for polydisperse particles becomes $\rho\eta(4\pi/3)a_a b_b c_c$ for an ellipsoid and $\rho\eta A_A B_B C_C$ for a cuboid.

The polydispersities of the dimensions were all approximated to be 1.2; this value is consistent with those reported by Elazzouzi-Hafraoui et al,[26] and also with our measurements from AFM. The dimensions calculated for a polydisperse population are also shown in Table 5.3. A much better coincidence with AFM is observed, especially when the particles are modeled as cuboids. A small overestimation with respect to AFM is still detected, except for the smallest axis. This could be caused by a slight underestimation of the polydispersity. It is also possible that the population of particles measured with AFM is smaller than real. During image analysis, only the particles that could be individually measured were included to avoid errors caused by perspective and agglomeration during drying. However, it is possible that some agglomerates exist in solutions that were not taken into account with AFM, even though they affect the light scattering results. Since the second virial coefficient resulted in a negative value it is actually expected that for the higher concentration samples some agglomerates may exist in suspension, thus affecting the extrapolation to infinite dilution. Alternatively, a hydration layer on the surface of the CNC could increase the effective dimensions of the nanoparticles Thus, the light scattering measurements would provide a more realistic representation of the sample in suspension.

Conclusions

Based on the polynomial expansion of the form factor we developed expressions, which are valid for every shape, for the moments of the difference of the distances within a nanoparticle. Information about the aspect ratio can be obtained from the analysis of the moments without making any assumptions regarding the shape or size of the nanoparticle. A method to calculate the dimensions of triaxial particles based on the moments was established and applied to a polydisperse population of cellulose nanocrystals. A very good agreement was found between the light scattering measurements and results from atomic force microscopy. It was observed that the CNC can be more accurately modeled if a cuboidal shape is assumed. The methodology described here can be easily applied to other systems of particles with complex shapes; moreover it can be applied to other scattering techniques such as small angle neutron and X-ray scattering.

Experimental Section

Materials

Whatman cellulose filter aid was employed as the cotton source to isolate CNC. Sulfuric acid was purchased with a concentration of 98% and then diluted to 64%.

Isolation of Cellulose Nanocrystals

Isolation of the CNC was achieved through an acid hydrolysis of cotton at 45°C for 50 min using 64 wt % sulfuric acid. At the end of the reaction time the suspension was diluted with cold deionized water to quench the reaction. Purification of the nanocrystals was done by precipitation, decantation, and dialysis of the slurry against deionized water. The suspensions were ultrasonicated to redisperse the CNC. More extensive procedures for CNC isolation can be found elsewhere.[1, 22, 29]

Atomic Force Microscopy

The dimensions of the CNC were measured with atomic force microscopy (AFM) to compare the results with those obtained from light scattering. The nanocrystals were deposited on a freshly cleaved mica surface, with an approximate area of 1.5cm^2, by drying a droplet of 0.01 wt% CNC suspension.[7] The shape of the tip was deconvoluted from the AFM pictures in order to minimize nanoparticles broadening.[30] A standard porous aluminum surface with sharp details was used to obtain the image of the tip employed for the correction. The three dimensions of a total of 122 particles were measured, only the particles that seemed isolated were included to minimize errors caused by agglomeration during drying.

Static Light Scattering

The CNC suspension was filtered through a 0.450 μm pore size filter and then diluted to five different concentrations: 3.10x10^{-6}, 6.15x10^{-6}, 8.78x10^{-6}, 2.06x10^{-5} and 4.46x10^{-5}

g/ml. The water employed was deionized and then filtered through a 0.020 μm pore size filter before use. All vials were previously cleaned with ethanol and water and allowed to dry covered before use. Static light scattering measurements were performed using a Wyatt Heleos II instrument in batch mode with vertically polarized light with a wavelength of 658 nm. The refractive index of water is 1.33147, and the refractive index increment is 0.103 ml/g.[31] The angle range studied spans from 32° to 147° ($0.0070 < q < 0.0244$ nm^{-1}).

References

1. Ureña-Benavides, E. E.; Brown, P. J.; Kitchens, C. L. Effect of Jet Stretch and Particle Load on Cellulose Nanocrystal-Alginate Nanocomposite Fibers. *Langmuir* **2010**, *26*, 14263-14270.

2. Xie, X.; Mai, Y.; Zhou, X. Dispersion and Alignment of Carbon Nanotubes in Polymer Matrix: A Review. *Materials Science and Engineering: R: Reports* **2005**, *49*, 89-112.

3. Cuenya, B. R. Synthesis and Catalytic Properties of Metal Nanoparticles: Size, Shape, Support, Composition, and Oxidation State Effects. *Thin Solid Films* **2010**, *518*, 3127-3150.

4. Kim, D. K.; Dobson, J. Nanomedicine for Targeted Drug Delivery. *J. Mater. Chem.* **2009**, *19*, 6294-6307.

5. Kumari, A.; Yadav, S. K.; Yadav, S. C. Biodegradable Polymeric Nanoparticles Based Drug Delivery Systems. *Colloids Surf. , B* **2010**, *75*, 1-18.

6. Liu, S.; Tang, Z. Nanoparticle Assemblies for Biological and Chemical Sensing. *J. Mater. Chem.* **2010**, *20*, 24-35.

7. Kvien, I.; Tanem, B. S.; Oksman, K. Characterization of Cellulose Whiskers and their Nanocomposites by Atomic Force and Electron Microscopy. *Biomacromolecules* **2005**, *6*, 3160-3165.

8. Guilbaud, J.; Saiani, A. Using Small Angle Scattering (SAS) to Structurally Characterise Peptide and Protein Self-Assembled Materials. *Chem. Soc. Rev.* **2011**, 40, 1200-1210.

9. Hammouda, B. SANS from Polymers—Review of the Recent Literature. *Polym. Rev.* **2010***, 50*, 14-39.

10. Zhang, F.; Ilavsky, J. Ultra-Small-Angle X-Ray Scattering of Polymers. *Polym. Rev.* **2010***, 50*, 59-90.

11. Wyatt, P. J. Light Scattering and the Absolute Characterization of Macromolecules. *Anal. Chim. Acta* **1993***, 272*, 1-40.

12. Kline, S. R. Reduction and Analysis of SANS and USANS Data using IGOR Pro. *J. Appl. Crystallogr.* **2006***, 39*, 895-900.

13. Debye, P. Molecular-Weight Determination by Light Scattering. *J. Phys. Chem.* **1947***, 51*, 18-32.

14. Terech, P.; Chazeau, L.; Cavaillé, J. Y. Small-Angle Scattering Study of Cellulose Whiskers in Aqueous Suspensions. *Macromolecules* **1999***, 32*, 1872-1875.

15. Braun, B.; Dorgan, J. R.; Chandler, J. P. Cellulosic Nanowhiskers. Theory and Application of Light Scattering from Polydisperse Spheroids in the Rayleigh-Gans-Debye Regime. *Biomacromolecules* **2008***, 9*, 1255-1263.

16. Zimm, B. H. The Scattering of Light and the Radial Distribution Function of High Polymer Solutions. *J. Chem. Phys.* **1948***, 16*, 1093-1099.

17. Zimm, B. H. Apparatus and Methods for Measurement and Interpretation of the Angular Variation of Light Scattering; Preliminary Results on Polystyrene Solutions. *J. Chem. Phys.* **1948***, 16*, 1099-1116.

18. Berry, G. C. Total Intensity Light Scattering from Solutions of Macromolecules. In *Soft Matter Characterization;* Borsali, R. P., Robert, P., Eds.; Springer: New York, 2008; pp 41-92.

19. Goldstein, M. Scattering Factors for Certain Polydisperse Systems. *J. Chem. Phys.* **1953***, 21*, 1255-1258.

20. Mittelbach, P.; Porod, G. Small-Angle x-Ray Scattering by Dilute Colloid Systems. The Calculation of Scattering Curves for Parallelepipeds. *Acta Phys. Austriaca* **1961***, 14*, 185-211.

21. Feigin, L. A.; Svergun, D. I. In *Structure Analysis by Small-Angle X-Ray and Neutron Scattering;* Taylor, G. W., Ed.; Plenum Press: New York, 1987; pp 90-94.

22. Dong, X. M.; Revol, J.; Gray, D. G. Effect of Microcrystallite Preparation Conditions on the Formation of Colloid Crystals of Cellulose. *Cellulose* **1998**, *5*, 19-32.

23. Habibi, Y.; Lucia, L. A.; Rojas, O. J. Cellulose Nanocrystals: Chemistry, Self-Assembly, and Applications. *Chem. Rev.* **2010**, *110*, 3479-3500.

24. Azizi Samir, M. A. S.; Alloin, F.; Dufresne, A. Review of Recent Research into Cellulosic Whiskers, their Properties and their Application in Nanocomposite Field. *Biomacromolecules* **2005**, *6*, 612-626.

25. Helbert, W.; Nishiyama, Y.; Okano, T.; Sugiyama, J. Molecular Imaging of Halocynthia Papillosa Cellulose. *J. Struct. Biol.* **1998**, *124*, 42-50.

26. Elazzouzi-Hafraoui, S.; Nishiyama, Y.; Putaux, J.; Heux, L.; Dubreuil, F.; Rochas, C. The Shape and Size Distribution of Crystalline Nanoparticles Prepared by Acid Hydrolysis of Native Cellulose. *Biomacromolecules* **2008**, *9*, 57-65.

27. Saunders, A. E.; Korgel, B. A. Second Virial Coefficient Measurements of Dilute Gold Nanocrystal Dispersions using Small-Angle X-Ray Scattering. *The Journal of Physical Chemistry B* **2004**, *108*, 16732-16738.

28. Deszczynski, M.; Harding, S. E.; Winzor, D. J. Negative Second Virial Coefficients as Predictors of Protein Crystal Growth: Evidence from Sedimentation Equilibrium Studies that Refutes the Designation of those Light Scattering Parameters as Osmotic Virial Coefficients. *Biophys. Chem.* **2006**, *120*, 106-113.

29. Beck-Candanedo, S.; Roman, M.; Gray, D. G. Effect of Reaction Conditions on the Properties and Behavior of Wood Cellulose Nanocrystal Suspensions. *Biomacromolecules* **2005**, *6*, 1048-1054.

30. Villarrubia, J. S. Algorithms for Scanned Probe Microscope Image Simulation, Surface Reconstruction, and Tip Estimation. *J. Res. Natl. Inst. Stand. Technol.* **1997**, *102*, 425-454.

31. De Souza Lima, M. M.; Borsali, R. Static and Dynamic Light Scattering from Polyelectrolyte Microcrystal Cellulose. *Langmuir* **2002**, *18*, 992-996.

CHAPTER SIX

CONCLUSIONS AND RECOMMENDATIONS

Conclusions

This dissertation provides a comprehensive analysis of the behavior of cellulose nanocrystal (CNC) aqueous suspensions and their use as a reinforcing agent in calcium alginate fibers. CNC aqueous suspensions transition from an isotropic behavior to a cholesteric liquid crystal as the concentration is increased, passing through a biphasic region were both morphologies coexist in equilibrium. Increasing the temperature gives more energy to the nanoparticles to stay in the isotropic state, thus reducing the volume of the liquid crystal. The biphasic suspensions, at low concentrations, coalesce in the quiescent state forming a distinguishable interface, until the viscosity is so large that the macroscopic separation is no longer visible. A change in slope is detected in the viscosity versus concentration curve when this occurs. Upon deformation, the relaxation mechanism varies throughout the biphasic region as a consequence of the variations in the area and morphology of the interface. However this contribution is only significant for the elastic component of the modulus, not for the viscous component. A well defined cholesteric order is only observed when the sample is completely liquid crystalline and it has not reached the gel region; otherwise the sample is identified as precholesteric. During the biphasic region the presence of isotropic phase is assumed to hinder the formation of a cholesteric order, while in the gel domain it is the stiffness of the sample itself that prevents the assembly of the CNC. Nevertheless the nature of the crystals to twist with respect to each other is confirmed.

Blending a small concentration of CNC with a solution of sodium alginate induces ordering of the alginate chains and consequently the formation of a liquid crystalline phase. When these suspensions are used to wet spin CNC – alginate nanocomposite fibers, the ordering is transferred to the fibers themselves. The consequence is the ability to tune the properties of the nanocomposite fibers by varying CNC load and amount of stretch during processing. If the nanoparticle load is approximately 2 wt% and the jet stretch is low, a tough fiber is obtained without compromising the strength of the material. However, addition of CNC allows increasing the jet stretch thus producing filaments with a higher degree of orientation, which are consequently stronger and stiffer. The tunability is the result of the type of order that the CNC induce in the alginate matrix. Given the intrinsic nature of the cellulose crystallites to twist, they lose orientation as the concentration increases, until a spiral assembly is formed, analogous to native cellulose fibers. The lost orientation and appearance of the spiral assembly increases the toughness and reduces the modulus. The opposite occurs if the jet stretch is increased given that the particles are forced to orient in the fiber axis direction.

Given the importance of the size and shape of any nanoparticle in any type of application, this work provides a simple method to determine the elongation of any nanoparticle using scattering data. If a specific shape is known, then the exact dimensions can be calculated. The method was applied to a suspension of polydisperse cellulose nanocrystals, yielding dimensions (6.4 x 28 x 152 nm) that are in close agreement to AFM measurements.

Recommendations

Isolation of Cellulose Nanocrystals with Sulfuric Acid

The isolation of the CNC can be improved if the 10 fold dilution is replaced by a 2 fold dilution with iced deionized water followed by an immediate centrifugation of the entire batch at 2 °C at maximum velocity (note that this velocity is different for each rotor used). Following centrifugation, the acid must be decanted and replaced with cold deionized water. Repeat the centrifugation and decantation processes until the suspension looks turbid. Dialysis of the suspensions is still recommended since the pH will be very low. After completing the dialysis, a neutralization of the batch should be added to the procedure since the suspensions are highly acidic and can corrode the equipment used to produce nanocomposites. It must be noted that the isoelectric point of the CNC suspensions isolated from sulfuric acid does not necessarily occurs at pH 7.0, as determined by titrating a suspension of the nanoparticles with NaOH; indeed a titration of a CNC suspension is presented in Figure 6.1; where the isolectric point occurred at pH 6.0. Once the CNC suspension is neutralized, it is ultrasonicated with the sonicating horn; the previous neutralization will increase the lifetime of the sonicating tip. Since the tip releases metallic particles to the solution, a final centrifugation at maximum possible speed is required; this time the metallic particles should precipitate while the CNC should stay in suspension.

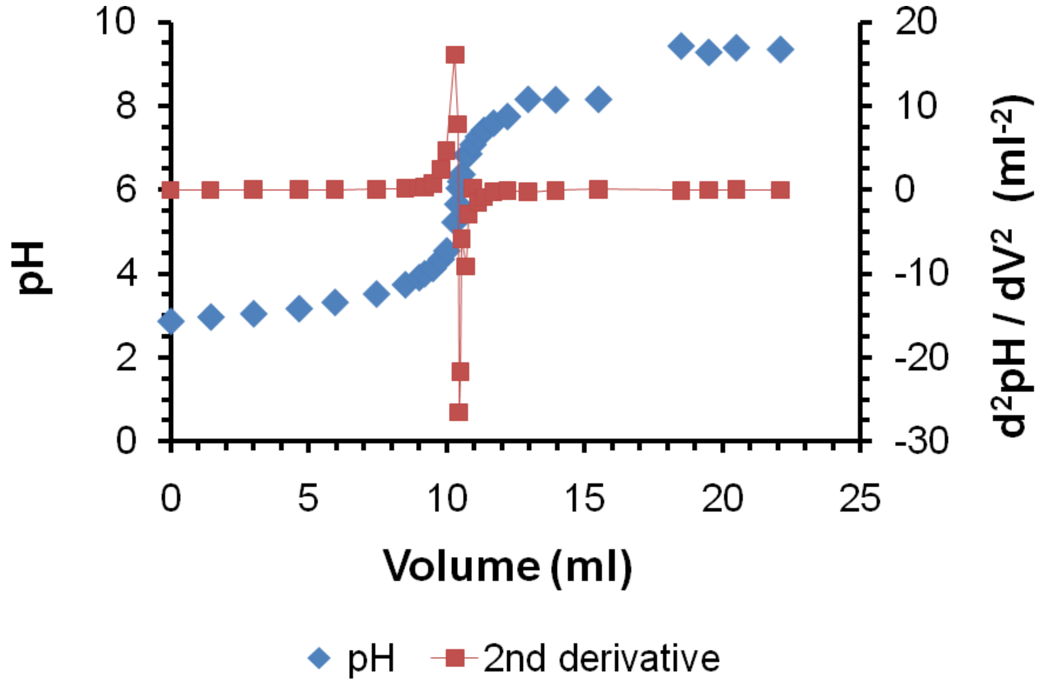

Figure 6.1. Titration of CNC with sodium hydroxide.

It is important to note the acidic sulfate group induces thermal degradation of the CNC at temperatures as low as 125°C.[1] This is a significant limitation of CNCs produced via sulfuric acid hydrolysis, since most thermoplastic polymers are processed by melt spinning at high temperatures. Nevertheless there have been reports that neutralization of the sulfate groups with sodium hydroxide significantly improves the thermal stability of cellulose nanocrystals.[2] CNCs isolated by HCl hydrolysis are thermally stable to temperatures greater than 325°C. Since the dispersions of CNC isolated from sulfuric acid are more stable than those isolated by HCl, it is worth verifying to what extent the thermal stability is improved by the neutralization; this can be easily achieved through a thermogravimetric analysis.

Wet Spinning of CNC – Calcium Alginate Fibers

Several improvements are possible to the wet spinning of calcium alginate fibers. A spinneret with a gradual reduction of the hole diameter would induce alignment and an increased strength of the fibers. The hole diameter (400 μm) of the spinneret that was used in this dissertation is relatively large; a smaller value of 80 – 100 μm would also improve the alignment within the fibers. For practical purposes, the number of holes in the spinneret is an important parameter to consider. A low number of holes would facilitate visual inspection of the filaments while processing (i.e. it is harder to observe one filament breaking if there are a lot of them); however since the number of filaments in the fiber is small, they must be strong enough as to allow measuring their tensile strength. If the sensitivity of the universal testing machine (Instron) is good, a single filament spinneret would be highly beneficial since it requires less dope solution, and facilitates inspection during spinning. If the sensitivity of the Instron does not allow a single filament measurement, then a spinneret with 5 to 10 holes would very likely yield a fiber with a measurable strength. It is also recommended to use low viscosity alginate to prepare more concentrated solutions which would yield stronger fibers. Another way to increase the strength of the fibers is to use a source of alginate with a larger G content like *Laminaria hyperborea*. The latter will change the structure of the fiber and potentially the interaction between the CNC and the alginate. In this case, wide angle X-ray diffraction can be used again to study the effect of the CNC on the alginate structure and the effect of alginate type on the orientation of the nanocrystals.

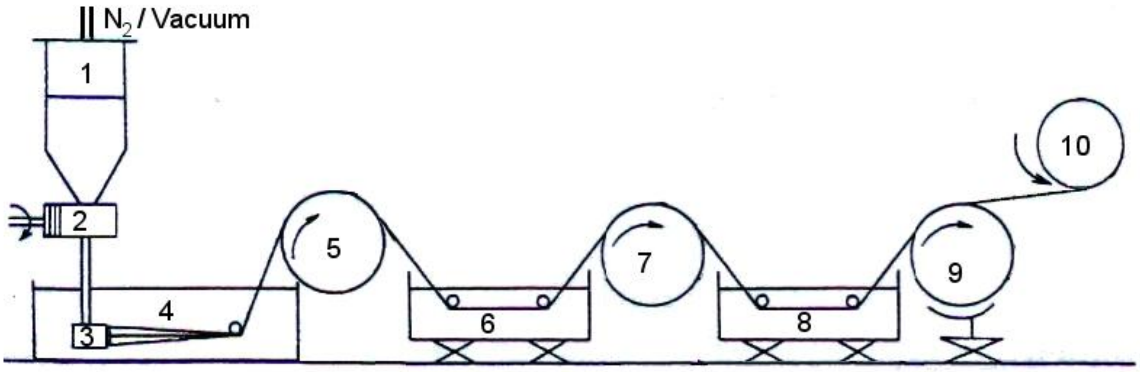

Figure 6.2. Proposed wet spinning setup. The numbers represent 1) vessel with dope solution, 2) metering pump, 3) spinneret, 4) coagulating bath, 5) take up roller, 6) hot water rinsing and stretching bath, 7) stretching roller, 8) dehydrating acetone or ethanol bath, 9) hot air roller and 10) winder. Notes: vacuum is used for degassing prior to spinning, and nitrogen is used to push the dope solution; degassing can be improved if a high shear stirrer is incorporated into the vessel; placing a mirror (or any reflecting surface) under the spinneret significantly helps to see the individual filaments for monitoring purposes. Modified from reference 3

Measurement of the cross sectional area was not possible for the fibers obtained because the filaments cross linked to each other. This can be avoided if the batch process is changed to continuous. Three long baths, three rollers and a winder are required as shown in Figure 6.2. The first bath would contain the $CaCl_2$ coagulating solution, the second hot deionized or distilled water to rinse excess salt, and the last one acetone or ethanol to dehydrate. A roller with controlled speed must be used between each bath and at the end. In this set up, the stretching should be done in the hot water bath by controlling the speed ratio between rollers 7 and 5 (Figure 6.2) and not the jet stretch; this would reduce the probability of $CaCl_2$ entering the spinneret. If problems arise with rinsing of excess salt and stretching simultaneously, then a warm water bath can be added before the stretching step.

While the fiber passes around the last roller, hot air is blown to dry it (hair dryer might work); a threaded Teflon tube can be used to increase the number of passes on this roller and provide more drying time. It is important to note that the tangential velocity is the important parameter to control with the rollers, thus all their diameters must be known with an acceptable precision. If the threaded Teflon tube is placed on top of one of the rollers, the external diameter of the tube must be used to find the tangential velocity. The last two rollers in Figure 6.2 and the winder should all run at the same velocity to avoid stretching and breaking the filaments, but care must be taken if the fiber starts to pile up on the winder and the diameter of the winder increases.

The times that the fiber is immersed in each bath are parameters to be adjusted in order to optimize the process. If filament crosslinking occurs due to excessive salt on the surface of the filaments, the times in the coagulation and rinsing baths can be increased. Another source of filament adhesion is the presence of water in the fibers; in this case a longer dehydration time is required. Two options are available to control the immersion time: varying the pumping flow rate and the roller speed to maintain the same velocity ratios, or change the length of the baths.

Rheology of CNC – Sodium Alginate Suspensions

Prior to spinning it is useful to study the rheological properties of the dope solutions used. This can give important information regarding shear induced orientation of the crystals and polymer chains. If a cup and bob geometry is used, a large shear rate, of even 1000 s^{-1}, might be possible, as long as the suspensions do not climb the bob. If some type of small angle scattering technique is used in conjunction with the rheological experiments, an order parameter can be obtained according to the method described by Oldenbourg et al. for rod shaped Tobacco-Mosaic-Virus[4, 5]. Alternatively, if wide angle diffraction data is measurable under shear, the orientation of the crystallites can be measured using the method employed in Chapter 4. It must be noted that the measured torques for CNC – alginate suspensions will generally be larger than those for pure CNC aqueous suspensions and might not require a highly sensitive force transducer, which was an important issue encountered in Chapter 2.

References

1. Roman, M.; Winter, W. T. *Biomacromolecules* **2004,** 5, 1671-1677.
2. Wang, N.; Ding, E.; Cheng, R. *Polymer* **2007,** 48, 3486-3493.
3. Qin, Y. *Polym. Int.* **2008,** 57, 171-180.
4. Oldenbourg, R.; Wen, X.; Meyer, R. B.; Caspar, D. L. D. *Phys. Rev. Lett.* **1988,** 61, 1851.
5. Orts, W. J.; Godbout, L.; Marchessault, R. H.; Revol, J. -. *Macromolecules* **1998,** 31, 5717-5725.

APPENDICES

Appendix A

Details Regarding Rheology Experiments

Rheological analysis of liquid crystals implies significant differences with respect to polymer melts or solutions. When running a steady shear experiment, the differences in the transient response must be taken into account. A typical polymer solution or melt show a viscosity overshoot and a subsequent steady value. A liquid crystal show a series of dampened oscillations after the first overshoot and consequently the time to reach steady state is significantly longer (Figure A.1). Consequently, it becomes impractical to run the experiment until the steady state is reached; instead, the time is chosen to measure one full oscillation. The viscosity averaged over that oscillation should give the steady shear value. Thus, a step rate experiment always has to be done before attempting to measure the steady shear viscosity.

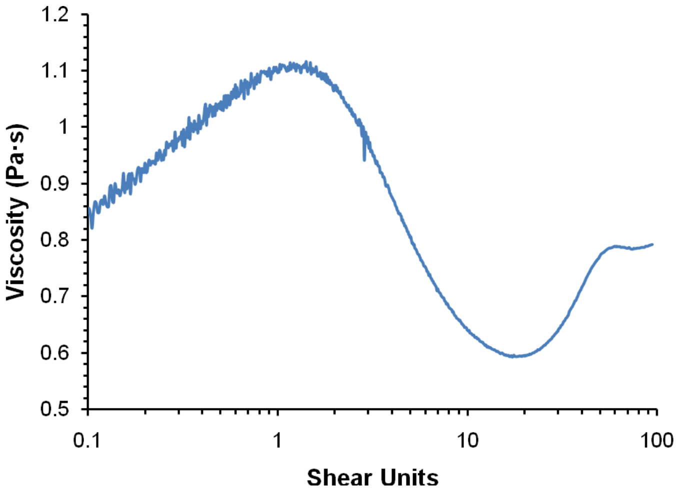

Figure A.1. Transient response of a 12.0 wt % CNC suspensions. Shear rate ($\dot{\gamma}$) = 0.1 s^{-1}

For one sample, the period of the oscillation is only a function of the shear units ($\dot{\gamma} \cdot t$), where $\dot{\gamma}$ is the shear rate and t is time. Consequently it suffices to do only one step rate experiment before running an entire flow curve (shear rate sweep). Once the period is defined in terms of shear units, the sampling time will be defined for every shear rate. A shear rate of 0.1 s^{-1} is typical for the step rate, but others can be more appropriate depending on the sample. The period generally increases with concentration and aspect ratio of the polymer or nanoparticles being studied; therefore a step rate experiment must be done for every different sample. If there is no knowledge about the sample being studied, a shear rate of 1 s^{-1} and a very long time (~ 2h) can be used to ensure that one or more oscillations are measured.

If a lyotropic liquid crystal is being studied there can be evaporation of the solvent with time, especially at high shear rates, which will necessarily affect the measurements. Thus the gap between the plates, or the cone and plate, must be carefully examined at the end of the experiment to detect if evaporation has occurred. If there is evidence of solvent loss, then the experimental setup has to be modified. Some rheometers have solvent traps that are designed to minimize evaporation, but often times they are not enough. An alternative is to reduce the temperature, however if it is lowered too much, condensation can occur on the fixture; 10 °C is typically used. Another option is to place a layer of a Newtonian fluid on the edge of the sample to maintain the solvent inside. The viscosity of the Newtonian liquid must be much lower than the sample, but it has to stick to the edge for the time required; it also has to be immiscible with the sample. If a solvent trap is available, oil can be used to provide a better seal at the edges of the trap; this should never be done on the shaft of the rheometer. If necessary, additional solvent can be introduced into the trap by placing wetted pads inside, but making sure that they do not interfere with the measurements. Very often a combination of all the previous modifications is necessary to minimize evaporation; plus the experimental time must be reduced as much as possible without affecting the reliability of the measurements.

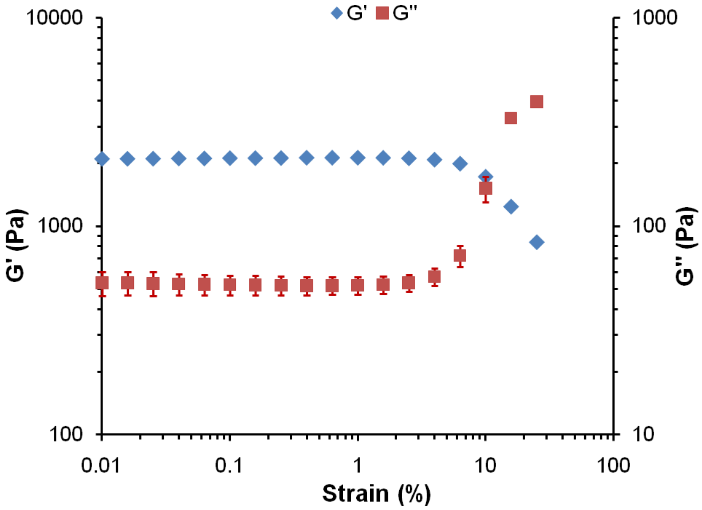

Figure A.2. Amplitude sweep of a 21.8 wt % CNC suspensions. Frequency = 10 rad/s

If an oscillatory experiment is desired, the linear viscoelastic region (LVR) must be defined first. This is the strain domain within which the structure of the sample is unaltered by the shear field. The LVR is determined through an amplitude sweep experiment which is generally done at a constant frequency of 10 rad/s (Figure A.2). The LVR is defined by the strain range where the moduli are constant, which in Figure A.2 was chosen below 1.58 %. When performing a small angle oscillatory shear (SAOS) experiment, such as a frequency sweep, it is recommended to use the largest possible strain that is within the linear viscoelastic region; if not the torque generated could be too low to measure. In this case, the oscillations that occur in liquid crystal materials will not affect the experimental parameters; however the same precautions regarding solvent evaporation has to be taken. Some additional details for the steady and oscillatory experiments are provided next.

General Details about sample handling and loading

- If evaporation is an issue, the samples have to be kept cold and properly sealed.
- The cone and/or plates must be equilibrated at the desired temperature before zeroing the gap.
- Once the temperature has reached equilibrium the gap can be zeroed.
- The samples have to be carefully homogenized before loading them; it is not recommended to vigorously stir them since it can alter the structure and introduce air bubbles. A good alternative is to use a spatula to gently mix it; if the sample is liquid enough, a few gentle shakes of the vial (or container) should meet the purpose.
- The samples should be loaded with a spatula if possible. If the sample is liquid a syringe without the plunger should be used; the liquid must be allowed to flow by itself onto the plate or cup without applying any pressure to it.
- The upper fixture has to be lowered very carefully, especially when approaching the surface of the sample. It must only be lowered a fraction of a millimeter at a time or air bubbles can enter the sample.
- If sample is squeezed out of the edges, it has to be cleaned with a soft spatula (rubber policeman works well), a cotton swab and/or a Kimwipe. Then the upper fixture can be slowly lowered until a good edge is obtained.

- The sample edge must be perfectly straight; it should look like a reflective surface.
- If a parallel plate geometry is used, the final gap must be between 0.5 and 1.0 mm. If a cone and plate geometry is used, the final gap is the nominal cone truncation gap.
- The normal force must be zeroed immediately before starting the experiment.

Details about the steady shear flow experiment

- It is a good practice to provide an equilibration time of 15 to 20 min before running any experiment to allow the sample to relax after loading. This time can also be determined by a two step experiment: first pre-shear for 10 min at high shear rate, then run a small amplitude oscillatory time sweep experiment at a frequency of 10 rad/s and a strain within the LVR. From the resulting curve choose the time required for G' to reach a stable value.
- To ensure that the shear history is erased, a pre-shear step of 10 min is common used. The shear rate is chosen beyond the first Newtonian plateau (within a shear thinning region); 0.1 s^{-1} is typically employed for liquid crystalline materials.
- The pre-shear can be set up as a step rate experiment to measure the transient response, if that is the case, it is necessary to give appropriate equilibration time before this step (after loading). If the pre-shear is not employed to determine the transient response (i.e., it is only used to erase the shear history) the preliminary equilibration step is not required.
- After pre-shearing, the sample should be allowed to relax again for an appropriate time (typically 15 to 20 min) before running the steady shear flow (SSF) experiment.
- The sampling time for the SSF is defined according to a step rate

- 5 points per decade is appropriate.
- After the first SSF it is recommended to wait again 15 to 20 min to allow relaxation and then run a second flow curve.
- To test reproducibility, at least two loadings of the same sample should be done, while collecting two flow curves per load.

Details about the small amplitude oscillatory shear experiment

- The sample must be allowed to relax after loading for an appropriate time (15 to 20 min), just like in the steady shear experiment.
- An amplitude sweep (AS) experiment must be done first (by duplicate). It is recommended to wait approximately 3 min between replicates; this time is much lower than the regular equilibration time because the SAOS experiment does not change the structure of the sample. However, if the final strain during the AS experiment is beyond the LVR, it is recommended to provide a longer stabilization time.
- The frequency sweep (FS) experiment is done after the AS using a strain within the LVR. It should be done by duplicates waiting approximately 3 minutes between each run.
- At least two loads of the same sample are recommended, each should be done by duplicate for a total of 4 replicates.
- If the same load is used for a SAOS and a SSF experiment, the SAOS should be completed first because the SSF can alter the structure of the fluid.

Appendix B

Supporting Information for Chapter III

Wet Spinning System

A lab scale wet spinning system was available which mainly consisted on a vessel for the dope solution, a metering pump, a computer (pump controller), one bath, one wind up unit, and a teflon tube with threads on the outer surface. Alginate yarns would stick to each other if they are drawn right after the $CaCl_2$ bath without going first through the washing and drying steps, thus forming a big "chunk" of polymer. Consequently an appropriate way to draw the fibers in a batch process while keeping the tension and at the same time avoiding self adhesion was required. The method developed consisted on mounting a Teflon cylindrical tube, with threads on the outer surface, on top of the winder and let the fiber wind up along the entire thread. Then the Teflon piece (with the fiber mounted on it) would be transferred to the subsequent baths and the drying step completing a batch process. Figure B.1 shows a diagram of the Teflon tube with its respective dimensions; the threads are round bottom with 0.125 in pitch and 0.0625 in deep. The wet spinning apparatus is described in Figures B.2 to B.6 and a picture of the fibers is shown in Figure B.7.

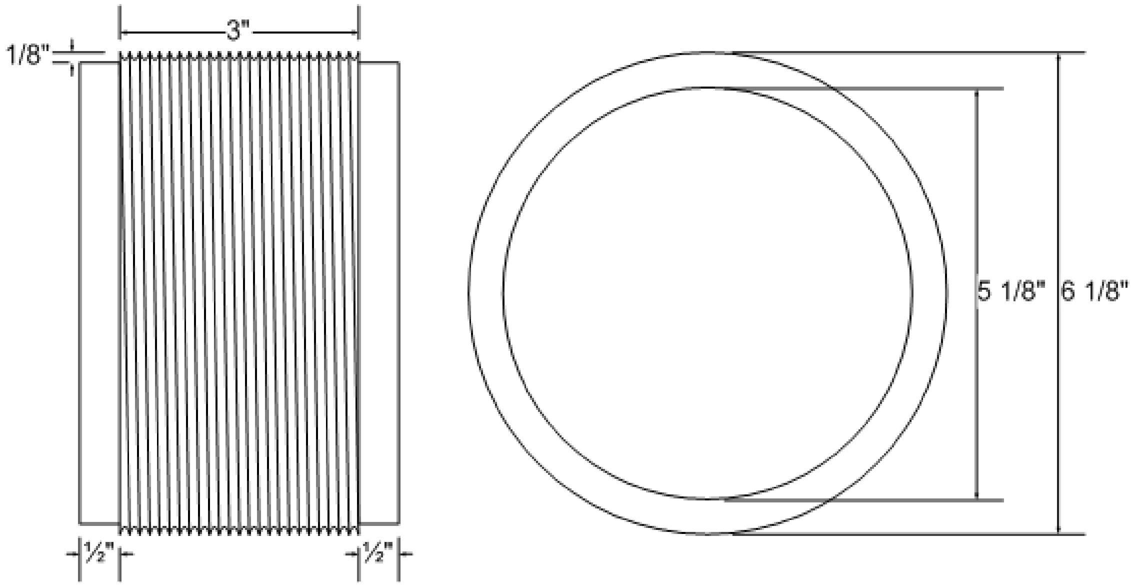

Figure B.1. Diagram of Teflon tube used to wind up fibers.

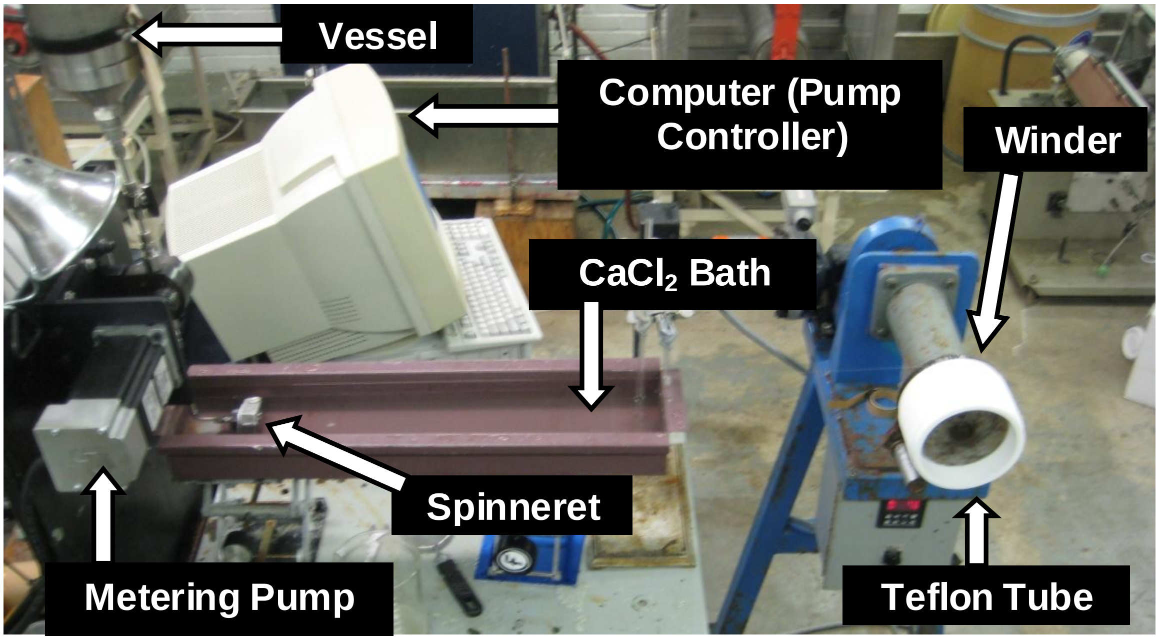

Figure B.2. Apparatus for wet spinning.

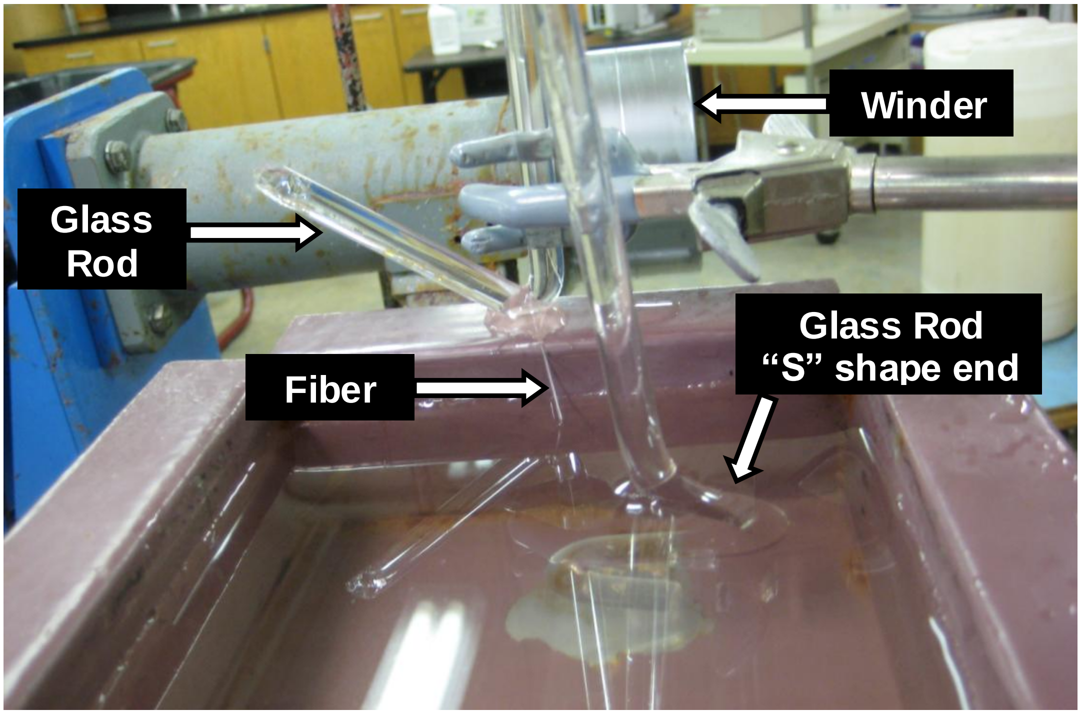

Figure B.3. The wet spun fiber is kept under the bath using a glass rod with an "s" shape end, and then directed to the winder by a second glass rod.

Figure B.4. Spinneret, O-ring, filter and housing. An O-ring must be placed between each part (3 O-rings total).

Figure B.5. Spinneret used for fiber spinning, 10 holes, 400 μm hole diameter.

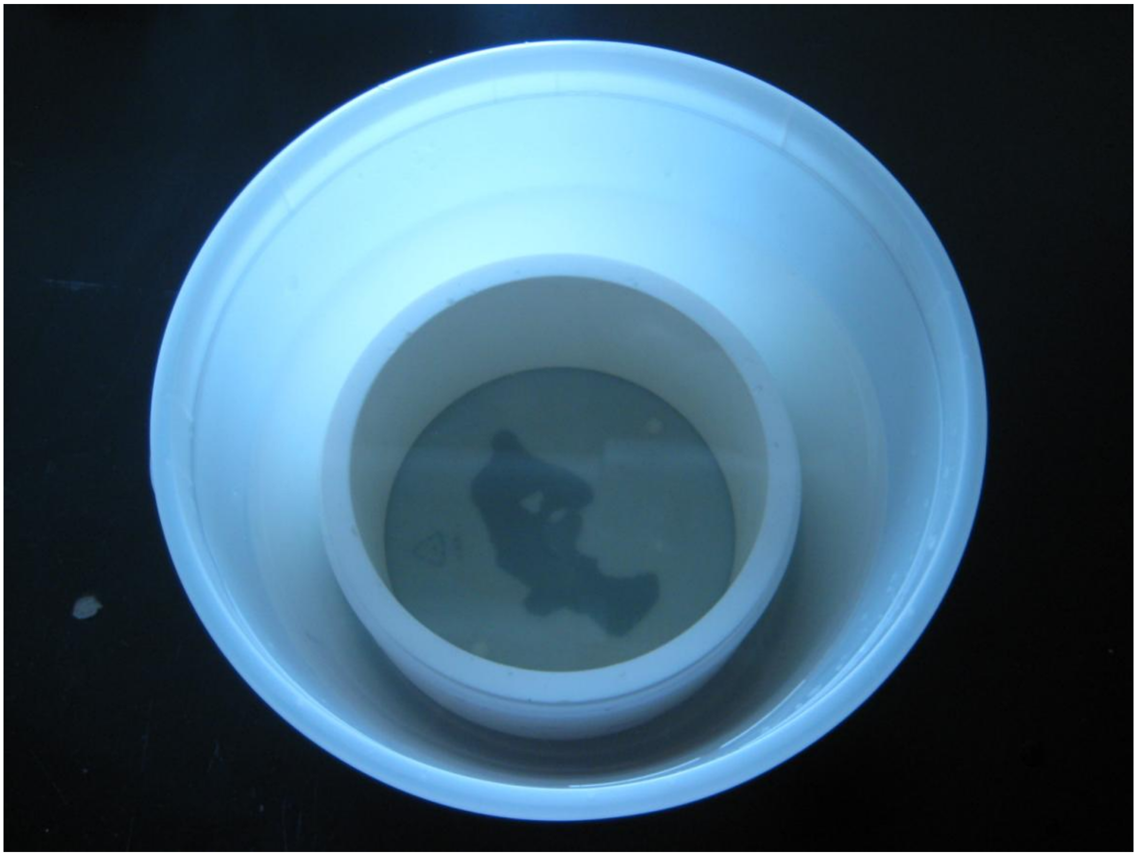

Figure B.6. Fiber on Teflon tube inside a water bath.

Figure B.7. Picture of CNC-Alginate fibers filled with 25%CNC spun at an apparent jet stretch of 4.6.

Polarized light microscopy of CNC/sodium alginate films

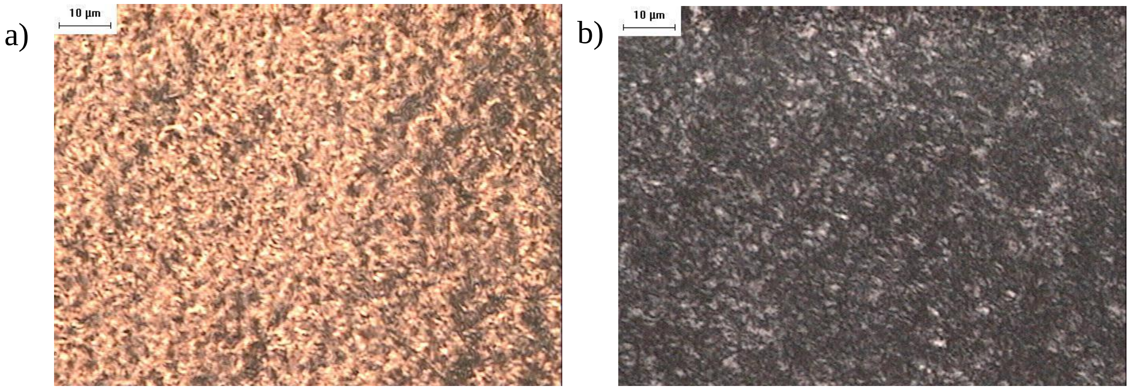

Figure B.8. Polarized light microscopy pictures of a 50%wt CNC/sodium alginate film. In a) the sample is placed between parallel polarizers, and in b) the sample is placed between crossed polarizers. Birefringent and non birefringent domains are visible, indicating that the sample still contains isotropic regions; a fingerprint texture is starting to form indicating that the preferred orientation is chiral nematic.

Tensile Properties of CNC-Alginate fibers

Table B.1. Yarn denier of CNC-Alginate fibers at Different Apparent Jet Stretches and CNC Lloads.

Jet Stretch	Denier					
	0%	2%	5%	10%	25%	50%
2.0	153±2	164±2	---	---	---	---
2.2	138±1	---	---	---	---	---
2.4	126±2	133±4	134±2	141±1	---	169±2
2.8	---	108±3	112±2	120±4	---	152±3
3.2	---	96±1	98±1	98±1	---	---
3.4	---	92±3	---	---	---	---
3.6	---	---	89±1	93.0±0.7	97±2	---
3.8	---	---	78±1	---	---	---
4.0	---	---	---	81.7±1.5	85±2	---
4.2	---	---	---	74±1	---	---
4.4	---	---	---	---	76±2	---
4.6	---	---	---	---	75±2	---

Table B.2. Elongation at Break of CNC-Alginate Fibers at Different Apparent Jet Stretches and CNC Loads.

Jet Stretch	Elongation at break (%)					
	0%	2%	5%	10%	25%	50%
2.0	37±1	35±1	---	---	---	---
2.2	30.2±0.8	---	---	---	---	---
2.4	33±1	37.3±0.7	37.5±0.9	35±1	---	18.7±0.3
2.8	---	27.0±0.6	28.5±0.9	31±1	---	15.6±0.4
3.2	---	28±1	24.7±0.5	24.9±0.5	---	---
3.4	---	28.4±0.9	---	---	---	---
3.6	---	---	24.1±0.7	19.6±0.6	21.0±0.5	---
3.8	---	---	19.0±0.4	---	---	---
4.0	---	---	---	20.0±0.6	14.2±0.4	---
4.2	---	---	---	15.6±0.4	---	---
4.4	---	---	---	---	15.5±0.3	---
4.6	---	---	---	---	12.7±0.5	---

Table B.3. Tenacity of CNC-Alginate fibers at Different Apparent Jet Stretches and CNC Loads.

Jet Stretch	Tenacity (gpd)					
	0%	2%	5%	10%	25%	50%
2.0	0.145±0.004	0.131±0.003	---	---	---	---
2.2	0.148±0.003	---	---	---	---	---
2.4	0.149±0.004	0.152±0.005	0.144±0.003	0.129±0.003	---	0.178±0.004
2.8	---	0.194±0.008	0.160±0.004	0.145±0.005	---	0.164±0.005
3.2	---	0.162±0.004	0.177±0.003	0.153±0.003	---	---
3.4	---	0.180±0.007	---	---	---	---
3.6	---	---	0.166±0.004	0.144±0.003	0.152±0.004	---
3.8	---	---	0.187±0.005	---	---	---
4.0	---	---	---	0.152±0.004	0.151±0.006	---
4.2	---	---	---	0.206±0.007	---	---
4.4	---	---	---	---	0.166±0.005	---
4.6	---	---	---	---	0.164±0.006	---

Table B.4. Modulus of CNC-Alginate Fibers at Different Apparent Jet Stretches and CNC Loads.

Jet Stretch	Modulus (gpd)					
	0%	2%	5%	10%	25%	50%
2.0	2.76±0.06	2.82±0.05	---	---	---	---
2.2	3.32±0.09	---	---	---	---	---
2.4	3.1±0.1	2.58±0.09	2.82±0.09	2.48±0.05	---	6.2±0.2
2.8	---	4.7±0.2	3.4±0.1	3.0±0.1	---	6.9±0.2
3.2	---	3.36±0.08	4.64±0.07	3.44±0.08	---	---
3.4	---	3.8±0.2	---	---	---	---
3.6	---	---	3.9±0.1	4.06±0.07	4.4±0.1	---
3.8	---	---	5.5±0.1	---	---	---
4.0	---	---	---	4.3±0.1	5.7±0.1	---
4.2	---	---	---	6.9±0.2	---	---
4.4	---	---	---	---	5.7±0.2	---
4.6	---	---	---	---	6.2±0.2	---

Table B.5. Tensile Energy at Break of CNC-Alginate Fibers at Different Apparent Jet Stretches and CNC Loads.

Jet Stretch	Tensile energy to break (gpd)					
	0%	2%	5%	10%	25%	50%
2.0	0.038±0.002	0.032±0.001	---	---	---	---
2.2	0.030±0.001	---	---	---	---	---
2.4	0.033±0.002	0.039±0.001	0.037±0.001	0.030±0.001	---	0.0235±0.0006
2.8	---	0.037±0.002	0.031±0.001	0.031±0.002	---	0.0184±0.0009
3.2	---	0.033±0.001	0.030±0.001	0.025±0.001	---	---
3.4	---	0.036±0.002	---	---	---	---
3.6	---	---	0.029±0.001	0.0211±0.0007	0.0221±0.0007	---
3.8	---	---	0.0244±0.0009	---	---	---
4.0	---	---	---	0.024±0.001	0.016±0.001	---
4.2	---	---	---	0.025±0.001	---	---
4.4	---	---	---	---	0.0201±0.0009	---
4.6	---	---	---	---	0.016±0.001	---

WAXD Measurements

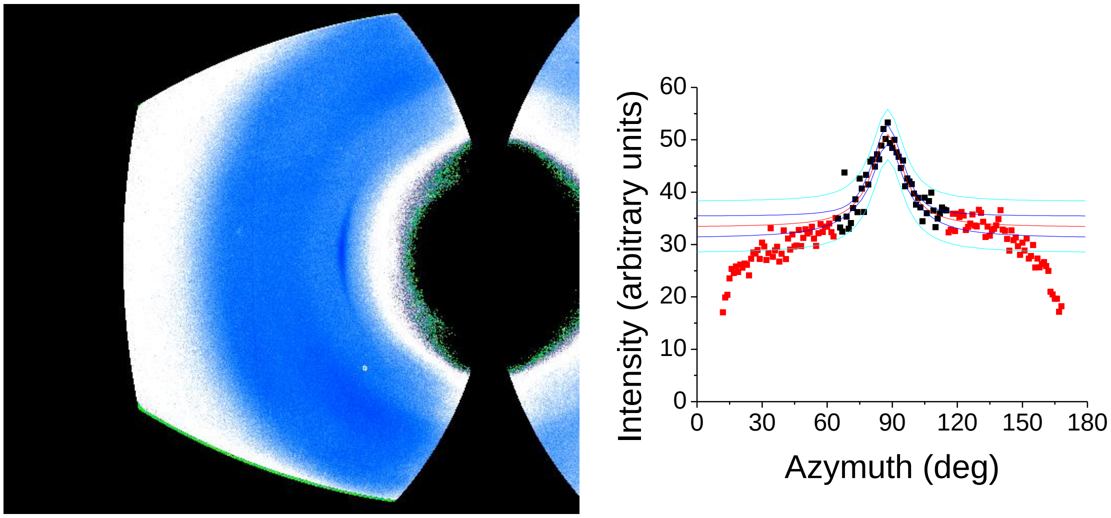

Figure B.9. WAXD pattern and azymuthal peak of the fiber containing 5%wt CNC, spun at a jet stretch of 2.4. The red line represents the fitted peak, the blue lines represent the 95% confidence bands, and the aqua colored lines represent the prediction bands.

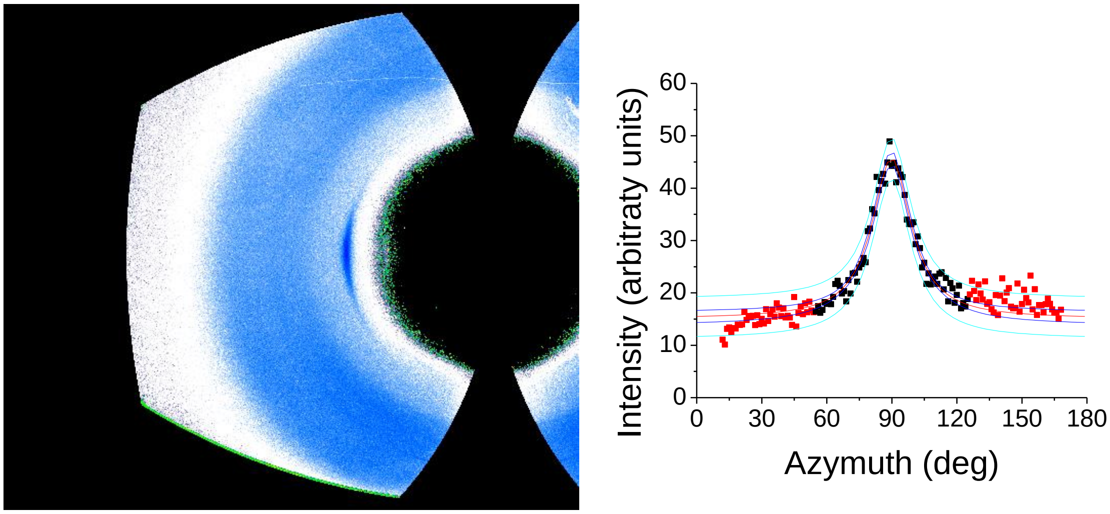

Figure B.10. WAXD pattern and azymuthal peak of the fiber containing 10%wt CNC, spun at a jet stretch of 2.4. The red line represents the fitted peak, the blue lines represent the 95% confidence bands, and the aqua colored lines represent the prediction bands.

Thermal stability of alginate fibers

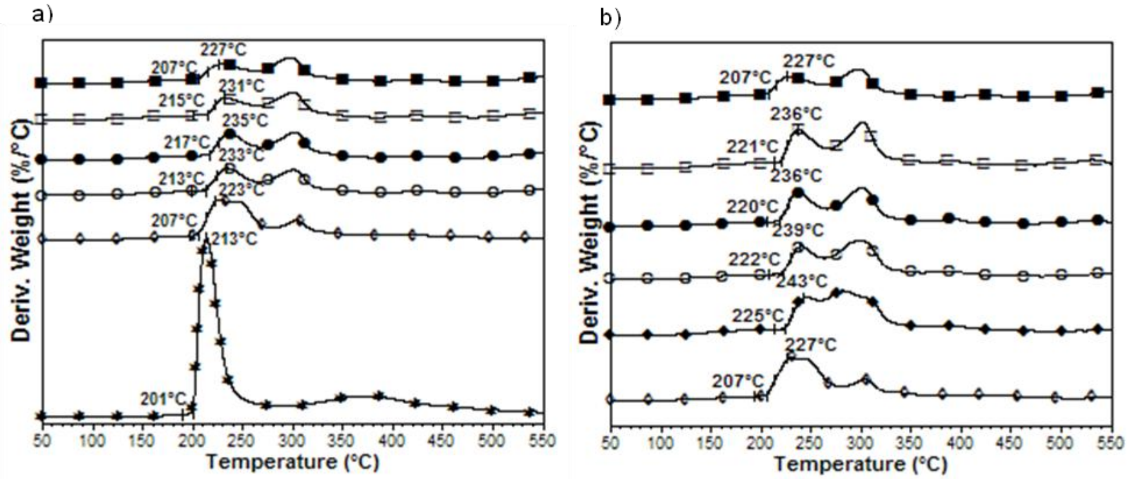

Figure B.11. DTG traces of a) CNC-alginate fibers spun at $J_A = 2.4$ and pure CNC; and b) CNC-alginate fibers spun at maximum J_A. Symbols key: pure CNC (stars), alginate fibers with cellulose loads of 0% (solid squares), 2% (open squares), 5% (solid circles), 10% (open circles), 25% (solid diamonds), and 50% (open diamonds).

Appendix C

Representative Force vs. Deformation Curves

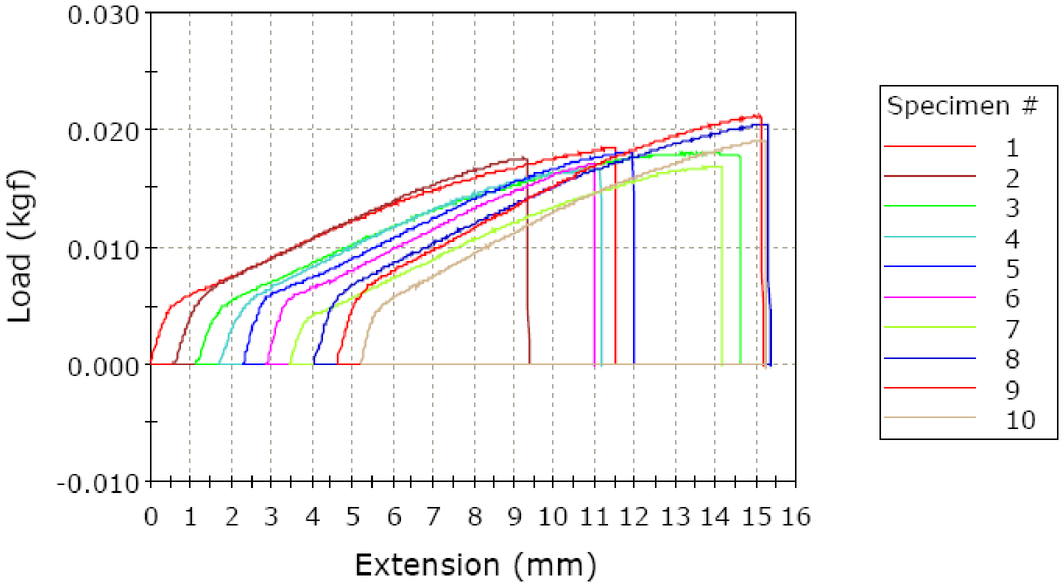

Figure C.1. Force vs. deformation curves for a pure Calcium alginate fiber spun at J_A = 2.4. The curves are shifted on the x axis for clarity.

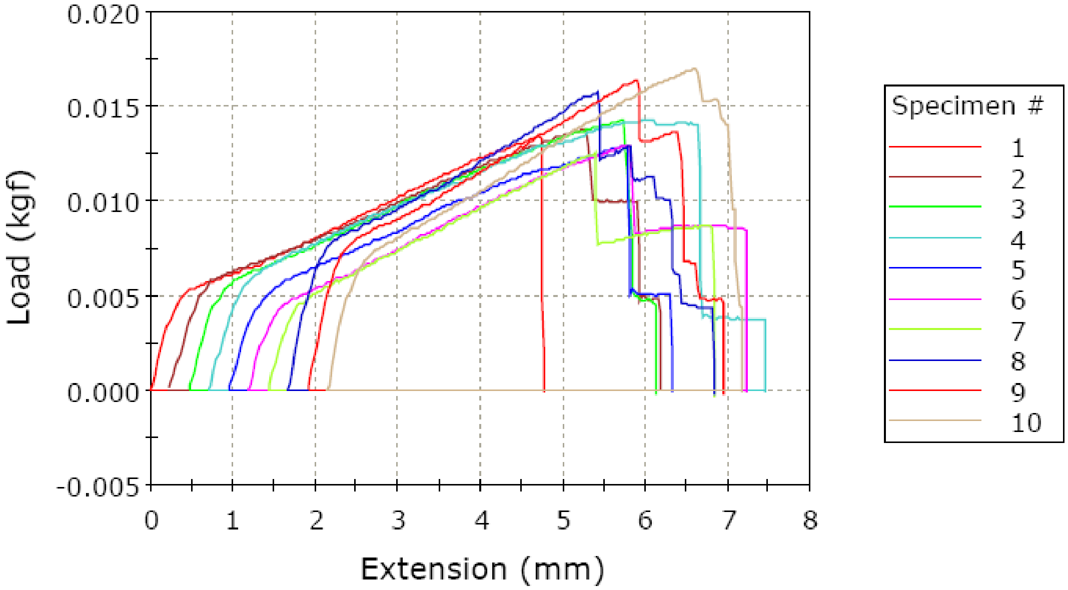

Figure C.2. Force vs. deformation curves for a Calcium alginate fiber with 10 wt % CNC spun at J_A = 4.2. The curves are shifted on the x axis for clarity.

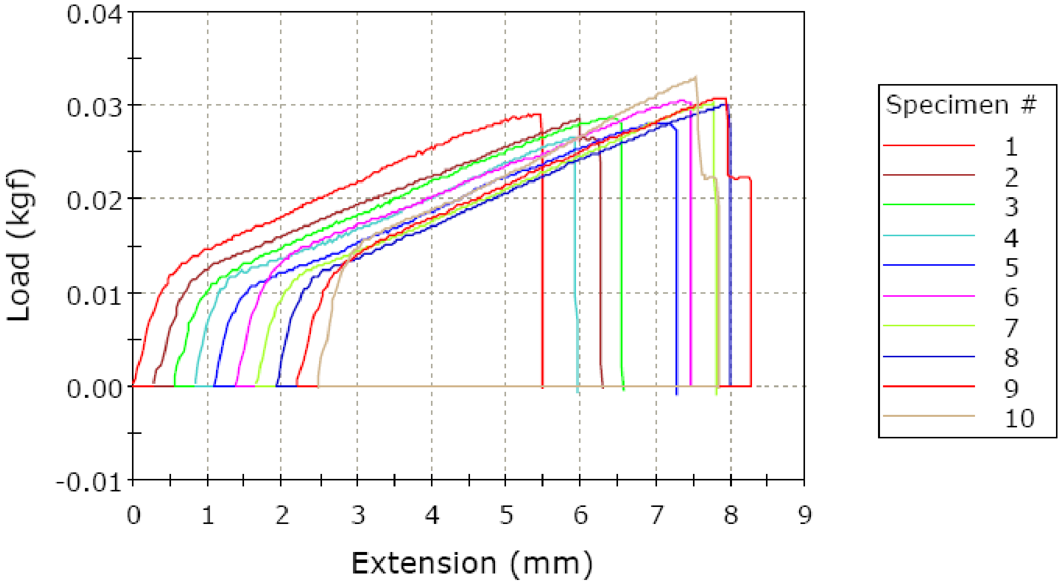

Figure C.3. Force vs. deformation curves for a Calcium alginate fiber with 50 wt % CNC spun at J_A = 2.4. The curves are shifted on the x axis for clarity.

Note: Complete raw data available in electronic format

Appendix D

Wide Angle X-Ray Diffraction Patterns

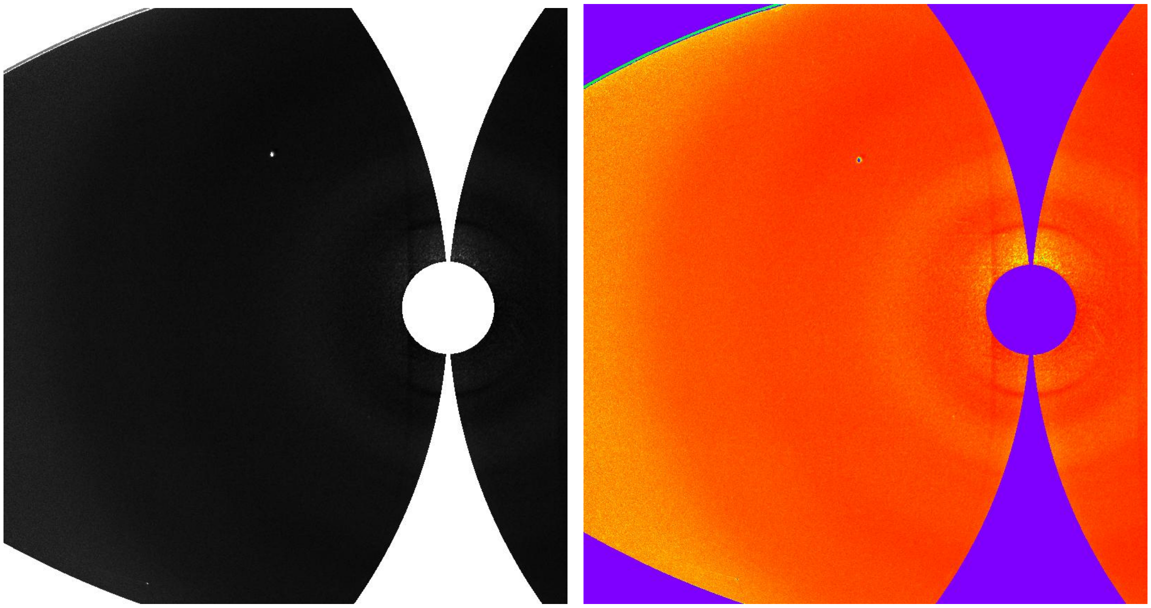

Figure D.1. WAXD, 0 wt % CNC fiber, J_A = 2.4. Left: Data corrected for air scattering, cosmic background and Frasier correction. Right: Colored contrast enhanced image.

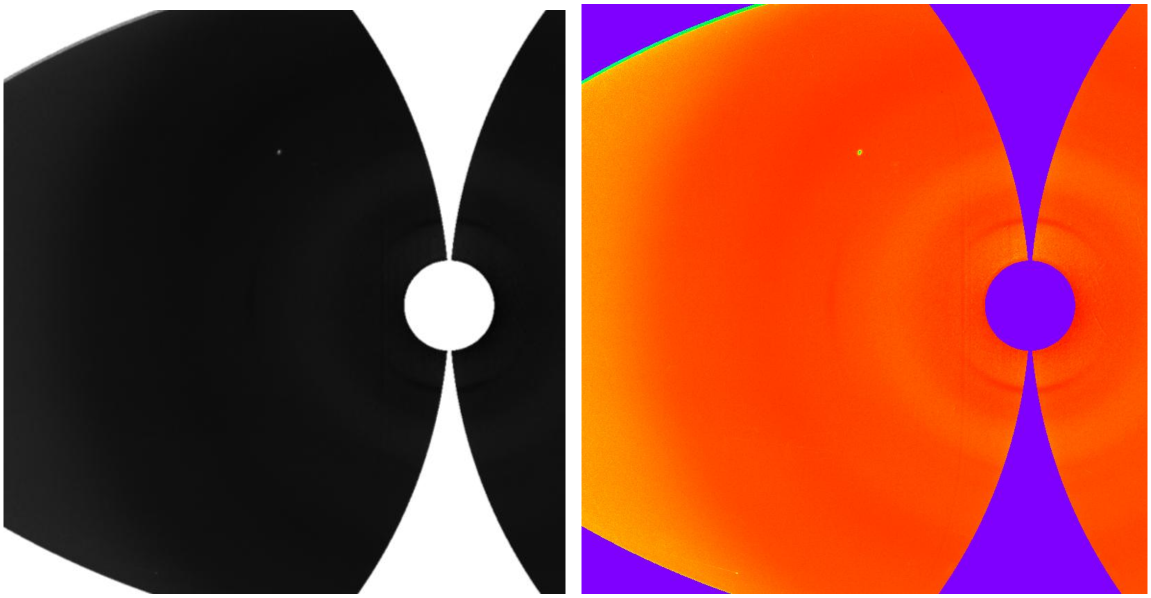

Figure D.2. WAXD, 2 wt % CNC fiber, J_A = 2.4. Left: Data corrected for air scattering, cosmic background and Frasier correction. Right: Colored contrast enhanced image.

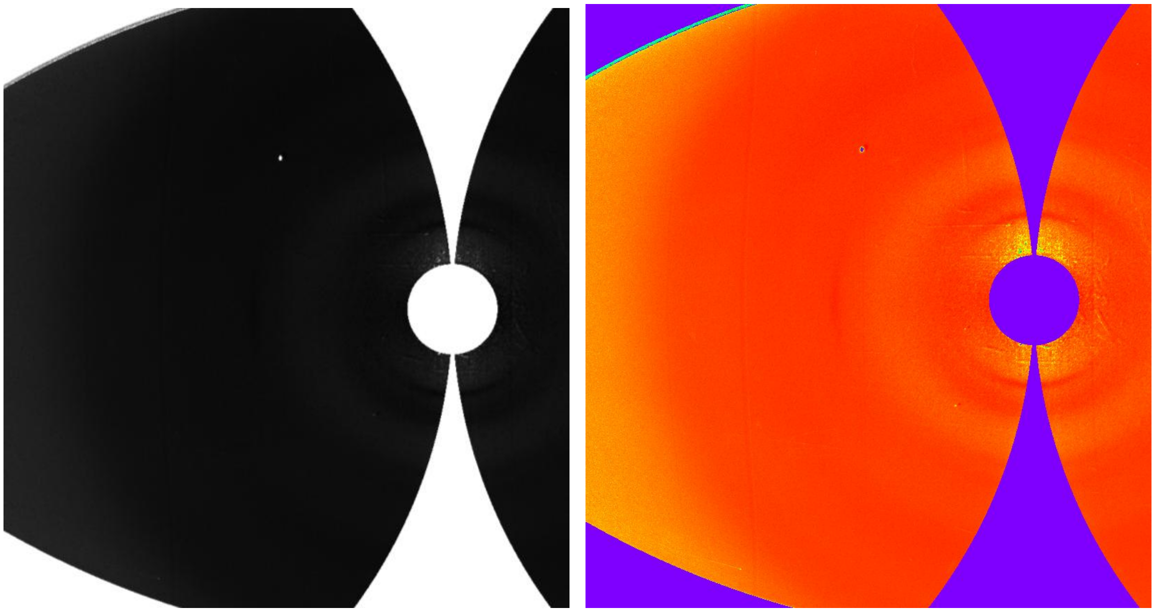

Figure D.3. WAXD, 2 wt % CNC fiber, $J_{\mathrm{A}} = 3.4$. Left: Data corrected for air scattering, cosmic background and Frasier correction. Right: Colored contrast enhanced image.

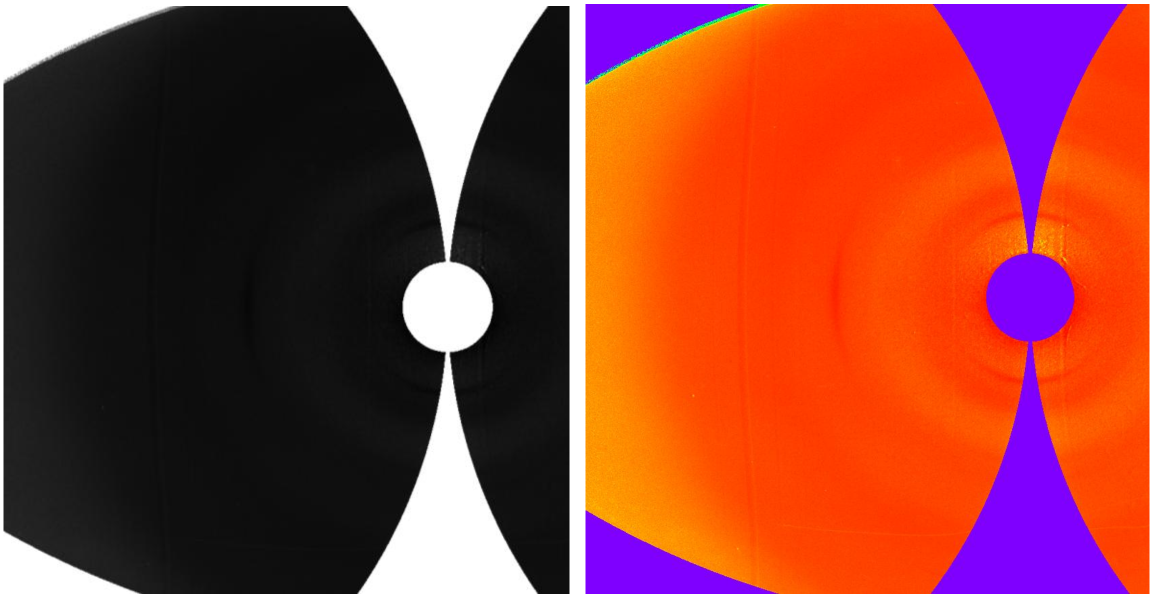

Figure D.4. WAXD, 5 wt % CNC fiber, $J_{\mathrm{A}} = 2.4$. Left: Data corrected for air scattering, cosmic background and Frasier correction. Right: Colored contrast enhanced image.

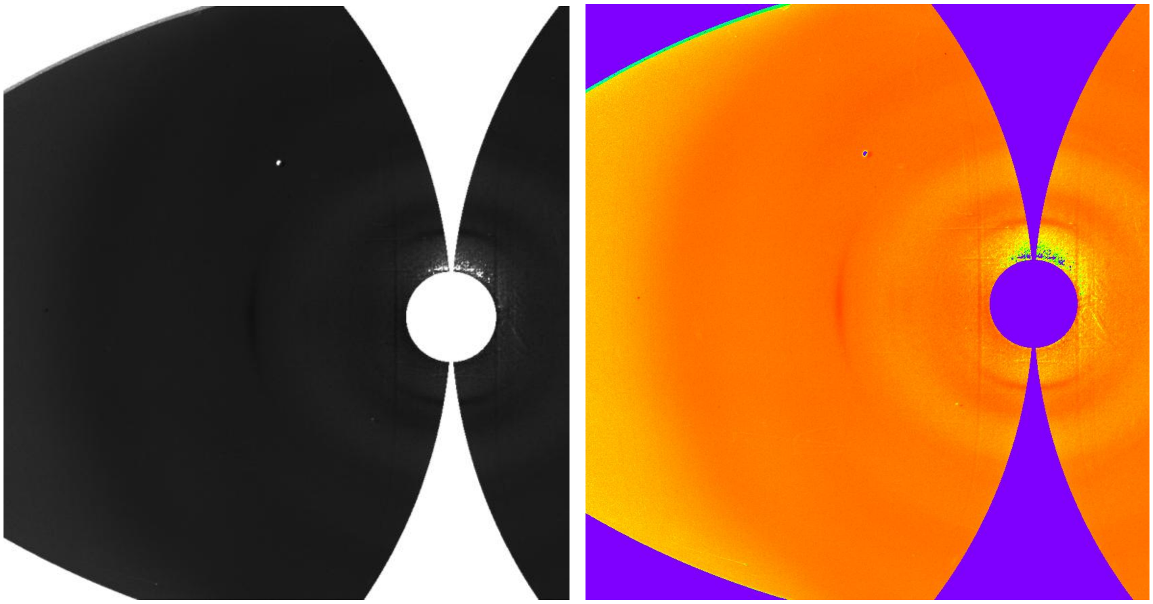

Figure D.5. WAXD, 5 wt % CNC fiber, $J_{\mathrm{A}} = 3.8$. Left: Data corrected for air scattering, cosmic background and Frasier correction. Right: Colored contrast enhanced image.

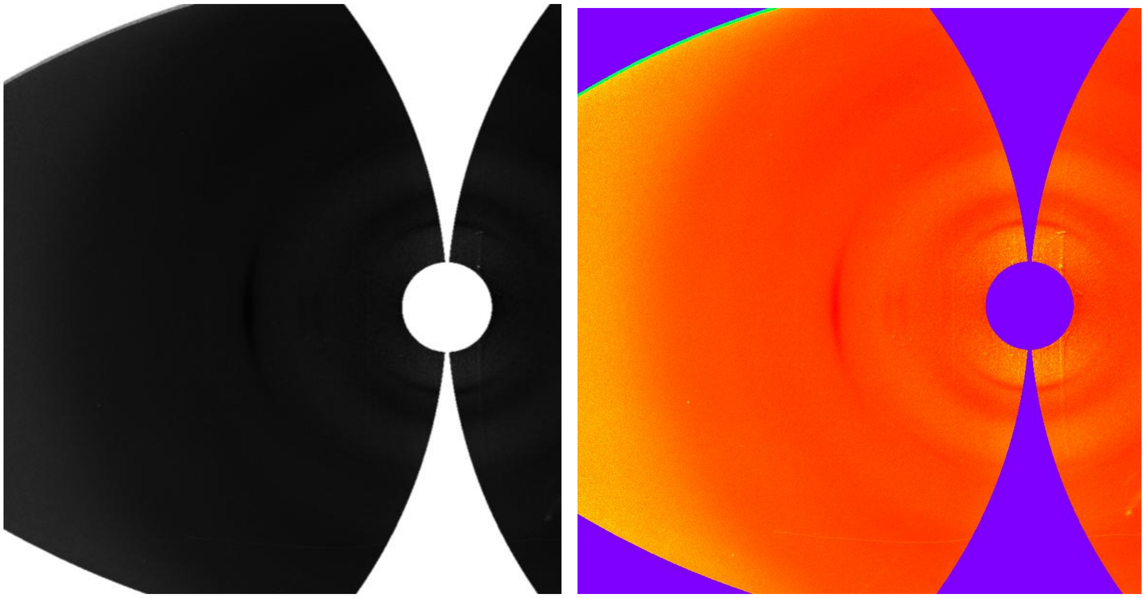

Figure D.6. WAXD, 10 wt % CNC fiber, $J_{\mathrm{A}} = 2.4$. Left: Data corrected for air scattering, cosmic background and Frasier correction. Right: Colored contrast enhanced image.

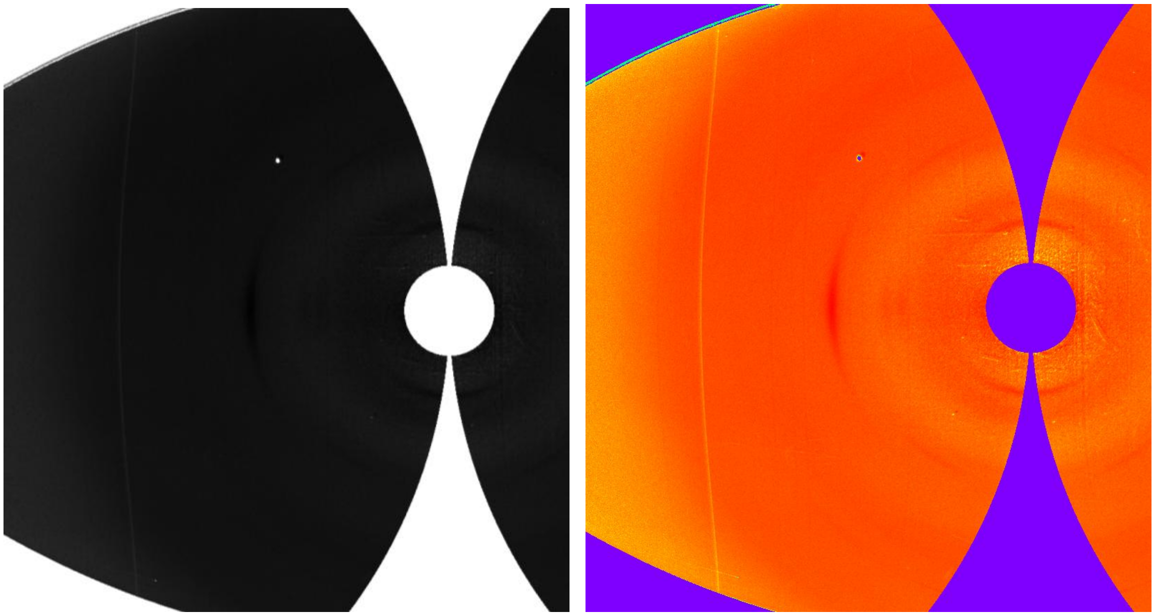

Figure D.7. WAXD, 10 wt % CNC fiber, $J_{\mathrm{A}} = 4.2$. Left: Data corrected for air scattering, cosmic background and Frasier correction. Right: Colored contrast enhanced image.

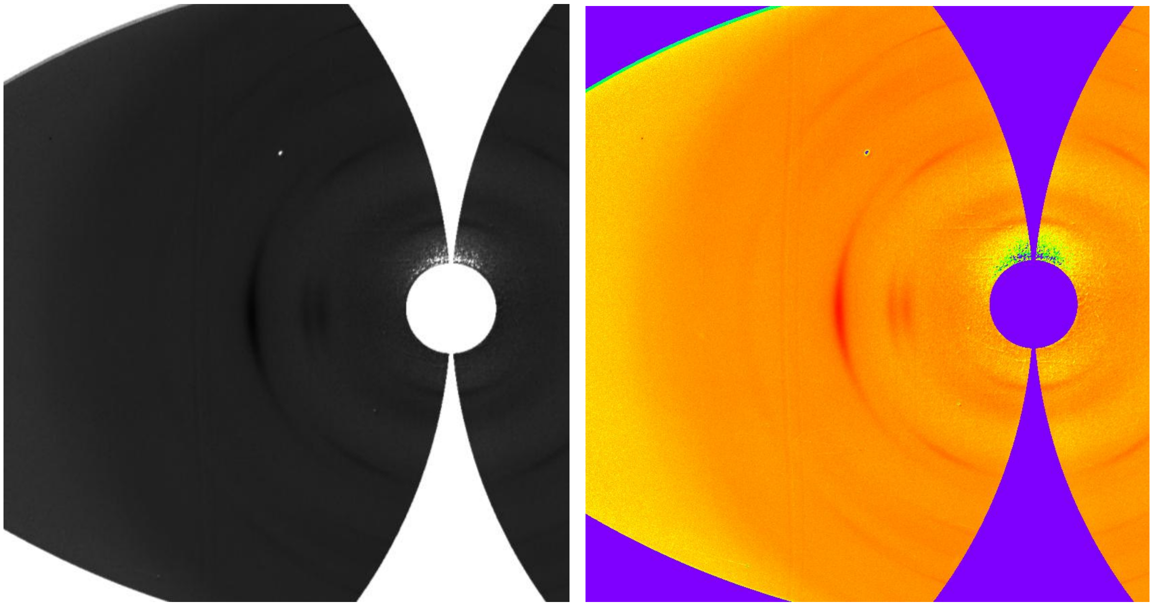

Figure D.8. WAXD, 25 wt % CNC fiber, $J_{\mathrm{A}} = 4.6$. Left: Data corrected for air scattering, cosmic background and Frasier correction. Right: Colored contrast enhanced image.

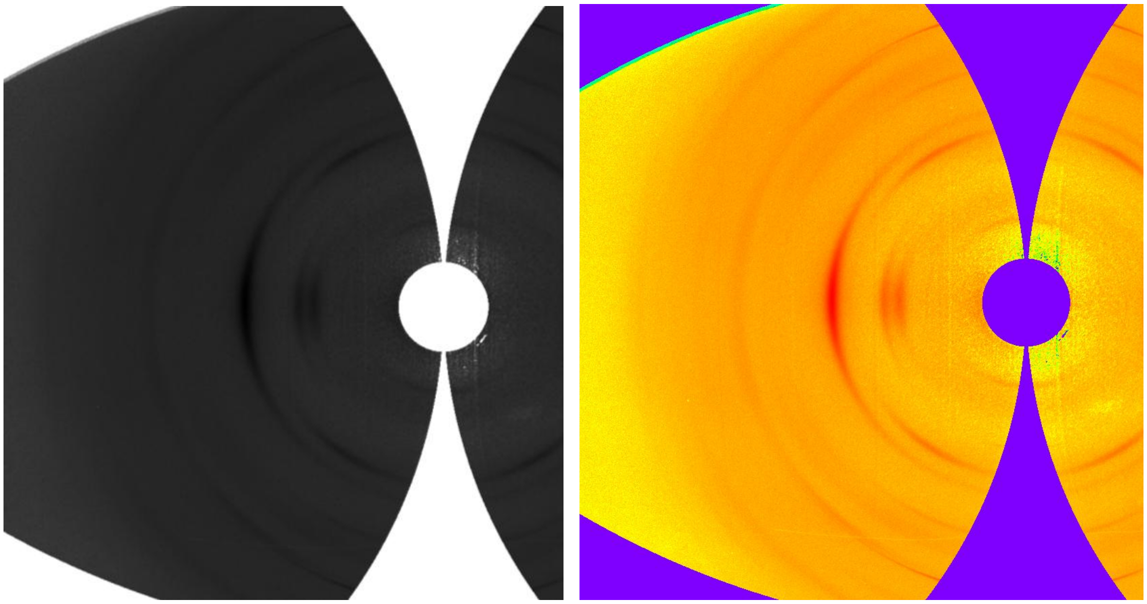

Figure D.9. WAXD, 50 wt % CNC fiber, $J_A = 2.4$. Left: Data corrected for air scattering, cosmic background and Frasier correction. Right: Colored contrast enhanced image.

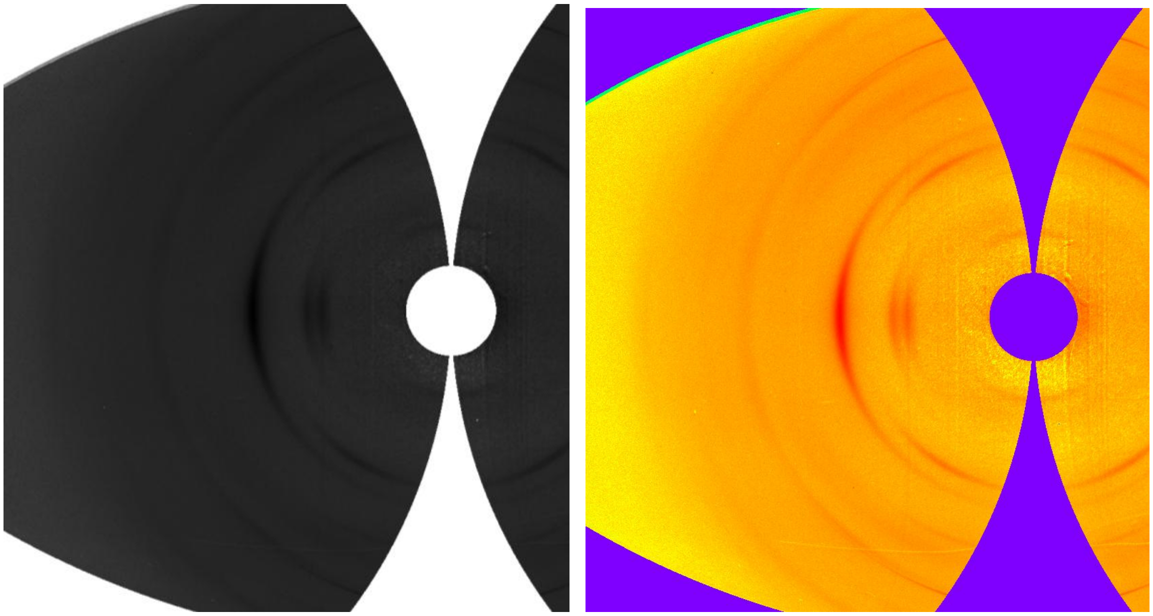

Figure D.10. WAXD, 50 wt % CNC fiber, $J_A = 2.8$. Left: Data corrected for air scattering, cosmic background and Frasier correction. Right: Colored contrast enhanced image.

Appendix E

Derivation of Equations for Chapter IV

Debye's expansion of the form factor

For illustrative purposes Debye's expansion of the form factor is presented first. Equation 5.3 is

$$P(\theta)=\frac{1}{N_\nu^2}\sum_i^{N_\nu}\sum_j^{N_\nu}\frac{\sin(qr_{\mathrm{ij}})}{qr_{\mathrm{ij}}} \qquad (5.3)$$

The Taylor series expansion of the function sin(x)/x is

$$\frac{\sin\left(x\right)}{x}=1-\frac{x^2}{3!}+\frac{x^4}{5!}-\frac{x^6}{7!}+\ldots \qquad (\mathrm{E}.1)$$

Substituting x in eq. E.1 by qr_{ij} and evaluating in eq. 5.3 gives eq. 5.5

$$P(\theta)=$$

$$1-\frac{1}{3}\left[\frac{1}{2N_\nu^2}\sum_i^{N_\nu}\sum_j^{N_\nu}r_{ij}^2\right]q^2+\frac{1}{60}\left[\frac{1}{2N_\nu^2}\sum_i^{N_\nu}\sum_j^{N_\nu}r_{ij}^4\right]q^4-\frac{1}{2520}\left[\frac{1}{2N_\nu^2}\sum_i^{N_\nu}\sum_j^{N_\nu}r_{ij}^6\right]q^6+(Oq^8) \qquad (5.5)$$

Derivation of Equation 5.8

The moment of r_{ij} are defined as

$$\Delta r_n=\frac{1}{2N_\nu^2}\sum_i^{N_\nu}\sum_j^{N_\nu}r_{ij}^n \qquad (\mathrm{E}.2)$$

Equation E.2 can be expressed in terms of volume elements rather than scattering elements

$$\Delta r_n=\frac{1}{2N_\nu^2}\sum_i^{N_\nu}\sum_j^{N_\nu}r_{ij}^n=\frac{1}{2N_\nu^2}\sum_h^{N_\beta}\sum_k^{N_\beta}N_hN_kr_{hk}^n \qquad (\mathrm{E}.3)$$

where r_{hk} is the distance from the center of the volume element h to the center of volume element k, N_β is the total number of volume elements h or k in a nanoparticle and N_h and N_k are the number of scattering elements that are found in each h or k.

If all volume elements h and k have an equal volume ΔV_h and ΔV_k, and since $N_v^2 = \Sigma\Sigma 1$, the moment Δr_n can be expressed as:

$$\Delta r_n = \frac{\sum_h^{N_\beta}\sum_k^{N_\beta} N_h N_k r_{hk}^n \Delta V_h \Delta V_k}{2\sum_h^{N_\beta}\sum_k^{N_\beta} N_h N_k \Delta V_h \Delta V_k} \tag{E.4}$$

According to Riemann's definition, the integral of function $f(x)$ can be expressed as

$$\int_a^b f(x)dx = \lim_{\Delta x_i \to 0} \sum_i^n f(x_i)\Delta x_i \tag{E.5}$$

Then if the number of scatterers is large enough such that all volume elements are infinitely small, Riemann's definition gives

$$\frac{\sum_i^{N_v}\sum_j^{N_v} N_i N_j r_{ij}^n \Delta V_j \Delta V_i}{2\sum_i^{N_v}\sum_j^{N_v} N_i N_j \Delta V_j \Delta V_i} = \frac{\int_{V_i}\int_{V_j} N_i N_j r_{ij}^n dV_j dV_i}{2\int_{V_i}\int_{V_j} N_i N_j dV_j dV_i} \tag{E.6}$$

The number of scatterers N_i in volume element i can be expressed as

$$N_i = \langle N \rangle g(\mathbf{r_i}) \tag{E.7}$$

where $\langle N \rangle$ is the average number of scattering elements in one volume element, and $g(\mathbf{r_i})$ is the radial distribution function. Substitution of eq. E.7 into eq. E.6 gives eq. 5.8

$$\Delta r_n = \frac{1}{2N_v^2}\sum_i^{N_v}\sum_j^{N_v} r_{ij}^n = \frac{\int\limits_{V_i}\int\limits_{V_j} g(\mathbf{r_i})g(\mathbf{r_j})r_{ij}^n dV_j dV_i}{2\int\limits_{V_i}\int\limits_{V_j} g(\mathbf{r_i})g(\mathbf{r_j})dV_j dV_i} \tag{5.8}$$

Derivation of Equations 5.9a to 5.9c

The difference r_{ij} is the magnitude of the vector $\mathbf{r_i}$ - $\mathbf{r}_\mathrm{j}$. Then if n is an even number

$$r_{ij}^n = \sqrt{\left(\mathbf{r_i} - \mathbf{r_j}\right)^{2n}} = \left(\mathbf{r_i} - \mathbf{r_j}\right)^n \tag{E.8}$$

and

$$r_{ij}^2 = \left(\mathbf{r_i} - \mathbf{r_j}\right)^2 = r_i^2 + r_j^2 - 2\left(\mathbf{r_i} \cdot \mathbf{r_j}\right) \tag{E.9a}$$

$$r_{ij}^4 = \left(\mathbf{r_i} - \mathbf{r_j}\right)^4 = r_i^4 + r_j^4 + 2r_i^2 r_j^2 - 4\left(r_i^2 + r_j^2\right)\left(\mathbf{r_i} \cdot \mathbf{r_j}\right) + 4\left(\mathbf{r_i} \cdot \mathbf{r_j}\right)^2 \tag{E.9b}$$

$$\begin{aligned} r_{ij}^6 = \left(\mathbf{r_i} - \mathbf{r_j}\right)^6 &= r_i^6 + r_j^6 + 3\left(r_i^4 r_j^2 + r_i^2 r_j^4\right) \\ &-6\left(r_i^4 + r_j^4 + 2r_i^2 r_j^2\right)\left(\mathbf{r_i} \cdot \mathbf{r_j}\right) + 12\left(r_i^2 + r_j^2\right)\left(\mathbf{r_i} \cdot \mathbf{r_j}\right)^2 - 8\left(\mathbf{r_i} \cdot \mathbf{r_j}\right)^3 \end{aligned} \tag{E.9c}$$

If the coordinates origin is chosen at the center of mass of the nanoparticle, then integration of eqs. E.9a, E.9b and E.9c according to eq. 5.8 cancel all the terms containing odd powers of $(\mathbf{r_i} \cdot \mathbf{r_j})$. Thus the second, fourth and sixth moments of r_{ij} are

$$\Delta r_2 = \frac{\int\limits_V g(\mathbf{r}) r^2 dV}{\int\limits_V g(\mathbf{r}) dV} \tag{E.10a}$$

$$\Delta r_4 = \frac{1}{\int\limits_{V_i}\int\limits_{V_j} g(\mathbf{r_i})g(\mathbf{r_j})dV_i dV_j}\left[\left(\int\limits_V g(\mathbf{r})dV\right)\left(\int\limits_V g(\mathbf{r})r^4 dV\right)+\left(\int\limits_V g(\mathbf{r})r^2 dV\right)^2 \right. \tag{E.10b}$$

$$\left. +2\int\limits_{V_i}\int\limits_{V_j} g(\mathbf{r_i})g(\mathbf{r_j})(\mathbf{r_i}\cdot\mathbf{r_j})^2 dV_i dV_j \right]$$

$$\Delta r_6 = \frac{1}{\int\limits_{V_i}\int\limits_{V_j} g(\mathbf{r_i})g(\mathbf{r_j})dV_i dV_j}\left[\left(\int\limits_V g(\mathbf{r})dV\right)\left(\int\limits_V g(\mathbf{r})r^6 dV\right)\right. \tag{E.10c}$$

$$\left. +3\left(\int\limits_V g(\mathbf{r})r^4 dV\right)\left(\int\limits_V g(\mathbf{r})r^2 dV\right)+12\int\limits_{V_i}\int\limits_{V_j} g(\mathbf{r_i})g(\mathbf{r_j})r_i^2(\mathbf{r_i}\cdot\mathbf{r_j})^2 dV_i dV_j \right]$$

If the particle is large enough to consider that it has a uniform mass distribution such that g(**r**)=1, the volume integrals can be taken over the nanoparticle shape and eqs. 5.9a, 5.9b and 5.9c are obtained

$$\Delta r_2 = \frac{1}{V}\int\limits_V r^2 dV \tag{5.9a}$$

$$\Delta r_4 = \frac{1}{V^2}\left[V\int\limits_V r^4 dV + \left(\int\limits_V r^2 dV\right)^2 + 2\int\limits_{V_i}\int\limits_{V_j}(\mathbf{r_i}\cdot\mathbf{r_j})^2 dV_j dV_i\right] \tag{5.9b}$$

$$\Delta r_6 = \frac{1}{V^2}\left[V\int\limits_V r^6 dV + 3\left(\int\limits_V r^4 dV\right)\cdot\left(\int\limits_V r^2 dV\right)+12\int\limits_{V_i}\int\limits_{V_j} r_i^2(\mathbf{r_i}\cdot\mathbf{r_j})^2 dV_j dV_i\right] \tag{5.9c}$$

Derivation of Schulz-Zimm distribution moments

Derivation of the expression for the n-moment of the Schulz-Zimm distribution is done for illustrative purposes. The moments of the distribution should not be confused with

Δr_n, which are the moments of the difference of distances within a nanoparticle. The Shulz-Zimm distribution function is

$$w(x) = \frac{h^{k+1}}{\Gamma\left(k+1\right)} x^{k} e^{-hx} \tag{E.11}$$

where h = (k+1)/x_x and k = 1/(P_x - 1); x is the x-averaged x and Px is the polydispersity of x defined as x_x/x_n, where x_n is the number average x. The n-moment of the distribution is

$$\left\langle x^{n} \right\rangle_{x} = \int_{0}^{\infty} w(x) x^{n} dx = \int_{0}^{\infty} \frac{h^{k+1}}{\Gamma\left(k+1\right)} x^{k} e^{-hx} x^{n} dx \tag{E.12}$$

Equation E.12 can be solved using integration by parts and assigning

$$u = x^{k+n} \qquad du = \left(k+n\right) x^{k+n-1}$$

$$dv = \frac{h^{k+1}}{\Gamma\left(k+1\right)} e^{-hx} dx \qquad v = \frac{-h^{k+1}}{h\Gamma\left(k+1\right)} e^{-hx}$$

thus

$$\begin{aligned} \left\langle x^{n} \right\rangle_{w} &= \int_{0}^{\infty} \frac{h^{k+1} e^{-hx}}{\Gamma\left(k+1\right)} x^{k+n} dx \\ &= -x^{n+k} \left. \frac{h^{k} e^{-hx}}{\Gamma\left(k+1\right)} \right|_{0}^{\infty} + \frac{\left(k+n\right)}{h} \int_{0}^{\infty} \frac{h^{k+1} e^{-hx}}{\Gamma\left(k+1\right)} x^{k+n-1} dx = \frac{k+n}{h} \int_{0}^{\infty} \frac{h^{k+1} e^{-hx}}{\Gamma\left(k+1\right)} x^{k+n-1} dx \end{aligned} \tag{E.13}$$

Integrating by parts n times gives

$$\left\langle x^{n} \right\rangle_{w} = \int_{0}^{\infty} \frac{h^{k+1} e^{-hx}}{\Gamma\left(k+1\right)} x^{k+n} dx = \frac{\left(k+n\right)\left(k+n-1\right)\ldots\left(k+n-\left(n-1\right)\right)}{h^{n}} \int_{0}^{\infty} \frac{h^{k+1} e^{-hx}}{\Gamma\left(k+1\right)} x^{k} dx \tag{E.14}$$

The integral in the last term corresponds to $\int w(x)dx = 1$, thus the moment of the Schulz-Zimm distribution is

$$\left\langle x^n \right\rangle_w = \int_0^\infty w(x) x^n dx = \int_0^\infty \frac{h^{k+1} e^{-hx}}{\Gamma(k+1)} x^{k+n} dx = \frac{(k+n)!}{h^n k!} = \frac{x_x^n (k+n)!}{(k+1)^n k!} \qquad (E.15)$$

Equation 5.11 arises from eq. E.15

$$\int_0^\infty\int_0^\infty\int_0^\infty w(A)w(B)w(C)A^n B^m C^p dAdBdC = \left[\frac{A_A^n (k_A+n)!}{(k_A+1)^n k_A!}\right]\left[\frac{B_B^m (k_B+n)!}{(k_B+1)^m k_B!}\right]\left[\frac{C_C^p (k_C+n)!}{(k_C+1)^m k_C!}\right]$$

(5.11)

Form factor of rectangular parallelepipeds and triaxial ellipsoids

The form factor of a rectangular parallelepiped with Axis A, B and C is[1]

$$P(q,a,c) = \int_0^1 \phi_Q\left(\mu\sqrt{1-\sigma^2}, a\right)\left[\frac{\sin(\mu c\sigma/2)}{\mu c\sigma/2}\right]^2 d\sigma \qquad (E.16)$$

where

$$\phi_Q(\mu, a) = \int_0^1 \left\{ \frac{\sin\left[\frac{\mu}{2}\cdot\cos\left(\frac{\pi}{2}\cdot u\right)\right]}{\frac{\mu}{2}\cdot\cos\left(\frac{\pi}{2}\cdot u\right)} \cdot \frac{\sin\left[\frac{\mu a}{2}\cdot\sin\left(\frac{\pi}{2}\cdot u\right)\right]}{\frac{\mu a}{2}\cdot\sin\left(\frac{\pi}{2}\cdot u\right)} \right\}^2 du \qquad (E.17)$$

$\mu = qB$, $a = A/B$, $c = C/B$ and $q = (4\pi n_S/\lambda_0)\sin(\theta/2)$

The form factor of a triaxial ellipsoid with semiaxis a, b and c is[2]

$$P(q,a,b,c) = \int_0^1\int_0^1 \phi^2 \left\{ q\left[a^2\cos^2(\pi x/2) + b^2\sin^2(\pi x/2)\left(1-y^2\right) + c^2 y^2\right]^{1/2} \right\} dxdy \qquad (E.18)$$

where

$$\phi^2(t) = 9\left(\frac{\sin t - t\cos t}{t^3}\right)^2 \qquad (E.19)$$

and $a < b < c$

References

1. Mittelbach, P.; Porod, G. Small-Angle X-Ray Scattering by Dilute Colloid Systems. The Calculation of Scattering Curves for Parallelepipeds. *Acta Phys. Austriaca* **1961***, 14*, 185-211.

2. Feigin, L. A.; Svergun, D. I. In *Structure Analysis by Small-Angle X-Ray and Neutron Scattering;* Taylor, G. W., Ed.; Plenum Press: New York, 1987; pp 90-94.

Appendix F

Correction of AFM Images for Tip Broadening

The image processing required for the analysis of AFM images is described here. The free license software Gwyddion 2.22 is employed. First open the raw data image from the File → Open menu. Figure F.1 describes an image of the raw data taken with the AFM.

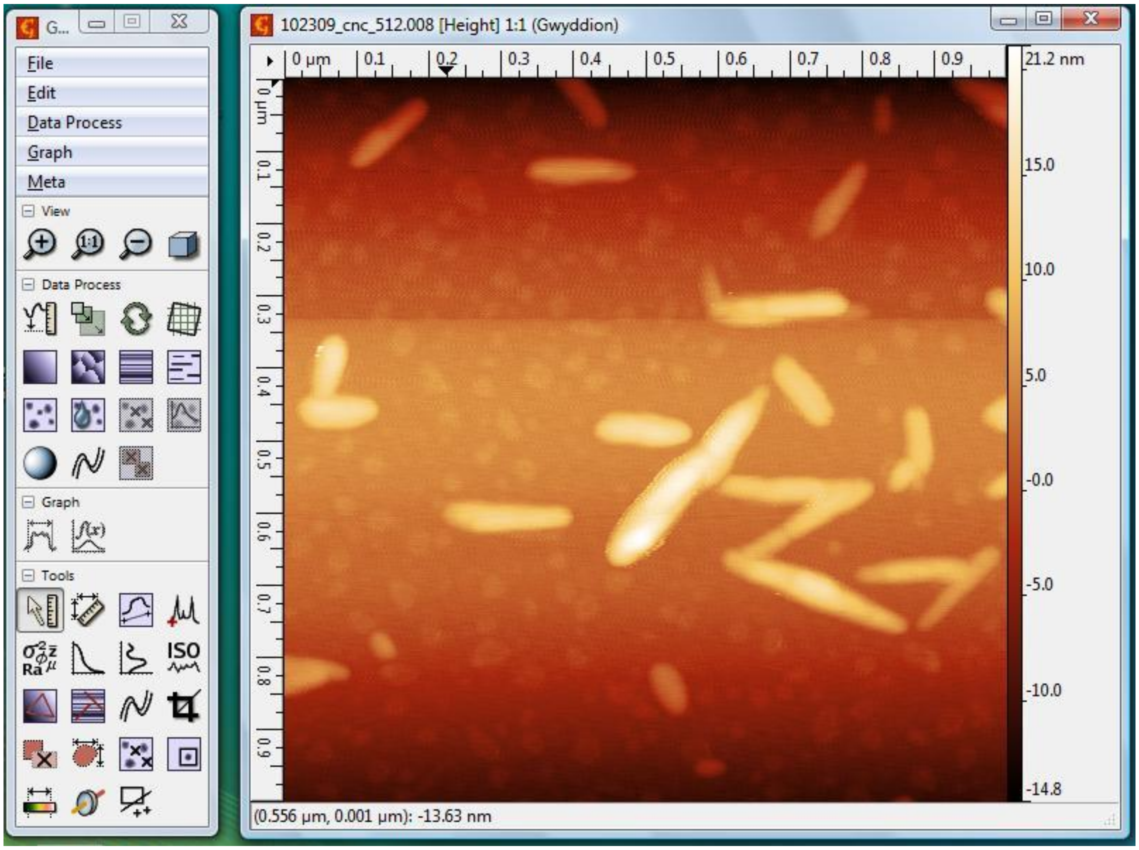

Figure F.1. Snapshot of a Gwyddion 2.22 session showing an AFM raw image.

The first step is to draw a mask on the particles. For this purpose click on the "Edit mask" icon under the "tools" section; the "Freehand mask drawing" tool is very useful. Figure F.2 shows the masked particles. Hide the mask editor when done. If the background on the raw image is too large it will not be possible to observe the particles. If that is the case, no attempt should be done to mask the particles; instead proceed to background subtraction.

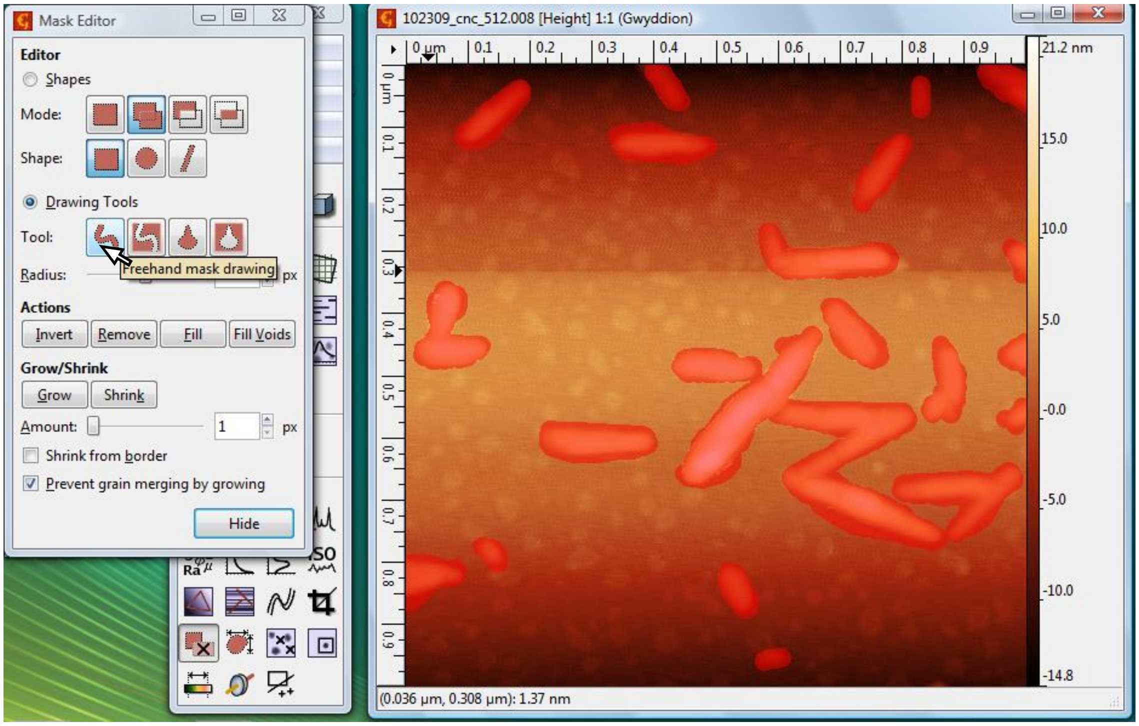

Amount: 1 px

☐ Shrink from border

☑ Prevent grain merging by growing

(0.036 µm, 0.308 µm): 1.37 nm

Figure F.2. Nanoparticles masked during a Gwyddion 2.22 session.

Click on the “Remove polynomial background” button under the “Data Process” section. A new window should appear as shown in Figure F.3. This tool fits the entire image in the x and y directions to polynomial functions and subtract it. If the particles are masked, then the “Exclude mask region” must be selected to exclude the nanoparticles from the background. Choose the order of the polynomials; they should not be more than order 2, since choosing a higher order can lead to a loss of details. This is especially important if the nanoparticles were not visible and could not be masked. Typically, an order two in the vertical direction, and an order 1 in the y direction is enough. If not sure, use the “Extract profile” button to get a height profile in both directions and then decide the order of the polynomials. Click on “OK”; the leveled image should appear next. To remove the mask, click on the “Edit mask” icon and choose “Remove”

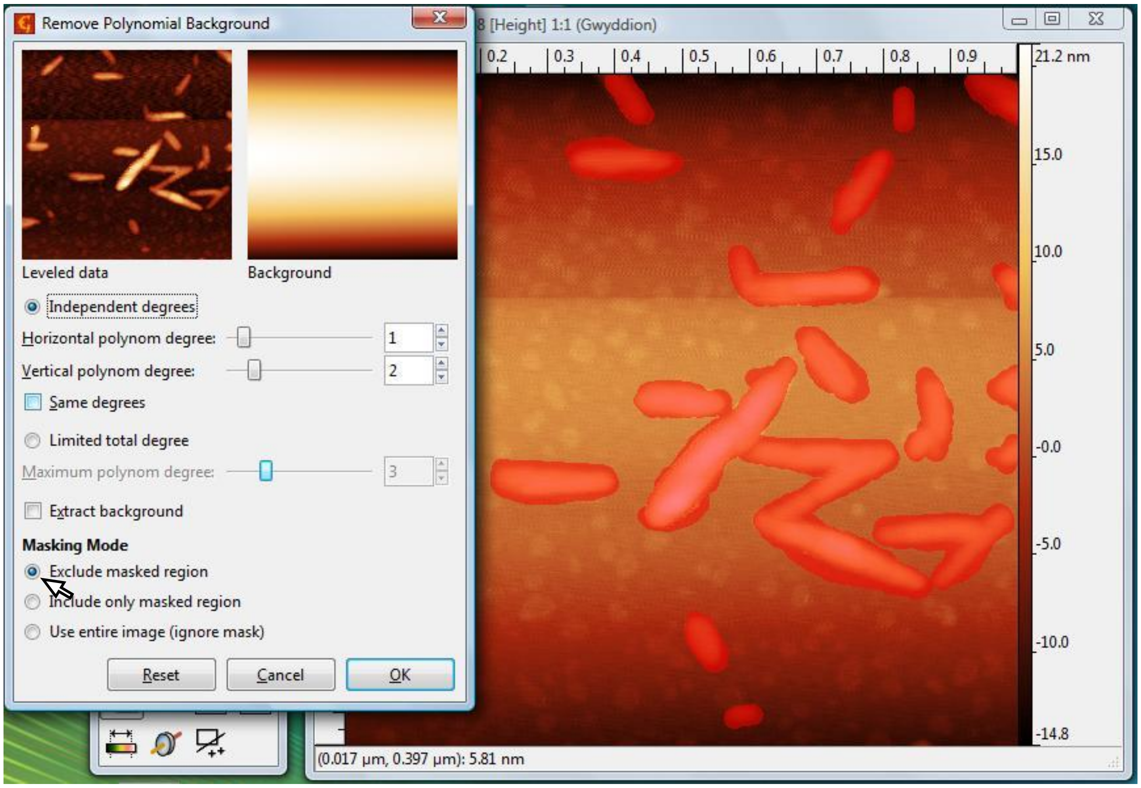

● Independent degrees
Horizontal polynom degree: 1
Vertical polynom degree: 2
☐ Same degrees
○ Limited total degree
Maximum polynom degree: 3
☐ Extract background

Masking Mode
● Exclude masked region
○ Include only masked region
○ Use entire image (ignore mask)

(0.017 µm, 0.397 µm): 5.81 nm

Figure F.3. Removal of background from an AFM image.

Very often the leveled image will show scan streaks; to eliminate them click on the “Correct lines by matching height median” button under the “Data Process” section. This tool calculates the median of all horizontal lines and then shifts each line to match the medians. The correction will be performed automatically after clicking on the link; there is no need to input any parameters. Unfortunately, the “match median height” tool does not allow excluding mask regions from the computation; however, given the definition of median, this should not affect considerably as long as the majority of the picture is composed by the substrate and not the nanoparticles. The image after background and scan lines corrections is shown in Figure F.4.

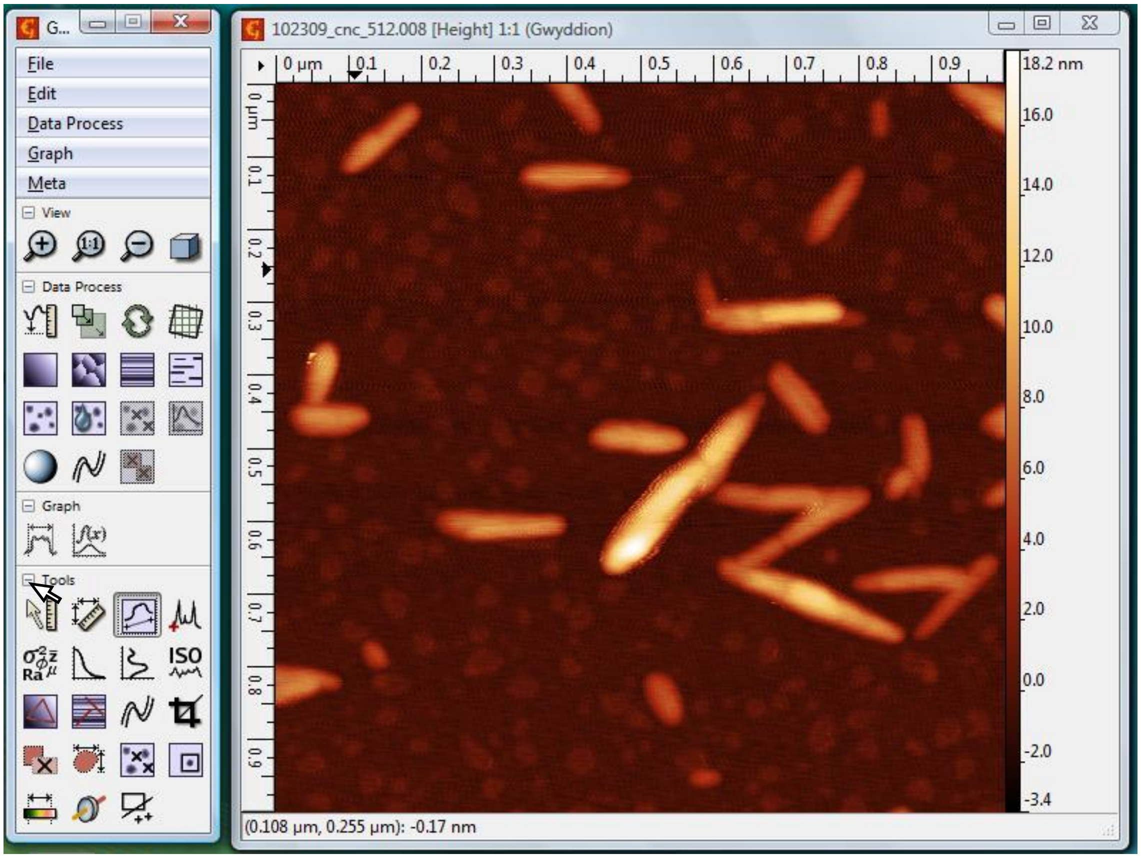

Figure F.4. Image corrected for background and scan lines.

The next step is to obtain a model for the tip used to take the picture. This is done by using the same tip to image a standard surface; the resolution must be the same for both pictures. First open the raw data image of the standard surface and perform a background correction; do not mask any details. If the same AFM head is used, the order of the polynomials should not vary given that the background arises from the properties of the piezo-tube and the scanner. The image of a porous aluminum standard surface after background correction is shown in Figure F.5.

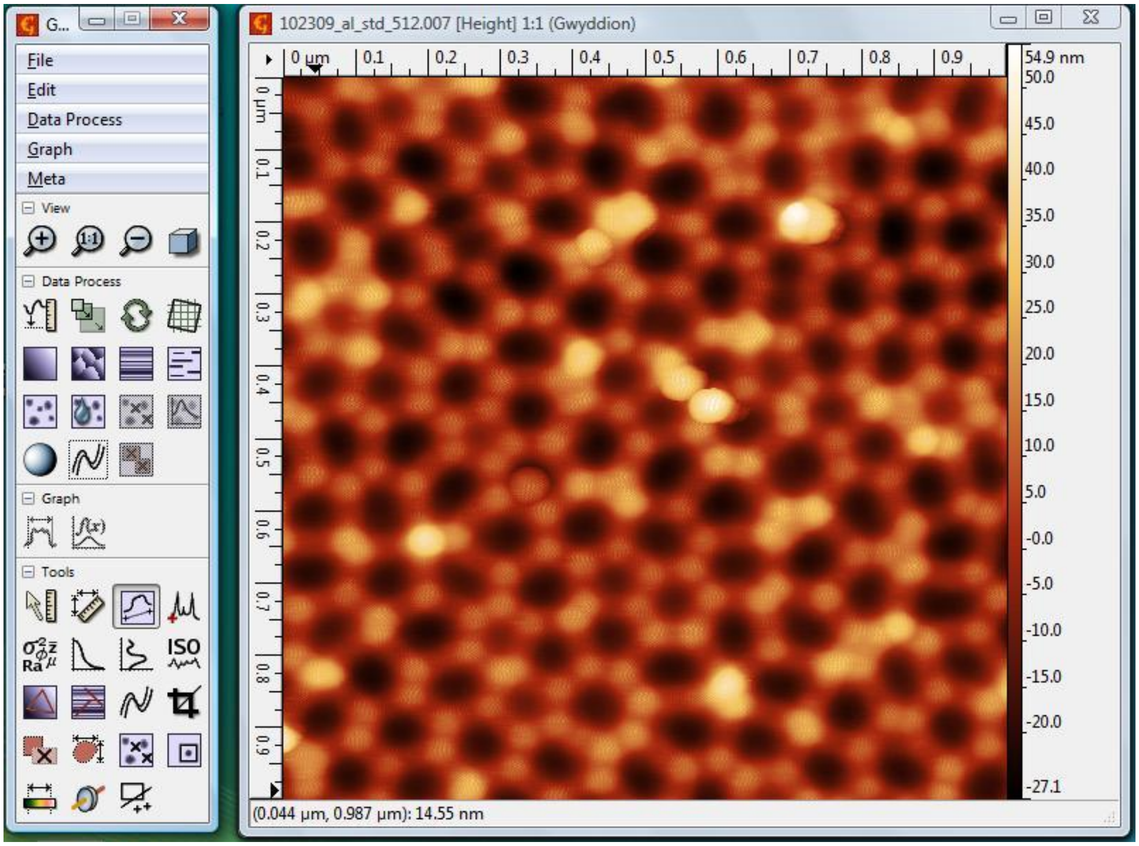

Figure F.5. AFM image of a porous aluminum surface during a Gwyddion 2.22 session.

To model the tip go to Data Process→Tip→Blind Estimation. A window will appear were some parameters must be introduced (Figure F.6). The estimated tip size depends on the resolution of the image used; for a picture with 512 points/line with dimensions of 1x1 µm, a tip size of 50 pixels is appropriate. The size must be overestimated to ensure that the entire tip is imaged. Click on the "Same resolution" box. A "noise suppression threshold" must be provided; since the image in Figure F.5 is very noisy the threshold was set to 11 nm. The partial estimation is recommended since it gives a good tip model and it is relatively fast, while the full estimation is too lengthy. The modeled tip is shown in Figure F.7; to obtain a 3D image click on the "Display a 3D view of data" icon

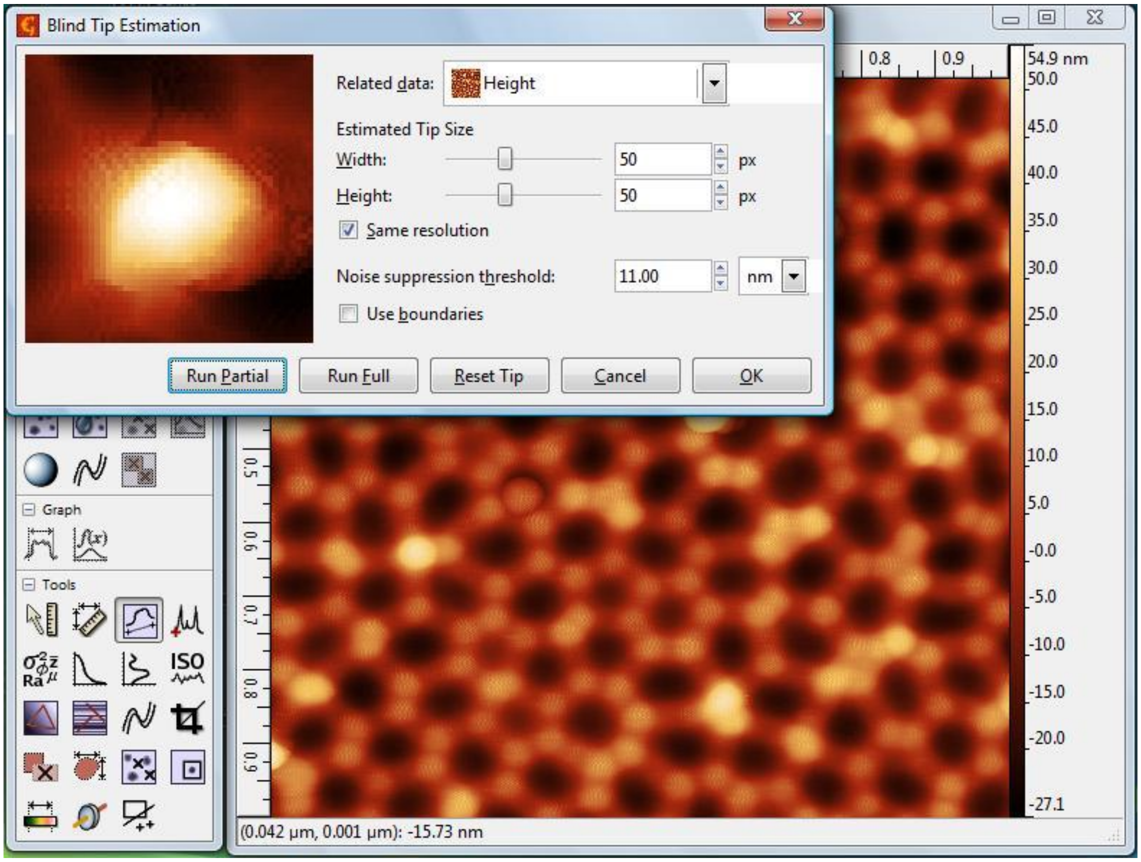

Blind Tip Estimation

Related data: Height

Estimated Tip Size

Width: 50 px

Height: 50 px

☑ Same resolution

Noise suppression threshold: 11.00 nm

☐ Use boundaries

Run Partial | Run Full | Reset Tip | Cancel | OK

(0.042 µm, 0.001 µm): -15.73 nm

Figure F.6. Blind tip estimation window.

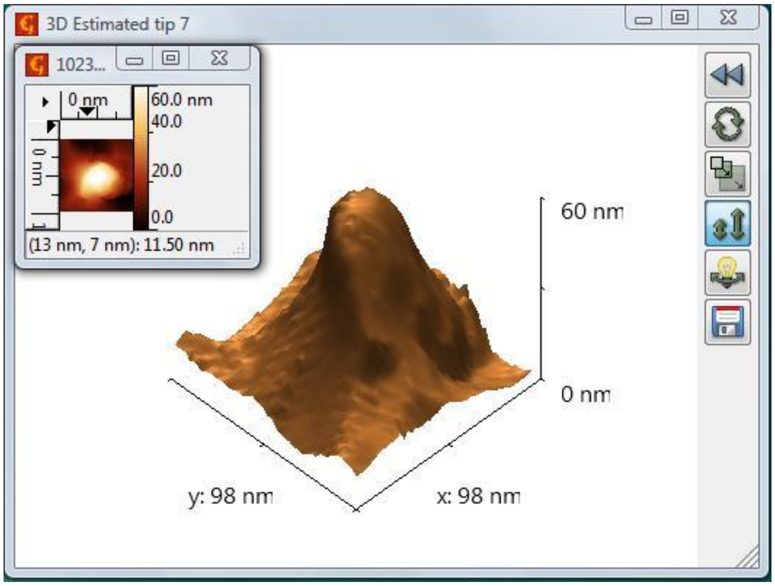

3D Estimated tip 7

1023...

(13 nm, 7 nm): 11.50 nm

Figure F.7. Tip model estimated with Gwyddion 2.22.

To deconvolute the tip shape from the picture in Figure F.4, go to Data Process→Tip→Surface Reconstruction (the window with the image of the nanoparticles must be active). From the "Surface Reconstruction" window, select the respective tip and click on "OK" (Figure F.8). The result is presented in Figure F.9.

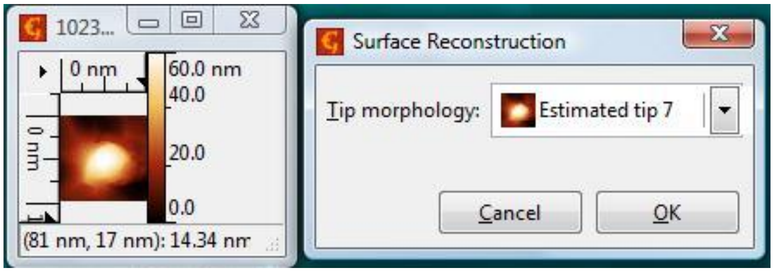

(81 nm, 17 nm): 14.34 nm

Tip morphology: Estimated tip 7

Figure F.8. Surface reconstruction and tip image windows.

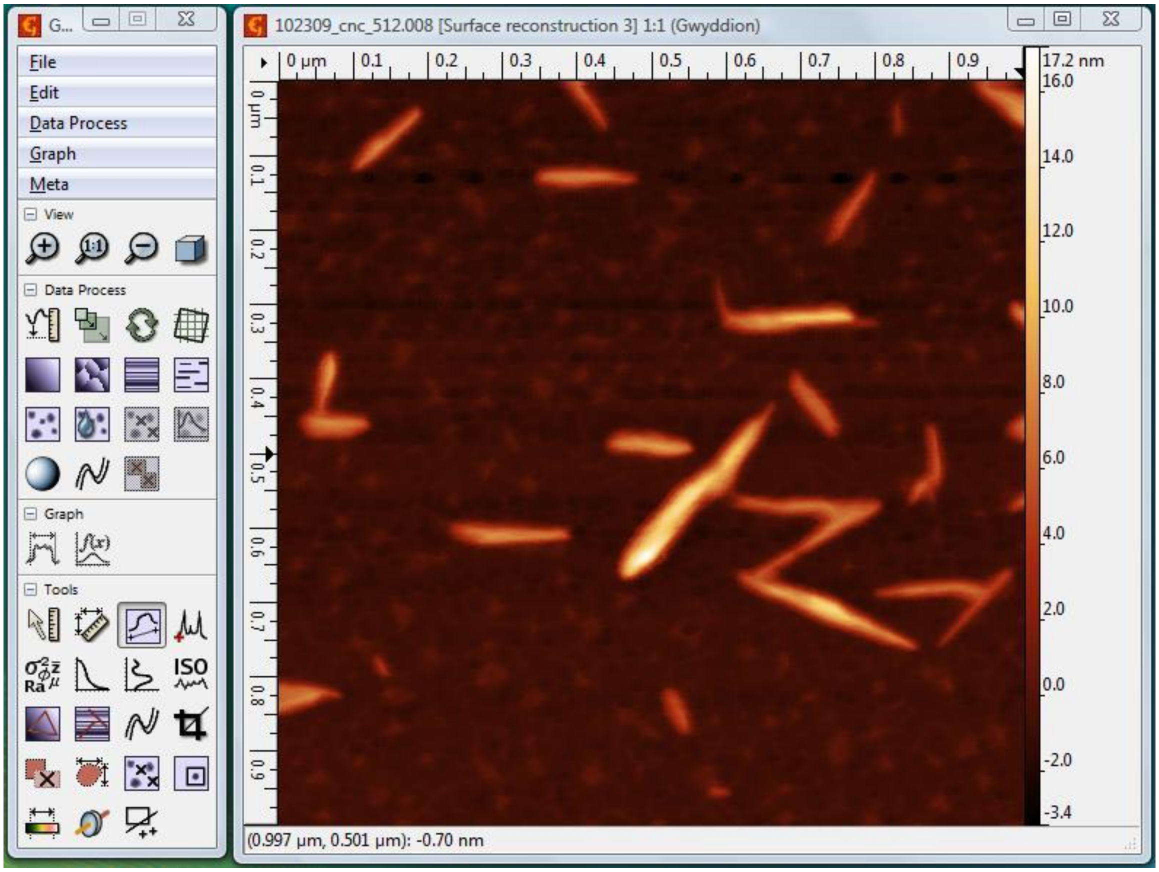

102309_cnc_512.008 [Surface reconstruction 3] 1:1 (Gwyddion)

(0.997 µm, 0.501 µm): -0.70 nm

Figure F.9. Image after tip deconvolution with Gwyddion 2.22.

Appendix G

Permissions

AMERICAN CHEMICAL SOCIETY LICENSE
TERMS AND CONDITIONS

Mar 03, 2011

This is a License Agreement between Esteban E Urena ("You") and American Chemical Society ("American Chemical Society") provided by Copyright Clearance Center ("CCC"). The license consists of your order details, the terms and conditions provided by American Chemical Society, and the payment terms and conditions.

All payments must be made in full to CCC. For payment instructions, please see information listed at the bottom of this form.

License Number	2621380102899
License Date	Mar 03, 2011
Licensed content publisher	American Chemical Society
Licensed content publication	Langmuir
Licensed content title	Effect of Jet Stretch and Particle Load on Cellulose Nanocrystal−Alginate Nanocomposite Fibers
Licensed content author	Esteban E. Ureña-Benavides et al.
Licensed content date	Sep 1, 2010
Volume number	26
Issue number	17
Type of Use	Thesis/Dissertation

Requestor type	Not specified
Format	Print
Portion	Full article
Author of this ACS article	Yes
Order reference number	
Title of the thesis / dissertation	CELLULOSE NANOCRYSTALS PROPERTIES AND APPLICATIONS TO RENEWABLE NANOCOMPOSITES
Expected completion date	Mar 2011
Estimated size(pages)	200
Billing Type	Invoice
Billing Address	804 Creekside Dr. Apt. 4 Clemson, SC 29631 United States
Customer reference info	
Total	0.00 USD

AMERICAN CHEMICAL SOCIETY LICENSE
TERMS AND CONDITIONS

Apr 19, 2011

This is a License Agreement between Esteban E Urena ("You") and American Chemical Society ("American Chemical Society") provided by Copyright Clearance Center ("CCC"). The license consists of your order details, the terms and conditions provided by American Chemical Society, and the payment terms and conditions.

All payments must be made in full to CCC. For payment instructions, please see information listed at the bottom of this form.

License Number	2652531421384
License Date	Apr 19, 2011
Licensed content publisher	American Chemical Society
Licensed content publication	Macromolecules
Licensed content title	Wide-Angle X-ray Diffraction of Cellulose Nanocrystal−Alginate Nanocomposite Fibers
Licensed content author	Esteban E. Ureña-Benavides et al.
Licensed content date	Apr 1, 2011
Volume number	0
Issue number	0
Type of Use	Thesis/Dissertation
Requestor type	Not specified
Format	Print
Portion	Full article
Author of this ACS article	Yes

Order reference number	
Title of the thesis / dissertation	CELLULOSE NANOCRYSTALS PROPERTIES AND APPLICATIONS IN RENEWABLE NANOCOMPOSITES
Expected completion date	May 2011
Estimated size(pages)	200
Billing Type	Invoice
Billing Address	804 Creekside Dr. Apt. 4 Clemson, SC 29631 United States
Customer reference info	
Total	0.00 USD

Terms and Conditions

Thesis/Dissertation

ACS / RIGHTSLINK TERMS & CONDITIONS
THESIS/DISSERTATION

INTRODUCTION
The publisher for this copyrighted material is the American Chemical Society. By clicking "accept" in connection with completing this licensing transaction, you agree that the following terms and conditions apply to this transaction (along with the Billing and Payment terms and conditions established by Copyright Clearance Center, Inc. ("CCC"), at the time that you opened your Rightslink account and that are available at any time at <http://myaccount.copyright.com>).

LIMITED LICENSE
Publisher hereby grants to you a non-exclusive license to use this material. Licenses are for one-time use only with a maximum distribution equal to the number that you identified in the licensing process.

GEOGRAPHIC RIGHTS: SCOPE
Licenses may be exercised anywhere in the world.

RESERVATION OF RIGHTS
Publisher reserves all rights not specifically granted in the combination of (i) the license details provided by you and accepted in the course of this licensing transaction, (ii) these terms and conditions and (iii) CCC's Billing and Payment terms and conditions.

PORTION RIGHTS STATEMENT: DISCLAIMER
If you seek to reuse a portion from an ACS publication, it is your responsibility to examine each portion as published to determine whether a credit to, or copyright notice of, a third party owner was published adjacent to the item. You may only obtain permission via Rightslink to use material owned by ACS. Permission to use any material published in an ACS publication, journal, or article which is reprinted with permission of a third party must be obtained from the third party owner. ACS disclaims any responsibility for any use you make of items owned by third parties without their permission.

REVOCATION
The American Chemical Society reserves the right to revoke a license for any reason, including but not limited to advertising and promotional uses of ACS content, third party usage, and incorrect figure source attribution.

LICENSE CONTINGENT ON PAYMENT
While you may exercise the rights licensed immediately upon issuance of the license at the end of the licensing process for the transaction, provided that you have disclosed complete and accurate details of your proposed use, no license is finally effective unless and until full payment is received from you (by CCC) as provided in CCC's Billing and Payment terms and conditions. If full payment is not received on a timely basis, then any license preliminarily granted shall be deemed automatically revoked and shall be void as if never granted. Further, in the event that you breach any of these terms and conditions or any of CCC's Billing and Payment terms and conditions, the license is automatically revoked and shall be void as if never granted. Use of materials as described in a revoked license, as well as any use of the materials beyond the scope of an unrevoked license, may constitute copyright infringement and publisher reserves the right to take any and all action to protect its copyright in the materials.

COPYRIGHT NOTICE: DISCLAIMER
You must include the following copyright and permission notice in connection with any reproduction of the licensed material: "Reprinted (“Adapted” or “in part”) with permission from REFERENCE CITATION. Copyright YEAR American Chemical Society."

WARRANTIES: NONE
Publisher makes no representations or warranties with respect to the licensed material.

INDEMNITY
You hereby indemnify and agree to hold harmless publisher and CCC, and their respective officers, directors, employees and agents, from and against any and all claims arising out of your use of the licensed material other than as specifically authorized pursuant to this license.

NO TRANSFER OF LICENSE
This license is personal to you or your publisher and may not be sublicensed, assigned, or transferred by you to any other person without publisher's written permission.

NO AMENDMENT EXCEPT IN WRITING
This license may not be amended except in a writing signed by both parties (or, in the case of publisher, by CCC on publisher's behalf).

OBJECTION TO CONTRARY TERMS
Publisher hereby objects to any terms contained in any purchase order, acknowledgment, check endorsement or other writing prepared by you, which terms are inconsistent with these terms and conditions or CCC's Billing and Payment terms and conditions. These terms and conditions, together with CCC's Billing and Payment terms and conditions (which are incorporated herein), comprise the entire agreement between you and publisher (and CCC) concerning this licensing transaction. In the event of any conflict between your obligations established by these terms and conditions and those established by CCC's Billing and Payment terms and conditions, these terms and conditions shall control.

JURISDICTION
This license transaction shall be governed by and construed in accordance with the laws of the District of Columbia. You hereby agree to submit to the jurisdiction of the courts located in the District of Columbia for purposes of resolving any disputes that may arise in connection with this licensing transaction.

THESES/DISSERTATION TERMS
Regarding your request for permission to include **your** paper(s) or portions of text from **your** paper(s) in your thesis/dissertation, permission is now automatically granted; please pay special attention to the **implications** paragraph below. The Copyright Subcommittee of the Joint Board/Council Committees on Publications approved the following:

Copyright permission for published and submitted material from theses and dissertations
ACS extends blanket permission to students to include in their theses and dissertations their own articles, or portions thereof, that have been published in ACS journals or

submitted to ACS journals for publication, provided that the ACS copyright credit line is noted on the appropriate page(s).

Publishing **implications** of electronic publication of theses and dissertation material
Students and their mentors should be aware that posting of theses and dissertation material on the Web prior to submission of material from that thesis or dissertation to an ACS journal may affect publication in that journal. Whether Web posting is considered prior publication may be evaluated on a case-by-case basis by the journal's editor. If an ACS journal editor considers Web posting to be "prior publication", the paper will not be accepted for publication in that journal. If you intend to submit your unpublished paper to ACS for publication, check with the appropriate editor prior to posting your manuscript electronically.

Reuse/Republication of the Entire Work in Theses or Collections: Authors may reuse all or part of the Submitted, Accepted or Published Work in a thesis or dissertation that the author writes and is required to submit to satisfy the criteria of degree-granting institutions. Such reuse is permitted subject to the ACS' "Ethical Guidelines to Publication of Chemical Research" (http://pubs.acs.org/page/policy/ethics/index.html); the author should secure written confirmation (via letter or email) from the respective ACS journal editor(s) to avoid potential conflicts with journal prior publication*/embargo policies. Appropriate citation of the Published Work must be made. If the thesis or dissertation to be published is in electronic format, a direct link to the Published Work must also be included using the ACS Articles on Request author-directed link - see http://pubs.acs.org/page/policy/articlesonrequest/index.html

* Prior publication policies of ACS journals are posted on the ACS website at http://pubs.acs.org/page/policy/prior/index.html

If your paper has not yet been published by ACS, please print the following credit line on the first page of your article: "Reproduced (or 'Reproduced in part') with permission from [JOURNAL NAME], in press (or 'submitted for publication'). Unpublished work copyright [CURRENT YEAR] American Chemical Society." Include appropriate information.

If your paper has already been published by ACS and you want to include the text or portions of the text in your thesis/dissertation in **print or microfilm formats**, please print the ACS copyright credit line on the first page of your article: "Reproduced (or 'Reproduced in part') with permission from [FULL REFERENCE CITATION.] Copyright [YEAR] American Chemical Society." Include appropriate information.

Submission to a Dissertation Distributor: If you plan to submit your thesis to UMI or to another dissertation distributor, you should not include the unpublished ACS paper in your thesis if the thesis will be disseminated electronically, until ACS has published your